Fundamentals and Applications of Mo and Nb Alloying in High Performance Steels

Volume 2

Proceedings of the Second International Symposium on Fundamentals and Applications of Mo and Nb Alloying in High Performance Steels. Held in Jeju Island, South Korea. 24–26 April 2013.

Editor-in-Chief

Hardy Mohrbacher, NiobelCon, Belgium

International Organizing Committee

Hardy Mohrbacher, NiobelCon, Belgium
Isaac Cho, H2 Corporation, South Korea
Nicole Kinsman, IMOA, UK
Marcos Stuart, CBMM, Brazil
Caroline Gomes, CBMM Asia, Singapore

CBMM | **IMOA** | **TMS**

TABLE OF CONTENTS
Fundamentals and Applications of Mo and Nb Alloying in High Performance Steels: Volume 2

Preface

Following the highly successful 'Fundamentals and Applications of Mo and Nb Alloying in High Performance Steels' symposium, held in Taiwan in 2011, Companhia Brasileira de Metalurgia e Mineração (CBMM) joined forces for a second time with The International Molybdenum Association (IMOA) to organize this latest unique event in South Korea. Based on per capita consumption, South Korea is the most 'steel intensive' country in the world and features, prominently, in the current 'top ten' of global steel producers. It is the home base of POSCO, a mega player on the world stage, the fast growing Hyundai Steel and many other smaller but significant suppliers. South Korea features particularly strong and active steel consuming industries, producing cars and trucks, consumer goods, heavy equipment, goods for the oil and gas industry, as well as ships and offshore platforms. All these sectors require high performance steels supplied as strip, plate, forgings or castings.

As a direct consequence of its rapidly increasing status in the field, South Korea also features world-class steel research in a variety of prestigious universities and institutes. This background identified the country as a perfect place to host a follow-up symposium dealing with the important interactions of the key elements niobium and molybdenum.

Accordingly, the two-day symposium presented carefully selected, invited talks focusing on aspects of niobium and molybdenum alloying along the processing chain and with respect to particular applications. The presentations were organized into three sessions:

- The opening session 'Physical Metallurgy' covered some of the fundamental aspects and effects of niobium and molybdenum as alloying elements in steel, based on dedicated academic research;
- The session 'Product Development and Applications' then demonstrated the benefits of niobium and molybdenum in state-of-the-art strip and plate products for use in major industrial sectors, such as automotive, oil and gas and construction;
- The symposium also extended its scope beyond flat products, and innovative, diverse and important developments in the forgings and casting areas were identified and discussed.

This highly successful second symposium on Mo and Nb Alloying in High Performance Steels was held on Jeju Island, South Korea in April 2013, with the additional support of POSCO, Hyundai Steel and the Korean Institute of Metals. Twenty-one high quality presentations detailed the specific metallurgical effects of both alloying elements in a wide range of steels and alloys covering automotive, structural, pipeline, machinery and mining applications. The audience consisted of 112 delegates from 16 countries, representing a total of 60 companies and research institutes. These proceedings contain papers covering most of the presentations held in the two-day program.

Hardy Mohrbacher
NiobelCon bvba
Editor-in-Chief

The International Molybdenum Association (IMOA)

IMOA represents 85% of mine production plus all conversion capacity in established markets and a growing proportion of production in developing markets, including significant producers in China. It also represents traders, downstream processors, consumers and other industry participants.

The Association is dedicated to serving the best interests of its members and works continually to enhance the reputation of the industry. The key areas of activity are:

- Proactive development of existing and potential new markets around the world through a network of technical, industry and application experts;
- Representing members in the increasingly global regulatory arena, engaging in science-based dialogue in support of the adoption of appropriate levels of regulation;
- Collecting, disseminating and maintaining statistics on the molybdenum market, excluding price and related information;
- Acting as a central repository of information about molybdenum, its properties, uses and products.

In addition IMOA's Annual General Meeting provides a secure forum for networking, exchanging views and ideas to the benefit of a wide cross section of the industry – producers, converters, traders, intermediate producers and users – within the bounds of international competition law.

Tim Outerridge
Secretary-General
IMOA

Companhia Brasileira de Metalurgia e Mineração (CBMM)

CBMM is the world's leading supplier of niobium products and technology. The Brazilian company earned this market position through more than four decades of ongoing investment in processes and applications research across a wide spectrum of important end uses.

Fully integrated from the mine to final products, the company's goals are not only to satisfy the worldwide niobium demand in the form of ferroalloys, oxides and pure metal, but also to provide a framework of technological development with the objective of identifying how the element can be employed to maximum effect to enable industry to overcome many of today's major technical challenges.

CBMM is guided by this strategy and develops its business in a commercially prudent manner, through sustainable growth and always conscious of energy savings, cost reductions and environmental protection. Even though the company's mineral resources are unrivalled in quantity and quality, CBMM constantly strives to improve the flexibility and efficiency of operations. The same approach is deployed to enhance the value that the effective, efficient use of the element can deliver to customers.

The company's niobium research and development program employs a strong technical group to develop niobium applications. This group works with industry, universities, research institutes and end users on diverse projects around the world, and pursues new partnerships to explore and optimize the use of niobium.

Participation in this important symposium that addresses the mutual benefits of niobium and molybdenum in high performance steels is testimony to CBMM's commitment to continually improve products through technological innovation and collaboration.

<div align="right">

Marcos Stuart
Director of Technology
CBMM

</div>

EFFECTS OF COMBINING NIOBIUM AND MOLYBDENUM IN HSLA STEELS: FROM AUSTENITE CONDITIONING TO FINAL MICROSTRUCTURE

N. Isasti, B. Pereda, B. López, J.M. Rodriguez-Ibabe and P. Uranga

CEIT and TECNUN (University of Navarra), Donostia-San Sebastian, Basque Country, Spain

Keywords: Austenite Conditioning, Phase Transformations, EBSD Quantification, Microstructure, Mechanical Properties

Abstract

Three main topics are covered in this paper regarding Nb-Mo interactions in microalloyed steels. First, the synergistic behavior of Nb and Mo in enhancing solute drag effects and modifying recrystallization and precipitation kinetics in austenite under hot working conditions is analyzed. Then, the effect of different microalloying additions on the final phase transformations is examined. In addition to composition and austenite conditioning effects on the phases formed and the corresponding CCT diagrams, a quantitative study using an EBSD technique is described which was performed in order to measure unit size distributions and homogeneity of complex microstructures. Finally, the contribution of different strengthening mechanisms to yield strength is evaluated for different coiling temperatures and compositions.

Introduction

Nowadays, combinations of high strength and high toughness are required for applications such as gas and oil transportation pipes, offshore facilities and naval technologies [1,2]. Suitable combinations of microalloying additions contribute to an increase in strength directly through microstructural refinement, solid solution strengthening and precipitation hardening, as well as indirectly, through enhanced hardenability and associated modification of the resultant microstructure [3]. Nevertheless, toughness may be impaired depending on the selected processing strategy followed to achieve the strength requirements.

In this context, Mo addition is a common practice to increase strength and toughness in low C steels because of its effect in promoting low temperature transformation products after hot rolling [4]. On the other hand, the use of Nb is well known because of its ability to retard recrystallization both by solute drag and by strain induced precipitation, which leads to pancaked austenite and, after transformation, provides fine room temperature microstructures with improved mechanical properties [5].

Obviously, this simplified approach needs to be modulated depending on the specific compositions of each steel grade and thermomechanical route because interactions between microalloying elements become complex and multiple effects are interacting at the same time. This paper seeks to analyze the different interactions during austenite conditioning and phase transformations. Resulting from the two previous steps, the mechanical strength will be modified and the balance of the different strengthening contributions will depend on the Nb and Mo effects on grain size refinement, dislocation substructure, second phase formation and precipitation.

Materials and Experimental

In the present study seven steels were studied, with two Nb levels (0.03 and 0.06%) and three Mo levels (0, 0.16 and 0.31%). A CMn steel was also used for comparison purposes only. All the steels were experimental heats and their chemical compositions are listed in Table I.

Table I. Chemical Compositions of the Steels (wt.%)

Steel	C	Mn	Si	Nb	Mo	Al	N
CMn	0.05	1.58	0.05	-	0.01	0.03	0.005
3NbMo0	0.05	1.6	0.06	0.029	0.01	0.028	0.005
3NbMo16	0.05	1.58	0.04	0.028	0.16	0.027	0.005
3NbMo31	0.05	1.57	0.05	0.028	0.31	0.028	0.005
6NbMo0	0.05	1.56	0.05	0.06	0.01	0.028	0.004
6NbMo16	0.05	1.6	0.05	0.061	0.16	0.03	0.005
6NbMo31	0.05	1.57	0.05	0.059	0.31	0.031	0.005

For the austenite conditioning, softening and strain induced precipitation kinetics determination, torsion samples with a gauge length of 17 mm and a diameter of 7.5 mm were machined from 40 mm thickness plates. The torsion tests were carried out using a computer controlled torsion machine. After reheating, the samples were deformed using pass strains ranging from 0.2 to 0.4 and different interpass times. The non-recrystallization temperature was determined by using the standard method proposed by Bai et al. [6].

For the phase transformation analysis, dilatometry tests were performed in a Bähr DIL805A/D quenching and deformation dilatometer. Solid cylinders with a diameter of 5 mm and a length of 10 mm were employed. The steels were subjected to different thermomechanical schedules in order to obtain different austenite conditions: undeformed, Cycle A, and deformed, Cycles B and C, respectively. A more detailed description of the procedure followed may be found in Reference 7. For the mechanical property evaluation, plane strain compression tests were performed. After deformation, the samples were cooled down at approximately 10 ºC/s to different coiling temperatures from 450 ºC to 650 ºC, so as to evaluate the effect of the coiling temperature on the phase transformation. Coiling was simulated by holding for 1 hour followed by slow cooling in the furnace to room temperature (≈1 ºC/s). The schemes of the different schedules are illustrated in Figures 1 and 2.
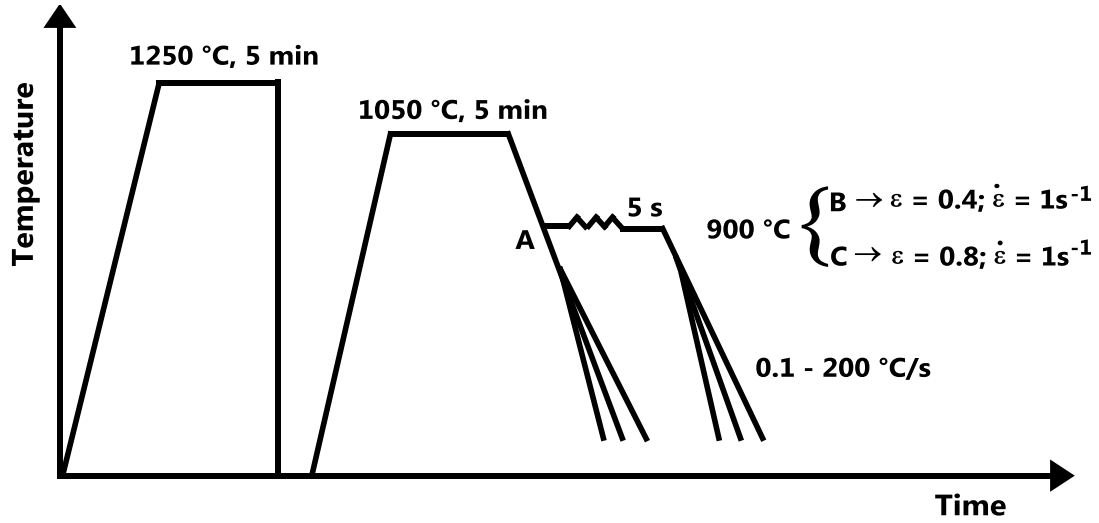
Figure 1. Schematic thermomechanical schedules applied for phase transformation analysis in dilatometry tests.
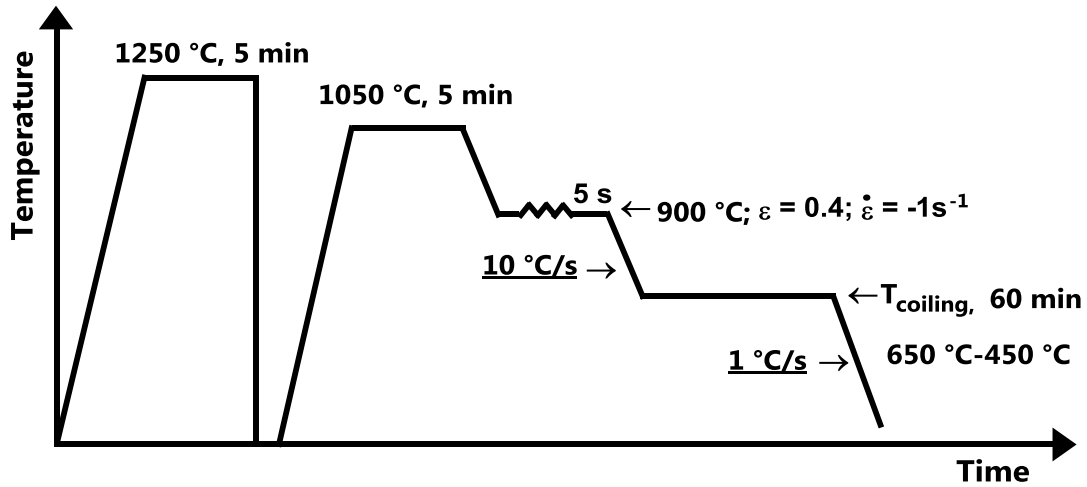
Figure 2. Schematic thermomechanical schedules for plane strain compression tests with different coiling temperatures (450, 550 and 650 °C).

The microstructures obtained from the samples were characterized, after etching in 2% Nital, by different characterization techniques: Optical Microscopy, Scanning Electron Microscopy (SEM) and Field Emission Gun Scanning Electron Microscopy (FEGSEM). In addition to the optical and scanning electron microscopy analysis, a more detailed microstructural characterization was performed on selected specimens using the EBSD technique (Electron Back Scattered Diffraction). On these samples the ferrite unit sizes and the Kernel Average Misorientation (KAM) parameter were measured. Scan step sizes ranging from 0.2 μm, for high resolution scans, to 1 μm, for general microstructural characterization, were used. Tensile specimens were machined from the plane strain compression samples. Tensile specimens with a diameter of

3

4 mm and an initial length of 17 mm were tested. The tensile tests were performed at room temperature at a strain rate of 10^{-3} s^{-1}.

Austenite Conditioning

The strain accumulation within recrystallized austenite prior to transformation is one of the key factors in order to achieve a fine and homogeneous final microstructure. Nb and Mo, by means of solute drag and strain induced precipitation mechanisms, are the most efficient elements to retain strain during the final deformation passes. Therefore, a deep understanding of the softening mechanism and strain induced precipitation kinetics is needed. The semi-empirical equations to model these mechanisms have been evolving to adapt them to new grades and new technologies, such as the direct rolling of thin slabs. In this regard, the kinetics of static recrystallization of microalloyed steels, covering a wide austenite size range, were investigated in previous works [8]. Taking into account the effect of microalloying elements in solution, the deformation parameters (ε strain, $\dot{\varepsilon}$ strain rate and T absolute temperature) and the initial austenite grain size (D_o), the following equation was deduced for low carbon microalloyed steels:

$$t_{0.5} = 9.92x10^{-11} \cdot D_0 \cdot \varepsilon^{-5.6D_0^{-0.15}} \cdot \dot{\varepsilon}^{-0.53} \cdot \exp\left(\frac{180000}{RT}\right) \cdot \exp\left[\left(\frac{275000}{T} - 185\right) \cdot [Nb]_{eff}\right] \quad (1)$$

where $t_{0.5}$ is the time required for 50% recrystallization and $[Nb]_{eff}$ is the amount of Nb in solution.

Softening Kinetics for Nb-Mo Steels

The extension of Equation 1 to Nb-Mo steels required the evaluation of the Mo solute drag effect. Akben et al. [9], defined a Solute Retardation Parameter (SRP) for static recrystallization describing the retardation produced by additions of 0.1 wt.% of the different microalloyed elements. For Nb in Nb-Mo steels this parameter reached a value of SRP = 265, 1.19 times higher than the value obtained for Nb steels, SRP = 222. On the other hand, the value associated with Mo in Nb-Mo steels, SRP = 20 was 0.09 times lower than the SRP corresponding to Nb. Using this relationship, one can amend the definition of $[Nb]_{eff}$ such as to obtain the same drag effect as that produced by Nb in Nb-Mo steels; a 1.19xNb factor must be considered, and 0.09xMo (eg. to obtain the same drag effect as that produced by 1 wt.% Mo, an amount of 0.09 wt.% of Nb would be sufficient). These values are in good agreement with the experimental data obtained in this work for the lowest Nb content steels (0.03%Nb), whereas, in the case of 6NbMo16 and 6NbMo31 steels, these values tend to overestimate the experimental data. In this case, a value of 0.032 was obtained, which is three times lower than the value proposed for 0.03%Nb steels. This suggests a weaker effect of Mo in the presence of high Nb additions. Therefore, the resulting values for $[Nb]_{eff}$ in Equation 1 are:

$[Nb]_{eff} = [Nb]$ for Nb microalloyed steels;
$[Nb]_{eff} = 1.19[Nb] + 0.09[Mo]$ for 0.03%Nb-Mo microalloyed steels;
$[Nb]_{eff} = 1.19[Nb] + 0.032[Mo]$ for 0.06%Nb-Mo microalloyed steels.

The effect of Nb and Mo on the austenite evolution during multipass deformation can be complex and it depends both on the Nb and Mo contents and also on the deformation parameters. The softening and hardening mechanisms, including solute drag and strain-induced precipitation and the interactions between them, which can be different depending on the situation, are time and money consuming to evaluate only with experimental data. In this situation, the application of models coupling all the aforementioned factors can be a helpful tool in order to understand the interaction between softening and hardening mechanisms. In previous work, models describing the austenite microstructural evolution of Nb microalloyed steels during hot working were detailed [10,11]. These models were implemented with expressions adjusted for Nb-Mo, such as Equation 1. Combining multipass torsion tests and the model, some conclusions regarding strain accumulation before transformation can be drawn.

Non-recrystallization Temperature

Figure 3 shows, as an example, the mean flow stress curves obtained for four of the steels analyzed tested at $\varepsilon = 0.4$ and interpass time $t_{ip} = 30$ s. As can be observed, the increase in Nb content and the addition of Mo lead to higher T_{nr} values. For these specific conditions, the addition of 0.31%Mo increases the T_{nr} temperature from 970 to 1010 °C in the case of 0.03%Nb and from 1030 to 1045 °C for 0.06%Nb. This indicates a smaller influence of Mo for the higher Nb content in good agreement with the above mentioned weaker drag effect on recrystallization kinetics.
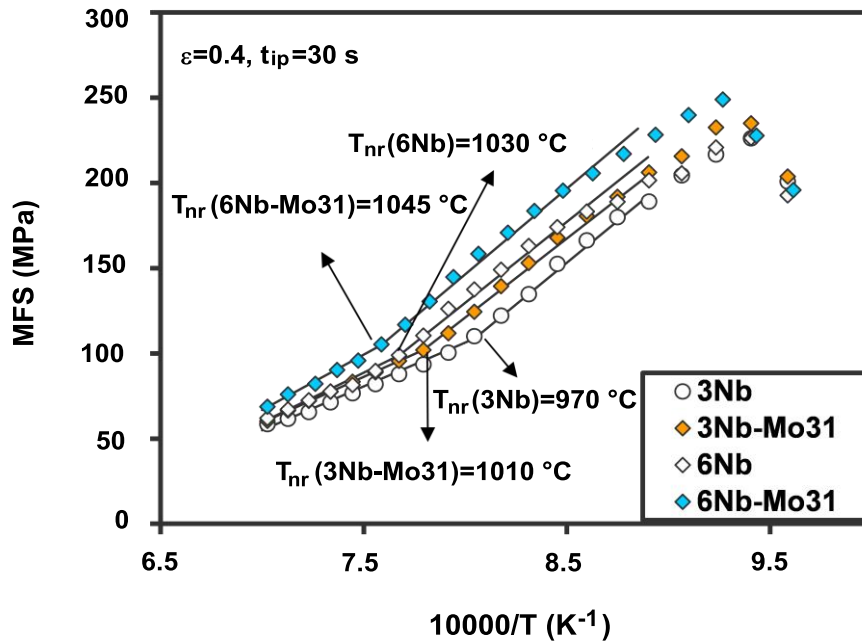

Figure 3. Mean flow stress against the inverse absolute temperature for steels 3NbMo0, 3NbMo31, 6NbMo0 and 6NbMo31.

5

In addition to composition, the non-recrystallization temperature depends also on deformation parameters, mainly pass strain and interpass time. The influence of interpass time is shown in Figure 4 for the condition corresponding to $\varepsilon = 0.4$. Firstly, for the lowest Nb content, 0.03%, there is a significant effect of Mo addition under all the test conditions considered. In contrast, when the Nb content increased to 0.06%, the addition of Mo seems to have less or even no influence. In the majority of the tests there were no differences in the T_{nr} values between the 6Nb, 6NbMo16 and 6NbMo31 steels. Only in the case of $t_{ip} = 30$ s and $\varepsilon = 0.4$ was there a small decrease in this temperature, for the 6Nb steel, not shown by the Mo-Nb grades. On the other hand, the increase in Mo content from 0.16 to 0.31% did not produce any change in the values of T_{nr} and was not dependent on the interpass time or pass strain.

Figure 5 shows the evolution of the measured and predicted softening fraction in both 3NbMo0 and 3NbMo31 steels for interpass times of 10 s and 30 s, Figure 5(a) and (b), respectively. It should be noted that in these calculations only recrystallization was taken into account, thus any deviation from the model can be interpreted as a result of the interaction with strain induced precipitation phenomena. As the temperature decreases the additional solute drag effect of Mo on the Nb-Mo steel plays an important role. The amount of softening starts to decrease at higher temperatures in this steel compared to the Nb steel, giving rise to higher values for T_{nr}. In the Nb steel, although initially the amount of softening dropped due to the solute drag of Nb, the T_{nr} is related to the interaction with precipitation, as is indicated by the deviation of the experimental results from the model below this temperature. Presumably, precipitation also takes place below this temperature in the Nb-Mo steel, since lower softening levels than predicted are measured in this range (after the ninth pass given at 986 °C). This occurred well below the T_{nr} determined for this steel, denoting that in this case the additional drag effect of Mo was the controlling mechanism in retarding recrystallization, T_{nr} being related to it. Similar behavior is observed for 30 s, although in this case the longer interpass time available allowed more recrystallization to occur and the T_{nr} in both steels was somewhat lower.
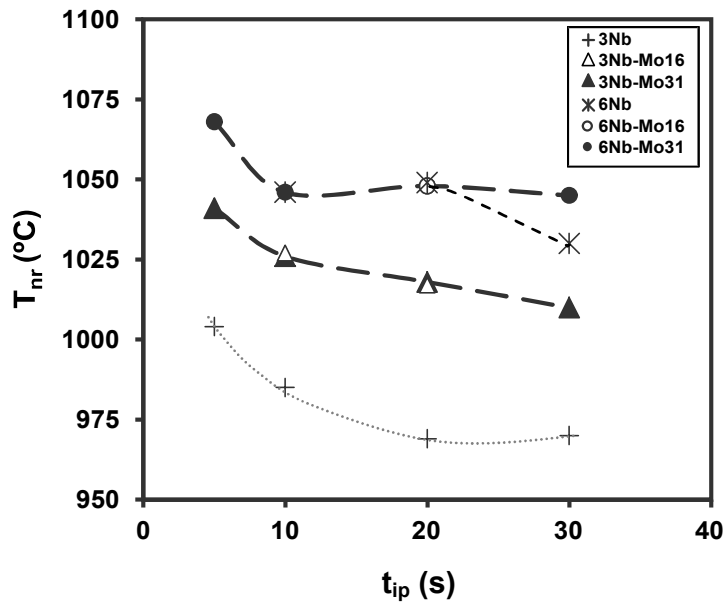

Figure 4. Dependence of T_{nr} on interpass time for a pass strain of $\varepsilon = 0.4$.
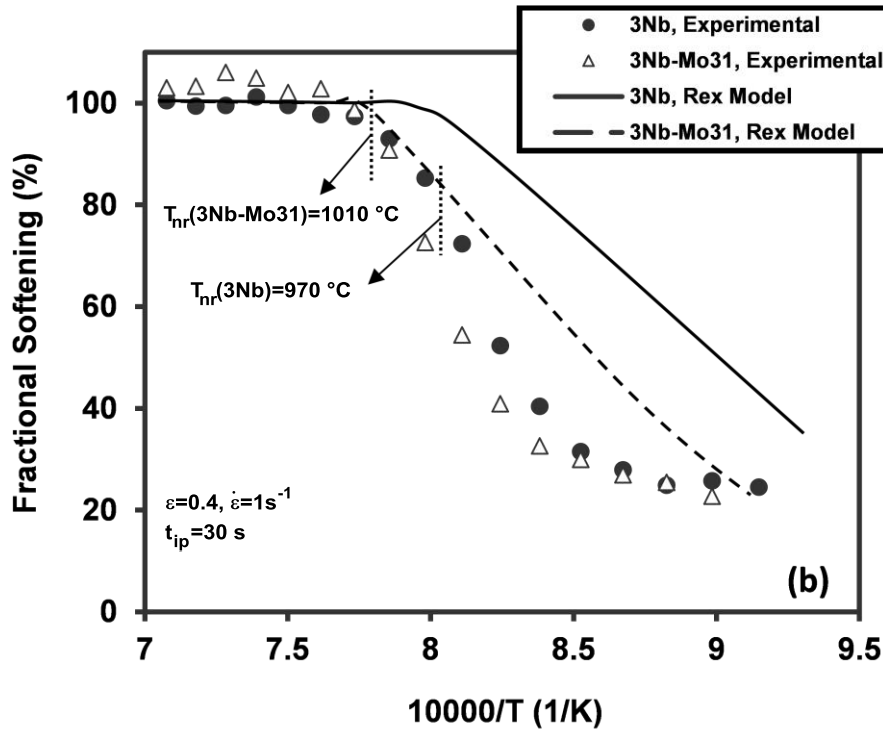
6
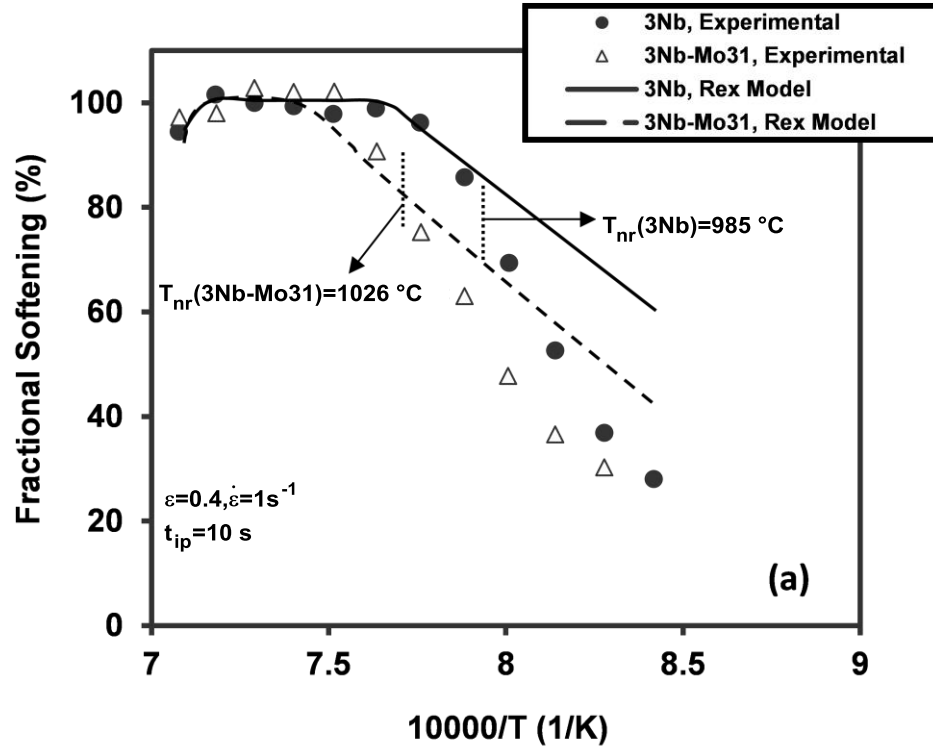
Figure 5. Experimental values and model predictions of fractional softening obtained with steels 3Nb and 3NbMo31 for ε = 0.4 and; (a) t_{ip} = 10 s and (b) t_{ip} = 30 s.

These results suggest that the differences reported in Figure 4, between the steels 3Nb and 3NbMo31 in the $t_{ip} = 10$ s and 30 s range of interpass times, were related to the additional solute drag effect of Mo. For $t_{ip} = 5$ s, the solute drag of Nb or Nb and Mo were the only retardation mechanisms active in both steels; however, for longer times strain induced precipitation interacts with recrystallization, and this was the mechanism responsible for the T_{nr} in the 3Nb steel (Figure 5).

In contrast, for the 3NbMo31 steel and in all the conditions tested, the non-recrystallization temperature was reached by a reduction in fractional softening due exclusively to solute drag; Nb(C,N) precipitation always occurred at temperatures well below the T_{nr}. This could also explain the decreasing trend observed in the T_{nr} values in Figure 4 for both 3NbMo16 and 3NbMo31 steels as the interpass time increases.

Phase Transformation

A complete characterization of phase transformations for the steels listed in Table I has been recently published [7]. Depending on the composition, the austenite conditioning and the cooling rate, a whole range of different microstructures are formed. When analyzing these complex microstructures, various classifications have been proposed to name them. In the present paper the ISIJ Bainite Committee notation is adopted, as the phases observed fit the proposed ones well. The phases are identified as Polygonal Ferrite (PF), Lamellar Pearlite (P), Degenerate Pearlite (DP), Quasipolygonal Ferrite (QF), Granular Ferrite (GF), Bainitic Ferrite (BF) and Martensite (M). Martensite–Austenite (M/A) constituents were also detected as secondary phases within QF and GF main phases. Figure 6 shows an example of the CCT diagrams obtained with the dilatometer and some characteristic microstructures for selected cooling rates for the 6NbMo31 steel. A combination of PF and DP was obtained for a slow cooling rate of 0.1 ℃/s, a mixture of QF and GF for the intermediate cooling rate of 5 ℃/s and, finally, M and BF were formed for the fastest cooling rate of 100 ℃/s.
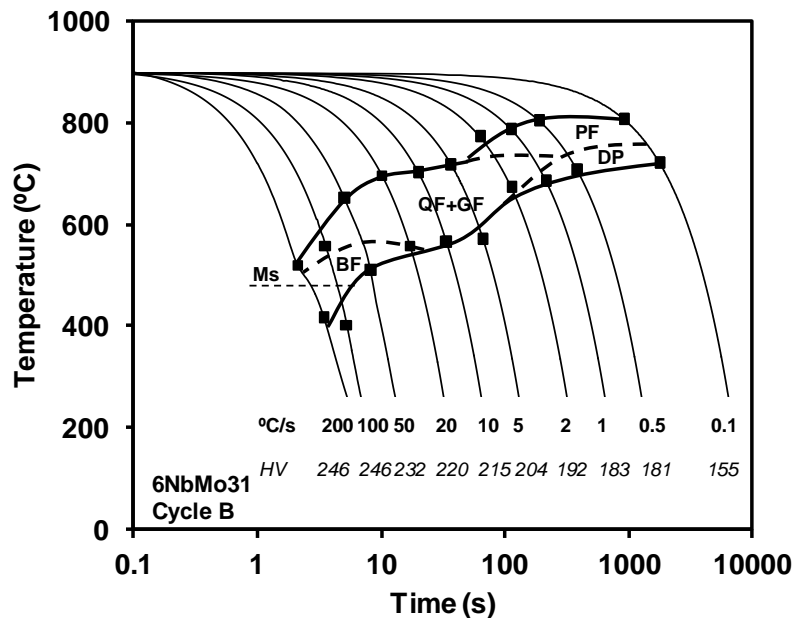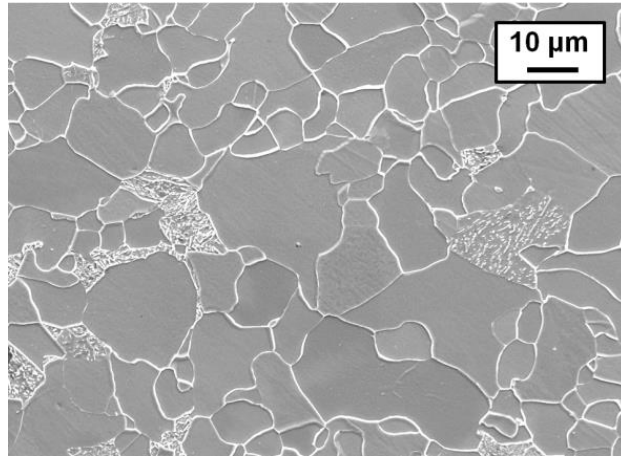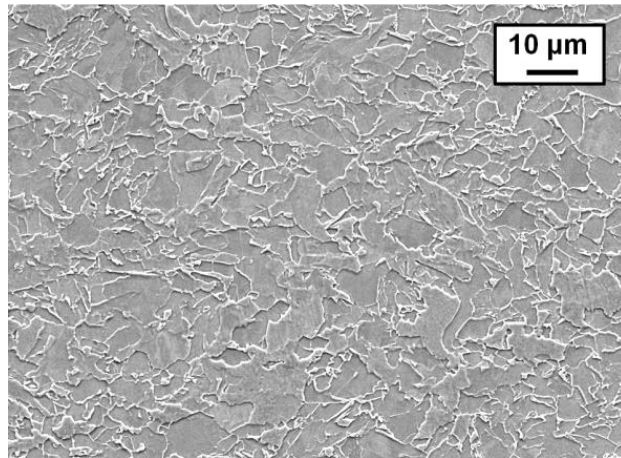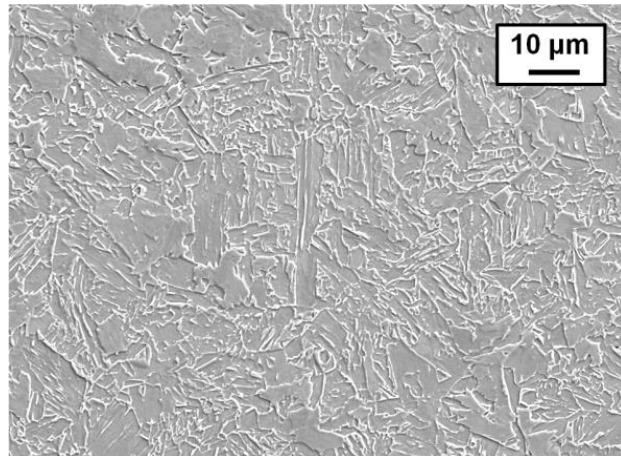
Figure 6. Examples of; (a) CCT diagram for steel 6NbMo31 transformed from deformed austenite (Cycle B) and several characteristic microstructures, (b) 0.1 ℃/s: PF+DP, (c) 5 ℃/s: QF+GF and (d) 100 ℃/s: M+BF.

Effect of Nb and Mo Additions

Figures 7 and 8, respectively, show the influence of Nb and Mo additions for phase transformations occurring from undeformed austenite (Cycle A). In Figure 7, the effect of Nb addition retarding PF formation is evident when the CMn and 3NbMo0 curves are compared. The Nb reduces the ferritic transformation field, as well as shifting the CCT diagram to lower bainitic transformation start temperatures (10-90 °C) for the highest cooling rates. The effect of the increment of Nb from 0.03 to 0.06% on the transformation kinetics is negligible for the Nb steels transforming from undeformed austenite. Transformation start and finish temperatures remain similar both for ferritic and bainitic phases. This small effect of Nb in solution was also reported by Rees et al. [12]. In this case, it can be inferred that the retarding effect of a higher Nb level is counterbalanced by the smaller prior austenite grain size in steel 6NbMo0 [7].

The addition of Mo causes a decrease in the transformation start temperature when the 6NbMo0 and 6NbMo31 steels are compared (Figure 8), especially in the non-polygonal phase region (QF start temperature shifts down 0-40 °C). For the steels containing a lower amount of Nb (Steels 3NbMo0 and 3NbMo31) a similar trend is observed. In this case, the PF start temperatures are decreased by 10-70 °C and the QF start temperatures by 30-70 °C. Therefore, the hardenability effect of Mo is confirmed for these compositions.
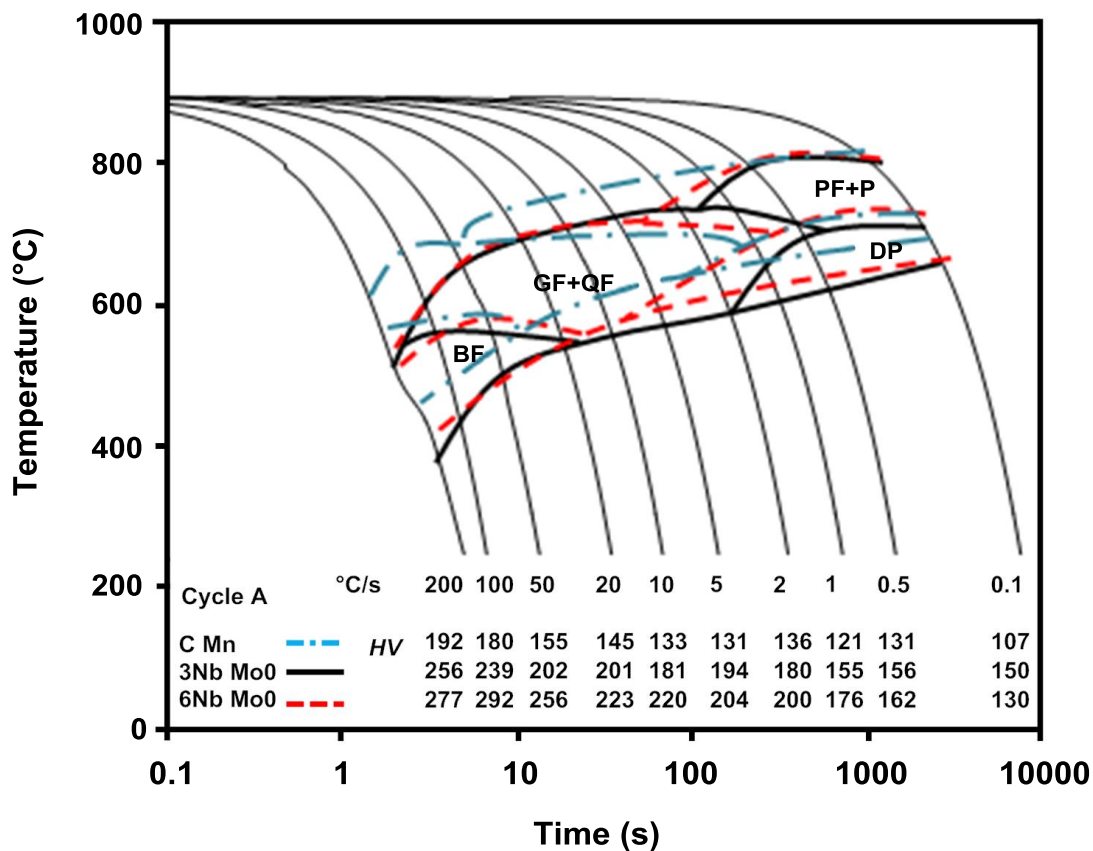
Figure 7. Effect of Nb on CCT diagrams obtained for Cycle A (undeformed austenite) - Steels CMn, 3NbMo0 and 6NbMo0.
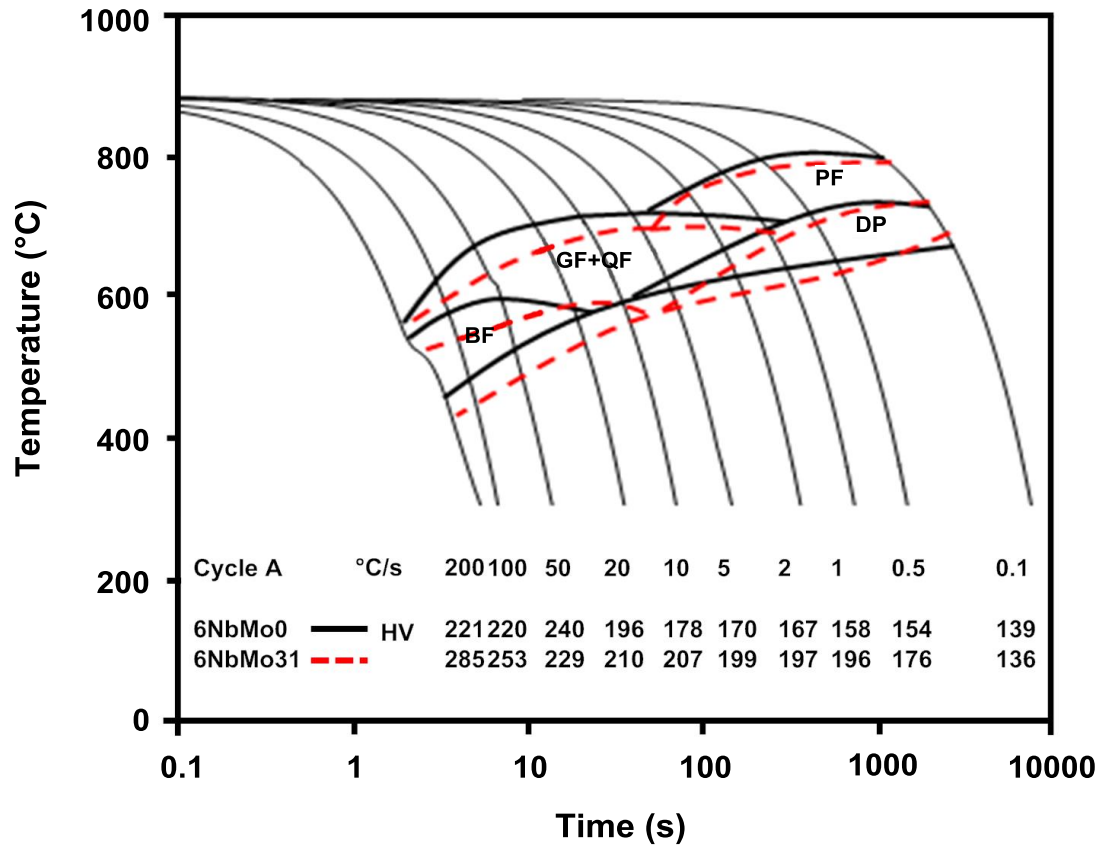
Figure 8. Effect of Mo on CCT diagrams obtained for Cycle A (undeformed austenite) - Steels 6NbMo0 and 6NbMo31.

Effect of the Amount of Deformation Retained in Austenite

The analysis of the effect of deformation on the CCT diagrams has been illustrated by comparing three diagrams for steel 6NbMo31 in Figure 9. Cycle A refers to transformation from undeformed austenite, Cycle B from austenite deformed to a strain of = 0.4 and Cycle C to a strain of 0.8 (see Figure 1). The deformation of the prior austenite promotes a slight acceleration of the transformations, this effect being more marked for the non-polygonal transformation start temperatures. The shift of the PF transformation field is important for Cycle C and the increment in the transformation start temperature as a result of accumulation of deformation in austenite is consistent with previously published data [13-15].

However, a limited effect of deformed austenite in low Nb steels was reported by Militzer et al. [16]. Similarly to what is observed in the present study, Lis et al. [17] and Olasolo et al. [18] observed that bainitic transformation was also accelerated in deformed austenite in the range of high cooling rates in 0.06%Nb microalloyed steels. These authors suggested that a higher dislocation density in the deformed austenite leads to a faster nucleation of the bainite laths.

1000

800

Temperature (°C)

PF

DP

600

QF+GF

Ms

BF

400

200

°C/s	200	100	50	20	10	5	2	1	0.5	0.1
6NbMo31										
$\varepsilon=0$ (Cycle A) HV	285	253	229	210	207	199	197	196	176	136
$\varepsilon=0.4$ (Cycle B)	246	246	232	220	215	204	192	183	181	155
$\varepsilon-0.8$ (Cycle C)	246	261	247	229	217	205	199	186	175	153

0

0.1   1   10   100   1000   10000

Time (s)
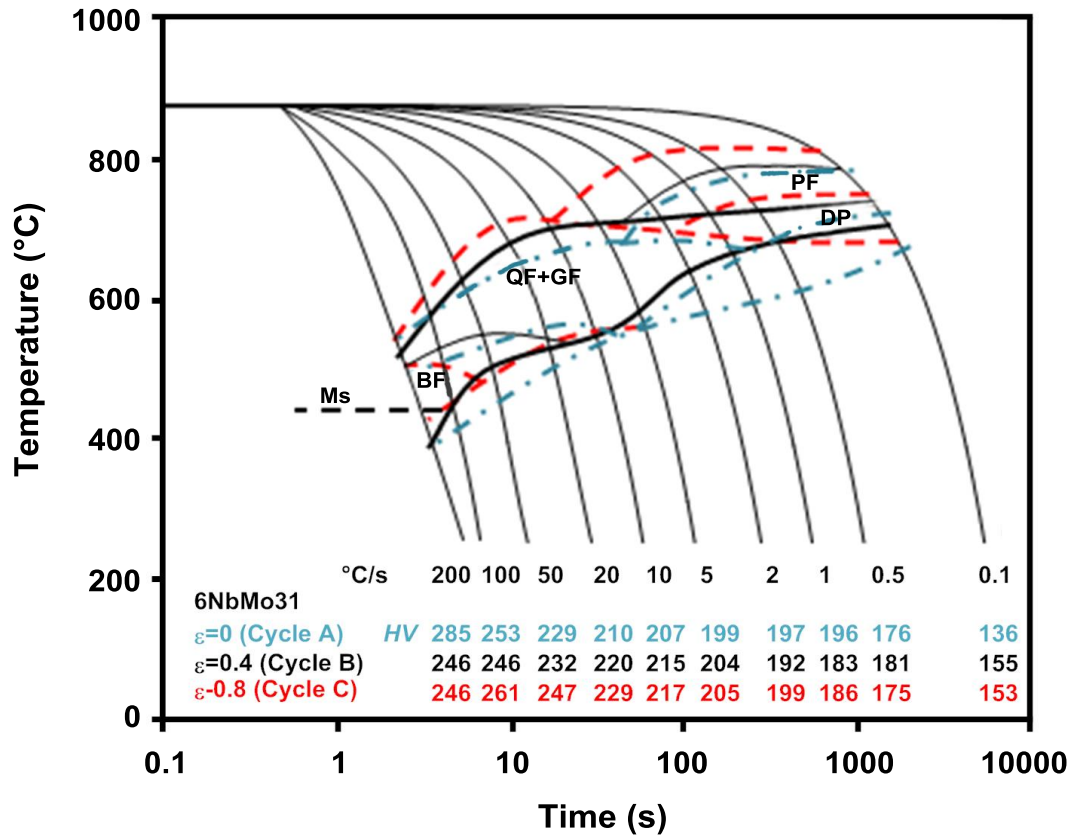
Figure 9. Comparison between the CCT diagrams obtained for steel 6NbMo31 in three austenite conditions (Cycle A: undeformed austenite, Cycle B: deformed austenite ($\varepsilon = 0.4$) and Cycle C: deformed austenite ($\varepsilon = 0.8$)).

Microstructural Unit Sizes and Homogeneity

CCT diagrams do not provide information regarding microstructural feature sizes. Therefore, a more detailed microstructural characterization is needed in order to evaluate the impact of composition on the mean unit sizes and homogeneity. Optical microscopy is suitable for ferritic microstructure characterization, however, when non-polygonal structures are measured, an EBSD analysis provides a more powerful tool to quantify them [19,20]. In order to quantify microstructure effect on strength and toughness, crystallographic unit sizes delimited by 4º and 15º misorientation low and high-angle boundaries were measured using the EBSD technique. Figure 10 exhibits the mean grain size as a function of the cooling rate for both misorientation criteria, for schedules B ($\varepsilon=0.4$) and C ($\varepsilon=0.8$) and different compositions. Figure 10(a) shows the influence of the cooling rate on the mean unit size taking the criterion of low angle misorientation of 4º into consideration for steels 6NbMo0 and 6NbMo31 and both schedules (Cycle B and Cycle C). As a general trend, the mean unit size decreases as the cooling rate increases. The refinement of the microstructure due to the cooling rate increasing is more noticeable in the ferritic range. On the other hand, a higher degree of deformation promotes a slight refinement at low cooling rates. This difference is more important if average values from

Cycle A are compared with those from Cycle B [7]. Finally, it was also observed that the addition of Mo leads to a slight refinement of the final microstructure.
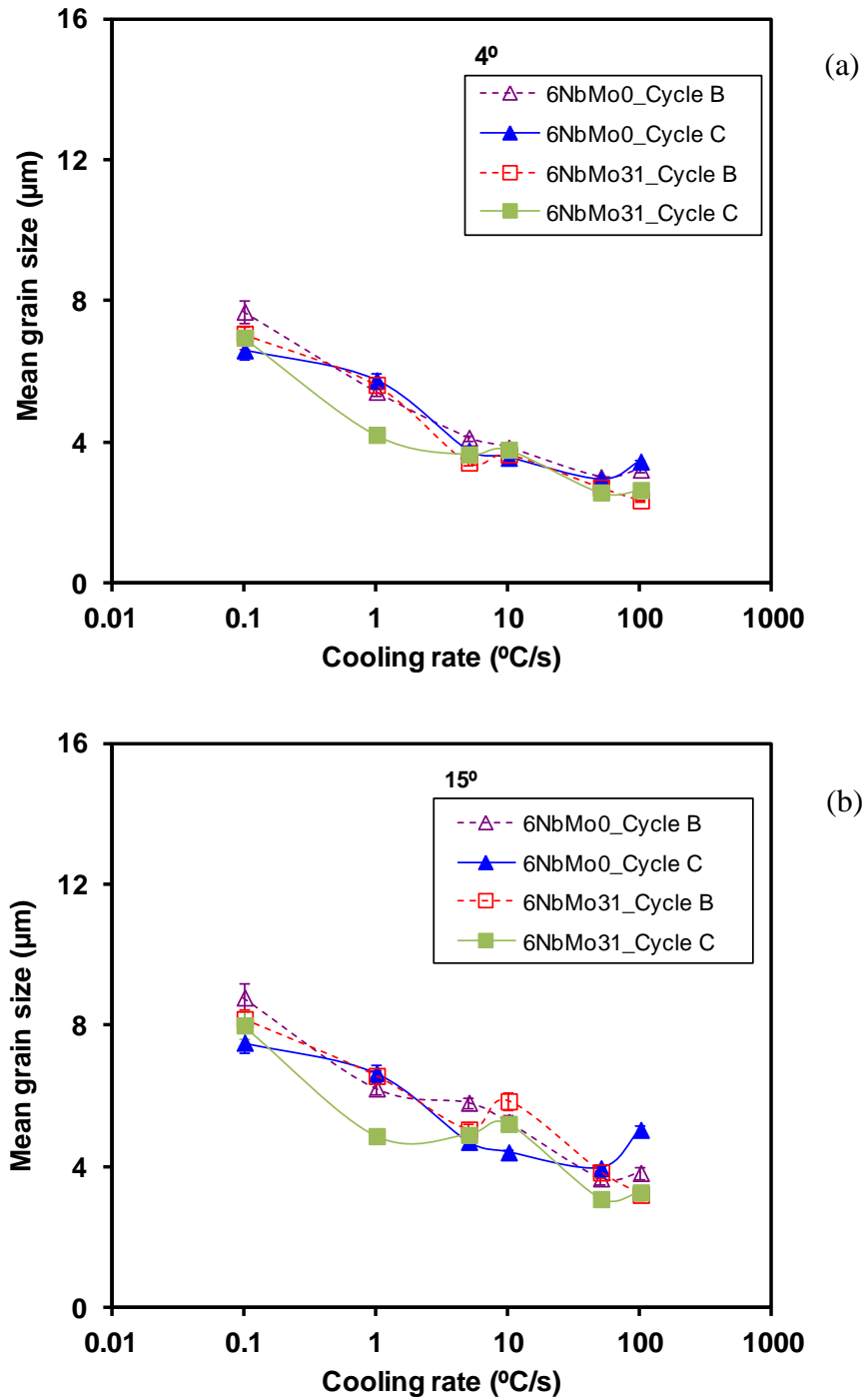
Figure 10. (a) Influence of cooling rate on the average unit size for steels 6NbMo0 and 6NbMo31 from both schedules, Cycle B ($\varepsilon = 0.4$) and Cycle C ($\varepsilon = 0.8$), using 4° threshold misorientation criterion and (b) using 15° threshold misorientation criterion.

When the 15° misorientation is used to define the unit size (see Figure 10(b)), unit sizes larger than for the 4° criterion are quantified in all conditions. Moreover, the mean grain size evolution as a function of the cooling rate is similar to the previously analyzed one with the 4° misorientation criterion. Even though there is not a significant influence of the accumulation of deformation for both compositions when the 4° criterion is used, the effect of a higher strain accumulation was more prominent when the high angle misorientation (15°) criterion is considered, especially in the bainitic range and for the Mo steel.

In order to evaluate the homogeneity of the resulting microstructure, the $Dc20\%/D_{mean}(15°)$ ratio as a function of the cooling rate has been plotted in Figure 11 for steels 6NbMo0 and 6NbMo31 and both schedules B and C. The Dc20% value refers to the cut-off grain size at 80% accumulated area fraction. Several trends can be observed on the $Dc20\%/D_{mean}(15°)$ ratio depending on the schedule and composition. For Cycle B, ferritic structures show the lowest values for the ratio and as QF and GF structures become dominant the ratio increases. This transition is reflected in a two-step regime and the ratio increases from approximately 2 to 7 for both steels. The behavior for Cycle C differs from that of Cycle B. In the 6NbMo0 steel, more homogeneous structures are observed when higher deformation is applied for the whole cooling rate range analyzed. However, for the highest cooling rates, the presence of BF promotes stronger heterogeneity in the 6NbMo31 steel and a later refinement when M is formed. This refinement was also observed for coarse austenite grain sizes [21]. Variant selection and nucleation inside grains is reported to be the most efficient way to reduce martensite/bainite block sizes and, consequently, to enhance homogeneity [22].
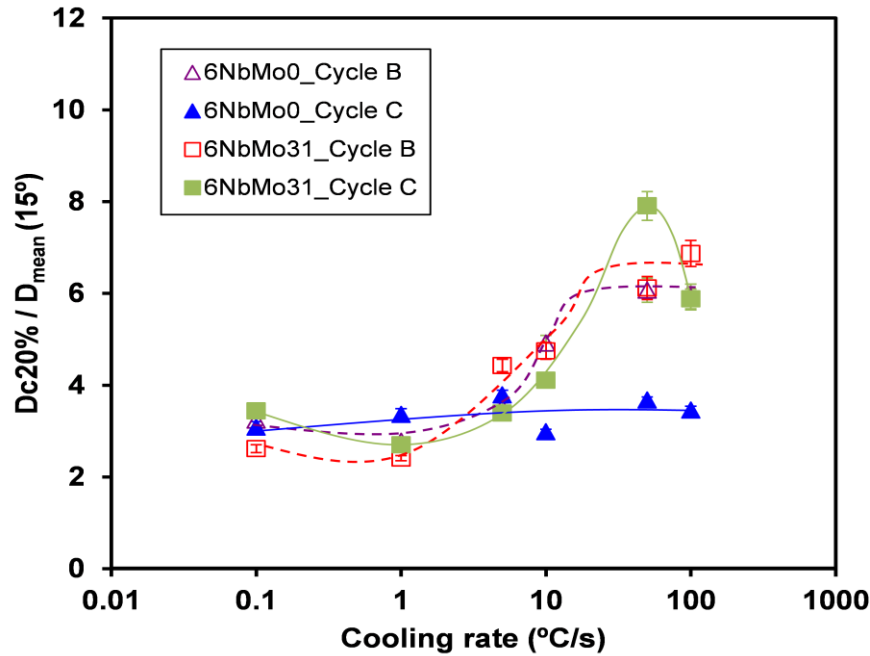
Figure 11. Evolution of $Dc20\%/D_{mean}(15°)$ ratio as a function of the cooling rate for steels 6NbMo0 and 6NbMo31 for both Cycles B ($\varepsilon = 0.4$) and C ($\varepsilon = 0.8$).

Microstructural Contributions to Mechanical Properties

The main goal of understanding the overall microstructural evolution during austenite hot working and final phase transformation is to acquire sufficient knowledge to link the mechanical properties of the steels with the resulting microstructure. So, several thermomechanical schedules have been carried out following the schemes shown in Figure 2. Tensile test samples were machined from the plane strain compression samples and a detailed microstructural characterization was performed.

Depending on the coiling temperature and the composition of the steel, the transformed microstructures change completely. Figure 12 exhibits several FEG-SEM micrographs for the steels containing the higher level of Nb at the coiling temperatures of 650 ºC, 550 ºC and 450 ºC (6NbMo0 in Figure 12(a), (b), (c) and 6NbMo31 in Figure 12(d), (e), (f)). In the steel 6NbMo0, for the higher coiling temperature of 650 ºC, a combination between PF and DP was obtained (see Figure 12(a)). By decreasing the coiling temperature, QF was formed accompanied by GF and the fraction of PF decreased considerably (see Figure 12(b)). Coiling at 450 ºC leads to the formation of a fully non-polygonal microstructure (QF and GF) (see Figure 12(c)). In the steel 6NbMo31, for the higher coiling temperatures (650 ºC and 550 ºC), M/A micro-regions retained between transformed phases were observed apart from the microstructures mentioned at those coiling temperatures (see Figure 12(d) and (e)). Furthermore, it is clearly evident that the amount of bainitic microstructure was higher when Mo was added. The microstructures related to the steels containing the low level of Nb (3NbMo0 and 3NbMo31) are similar to the previously analyzed microstructures.

6NbMo0 **6NbMo31**

Figure 12. FEG-SEM micrographs of the steel 6NbMo0 and steel 6NbMo31 at different coiling temperatures; (a) and (d) 650 ºC, (b) and (e) 550 ºC and (c) and (f) 450 ºC.

Figures 13(a) and (b) exhibit tensile curves obtained for steel 3NbMo0 and steel 3NbMo31 at selected coiling temperatures (650, 550 and 450 ℃). The addition of Mo led to higher yield and tensile strengths, as well as lower elongation in all cases. Furthermore, for both compositions, higher yield and tensile strengths were obtained by decreasing the coiling temperature, with the exception of steel 3NbMo31 where the maximum strength is reached at the intermediate coiling temperature of 550 ℃.
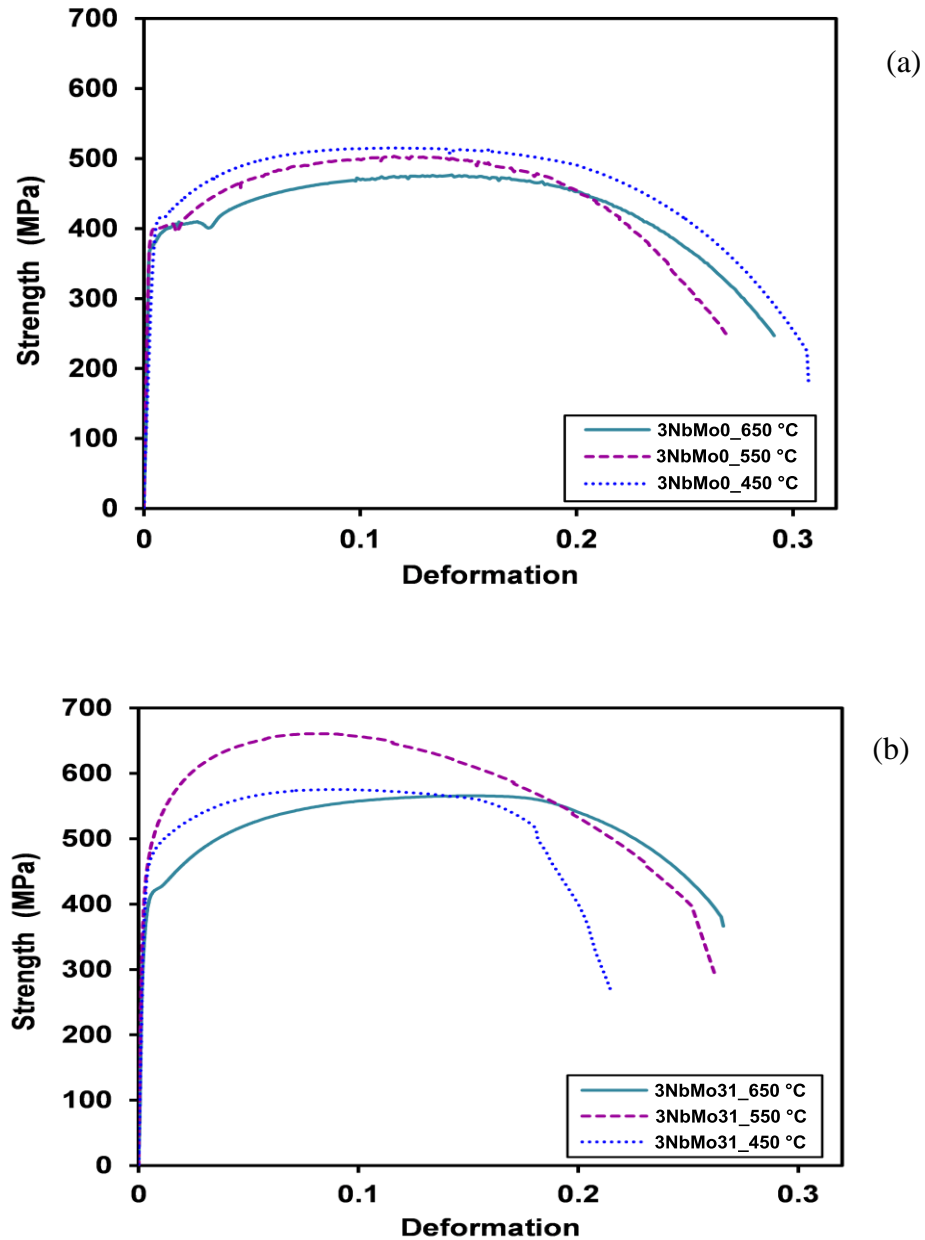

Figure 13. Engineering tensile curves obtained at different coiling temperatures (650, 550 and 450 ℃) for; (a) steel 3NbMo0 and (b) steel 3NbMo31.

In Table II, yield strength, tensile strength, elongation and area reduction values are shown for all the studied steels, for the entire range of coiling temperatures (650, 550 and 450 ºC). In reference to yield strength, YS values varied from 387 to 460 MPa, depending on the composition and applied coiling temperature. Higher YS values were obtained for Nb-Mo steels compared to the values obtained for steels containing Nb alone. Moreover, the highest YS value was obtained at the coiling temperature of 450 ºC in the steel 3NbMo31, reaching a value of 460 MPa. On the other hand, YS increased as coiling temperature decreased, due to a major presence of non-polygonal or bainitic microstructures (a mixture of QF and GF). Similar to what happened in YS values, significantly higher TS values were observed when Mo was added, reaching the highest tensile strength of 660 MPa at the intermediate coiling temperature (550 ºC) in the steel 3NbMo31.

Table II. Yield Strength (YS), Tensile Strength (TS), Elongation (%) and Area Reduction (%) Values for Different Compositions and Coiling Temperatures

Steel	Coiling T (ºC)	YS (MPa)	TS (MPa)	Elongation (%)	Area Reduction, RA (%)
3NbMo0	650	387	485	35	84
	550	401	506	36	85
	450	414	522	34	84
3NbMo31	650	393	571	28	77
	550	457	660	29	80
	450	460	575	34	89
6NbMo0	650	406	490	39	83
	550	410	512	39	86
	450	408	514	36	87
6NbMo31	650	426	594	33	71
	550	435	627	35	81
	450	473	582	33	82

Similar to what was found in the engineering tensile curves (Figure 13), a lower elongation was observed when Mo was added. Elongation is reduced from 39 to 33% at the coiling temperature of 650 ºC, for the steels 6NbMo0 and 6NbMo31 respectively. A significant influence of coiling temperature on the area reduction is observed, obtaining higher area reduction values as coiling temperatures decreases, except for steel 3NbMo0, where RA is approximately constant for the three coiling temperatures. Furthermore, as expected, the steels containing Mo exhibit lower area reduction values than those shown by the steels containing only Nb.

Strengthening Mechanisms

The yield strength (σ_y) of low carbon microalloyed steels can be expressed as a summation of different strengthening mechanisms [23]. Even though the lineal sum of components is the most widely used approach, other non-linear relationships have been also proposed so as to predict tensile properties. This is important when the contribution of different strengthening mechanisms is not equal and interactions between the different strengthening mechanisms exist. In this particular case, Equation 2, proposed by Yakubtsov et al. [24], shows the best fit between experimental and calculated values.

$$\sigma_y = ((\sigma_0 + \sigma_{ss} + \sigma_{ppt} + \sigma_{MA})^2 + \sigma_\rho^2 + \sigma_{gs}^2)^{0.5} \tag{2}$$

where σ_0 is the lattice friction stress, σ_{ss} is the solid solution strengthening, σ_{ppt} is the contribution of precipitation, σ_{MA} is the hardening due to the presence of MA islands, σ_ρ is the dislocation hardening and σ_{gs} is the strengthening effect of grain size. The equation shows a root mean summation and is suitable for combinations where the contributions of dislocations and grain size strengthening are relevant.

Strengthening Contribution due to Solid Solution. The contribution of solid solution to the yield strength was determined according to Equation 3 [25]. This equation has been widely used for low carbon steels.

$$\sigma_{ss} = \sigma_0 + 32.3Mn + 83.2Si + 11Mo + 354 \, (N_{free})^{0.5} \tag{3}$$

where σ_0 is the lattice friction stress (σ_0=53.9 MPa) and the concentrations are expressed in weight percent. In the current study, the total amount of N is assumed to be precipitated in combination with Nb and consequently, there is no free N (N_{free}=0).

Strengthening Contribution Related to Grain Size. The contribution of the final microstructure grain size (σ_{gs}) follows the Hall-Petch relationship. Even though the Hall-Petch equation was developed for high angle boundaries, it has been progressively extended to subgrains and cell boundaries. The strengthening on account of sub-boundaries depends on their misorientation, resulting in a modified Hall-Petch exponent. In this work, a new approach recently published by Iza-Mendia et al. [26] has been adopted and the resulting equation is shown in Equation 4. The first term refers to low angle boundaries, while the second term is related to the contribution of high angle misorientation units. Therefore, especially in bainitic (QF+GF) microstructures, apart from high angle boundaries, it is important to take into account the contribution of boundaries in the interval $2<\theta<15°$, due to a high fraction of those kind of boundaries.

$$\sigma_{gs} = 1.05\alpha M\mu\sqrt{b}\left[\sum_{\substack{2\leq\theta_i\leq15° \\ i}} f_i\sqrt{\theta_i} + \sqrt{\frac{\pi}{10}} \sum_{\substack{\theta_i\geq15° \\ i}} f_i \right] \cdot d_{2°}^{-\frac{1}{2}} \tag{4}$$

where α is a constant, M the average Taylor factor, μ is the shear modulus and b is the Burger's vector (α=0.3, M=3, μ=8x10^4 MPa and b=2.5 10^{-7} mm). θ_i and f_i, are the mean misorientation angle in the interval i and the relative frequency, respectively. d$_{2°}$ is the mean grain size considering a 2° criterion. These parameters are determined by EBSD.

In order to evaluate the interaction between the microstructural refinement and the contribution related to low angle boundary unit size, yield strength values are plotted in Figure 14 as a function of the mean unit size considering the low angle misorientation criteria of 2°. Two different trends are observed depending on whether the steel is microalloyed only with Nb or with both Nb and Mo. For Nb steels, there is not a clear dependence of yield strength on low angle boundary size. Nevertheless, for the Nb-Mo steels, where a very fine substructure is formed, with unit sizes ranging from 3 to 4 microns, a sharp increase in yield strength is measured as the unit size decreases.
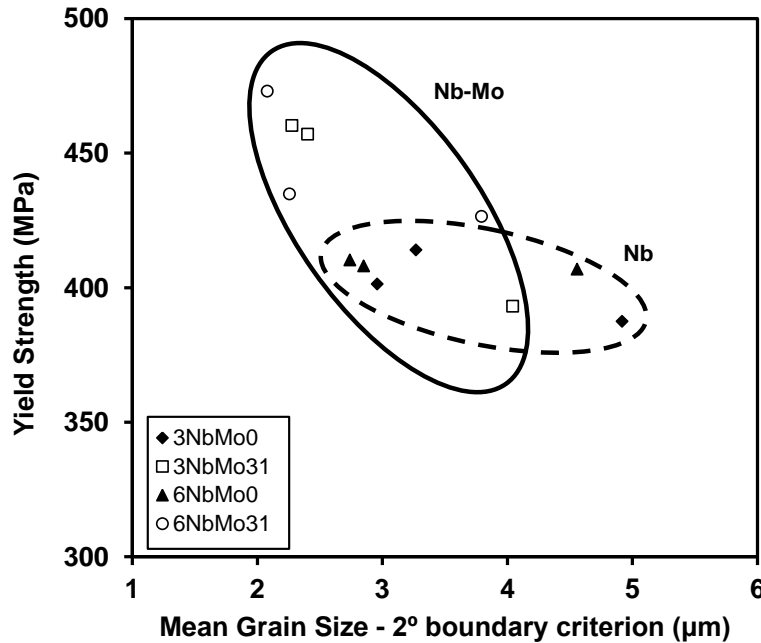
Figure 14. Yield strength as a function of 2° grain size for steels
3NbMo0, 3NbMo31, 6NbMo0 and 6NbMo31.

<u>Strengthening Contribution due to Dislocations.</u> In addition to solid solution and grain size contributions, the term related to dislocation density has to be considered. The contribution of the dislocation density can be expressed by Equation 5 [27].

$$\sigma_\rho = \alpha M \mu b \sqrt{\rho} \qquad (5)$$

where α is a numerical factor, M is the Taylor factor, μ is the shear modulus, b is the Burger's vector and ρ is the dislocation density. A value of $\alpha M = 0.38$ has been established for body-centered cubic metals [28].

20

Strengthening due to dislocation density has been evaluated by other authors [26,27], through the analysis of the local misorientation gradients within a given region by means of the calculation of the Kernel Average Misorientation (KAM) parameter. In order to estimate dislocation density values from KAM data, Kubin and Mortensen's [29] approach was adopted:

$$\rho = \frac{2\vartheta}{ub} \tag{6}$$

where *u* is the unit length and *b* is the Burger's vector. The local misorientation value is achieved directly from EBSD data and is related to the kernel average misorientation value (ϑ). Kernel average misorientation for $\theta < 2°$ and second neighbor criterion have been considered in order to evaluate the contribution of dislocation strengthening [27].

In Figure 15, calculated dislocation density values for the steels 3NbMo0, 3NbMo31, 6NbMo0 and 6NbMo31 are plotted as a function of coiling temperature. Dislocation density values vary from $3.42\cdot10^{14}$ to $5.92\cdot10^{14}$ m^{-2}, depending on the composition and applied coiling temperature. Even though in Nb steels the dislocation density remains nearly constant for all the range of coiling temperatures (ρ varies from $3.43\cdot10^{14}$ to $3.87\cdot10^{14}$ m^{-2}), when Mo is added a different trend is observed. Furthermore, the decreasing of coiling temperature (from 650 to 450 ℃) and consequently, the modification of the resultant microstructure from polygonal ferrite to a mixture of QF and GF, leads to a significant increment of dislocation density. For example, in steel 3NbMo31, ρ increases from $3.42\cdot10^{14}$ to $5.92\cdot10^{14}$ m^{-2}, when decreasing the coiling temperature from 650 to 450 ℃.
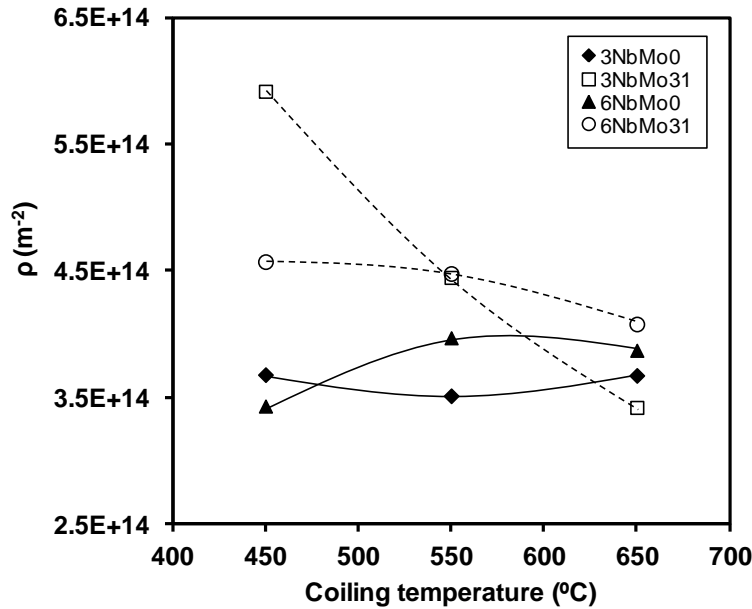

Figure 15. Dislocation density as a function of coiling temperature for all the steels studied (3NbMo0, 3NbMo31, 6NbMo0 and 6NbMo31).

21

Strengthening Contribution Caused by Precipitation. Precipitation strengthening has been successfully described by the Ashby-Orowan model (Equation 7) [30].

$$\sigma_{ppt} = 10.8 \frac{f_v^{0.5}}{x} \ln(\frac{x}{6.125 \cdot 10^{-4}}) \tag{7}$$

where f_v is the volume fraction of precipitates and x the mean planar intercept diameter of the particles (μm). Precipitate size distributions and average sizes, for each steel (3NbMo0, 3NbMo31, 6NbMo0 and 6NbMo31) and selected coiling temperatures (650, 550 and 450 ºC) were measured [31]. Finer precipitate mean sizes and higher fractions were measured in the Nb-Mo steels compared to Nb steels with the same level of Nb.

One of the biggest limitations for evaluating the contribution of precipitation hardening is to achieve an accurate calculation of the volume fraction of precipitates [32,33]. Even though the limitations of extraction replicas are widely known, an approximate volume fraction of precipitates was measured by means of TEM. The measurements of precipitate densities (amount of precipitates per unit area) of each steel and selected coiling temperatures (650, 550 and 450 ºC) were performed [31]. The estimation of the volume fraction of precipitates was achieved by means of Equation 8 [34].

$$f_v = k \frac{\pi}{6} N_S (x^2 + \sigma^2) \tag{8}$$

where k is a correction factor, N_s is the number of particles per unit area, x is the average particle size and σ is the standard deviation from x. A correction factor of 1/4 was applied based on a method that considers an estimated sampling depth for precipitates captured by replicas which is related to the approximate ratio between the average diameter of the small particles and the diameter of the largest particles captured by the replicas [33].

Strengthening Contribution Caused by M/A Islands. An additional strengthening effect limited to microstructures with the presence of M/A islands has to be taken into account. This contribution is proportional to the M/A volume fracion, f_{MA}, and was determined according to Equation 9 [35].

$$\sigma_{MA} = 900 f_{MA} \tag{9}$$

Evaluation of Strengthening Contributions

Taking into account all the individual strengthening contributions estimated according to the methodology described above, yield strength values were calculated for each composition and coiling temperature. These values are summarized in Table III and compared with the measured ones. Within the limitations of the method a satisfactory result is obtained in most cases. The biggest differences between calculated and measured values are achieved at the coiling temperature of 450 °C. The precipitation strengthening contribution is expected to be underestimated in these cases. However, it can be concluded that the proposed strategy is useful for the interpretation of each particular contribution to the overall yield strength.

Table III. Comparison Between Experimental and Calculated Yield Strengths

$T_{coiling}$ (°C)	YIELD STRENGTH (MPa)							
	3NbMo0		3NbMo31		6NbMo0		6NbMo31	
	σ_{y_calc}	σ_{y_exp}	σ_{y_calc}	σ_{y_exp}	σ_{y_calc}	σ_{y_exp}	σ_{y_calc}	σ_{y_exp}
650 °C	341	388	374	393	349	407	392	426
550 °C	387	401	429	457	415	410	475	435
450 °C	373	414	412	460	414	408	422	473

The estimated individual strengthening contributions, considering Equation 2, are plotted in Figure 16. It is clearly evident that the grain size strengthening is the most relevant contribution, with relative percentages between 51% and 69%, depending on the composition and coiling temperature. The highest influence of the grain size refinement was obtained for steel 6NbMo31 at the lowest coiling temperature of 450 °C. Regarding dislocation strengthening, higher strength values are obtained for lower coiling temperatures, especially in Nb-Mo steels, due to a major fraction of non-polygonal microstructures at low coiling temperatures. For example, in the steel 3NbMo31, the strengthening caused by dislocations increased from 13% to 19% by reducing the coiling temperature from 650 °C to 450 °C. Finally, Figure 16 exhibits a negligible effect of precipitation in steel 3NbMo0 (contribution from 3% to 7%). However, the influence of a fine precipitation is higher in the steels containing the higher level of Nb, due to a higher amount of solute Nb available for precipitation during transformation. In addition, Figure 16 shows that the highest contribution of precipitation was achieved at the intermediate coiling temperature (550 °C) in the steel 6NbMo31.
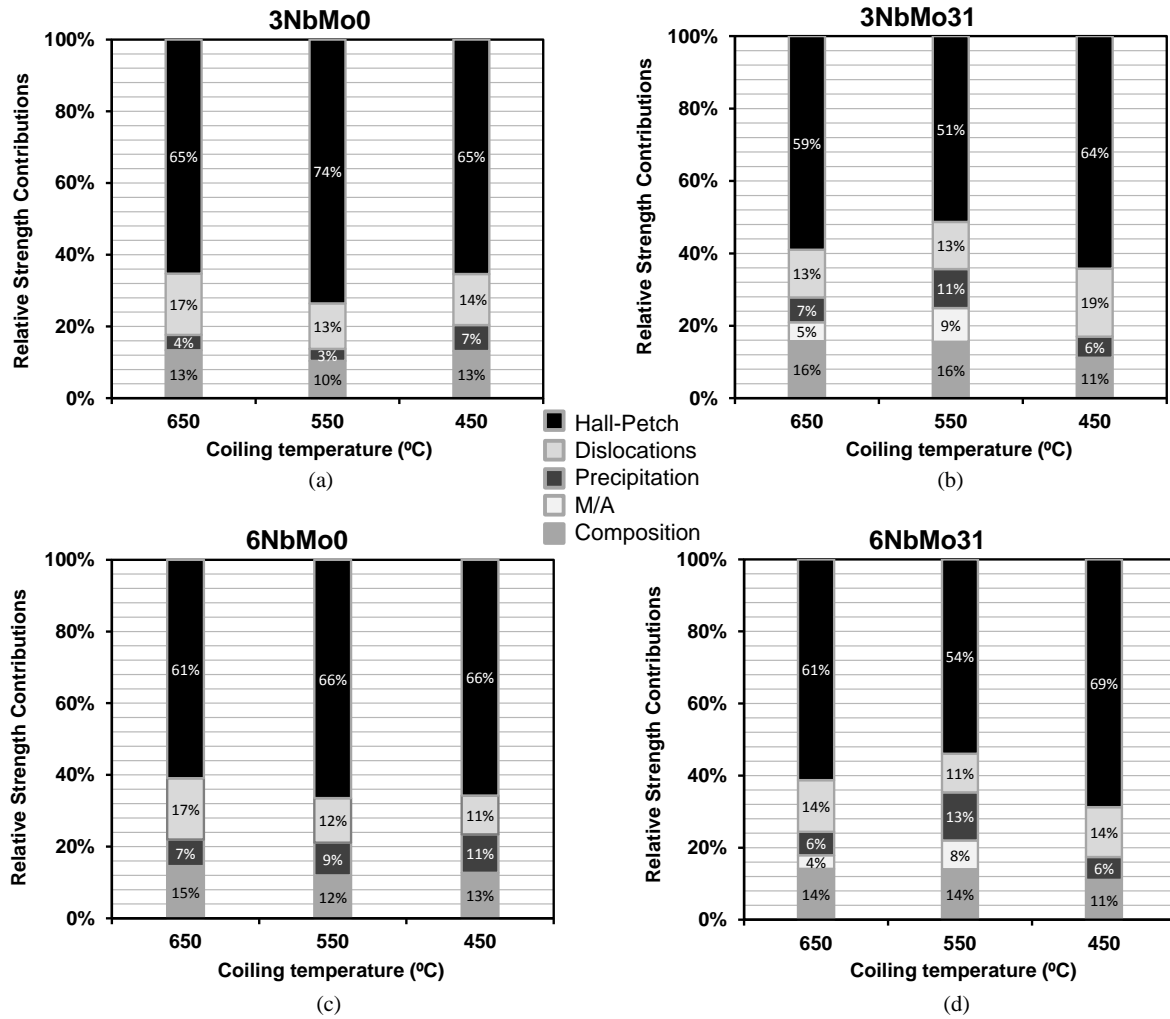
Figure 16. Strengthening contributions for steel 3NbMo0, 3NbMo31, 6NbMo0 and 6NbMo31.

Conclusions

Regarding austenite conditioning, Mo addition to Nb microalloyed steels results in a retardation of recrystallization kinetics due to the solute drag effect. However, this effect is weaker in the 0.06%Nb steels compared to the 0.03%Nb steels. A previous equation available for predicting the 50% recrystallization time, $t_{0.5}$, for Nb and Nb-Ti steels was extended to Nb-Mo steels, assuming an effective Nb level which captures the different solute drag contribution of Mo at the different Nb levels. The Nb and Mo solute drag effect seems to govern the non-recrystallization temperature, T_{nr}, in the Mo-Nb steels. Nevertheless, the addition of Mo to Nb microalloyed steels has other effects on the T_{nr} value, depending on the Nb content. In the range of medium Nb contents (0.03%Nb), the additional solute drag effect produced by Mo allows the T_{nr} values to be higher in the Nb-Mo than in the Nb steels. However, increasing the Nb content to values as high as 0.06%Nb, the acceleration of strain induced precipitation makes the contribution of Mo to solute drag, less relevant.

24

In terms of phase transformations, the addition of Mo to Nb steels ensures a higher retention of accumulated deformation before transformation. For low and intermediate cooling rates, the retained deformation favors the formation of polygonal phases, decreases the unit size of the phases formed and therefore, reduces the risk of the presence of heterogeneous structures.

An increase in the amount of accumulated strain provides an improvement in microstructural homogeneity; this improvement being more important for ferritic structures. Therefore, an optimized combination of chemical composition, thermomechanical schedule and cooling strategy in Nb-Mo microalloyed steels is needed in order to maximize the amount of applied strain below the non-recrystallization temperature, and consequently promote finer and more homogeneous structures.

Different strengthening mechanisms contribute to the high strength of microalloyed steel. The quantification of each strengthening contribution has shown that grain refinement plays a major role for the present steels, accounting for up to 60-70% of the yield strength. The addition of Mo to Nb microalloyed steels promotes the formation of a low angle misorientation substructure which enhances the strengthening effect arising from grain size reduction. The combination of Nb and Mo reduces the precipitate size and therefore, increases the strengthening contribution of fine carbides precipitated at low temperatures.

Acknowledgments

References

1. S.G. Jansto, "Niobium-bearing Steel Development for Value-added Structural Applications," *Proceedings of New Developments on Metallurgy and Applications of High Strength Steels Conference,* Buenos Aires, (2008), 1313.

2. D. Bhattacharya, *Proceedings of 6th International Conference on High Strength Low Alloy Steels, HSLA 2011*, Beijing, China, (2011), CD-Rom.

3. H. Mohrbacher, "Phase Transformation Study in Nb-Mo Microalloyed Steels Using Dilatometry and EBSD Quantification," *Proceedings of International Seminar on Applications of Mo in Steels,* Beijing, (2010), 75.

4. X. Sun and Q. Yong, "Phase Transformation Study in Nb-Mo Microalloyed Steels Using Dilatometry and EBSD Quantification," *Proceedings of International Seminar on Applications of Mo in Steels,* Beijing, (2010), 61.

5. O. Kwon and A.J. DeArdo, "Effect of Precipitation on the Recrystallization Behavior of a Nb Containing Steel," *Acta Metallurgica et Materialia*, 39 (1991), 529.

6. D.Q. Bai et al., "Effect of Deformation Parameters on the No-recrystallization Temperature in Nb-bearing Steels," *Metallurgical Transactions A*, 24 (10) (1993), 2151.

7. N. Isasti et al., "Phase Transformation Study in Nb-Mo Microalloyed Steels Using Dilatometry and EBSD Quantification," *Metallurgical and Materials Transactions A*, 44 (8) (2013), 3552 – 3563 (DOI: 10.1007/s11661-013-1738-3).

8. A.I. Fernández et al., "Static Recrystallization Behaviour of a Wide Range of Austenite Grain Sizes in Microalloyed Steels," *The Iron and Steel Institute of Japan International,* 40 (9) (2000), 893-901.

9. M.G. Akben and J.J. Jonas, "Influence of Multiple Microalloy Additions on the Flow Stress and Recrystallization Behavior of HSLA Steels," *HSLA Steels: Technology and Applications*, ed. M. Korchynsky (ASM, 1983), 149.

10. P. Uranga et al., "Modeling of Austenite Grain Size Distribution in Nb Microalloyed Steels Processed by Thin Slab Casting and Direct Rolling (TSRD) Route," *The Iron and Steel Institute of Japan International,* 44 (2004), 1416.

11. B. Pereda, B. López and J.M. Rodriguez-Ibabe, "Increasing the Non-Recrystallization Temperature of Nb Microalloyed Steels by Mo Addition", eds. A.J. DeArdo, C.I. Garcia, *Proceedings of the International Conference on Microalloyed Steels: Processing, Microstructure, Properties and Performance,* Pittsburgh, AIST, Warrendale, PA, (2007), 151-159.

12. G.I. Rees et al., "The Effect of Niobium in Solid Solution on the Transformation Kinetics of Bainite," *Materials, Science and Engineering A*, 194 (1995), 179.

13. D.N. Hanlon, J. Sietsma and S. van der Zwaag, "The Effect of Plastic Deformation of Austenite on the Kinetics of Subsequent Ferrite Formation," *The Iron and Steel Institute of Japan International*, 41 (2001), 1028.

14. C. Calvo et al., "Influence of the Chemical Composition on Transformation Behaviour of Low Carbon Microalloyed Steels," *Materials, Science and Engineering A,* 520 (2009), 90.

15. R.Y. Zhang and J.D. Boyd, "Bainite Transformation in Deformed Austenite," *Metallurgical and Materials Transactions*, 41A (2010), 1448.

16. M. Militzer, E.B. Hawbolt and T.R. Meadowcroft, "Microstructural Model for Hot Strip Rolling of High Strength Low-alloy Steels," *Metallurgical and Materials Transactions*, 31A (2000), 1247.

17. A.K. Lis and J. Lis, "Effect of Hot Deformation and Cooling Rate on Phase Transformations in Low Carbon HN5MVNb Bainitic Steel," (Thermec 2006), *Materials Science Forum,* 539-543 (2007), 4620.

18. M. Olasolo et al., "Effect of Austenite Microstructure and Cooling Rate on Transformation Characteristics in a Low Carbon Nb–V Microalloyed Steel," *Materials, Science and Engineering A*, 528 (2011), 2559.

19. F. Gerdemann, et al, "Metallographic Characterization of Bainitic Microstructures," *International Conference on New Developments in Advanced High-Strength Sheet Steels*: *June 15-18, 2008 Orlando, Florida, U.S.A.* (Warrendale, PA: AIST, 2008) S. 93.

20. A.W. Wilson and G. Spanos, "Application of Orientation Imaging Microscopy to Study Phase Transformations in Steels," *Materials Characterization*, 46 (2001), 407.

21. N. Isasti et al., "Effect of Composition and Deformation on Coarse-grained Austenite Transformation in Nb-Mo Microalloyed Steels," *Metallurgical and Materials Transactions* 42A (2011), 3729.

22. T. Furuhara, N. Takayama and G. Miyamoto, "Key Factors in Grain Refinement of Martensite and Bainite," *Materials Science Forum*, 638-642 (2010), 3044.

23. F.B. Pickering, *Physical Metallurgy and the Design of Steels* (London, UK: Applied Science Publishers Ltd, 1978), 10.

24. I.A. Yakubtsov et al., "Strengthening Mechanism in Dual-phase Acicular Ferrite + M/A Microstructures," *Proceedings of 42nd Mechanical Working and Steel Processing Conference,* Toronto, Ontario, (2000), 429.

25. F.B. Pickering and T. Gladman, "Metallurgical Developments in Carbon Steels, Iron and Steel Institute" (Special Report No. 81, London, 1963).

26. A. Iza-Mendia and I. Gutiérrez, "Generalization of the Existing Relations Between Microstructure and Yield Stress from Ferrite–Pearlite to High Strength Steels," *Materials, Science and Engineering A*, 561 (2013), 40.

27. M. Calcagnotto et al., "Orientation Gradients and Geometrically Necessary Dislocations in Ultrafine Grained Dual-phase Steels Studied by 2D and 3D EBSD," *Materials, Science and Engineering A,* 527 (2010), 2738.

28. A.S. Keh and S. Weissmann, "Deformation Substructure in Body-centered Cubic Metals," *Electron Microscopy and the Strength of Crystals,* eds. G. Thomas and J. Washburn, (New York, NY: Interscience, 1963), 231.

29. L.P. Kubin and A. Mortensen, "Geometrically Necessary Dislocations and Strain-gradient Plasticity: A Few Critical Issues," *Scripta Materilia*, 48 (2003), 119.

30. T. Gladman, "Precipitation Hardening in Metals," *Materials Science and Technology*, 15 (1999), 30.

31. N. Isasti, "Estudio de las Transformaciones de Fase en Aceros Microaleados con Nb y Nb-Mo. Relación Entre Microestructura y Propiedades Mecánicas" (Ph.D. thesis, San Sebastian, University of Navarra, 2013).

32. J. Lu, D. Ivey and H. Henein, "A Review of Methods to Quantify Nanoscale Precipitates in Microalloyed Steels - Part I," *AIST Transactions*, 10 (2013), 232.

33. K. Poorhaydari and D.G. Ivey, "Precipitate Volume Fraction Estimation in High Strength Microalloyed Steels," *Canadian Metallurgical Quarterly*, 48 (2009), 115.

34. M.F. Ashby and R. Ebeling, "On the Determination of the Number, Size, Spacing and Volume Fraction of Spherical Second-phase Particles from Extraction Replicas," *Transactions of the Metallurgical Society of AIME*, 236 (1966), 1396.

35. M.E. Bush and P.M. Kelly, "Strengthening Mechanisms in Bainitic Steels," *Acta Metallurgica*, 19 (1971), 1363.

THE SYNERGISTIC EFFECT OF NIOBIUM-MOLYBDENUM ADDITIONS ON THE MICROSTRUCTURE OF LOW-CARBON BAINITIC STEEL

B.M. Huang[1], J.R. Yang[1] and C.Y. Huang[2]

[1]Department of Materials Science and Engineering, National Taiwan University, Taipei, Taiwan, ROC
[2]Steel & Aluminum Research & Development Department, China Steel Corporation, Kaohsiung, Taiwan, ROC

Keywords: Niobium, Molybdenum, Bainitic Steels, Accelerated Cooling, Tempering, SEM, TEM, Precipitation, EBSD, Mechanical Properties, Hardness

Abstract

The main purpose of this work was to elucidate the effect of Mo additions on the development of microstructure in hot rolled low-C Nb-containing bainitic steels. Three experimental steels have been investigated; they had the same base composition of 0.05%C-1.7%Mn-0.08%Nb (wt.%); one had no Mo addition and the other two contained 0.1 wt.% and 0.3 wt.%Mo, respectively. The steel strips were manufactured by a combined process of controlled rolling and accelerated cooling. After finish rolling at 900 °C, the steels were treated by accelerated cooling to 650 °C, 550 °C and 450 °C respectively, and immediately held at that temperature for 10 minutes so that the effects on coiling at the different temperatures could be simulated.

Tempering treatments at 600 °C for different times ranging from 0.5 to 8 hours were performed to investigate the tempered structures and related properties. Through a series of Optical Microscopy (OM), SEM and TEM examinations and mechanical testing, the results indicated that the steel with the addition of 0.3 wt.%Mo had the advantage of producing a high volume fraction of granular bainite, which gained significant benefits from precipitation hardening whilst achieving increased elongation after the tempering treatment.

Introduction

In accordance with the demand for reduced fuel consumption and CO_2 emissions in the automotive and construction industries, the development of advanced high strength steels has been progressing. Weight reduction can be achieved through the use of higher strength steels, however, formability and weldability are also vital factors in the majority of industrial applications. In addition, sufficient toughness is a prerequisite to ensure structural integrity. Ideally, a low-C bainitic microstructure offers an excellent combination of good toughness, strength and weldability [1-3]. The development of low-C bainitic steels originates from the concept that an extremely low C concentration can reduce or eliminate the interplate cementite in a bainitic ferrite matrix and hence the steel's toughness can be further improved.

Under a combined process of controlled-rolling and accelerated-cooling, the production of a high quantity of a bainitic microstructure in low-C low-alloy steels can be achieved. This processing procedure highly depends on the microalloying of Nb [2-5], since Nb has a significant effect on the retardation of recovery and recrystallization of austenite during hot rolling. With this alloy design, the recrystallization stop temperature can be shifted to higher levels. The temperature at which the rolling operation finishes is critical in the sense that it should leave the final austenite grains in an unrecrystallized pancake shape. This ensures a further degree of microstructure refinement from the bainite transformation.

In low-C bainitic steels, bainitic microstructures possess a much finer effective grain size (a platelet thickness of about 0.5 μm) and a higher dislocation density (about 1.7×10^{14} m^{-2}) [1]; relative to conventional ferrite/pearlitic steels. With higher amounts of bainite, higher strengths can be achieved due to the fine size of the bainite platelets and the high dislocation density. The characteristic structures do not impair toughness since the finer grain size compensates for the deterioration in toughness caused by dislocation hardening. The low-C bainitic microstructure achieves the required properties of increased strength without an adverse effect on toughness.

It has been asserted [6-8] that Nb-Mo containing HSLA steels produce a bainitic structure and possess excellent strength-retention characteristics at high temperatures (up to 600 °C or 700 °C), in comparison to conventional HSLA steels containing Nb and V. This finding strongly indicates that the combined addition of Nb and Mo plays an important role in significantly improving the strength of the HSLA steels at both room temperature and high temperatures (up to 700 °C). The information concerning the nano-structural characterization is absolutely essential for alloy design. However, the microstructural evolution associated with a consequent strengthening mechanism has not been studied systematically in previous research. The purpose of this study is to gain an improved and detailed appreciation of the low-C bainite substructure and to evaluate its characteristics and effect on the mechanical properties. The synergistic effect of Nb-Mo additions on the formation of low-C bainite is evaluated. The work also focuses on the tempering effect on the developed low-C bainitic strips in order to evaluate the corresponding secondary hardening.

Experimental Procedure

The investigation involved three different steels. These three experimental steels were prepared by vacuum melting, and then cast into 100 kg slabs with a thickness of 160 mm. The chemical compositions of the steels are listed in Table I. The Nb-containing (0.05%C-1.7%Mn-0.08%Nb (wt.%)) steel was chosen as the reference steel. To determine the synergistic effects of Nb-Mo additions, the other two steels had the same base composition (0.05%C-1.7%Mn-0.08%Nb (wt.%)) and were alloyed with 0.1 and 0.3 wt.%Mo separately. The reference steel was designated as Steel Nb, while the 0.1 and 0.3 wt.%Mo containing steels were designated as Steel Nb-Mo and Steel Nb-3Mo respectively. The steels also contained 0.016 wt.%Ti in order to fix the N by producing stable TN particles. It was calculated that the Ti concentration (wt.%) should be about 3.4 times that of N if the latter was to be fixed [1]. The steel strip samples were produced from the slabs by a combined process of controlled-rolling and accelerated-cooling. A schematic diagram of the whole process is presented in Figure 1. During rolling in the austenite phase a portion of the Nb would precipitate as NbC due to strain-induced precipitation. The NbC

and TiN precipitates serve to prevent austenite grain growth during controlled-rolling operations, which is an additional, essential feature of these steels. A higher portion of Nb (estimated to be as high as 0.04 wt.%) is designed to remain in austenite solid solution. The unrecrystallized, pancake-shaped austenite with a high "soluble" Nb content promotes bainite formation during the accelerated cooling. The major task in the project was to investigate whether secondary hardening occurs in the bainite within these three experimental steels after tempering treatments.

Table I. The Composition of Hot Rolled Strip (wt.%)

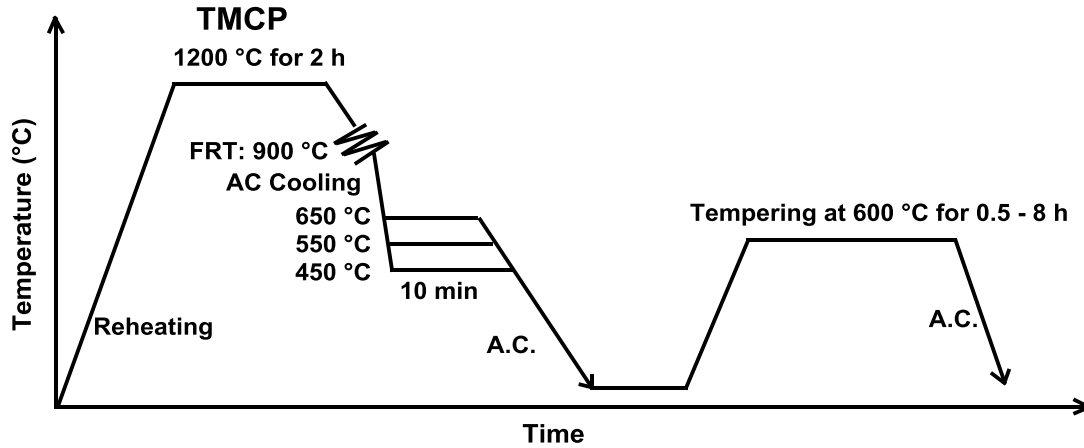| Strip	C	Mn	Si	Nb	Mo
Nb	0.05	1.7	0.2	0.08	—
Nb-Mo	0.05	1.7	0.2	0.08	0.1
Nb-3Mo	0.05	1.7	0.2	0.08	0.3

Figure 1. Schematic diagram of the thermomechanical process (with accelerated-cooling and isothermal holding) and the tempering process.

The slabs were heated to 1200 °C and held for 2 hours before rough rolling, which began at 1050 °C. During the course of rolling, the temperatures were measured by an optical pyrometer. The rolling reduction per pass was about 20% and the finish-rolling thickness was 5 mm. After finish-rolling at 900 °C, the strips were accelerated cooled to 650 °C, 550 °C and 450 °C respectively, then held at this temperature for 10 minutes, and finally cooled to room temperature by air cooling (A.C.). Depending on the holding temperatures (650, 550 and 450 °C), these three different steels were designated as Nb-650, Nb-Mo-650, Nb-3Mo-650; Nb-550, Nb-Mo-550, Nb-3Mo-550, Nb-450, Nb-Mo-450 and Nb-3Mo-450, accordingly. The samples were then tempered at 600 °C for different time periods (0.5, 1, 2, 4, and 8 hours) in order to investigate the effect of tempering the bainite.

The specimens for optical metallography (OM) and scanning electron microscopy (SEM), which were cut from the hot rolled strip samples, were mechanically ground with various SiC papers. The specimens were polished and then etched with 3% nitric acid. The Vickers hardness test was conducted under the condition of 1 kg load and 5 seconds loading time. Transmission electron microscopy (TEM) specimens were prepared by cutting discs from the strip samples (along the cross-section), thinning mechanically to 0.06 mm and then twin jet electropolishing to perforation using a mixture of 5% perchloric acid, 20% glycerol, and 75% ethanol at -2 °C, at a potential of 35 V. The specimens were examined on a Tecnai F30 field emission gun scanning transmission electron microscope equipped with an energy dispersive X-ray (EDX) spectrometer. The specimens for the Tecnai Nova 450 SEM-EBSD (electron backscatter diffraction) were prepared by the same method as the TEM thin foils, but without perforation. Orientation mapping for the EBSD data was performed with a 200 nm step size. Bruker-CrystAlign software was used for orientation measurement and analysis.

Results and Discussion

SEM examination of strip samples Nb-450, Nb-Mo-450, Nb-550 and Nb-Mo-550 are presented in Figure 2. They show that the second-phase particles are dispersed among coarse ferrite plates, which appear to have a granular morphology (ie. conventionally so-called granular bainite). In Figure 3, under SEM examination a striking feature of Strip Nb-3Mo is that the prior austenite grain boundaries are aligned along the rolling direction and appear as straight markings. This is because the finish-rolling leaves the final austenite in an unrecrystallized pancake shape. However, parts of the prior austenite grain boundaries become unclear as they are decorated by fine grains of allotriomorphic ferrite (as shown in Figure 3). Optical micrographs, as shown in Figure 4, show the microstructures of strip samples Nb-450, Nb-Mo-450 and Nb-3Mo-450. Microstructural characterization focused on these three samples as they consisted of high quantities of granular bainite. It is absolutely vital to have the quantitative volume fractions of granular bainite, M/A constituents etc., so that the structure-property relationships can be evaluated. As will be seen later in this section, quantitative metallography assessed by using SEM-EBSD is utilized in this work. The volume percentages (vol.%) of different phases in the three hot-rolled strip samples are listed in Table II. It is apparent that the addition of Mo can improve the hardenability with respect to bainitic transformation. The detailed structures of the samples have been studied by TEM. The representative TEM images for allotriomorphic ferrite and granular bainite are presented in Figure 5. Figure 5(a) shows that the allotriomorphic ferrite possesses an equi-axed morphology, which does not contain any subgrain structure; the strain-induced Nb carbides can be seen in the allotriomorphic ferrite grains. Figure 5(b) displays the typical substructural features of granular bainite, which clearly indicates that the coarse ferrite plates referred to as granular bainite do not really exist. In fact, the TEM micrograph clearly indicates that the coarse plate of granular bainite is composed of parallel fine elongated platelets, with a thickness of about 0.5 μm. The TEM results are very similar to those reported elsewhere [9-14]. The morphology of fine elongated platelet shapes is directly related to the displacive transformation [15]. The parallel fine elongated platelets have a similar orientation and form a sheaf morphology, which is not different from ordinary bainite. The peculiar feature of granular bainite is the lack of the austenite thin films and carbides within the bainitic ferrite because of the low C content. The formation of second phases (M/A constituents) results from the C that is partitioned from the bainitic ferrite stabilizing the residual austenite, so that the final

microstructure contains both retained austenite and some high-C martensite. The microstructures of the second phases depend on the degree of C enrichment.

Table II. The Volume Fraction of Phases in the Three Hot Rolled Strip Samples
(F: allotriomorphic ferrite, G.B.: granular bainite, M/A: martensite/austenite constituent,
D.P.: degenerate pearlite, vol.%)

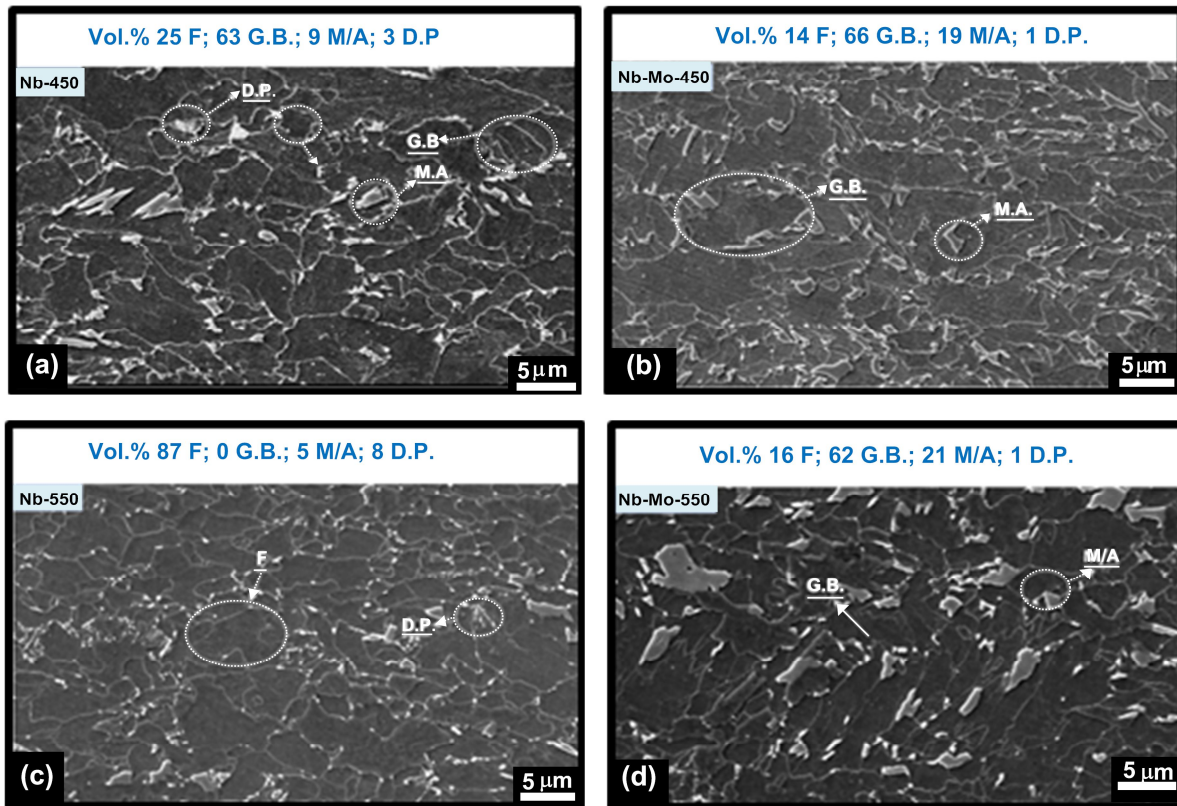| Phases/Strip	Nb-450	Nb-Mo-450	Nb-3Mo-450
F	25	14	8
G.B.	63	66	79
M/A	9	19	2
D.P.	3	1	11

Figure 2. SEM micrographs illustrating all phases including granular bainite (G.B.), allotriomorphic ferrite (F), martensite/austenite constituents (M/A), and degenerate pearlite (D.P.) in; (a) Nb-450, (b) Nb-Mo-450, (c) Nb-550 and (d) Nb-Mo-550.
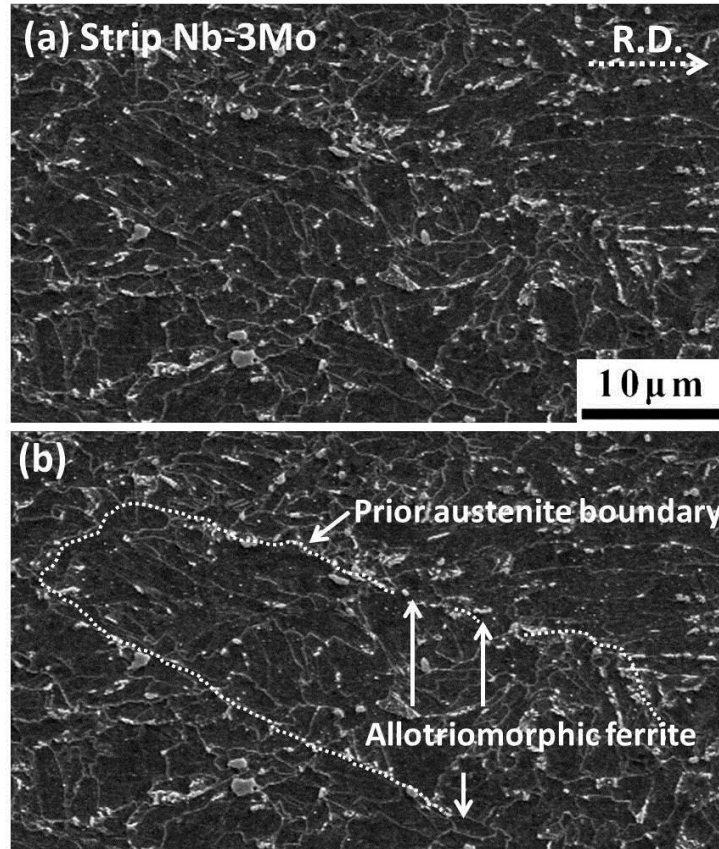
Figure 3. (a) SEM image showing the microstructure of Strip Nb-3Mo, (R.D.: rolling direction), (b) the prior austenite grain boundary depicted with dashed lines and arrowed lines indicating the distribution of allotriomorphic ferrite along grain boundary in (a).
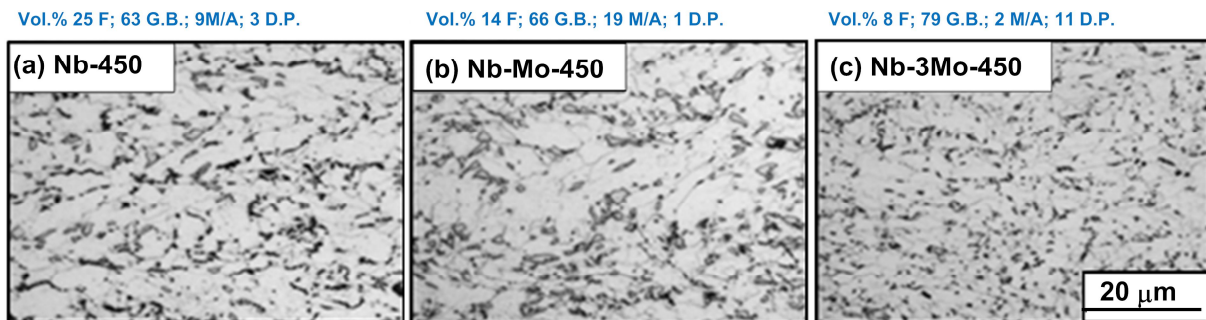

Figure 4. OM micrographs showing the microstructures of; (a) Nb-450, (b) Nb-Mo-450, (c) Nb-3Mo-450. Granular bainite (G.B.), allotriomorphic ferrite (F), martensite/austenite constituents (M/A), and degenerate pearlite (D.P.).
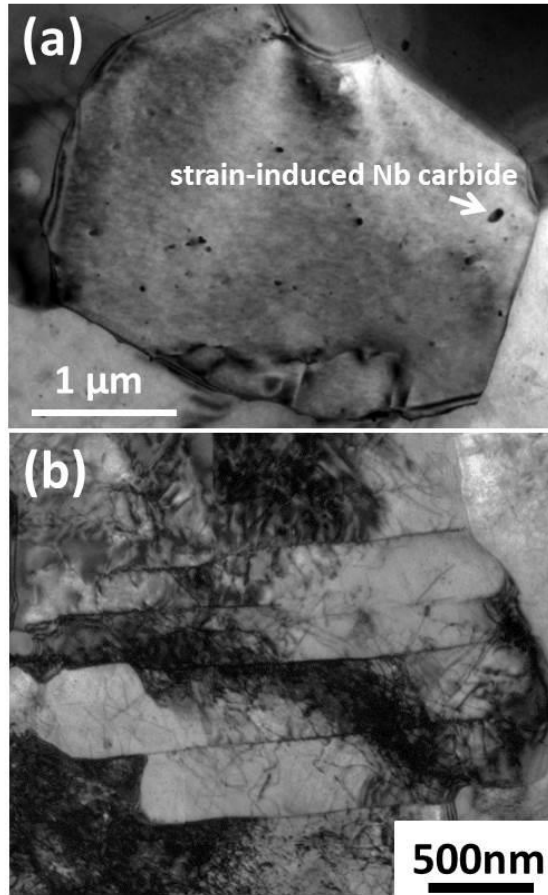
34

Figure 5. TEM micrographs showing; (a) allotriomorphic ferrite and (b) granular bainite in Nb-Mo-450 strip.

Although TEM can be used to observe the morphology of granular bainite and determine the sub-unit ferrite platelet boundaries, it has difficulty in assessing the volume fraction of granular bainite in the steel strips, with varying Mo additions, due to the limits of the analyzed area. In this work a SEM-EBSD technique has been utilized to obtain crystallographic data for quantitative metallography. The orientation relationship between a pair of like crystals, the crystallographic bases of which are defined from a common origin, can be presented using a rotation matrix. From the rotation matrix, a corresponding axis/angle pair can be derived. This infers that, if one of the crystals is rigidly rotated about the specified axis which passes through the original, through a right-handed angle of rotation h, its orientation coincides with that of the other. For each pair of ferrite (body-centered cubic, bcc) crystals, there are 24 crystallographically equivalent descriptions in terms of axis angle pairs or rotation matrices [16]. In the present EBSD work, the equivalent axis angle pair with the smallest angle of rotation was chosen for each pair of adjacent ferrite grains in order to interpret the data clearly.

The orientation micrograph in Figure 6(a) is obtained from EBSD imaging of the granular bainite in strip sample Nb-450; the distribution of colors in the overall microstructure depends on the crystal orientation. The image is associated with the contrasts in brightness for corresponding Kikuchi patterns generated from all points on the analyzed sample. The image quality of granular bainite is a matter of concern because the high dislocation densities in bainite can reduce the quality of Kikuchi patterns and cause misleading representations of the misorientation angle. In order to elucidate this, the regions marked with A and B in Figure 6(a) have been examined. The corresponding Kikuchi patterns for point A and point B, in Figures 6(d) and 6(e), are clearly shown with an image quality of over 0.6, which indicates that the dislocation density in granular bainite does not have a serious effect on the EBSD imaging. In the present study, the detection of the misorientation angle is significant for microstructural characterization and needs to be elucidated clearly. In the cubic system, there are 24 axis angle pairs for a given adjacent ferrite sub-unit. The misorientation angle can be obtained after the axis angle pair was calculated. The misorientation angle profile versus the scanned distance (as shown in 6(b)) is obtained by using CrystAlign software of Bruker Corp. It indicates that Point A (A matrix) has a relative 2.99º misorientation angle to Point B (B matrix). The Euler angles of Points A and B are (324º 21º 12º) and (320º 19º 14º) respectively, relative to the coordination of the sample (S). They can be derived to the following rotation matrixes relative to the coordination of the sample.

Coordinate transformation matrix for S to A $\quad (A \, J \, S) = \begin{bmatrix} 0.905 & \overline{0.418} & 0.075 \\ 0.369 & 0.861 & 0.351 \\ \overline{0.211} & \overline{0.290} & 0.934 \end{bmatrix}$

Coordinate transformation matrix for S to B $\quad (B \, J \, S) = \begin{bmatrix} 0.890 & \overline{0.448} & 0.079 \\ 0.404 & 0.858 & 0.316 \\ \overline{0.209} & \overline{0.249} & 0.946 \end{bmatrix}$

The coordinate transformation matrix for B to A can be derived as follows.

$$(A \, J \, B) = \begin{bmatrix} 0.999 & 0.037 & 0.013 \\ \overline{0.037} & 0.999 & 0.035 \\ \overline{0.011} & \overline{0.035} & 0.999 \end{bmatrix}$$

The detailed notation of coordinate transformation matrices can be referred to the relevant worked example in [16]. From the coordinate transformation matrix (A J B), 24 equivalent axis-angle pairs can be obtained as shown in Table III. The axis angle pair with the smallest angle of rotation, [0.9971 -0.2312 0.7082]/2.99°, is listed first. It is noted that the smallest angle has been chosen for the general interpretation of the misorientation of the adjacent structures in the EBSD image. In Figure 6(a), the coarse plate region (marked by A-B) is recognized as granular bainite because of the low-angle misorientation boundary of sub-unit platelets; the corresponding plot for misorientation angle versus the detected distance is shown in Figure 6(b). On the other hand, the region marked by C-D in Figure 6(a) is recognized as a ferrite microstructure since no subgrain boundary can be detected (as shown in Figure 6(c)). EBSD measurements were carried out to provide information regarding the density distribution for the misorientation of the boundaries in the microstructure for samples Nb-450, Nb-Mo-450 and Nb-3Mo-450. The density distributions of grain boundary misorientation angles for these strips (with a scanned area of 100 x 100 µm in each sample) are displayed in Figure 7; it is clearly demonstrated that two peaks (with highest frequency) are located around 0-10° and 50-60°. The result is consistent with that reported in the previous work for a high quantity of bainitic structure [17]. In this work, the volume percentages of ferrite and granular bainite were measured from EBSD images, and the volume percentages of M/A phases and degenerate pearlite in second phases were estimated from SEM images. The combined data from SEM and EBSD images were used to estimate the volume percentages of phases and the results are shown in Table II. They indicate that the addition of 0.1 wt.%Mo obviously retards the allotriomorphic ferrite formation but only slightly promotes the granular bainite formation. Rather, there is a significant increase in M/A constituent instead. They also show that the addition of 0.3 wt.%Mo greatly suppresses allotriomorphic ferrite formation but significantly promotes granular bainite transformation and refines the whole microstructure.

Table III. The 24 Axis-Angle Pairs for Adjacent Grains A and B

| No.	Axis			Angle (°)
1	0.6671	-0.2312	0.7082	2.99
2	-0.5216	-0.5769	-0.6286	119.8
3	0.523	0.6296	0.5745	120.5
4	-0.0015	-0.7052	0.709	172.5
5	0.7379	-0.674	0.0354	176.4
6	-0.7395	-0.0301	0.6725	176.1
7	-0.9957	0.0021	-0.0926	89.9
8	-0.0406	0.9981	-0.0457	95.5
9	-0.674	-0.738	-0.0316	175.9
10	0.6305	-0.5238	-0.5728	120.2
11	0.5949	-0.5378	0.5974	114.1
12	-0.0474	0.0027	0.9989	174.8
13	0.9957	0.0921	0.0021	90.6
14	0.6724	0.0339	0.7394	176.6
15	0.0479	0.0427	-0.9979	95.3
16	-0.6277	0.5786	0.5209	120.1
17	-0.5955	-0.5929	0.5421	113.7
18	0.0453	-0.999	0.0027	174.6
19	0.0503	-0.9977	-0.0446	84.7
20	0.0654	-0.7075	-0.7037	179.8
21	-0.0468	0.0524	0.9975	85
22	0.5618	0.6095	-0.5594	126.3
23	-0.5573	0.5597	-0.6134	126
24	-0.9979	-0.0452	-0.0473	179.7
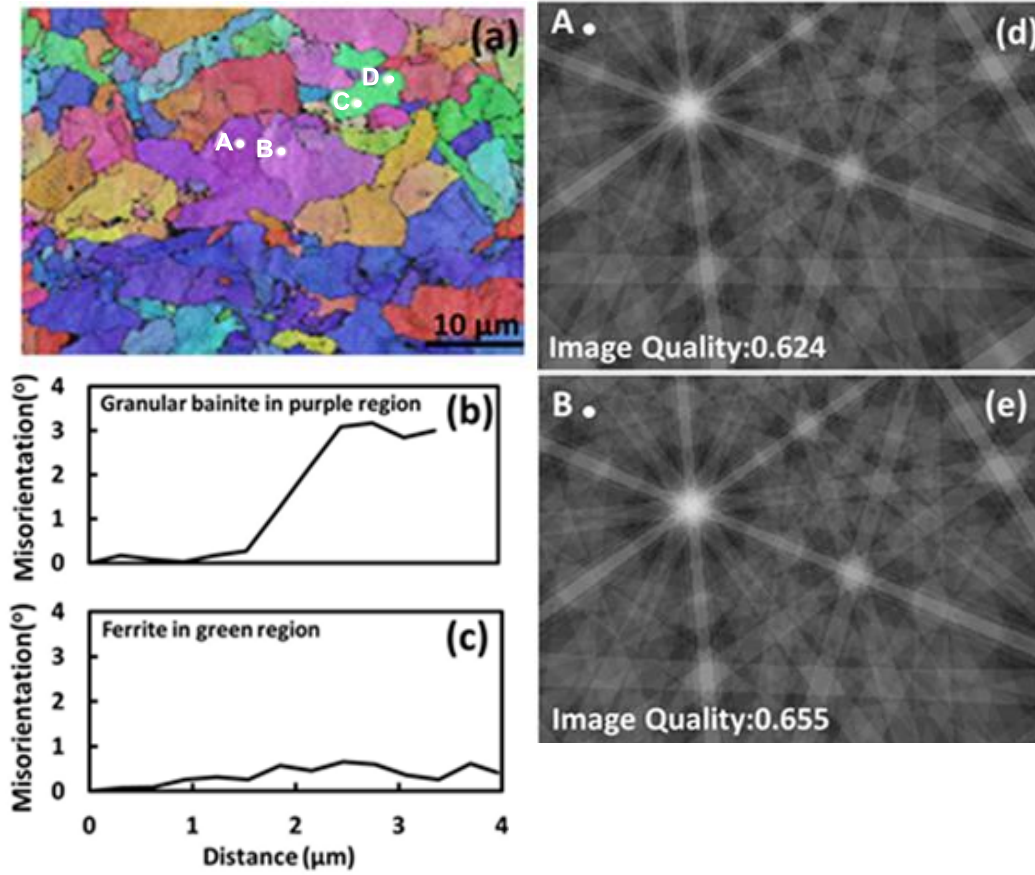
Figure 6. (a) EBSD map of Nb-450 Strip, (b) The variation of misorientation angle from point A to B in purple region, (c) The variation of misorientation angle from point C to D in green region, (d) and (e) the corresponding simulated Kikuchi patterns at points A and B in (a).
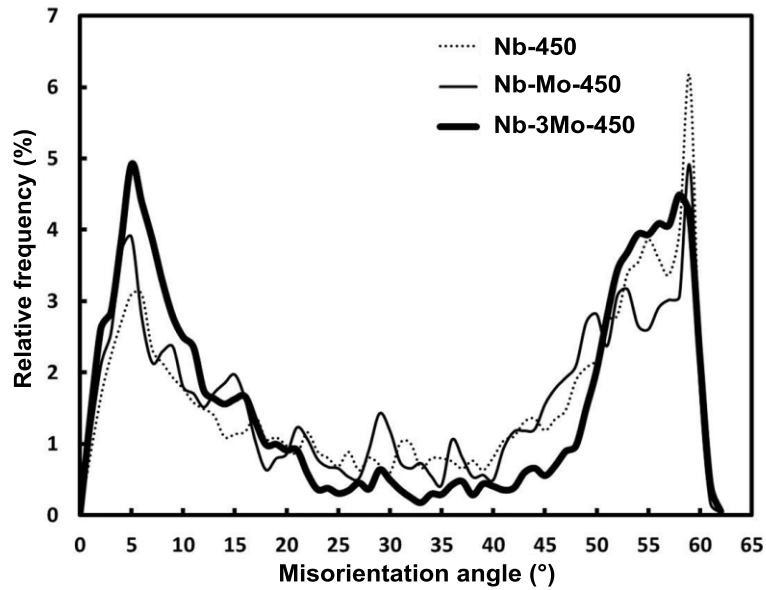

Figure 7. The misorientation angle profiles for Steels Nb-450, Nb-Mo-450 and Nb-3Mo-450.

In this work, the tempered bainite in the strip samples has been studied using Vickers hardness measurements and HRTEM examination. Vickers hardness measurement for granular bainite was performed under a load of 1 kg in order to indent on the granular bainite only. Each data point of Vickers hardness (with the standard deviation of about HV 5 – 8) was obtained from 30 measurements on granular bainite areas on each sample. Figure 8 shows the Vickers hardness data for strip samples Nb-450, Nb-Mo-450 and Nb-3Mo-450 after tempering at 600 ℃ for different time intervals, ranging from 0.5 to 8 hours. It is clearly indicated that tempering steels Nb-450, Nb-Mo-450 and Nb-3Mo-450 does not cause a decrease in hardness after low tempering times; this behavior is obviously different from that of tempering martensite. For martensite, secondary hardening definitely involves the replacement of metastable cementite with the alloy carbides. The formation of these alloy carbides requires the long-range diffusion of the corresponding substitutional atoms and their precipitation is rather sluggish. It has been generally recognized that secondary hardening reactions in alloy steels with a bainitic microstructure are slower than with martensite because the coarser cementite particles in bainite take a longer time to dissolve before alloy carbides form [15]. However, in the present work, the experimental steels have an extremely low C concentration (0.05 wt.%C) in order to reduce or eliminate the interplate cementite in the bainitic ferrite matrix; interference from cementite during tempering can be surely avoided. It is worth noting that during the course of tempering at 600 ℃ the hardness of sample Nb-3Mo increased to its highest value, HV 245, (by an increment of HV 20) after the 1 hour tempering treatment and the hardness is maintained at the same high level even after 8 hours. The hardness of samples Nb-Mo and Nb-450 showed similar trends, rising to the peak values, HV 233 (by an increment of HV 18) and HV 228 (by an increment of HV 20), respectively, after a 1 hour tempering time; after the peaks, their hardness declined sluggishly and decreased only by a small amount even after an 8 hour tempering time. It is evident that the Nb and Nb-Mo containing low-C bainitic steel strips have the advantage of obtaining secondary hardening at a 600 ℃ tempering temperature.

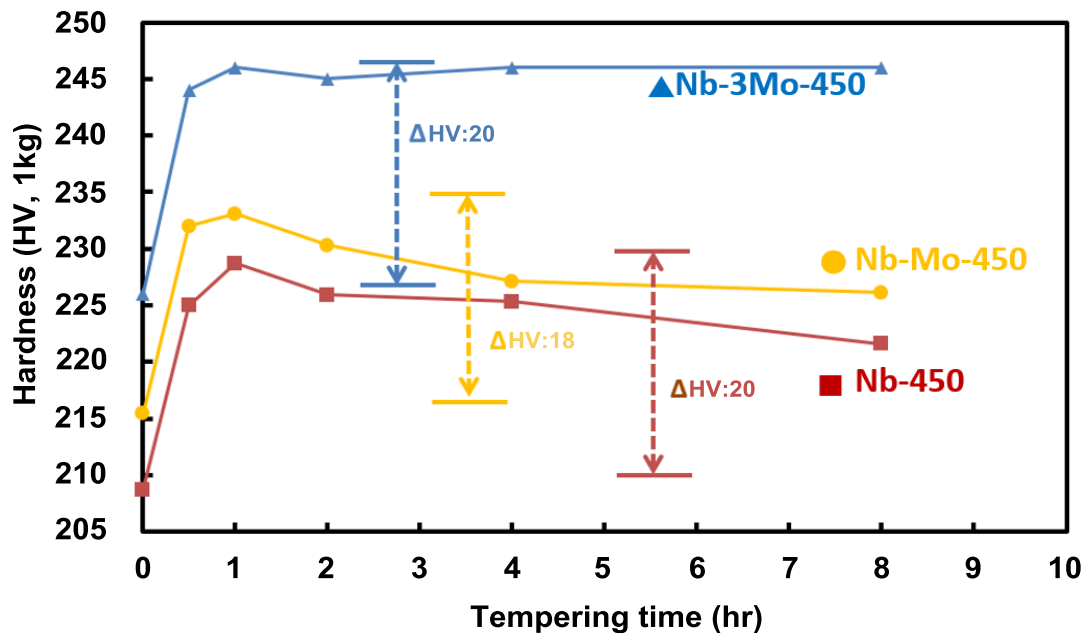
Figure 8. Hardness of granular bainite vs. tempering time at 600 ℃.

During the hot deformation of the prior austenite, the strain-induced Nb carbides precipitate and possess a cube-cube orientation relationship with the prior austenite [18]. In the course of cooling to room temperature, the deformed austenite transforms to allotriomorphic ferrite and bainite. The strain-induced Nb carbides usually have a size of more than 20 nm [19] and they possess no particular orientation relationship with the allotriomorphic ferrite [20], but adopt a Kurdjumov-Sachs (K-S) orientation relationship with bainite [19]. In contrast, during the tempering of bainite, nanometer-sized Nb carbides precipitate and have a Baker-Nutting orientation relationship with the tempered bainite [21-23]. Thus, the difference in orientation relationships can be utilized to identify the Nb carbides formed in the tempered bainite. TEM micrographs in Figure 9 display the tempered granular bainite in steel Nb-450 after tempering at 600 ℃ for 1 hour; they show that nanometer-sized Nb carbides preferentially precipitated at dislocation lines. It is reasonably assumed that Nb atoms, a strong carbide-forming element, would diffuse toward the dislocation line and associate with C to precipitate MC-type carbides to reduce the lattice strain [24]. It is clear that granular bainite exhibits a significant secondary hardening effect by precipitating nanometer-sized carbides at dense dislocation lines. However, the addition of Mo raises the hardness of granular bainite in steels Nb-Mo-450 and Nb-3Mo-450 (as shown in Figure 8). As the secondary hardening is associated with alloy-carbide forming, it is vital to reveal the detail of the nanometer-sized carbides evolution in low-C bainite during the course of tempering. In previous conventional TEM research work for tempered bainite in low-C Nb and Nb-Mo containing steels [21-23], the Baker-Nutting (B-N) orientation relationship for carbide/ferrite matrix has been reported. However, the HRTEM image with its corresponding FFT (Fast Fourier Transformation) diffractogram provides a unique way for investigation of the nano-sized carbide/ferrite orientation [25]. In the present work, it has been confirmed that during tempering, extremely small nano-sized carbides are formed and these carbides satisfy the B-N orientation relationship with the bainitic ferrite matrix, $(0\ \ 0\ \ 1)_{carbide}//(0\ \ 0\ \ 1)_\alpha$ and $[\bar{1}\ \ 1\ \ 0]_{carbide}//[1\ \ 0\ \ 0]_\alpha$. In the habit plane of carbides on $(0\ \ 0\ \ 1)_{carbide}$, the lattice mismatch is extremely small: $[d_{(0\ \ 1\ \ 1)carbide} - d_{(0\ \ 1\ \ 0)_\alpha}] / d_{(0\ \ 1\ \ 0)_\alpha} = (0.313 - 0.2866) / 0.2866 = 0.093$, whereas perpendicular to the habit plane, the lattice mismatch is relatively large: $[d_{(0\ \ 0\ \ 2)carbide} - d_{(0\ \ 0\ \ 1)_\alpha}] / d_{(0\ \ 0\ \ 1)_\alpha} = (0.443/2 - 0.2866) / 0.2866 = -0.227$. Therefore, such lattice mismatches favor the formation of thin platelets. It is probable that carbides nucleate as spherical particles to maintain the minimum interface energy with the ferrite matrix in the early stages, and then grow rapidly in the best matched direction in a plate-like form during tempering, as shown in Figures 9 and 10. When the zone axis $[\bar{1}\ \ 1\ \ 0]_{carbide}//[1\ \ 0\ \ 0]_\alpha$ is chosen for HRTEM observation, the habit plane $(0\ \ 0\ \ 2)_{carbide}//(0\ \ 0\ \ 2)_\alpha$ presents an edge-on configuration to the incident beam direction, as shown in Figures 8 and 9.
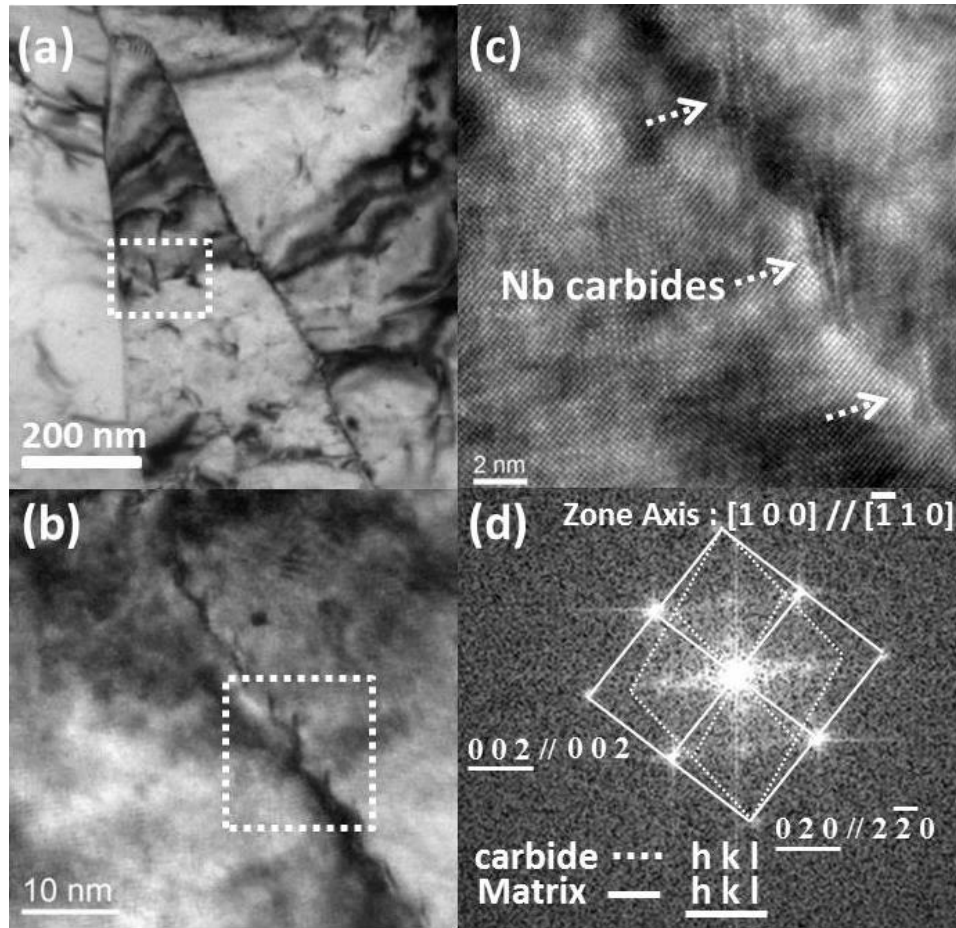
Figure 9. (a) Substructure of tempered granular bainite in Steel Nb-450 after tempering at 600 ℃ for 1 hour, (b) the distribution of nanometer-sized carbides located at the dislocation line in the enlarged region of (a) with dashed white frame, (c) the detailed morphology of nanometer-sized carbides in the enlarged region of (b) with dashed white frame, (d) corresponding FFT image of carbides and bainitic matrix in (c).
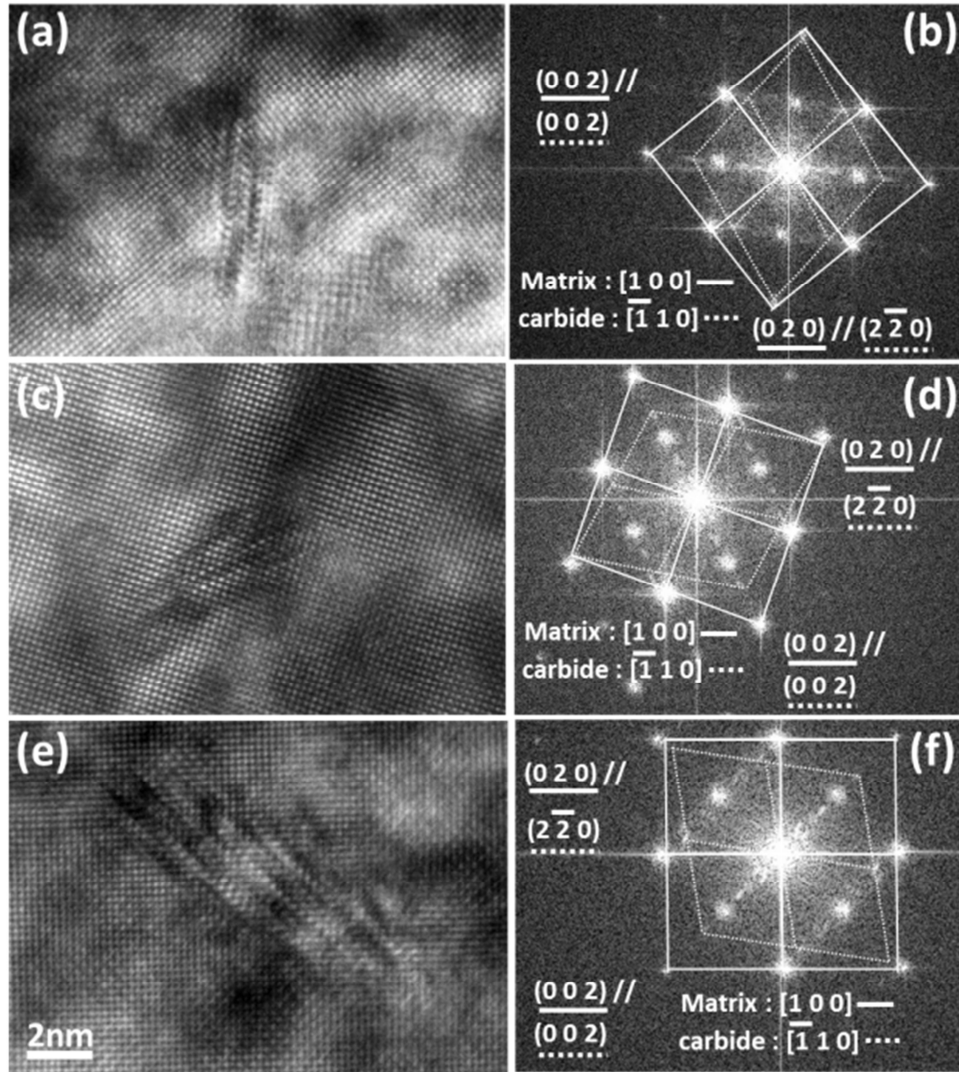
Figure 10. HRTEM images illustrating the nanometer-sized carbides in bainitic matrix of; (a) Nb-strip, (c) Nb-Mo strip, and (e) Nb-3Mo strip after 1 hour tempering; (b), (d) and (f) are the corresponding FFT images.

The effect of Mo addition on the size of Nb carbides can be clarified by evaluating variations in the length of carbides with tempering as shown in Figure 11. Each data point of average carbide length and Mo/Nb atomic ratio was estimated by 50 and 20 measurements respectively, on nanometer-sized carbides. For the samples tempered at 600 °C for 1 hour, average lengths of carbide in strip samples Nb-450, Nb-Mo-450 and Nb-3Mo-450 were respectively 3.7±1.1 nm, 3.8±0.6 nm, and 4.4±1.6 nm. For the samples tempered at 600 °C for 8 hours, average lengths of carbide in strip samples Nb, Nb-Mo and Nb-3Mo were respectively 4.3±0.8 nm, 4.3±1.3 nm and 5.5±2.1 nm.
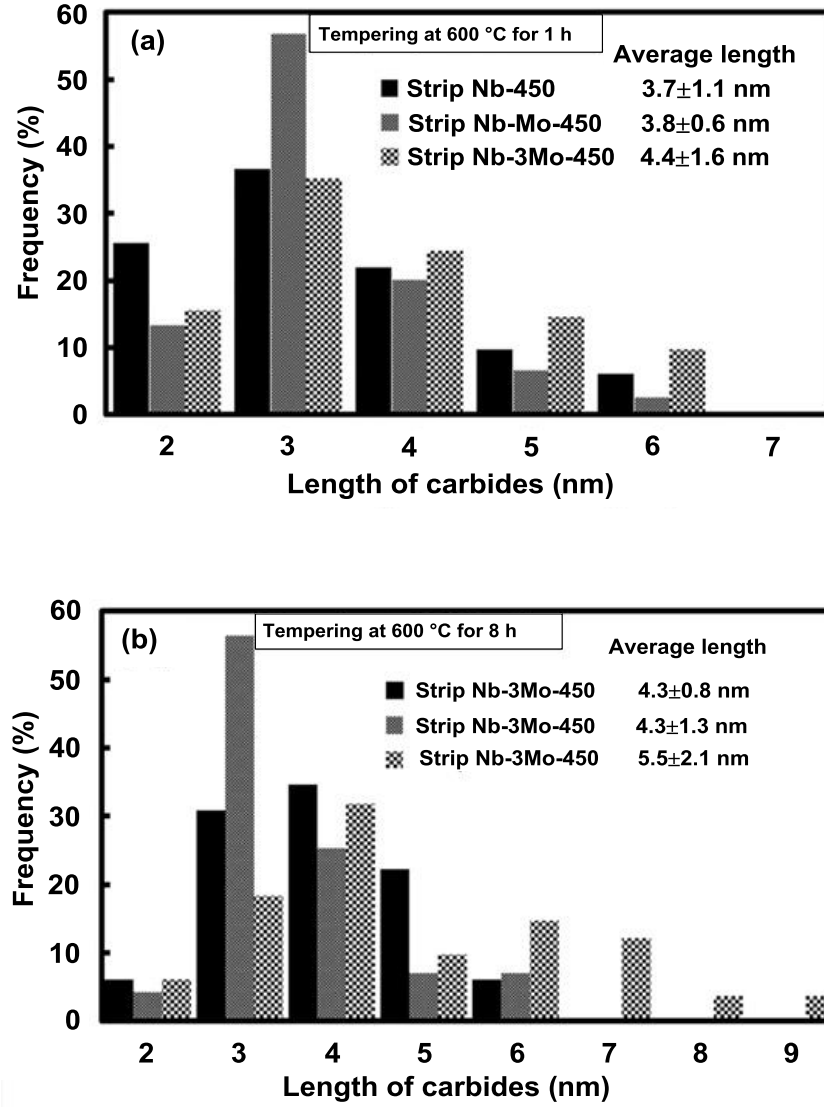
43

Figure 11. The distribution of nanometer-sized carbides in length in all three steels after;
(a) 1 hour of tempering and (b) 8 hours of tempering.

It is worth noting that the addition of Mo did not have a significant effect on the size of nanometer-size carbides formed in the tempered granular bainite structures investigated. The degree of incorporated Mo atoms in Nb carbides has been simultaneously assessed by nano-probe EDX spectroscopy. The spectra in Figures 12(a) and (b) were obtained from strip sample Nb-Mo tempered at 600 °C for 1 and 8 hours respectively; the atomic ratio Nb/Mo for the former was 4.87 and the latter 4.07. The spectra in Figures 11(c) and (d) were obtained from sample Nb-3Mo tempered at 600 °C for 1 and 8 hours respectively; the atomic ratio Nb/Mo for the former was 1.12 and the latter 1.10. Mo plainly becomes a dominant carbide forming element in (Nb_xMo_{1-x}) carbides with increasing Mo addition, which is consistent with thermodynamic calculations in previous research [26].
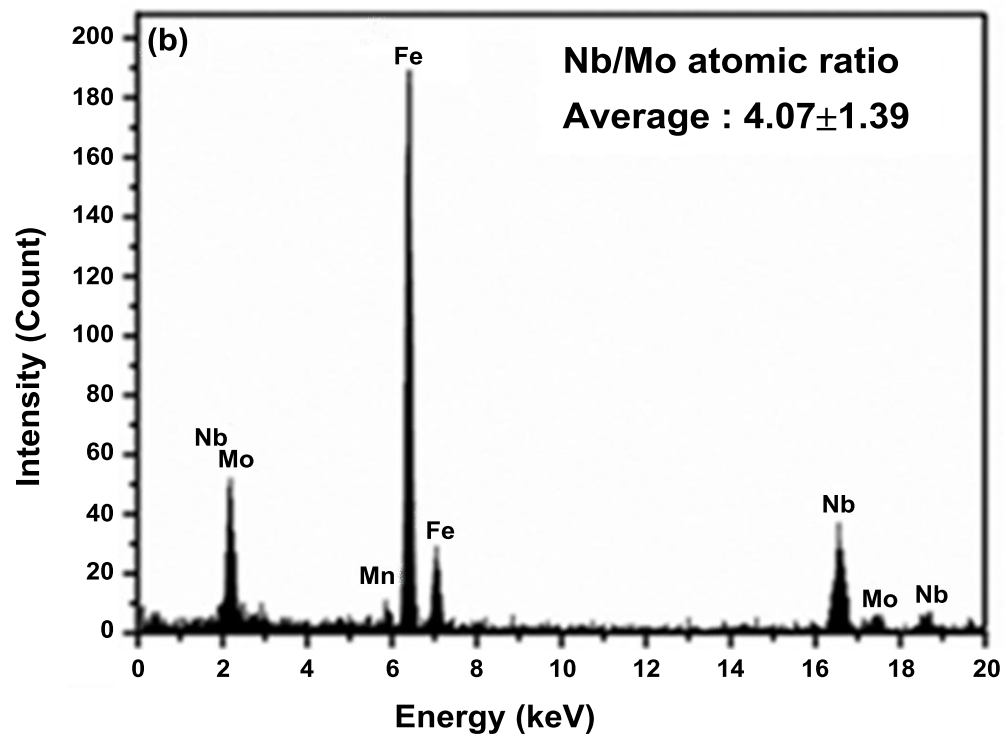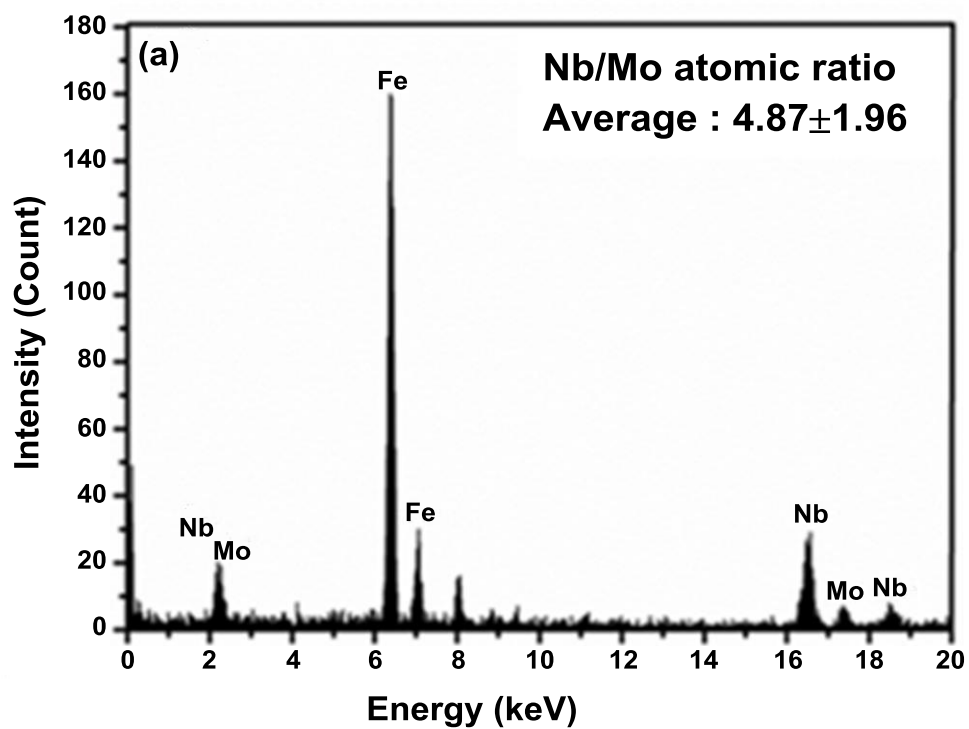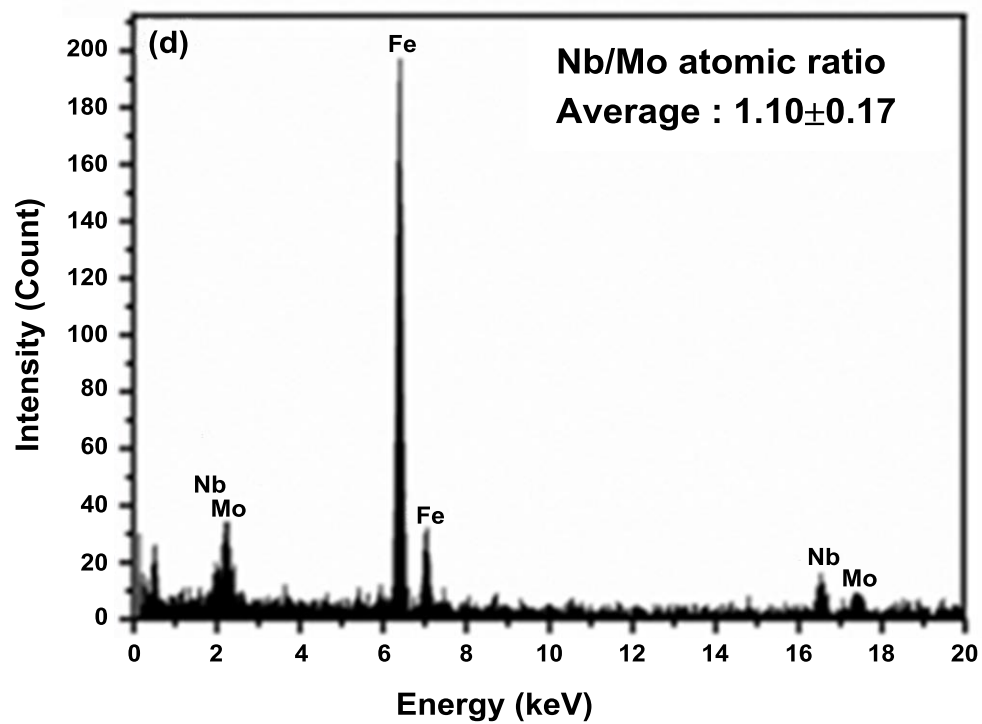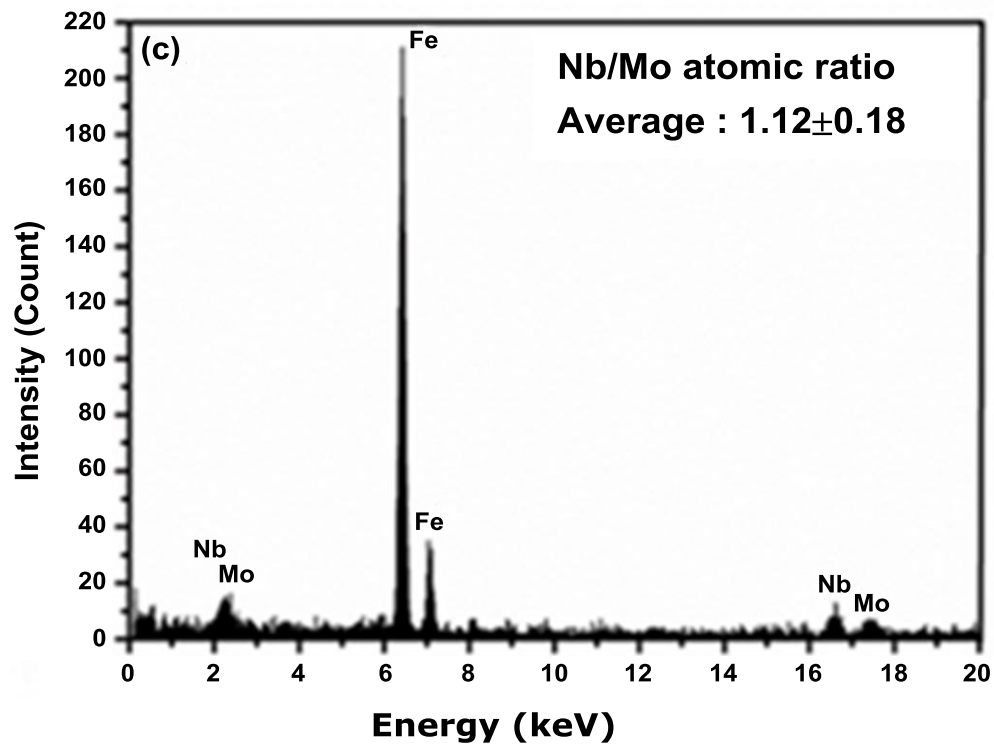
Figure 12. EDX spectra in (a) and (b) obtained from steel Nb-Mo tempered at 600 °C for 1 and 8 hours, respectively; the spectra (c) and (d) obtained from steel Nb-3Mo tempered at 600 °C for 1 and 8 hours, separately.

In this work, the granular bainite in the bainitic steel strips possessed a high dislocation density of about $5.3 \times 10^{14}\,\text{m}^{-2} - 5.6 \times 10^{14}\,\text{m}^{-2}$. The detailed method for dislocation density measurement has been described elsewhere [27]. The dislocations are apparently stable at high temperatures; the dislocation density does not change significantly during tempering at 600 °C as seen in Table IV, which indicates that the dislocation densities of the tempered samples Nb-450, Nb-Mo-450 and Nb-3Mo-450 had only reduced to the range of $3.6 \times 10^{14}\,\text{m}^{-2} - 4.9 \times 10^{14}\,\text{m}^{-2}$. It is obvious that the dislocations in the Nb and Nb-Mo bearing steels investigated in this work possessed a remarkable thermal stability during tempering at 600 °C.

Table IV. The Dislocation Density (m^{-2}) of Granular Bainite in the Three Steels after Tempering at 600 °C for 0, 1 and 8 hours

Time/hours	Nb-450	Nb-Mo-450	Nb-3Mo-450
0	$(5.3\pm1.2)\,\text{x}10^{14}$	$(5.4\pm0.9)\,\text{x}10^{14}$	$(5.6\pm0.8)\,\text{x}10^{14}$
1	$(4.6\pm0.8)\,\text{x}10^{14}$	$(4.8\pm1.2)\,\text{x}10^{14}$	$(4.9\pm1.0)\,\text{x}10^{14}$
8	$(3.9\pm1.3)\,\text{x}10^{14}$	$(3.9\pm1.4)\,\text{x}10^{14}$	$(3.6\pm1.1)\,\text{x}10^{14}$

The mechanical properties for the strip samples are presented in Tables V and VI. The data clearly shows that steel Nb-3Mo possessed the optimum combination of strength and elongation after tempering at 600 °C for 1 hour. Steel Nb-3Mo with the addition of 0.3 wt.% Mo had the advantage of producing a high volume fraction of granular bainite, which gained significant benefits from secondary hardening. It can be concluded that during tempering, the amount of nanometer-sized carbides increases in bainitic strip steels with a higher level of Mo content, since the number of alloy carbides formed in the granular bainite is proportional to the volume fraction of granular bainite.

Table V. The Yield/Tensile Strength Values(MPa) of the Three Steels after Tempering at 600 °C for 0, 1 and 8 hours

Time/hours	Nb-450	Nb-Mo-450	Nb-3Mo-450
0	512/630	479/683	575/679
1	594/652	619/678	672/718
8	586/638	605/655	651/702

Table VI. The Elongation (%) of the Three Steels after Tempering at 600 °C for 0, 1 and 8 hours

Time/hours	Nb-450	Nb-Mo-450	Nb-3Mo-450
0	22	21	19
1	29	27	27
8	30	27	27

Conclusions

In this work, three low-C Nb-containing strip steels with different levels of Mo (0, 0.1 and 0.3 wt.%) have been produced using a controlled-rolling and accelerated-cooling process. The findings can be summarized as follows:

1. All the steels contained large amounts of granular bainite. The substructure of granular bainite has been revealed by TEM; granular bainite is composed of parallel sub-unit ferrite platelets, with a thickness of about 0.5 μm. The parallel sub-unit ferrite platelets have a similar orientation and form a sheaf morphology, which is not different from ordinary bainite.

2. SEM-EBSD techniques have been utilized to obtain quantitative metallography data for the steels. The results clearly indicate that the addition of Mo promotes the formation of granular bainite.

3. The steel with the addition of 0.3 wt.%Mo had the advantage of producing a high volume fraction of granular bainite, and gained significant benefits from secondary hardening. Mo did not appear to further refine the (Nb,Mo) carbides but the increased proportion of the precipitate rich granular bainite led to increased strength whilst maintaining good ductility

Acknowledgement

References

1. H.K.D.H. Bhadeshia, Steel Technology International 1989, Ed. P. H. Scholes, (Sterling Publication International Ltd, 1989), 289-294.

2. T. Gladman, *The Physical Metallurgy of Microalloyed Steels*, (London, UK: The Institute of Materials, 1997).

3. N.K. Balliger and R.W.K. Honeycombe, "The Effect of Nitrogen on Precipitation and Transformation Kinetics in Vanadium Steels," *Metallurgical Transaction A*, 11 (1980), 420-430.

4. H.L. Andrade, M.G. Akben and J.J. Jonas, "Effect of Molybdenum, Niobium and Vanadium on Static Recovery and Recrystallisation on Solute Strengthening in Microalloyed Steels," *Metallurgical Transaction A*, 14 (1983), 1976-1984.

5. B. Dutta and C.M. Sellars, "Effect of Composition and Process Variables on Nb(C,N) Precipitation in Niobium Microalloyed Austenite," *Materials Science and Technology*, 3 (1987), 197-206.

6. C. Fossaert et al., "The Effect of Niobium on the Hardenability of Microalloyed Austenite," *Metallurgical and Materials Transactions A*, 26 (1995), 21-30.

7. M.G. Akben, B. Bacroix and J.J. Jonas, "Effect of Vanadium and Molybdenum Additions on High Temperature Recovery, Recrystallisation and Precipitation Behaviour of Niobium Based Microalloyed Steels," *Acta Metallurgica*, 31 (1983), 161-174.

8. M. Charleux et al., "Precipitation Behaviour and its Effect on Strengthening of an HSLA – Nb/Ti Steel," *Metallurgical and Materials Transactions A*, 32A (2001), 1635-1647.

9. S.C. Wang and J.R. Yang, "Effects of Chemical Composition, Rolling and Cooling Conditions on the Amount of Martensite/Austenite (M/A) Constituent Formation in Low Carbon Bainitic Steels," *Materials Science and Engineering A,* 154 (1992), 43-49.

10. S.C. Wang, R.I. Hsieh and J.R. Yang, "Effect of Rolling Processes on the Microstructure and Mechanical Properties of Ultralow Carbon Bainitic Steels," *Materials Science and Engineering A,* 157 (1992), 29-36.

11. J.R. Yang, C.Y. Huang and S.C. Wang, "The Development of Ultra Low Carbon Bainitic Steels," *Materials & Design*, 13 (1992), 335-338.

12. C.Y. Huang, J.R. Yang and S.C. Wang, "Effect of Compressive Deformation on the Transformation Behaviour of an Ultra Low Carbon Bainitic Steel," *Materials Transactions - The Japan Institute of Metals*, 34 (1993), 658-668.

13. J.R. Yang et al., "The Influence of Plastic Deformation and Cooling Rates on the Microstructural Constituents of an Ultra Low Carbon Bainitic Steel," *The Iron and Steel Institute of Japan International,* 35 (1995), 1013-1019.

14. C.S. Chiou, J.R. Yang and C.Y. Huang, "The Effect of Prior Compressive Deformation of Austenite on Toughness Property in an Ultra Low Carbon Bainitic Steel," *Materials, Chemistry and Phys*ics, 69 (2001), 113-124.

15. H.K.D.H. Bhadeshia, *Bainite in Steels*, 2nd edition, (London, UK: Iom Communications Ltd, 2001), 91-98.

16. H.K.D.H. Bhadeshia, *Worked Examples in the Geometry of Crystals*, (London, UK: Institute of Metals, 1987).

17. K.Y. Zhu et al., "An Approach to Define the Effective Lath Size Controlling Yield Strength of Bainite," *Materials Science and Engineering A*, 527 (2010), 6614-6619.

18. M. Enomoto, "Nucleation of Phase Transformations at Intragranular Inclusions in Steel," *Metals and Materials*, 4 (1998), 115-123.

19. W.B. Lee et al., "Carbide Precipitation and High Temperature Strength of Hot Rolled HSLA Steel," *Metallurgical and Materials Transactions A,* 33 (2002), 1689-1698.

20. F. Perrard et al., "TEM Study of NbC Heterogeneous Precipitation in Ferrite," *Philosophical Magazine,* 27 (2006), 4271-4284.

21. W.B. Lee et al., "Influence of Mo on Precipitation Hardening in Hot Rolled HSLA Steels Containing Nb," *Scripta Materialia*, 43 (2000), 319-324.

22. W.B. Lee et al., "Carbide Precipitation and High Temperature Strength of Hot Rolled High Strength, Low Alloy Steels Containing Nb and Mo," *Metallurgical and Materials Transactions A*, 33A (2002) 1689-1698.

23. K. Maruyama, K. Sawada and J. Koike, "Strengthening Mechanisms of Creep Resistant Tempered Martensitic Steel," *The Iron and Steel Institute of Japan International*, 41 (2001), 641-653.

24. H-J. Kestenbach, "Dispersion Hardening by Niobium Carbonitride Precipitation in Ferrite," *Journal of Materials Science and Technology,* 13 (1997), 731-739.

25. H.W. Yen et al., "Orientation Relationship Transition of Nanometer Sized Interphase Precipitated TiC Carbides in Ti Bearing Steel," *Journal* of *Materials Science and Technology,* 26 (2010), 421-430.

26. C.M. Enloe et al., "Compositional Evolution of Microalloy Carbonitrides in a Mo Bearing Microalloyed Steel," *Scripta Materilia,* 68 (2013), 55-58.

27. J.R. Yang and H.K.D.H. Bhadeshia, "The Dislocation Density of Acicular Ferrite in Steel Welds," *Welding Journal,* 69 (1990), 305-307.

EFFECT OF MOLYBDENUM ON THE PRECIPITATION BEHAVIOR IN TITANIUM MICROALLOYED HSLA STEELS PART I – PRECIPITATION IN AUSTENITE

Sun Xinjun, Wang Zhenqiang, Yong Qilong and Dong Han

Central Iron and Steel Research Institute (CISRI), Beijing, China

Abstract

The carbide precipitation behavior in austenite of a 0.04%C-0.10%Ti-0.21%Mo microalloyed steel was investigated by the stress relaxation test method and transmission electron microscopy. Results showed that the precipitation-time-temperature diagram for carbide precipitation exhibited a typical "C" curve, the nose of which was located at about 925 °C. The carbide was identified as a (Ti,Mo)C particle with a NaCl-type crystal structure that contained a certain amount of Mo. As compared with TiC particles in a Ti steel, (Ti,Mo)C particles in a Ti-Mo steel exhibit a superior coarsening resistance during the coarsening stage. The fraction of Mo in the (Ti,Mo)C particles decreases with longer isothermal holding time or particle growth, indicating that the high level of replacement of Ti by Mo in the TiC lattice is in a "metastable" state with respect to the equilibrium precipitation of (Ti,Mo)C in austenite.

Introduction

In order to reduce fuel consumption, weight and improve product quality in automobiles, advanced high strength low alloy steels have been investigated and developed [1-5]. In recent work performed at JFE Steel Corporation [1], tensile strengths of 780 MPa with excellent stretch flange formability have been obtained in Ti-Mo bearing, low C sheet steels, by producing a microstructure that only consists of ferrite and nanometer-sized carbides. The contribution to the yield strength from precipitation strengthening was estimated to be approximately 300 MPa, which was attributed to nanometer-sized (Ti,Mo)C precipitates that were formed at the austenite-ferrite interfaces during transformation. Subsequently, many researchers, eg. Yen et al. [6,7] and Jang et al. [8], using high resolution transmission electron microscopy (HRTEM) and/or first-principles calculations, systematically studied these nanometer-sized (Ti,Mo) carbides, including their crystal structure, orientation relationship with respect to the ferrite and the role of Mo in relation to coarsening resistance. They found that the (Ti,Mo) carbides possessed a NaCl-type crystal structure with a lattice parameter of ~0.430 nm, and adopted a Baker–Nutting orientation relationship with respect to ferrite. More importantly, these (Ti,Mo)C particles had an excellent thermal stability due to the decrease in the interfacial energy with the ferrite matrix caused by the partial replacement of Ti by Mo in the TiC lattice [8].

Another significant contribution to the yield strength, up to ~280 MPa, in Ti-Mo bearing steels produced by JFE Steel Corporation, came from grain refinement strengthening. The average ferrite grain size of a Ti-Mo microalloyed steel in their work was measured as only 3.1 μm. It is well established that the precipitation of microalloying elements in austenite plays an important role in controlling the final microstructure. In the case of conventional controlled rolling, roughing deformation is succeeded by a fast cooling phase and finishing passes are carried out at temperatures where the austenite remains unrecrystallized. Microalloying elements such as Ti, which remain in solution during roughing deformation, start precipitating following the finish rolling at low temperatures. These fine precipitates, such as TiC, play an effective role in retarding recovery and recrystallization of deformed austenite, thus helping to retain the accumulated strain and deformed structure of the austenite grains. This in turn leads to a high ferrite nucleation rate during subsequent $\gamma\rightarrow\alpha$ phase transformation, thus favoring the refinement of the final microstructure and the improvement of the product properties [9-11]. In our previous reports and some other references [12-14], the carbonitride precipitation behavior after austenite deformation in Ti microalloyed steels was systematically studied using various hot deformation methods, including high temperature flow curves, stress relaxation tests and the two stage interrupted method. The precipitation kinetics curves, ie. precipitation-time-temperature (PTT) diagrams, were determined by different methods and all exhibited a typical "C" shape curve. In addition, the precipitates were identified by TEM as TiC or Ti(C,N) particles with a NaCl-type crystal structure, and they were considered to be nucleated on dislocations and dislocation sub-structures in hot worked austenite. The growth of the precipitates approximately followed a parabolic law during the growth stage, and then entered into a coarsening stage with a time exponent of ~0.1 [12,13]. However, as compared to carbonitride precipitation in Ti microalloyed steel and other complex carbonitride precipitation in Ti-V and Nb-V microalloyed steels [15], carbide precipitation in Ti-Mo microalloyed steels during hot working in austenite has not been extensively investigated, although many studies on carbide precipitation in ferrite or during $\gamma\rightarrow\alpha$ phase transformation of Ti-Mo microalloyed steel have been conducted by many researchers as mentioned above. Therefore, based on the importance of microalloying element precipitation in hot worked austenite, the purpose of this work was to investigate, using systematic stress relaxation experiments, high resolution electron microscopy and thermodynamics calculation, the kinetics of carbide precipitation in austenite and the crystal structure, nucleation, growth, coarsening and compositional evolution of precipitates in a Ti-Mo microalloyed steel. In addition, the coarsening resistance of carbides in a Ti-Mo microalloyed steel is discussed by comparing with that in a Ti microalloyed steel.

Experimental

The chemical compositions of the investigated steels are given in Table I. The Ti-Mo microalloyed steel has a base composition of 0.04%C-0.10%Ti-0.21%Mo wt.%. A Ti microalloyed steel with the composition of 0.05%C-0.10%Ti wt.% was used here as a reference steel to study the role of Mo in terms of the size evolution of precipitates. The two experimental steels were prepared by vacuum melting, and then hot forged to 20 mm diameter rods. After homogenization in the austenite phase field for 300 minutes at 1200 °C, followed by water quenching, the cylindrical specimens, with 8 mm diameter and 12 mm length for hot compression tests, were cut from the center of the as-homogenized rods using electrical discharge machining. In order to study the precipitation kinetics in the Ti-Mo microalloyed steel,

stress relaxation tests [12] were performed using a Gleeble 1500D simulator. The specimens were first preheated at 1150 °C for 3 minutes to dissolve all carbides except a small amount of TiN particles, and then cooled to a deformation temperature in the range of 875 °C to 975 °C, which was chosen to be in the austenitic phase field due to the phase transformation critical temperature (Ae$_3$) being 855 °C as calculated by Thermo-calc with database TCFE6. At this temperature, the specimen was compressively deformed by a 20% reduction along its main axis at a strain rate of 1.0 s^{-1}. The reduction of 20% is very close to the value attained in one industrial rolling pass. Relaxation of the applied compressive stress was then monitored as a function of time up to 50 minutes, before the specimen was cooled by water quenching. In order to study the size evolution of precipitates in Ti-Mo and Ti microalloyed steels, stress relaxation tests with shorter holding times were also conducted. Extraction replica methods [12,13] were used to study the precipitates in the investigated specimens. Each specimen was sectioned perpendicular to the deformation axis, polished, and then etched in 4% nital for about 1 minute. A carbon layer about 20 nm in thickness was deposited on the treated surface using an evaporator. The carbon coated surfaces of the specimens were then scribed using a knife to produce squares about 3×3 mm in size. The replicas were released in the same etching solution, and then analyzed in a field emission gun scanning transmission electron microscope (Tecnai F20). The sizes of the precipitates were measured by a quantitative image analyzer, and the results were obtained by averaging at least two hundred measurements. Chemical analyses of the precipitates were determined using nano-beam energy-dispersive spectroscopy (EDS). At least ten precipitates, formed during stress relaxation, were analyzed for each specimen by TEM/EDS to examine the compositional evolution of precipitates in the Ti-Mo microalloyed steel with isothermal holding time. Each EDS data point was obtained from the whole area of each individual precipitate projection as viewed in TEM mode. In addition, the equilibrium chemical composition of the precipitate, in the Ti-Mo microalloyed steel, over the temperature range 500-1000 °C was calculated by Thermo-calc with the database TCFE6.

Table I. Chemical Compositions of the Investigated Steels

Steel		C	Mn	Si	Ti	Mo	N
Ti-Mo	wt.%	0.04	1.51	0.20	0.10	0.21	0.002
	at.%	0.19	1.54	0.40	0.12	0.12	0.008
Ti	wt.%	0.05	1.47	0.12	0.10	-	0.002
	at.%	0.23	1.50	0.24	0.12	-	0.008

Results and Discussion

<u>Stress Relaxation Curve and Precipitation-time-temperature Diagram of Ti-Mo Microalloyed Steel</u>

The stress relaxation curves of the Ti-Mo microalloyed steel at different temperatures are shown in Figure 1. As stated earlier, all the deformation temperatures were chosen to be in the austenitic phase field. Liu and Jonas [12] suggested that strain induced precipitation in deformed austenite occurs mostly on the dislocations and sub-boundaries developed by deformation, which implies that austenite grain size will not be a dominant factor in influencing the precipitation kinetics. In Figure 1, the stress relaxation curves at 950 ℃ and below exhibit an initial linear stress drop (with respect to log time), which corresponds to a static recrystallization process [15]. After the linear stress drop process, a relaxation stress plateau appears in these curves, indicating the onset of strain induced precipitation, which halts the progress of recrystallization. The relative dominance of these two processes depends on the relative magnitudes of F_R (driving force for recrystallization front migration) and F_{Pin} (retarding force due to pinning of dislocations by precipitated particles). If $F_R < F_{Pin}$, the interfaces will be completely arrested. Initially the driving force for recrystallization is greater owing to a large amount of stored energy in the form of a heavily dislocated matrix. Recrystallization and precipitation are competing processes and progress of recrystallization can be halted by the drag exerted on the migrating grain boundaries by the presence of solute Ti and Mo or by Zener pinning exerted by the strain induced precipitates which preferentially nucleate on dislocations. The precipitates grow faster due to pipe diffusion along dislocations and once the precipitates coarsen sufficiently, recrystallization again takes over resulting in the fall in stress as indicated in the relaxation curves. Liu and Jonas [12] also suggested that the stress vs log (time) relationship under this condition can be described as follows:

$$\sigma = \sigma_0 - \alpha \log(1 + \beta t) + \Delta\sigma \tag{1}$$

where σ is the relaxation stress, σ_0 is the initial stress, t is the holding time after deformation in seconds, α and β are experimental constants and $\Delta\sigma$ is the stress increment due to precipitation. For sufficiently long times, $\beta t \gg 1$, Equation (1) becomes:

$$\sigma = A - \alpha \log t + \Delta\sigma \tag{2}$$

Here, $A = \sigma_0 - \alpha \log \beta$. According to Equation (2), $\Delta\sigma$ equals ~0 during the initial linear stress drop stage. As relaxation proceeds, $\Delta\sigma$ increases gradually and finally reaches the maximum value at a certain time which is marked by arrow (P_f) in Figure 1. The maximum value of $\Delta\sigma$ is also a function of testing temperature and it decreases with increasing temperature as shown in Figure 2. That is because of the decrease of the volume fraction of precipitates and the increase of precipitate size with increasing isothermal temperature [9,10,13]. The stress relaxation curve at 975 ℃ does not show a relaxation plateau just after a linear-drop stage. Instead, a fast drop in stress value appears after a linear-drop stage, which indicates the occurrence of static recrystallization, as marked by SRX in Figure 1. It is known that the recrystallization progress results in a rapid drop in the density of structural defects such as dislocations in the deformed

austenite matrix. Since these defects are the nucleation sites for strain induced precipitates [16], their rapid disappearance at the high temperature of 975 ºC is expected to hinder the precipitation process. The stress plateau after the fast-drop stage could result from static recovery of austenite.
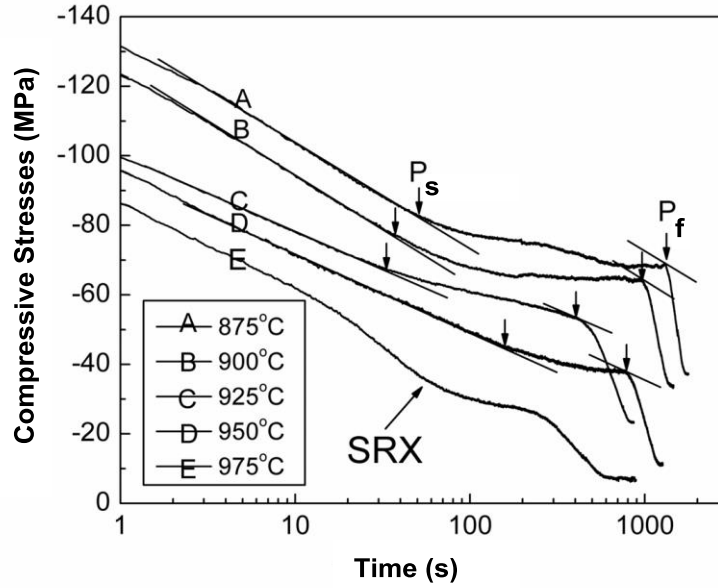

Figure 1. Stress relaxation curves of the Ti-Mo microalloyed steel at different temperatures. SRX denotes fast static recrystallization. P_s and P_f represent the start and finish times of the plateau, respectively.
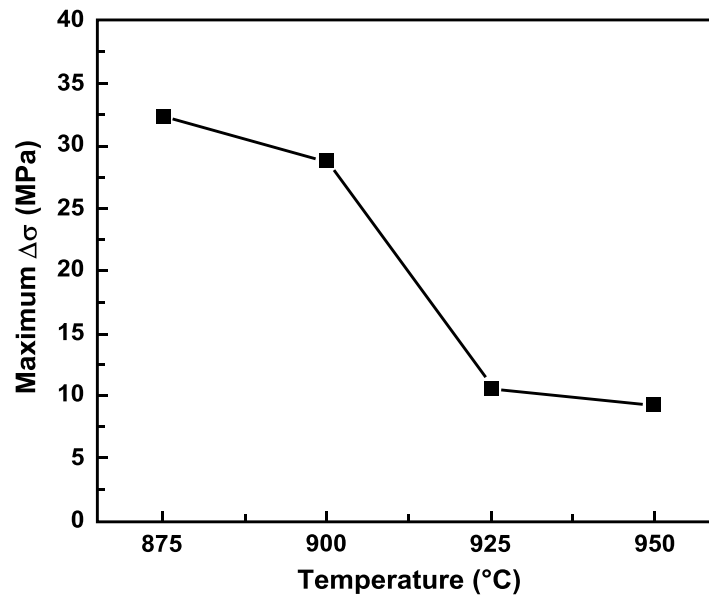
Figure 2. Maximum $\Delta\sigma$ as a function of testing temperature.

According to previous workers [12], the start and finish times of the plateau on the stress relaxation curves, which are marked by arrows in Figure 1, are defined as the onset (P_s) and end (P_f) times respectively of the precipitation process induced by strain. The P_s point indicates the onset of the precipitation, and the P_f point represents the time at which the precipitation hardening reaches the maximum, ie. $\Delta\sigma$ reaches its maximum value. It should be noted that the P_f point does not denote the volume fraction of precipitates reaching an equilibrium value, but possibly represents the transition of the mechanism of particle growth [16]. The precipitation-time-temperature (PTT) diagram for carbide precipitation in the Ti-Mo microalloyed steel was successfully obtained as shown in Figure 3. The PTT diagram exhibits a typical "C" shape; its nose, which corresponds to the minimum incubation time for precipitation, is located at about 925 ℃. This temperature is very close to that of TiC precipitation reported in our previous work on a Ti microalloyed steel with a similar chemical composition, but without a Mo addition [13]. In addition, the start time shown in the PTT diagram is within 50 seconds in the temperature range of 875-925 ℃, but exceeds 150 seconds at 950 ℃.
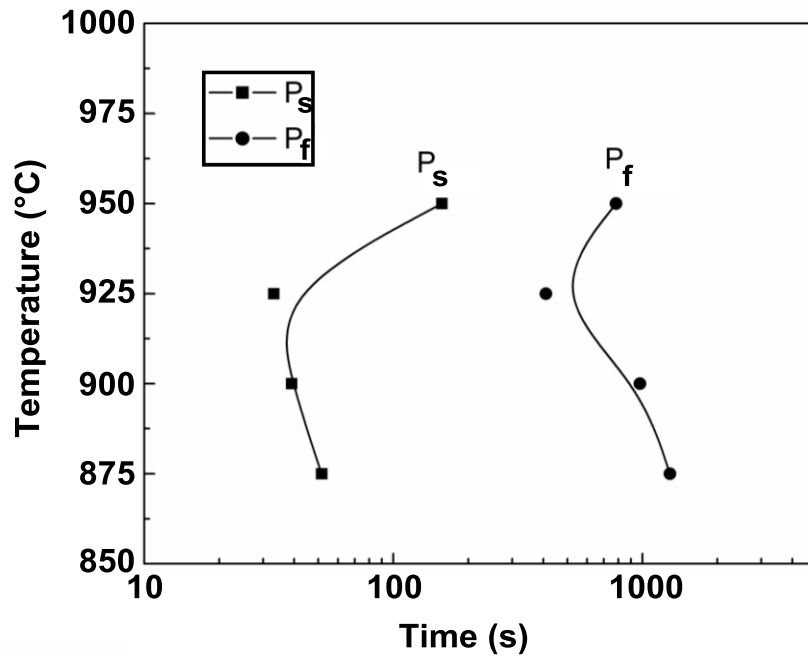

Figure 3. The PTT diagram of the studied Ti-Mo microalloyed steel, where P_s and P_f are the start and finish times of carbide precipitation, respectively.

Characterization of Precipitates in Ti-Mo Microalloyed Steel - Undissolved Precipitates

In the present work, a certain number of undissolved cube-shaped TiN particles, which could be formed during steelmaking and/or casting [17], were occasionally observed by TEM in the Ti-Mo microalloyed steel. As shown in Figure 4, these particles have a typical size of ~1 μm, so that they had little effect on the recovery and recrystallization of deformed austenite during stress relaxation [9,18]. Their number density was very small on the carbon replica film, which is due to the limited N content, 0.002 wt.%, in the studied alloy.
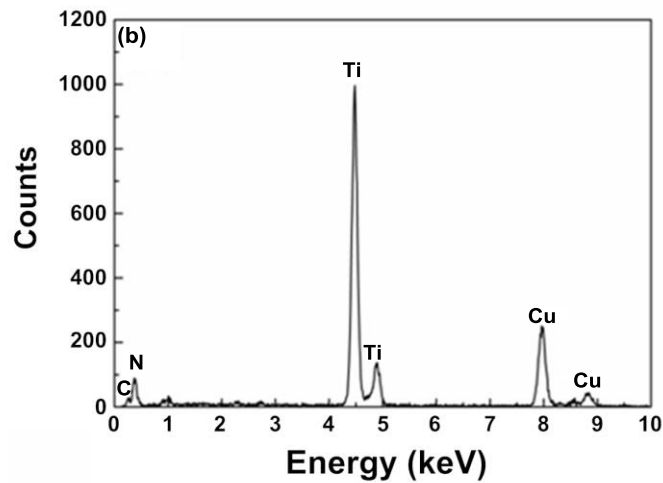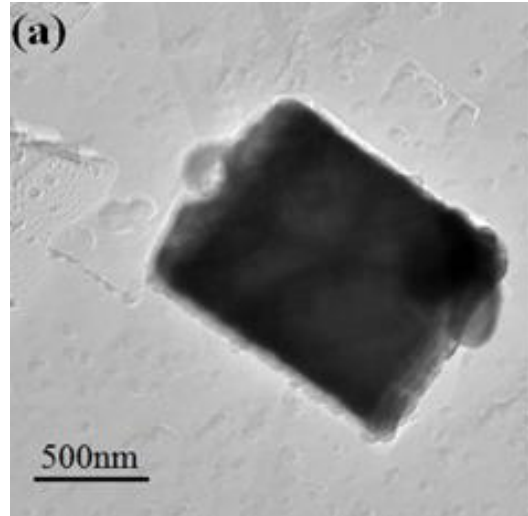
Figure 4. (a) TEM image showing an undissolved TiN particle in Ti-Mo microalloyed steel and (b) the corresponding EDS analysis of this TiN particle. It should be noted that the peaks of Cu on the EDS spectrum are from the Cu grid used to support the carbon replica film.

Precipitates Formed During Stress Relaxation in Ti-Mo Microalloyed Steel

Figure 5(a) is a TEM image showing a carbide particle formed in the specimen deformed at 925 ℃ followed by a hold for 1800 seconds, and it was identified as a Ti-rich MC carbide type with the NaCl-type crystal structure, containing a certain amount of Mo, by selected area electron diffraction (SAD) and EDS analysis as shown in Figures 5(b) and (c). The atomic ratio of Ti/Mo, quantified by EDS, in the carbide is about 8.0, which is larger than that of the (Ti,Mo)C particles in ferrite reported by Jang et al. [8] and Funakawa et al [1].
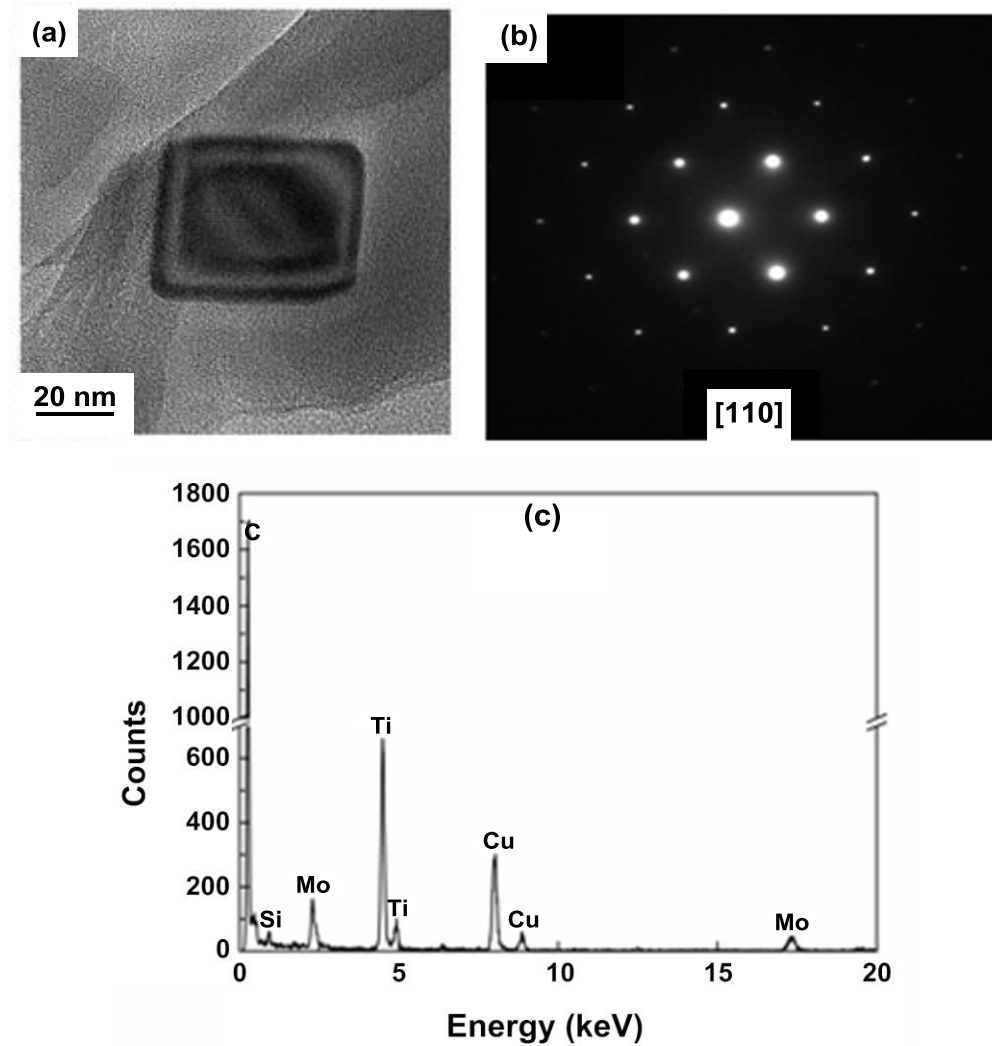
Figure 5. (a) TEM image showing a (Ti,Mo)C precipitate, (b) selected area electron diffraction (SAD) and (c) energy dispersive spectroscopy (EDS). It should be noted that the peaks of Cu and Si on the EDS spectrum are from the Cu grid used to support the carbon replica film and an inclusion on the carbon replica film, respectively.

The nucleation sites of the precipitates formed in the Ti-Mo microalloyed steel during stress relaxation can be confirmed indirectly by analyzing the distribution of particles on the carbon replica film. A high-angle annular dark-field scanning transmission electron microscopy (HAADF-STEM) image, shown in Figure 6, clearly exhibited a cell-like distribution of precipitates on the carbon replica, implying that the precipitates nucleated on dislocations or on dislocation sub-structures [13]. The sizes of these "sub-grains", which were produced during deformation and a subsequent recovery process, were measured to be in the range of 0.2-1.0 μm, which is much smaller than the prior austenite grain size of ~100 μm.
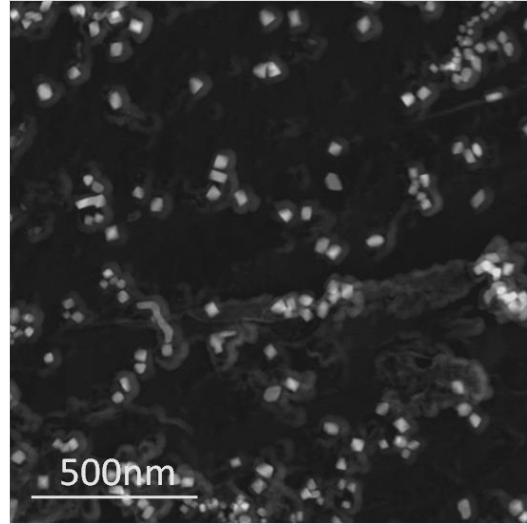
Figure 6. HAADF-STEM image showing the cell-like distribution of (Ti,Mo) carbides on carbon replica film, formed in the specimen deformed at 900 ℃ and held for 1800 seconds.

In addition, the shape of most of the precipitates, as seen in Figure 6, is polyhedral rather than a cube which had been identified from the TEM image in Figure 5. A precipitate which looked like a cube observed from a TEM image was selected as an example to clarify the difference. Figure 7 shows the TEM image (Figure 7(a)), STEM image of the precipitate (Figure 7(b)) and the corresponding selected area electron diffraction pattern (SAD) with a magnetic rotation angle of 90˚ relative to the TEM and STEM images (Figure 7(c)). It can be seen that the precipitate seems to have an almost perfect cube-like shape as shown in Figure 7(a). However, the strong three-dimensional contrast in Figure 7(b) together with the annular equal thickness fringes in Figure 7(a) indicate that the precipitate has a pyramid-like shape or an octahedral shape if the precipitate has a symmetry with respect to the observation plane, rather than a cube-like shape. Moreover, the two diagonals of this pyramid-like or octahedron-shaped precipitate were determined to be parallel with plane {200} of the precipitate, indicating that the majority of the facets were not on plane {200}. But the facet of the cube-like TiN particle precipitated in austenite is just in the plane {200} [19]. The equilibrium shape of M(C,N) particles with B1 structure, where M=Ti, Nb, V, Mo or their combination, depends on the interplay between interfacial and elastic strain energy minimization during precipitation in austenite [20]. According to Yang and Enomoto [19], the interfacial energy includes structure energy arising out of the lattice misfit between M(C,N) and the austenite matrix, and chemical energy from the difference in chemical composition at the M(C,N)/austenite interface. The elastic strain energy comes from the difference in elastic properties between M(C,N) and austenite. Yang and Enomoto [19] stated that the cube shape of TiN particles that adopt a cube-on-cube orientation relationship with respect to the austenite matrix, was mainly attributed to the anisotropy of the chemical interfacial energy, because the anisotropy of the structural interfacial energy of TiN/austenite interfaces (~15%) and the elastic strain energy are not large at higher temperatures. However, for other B1-carbides (and nitrides), ie. NbC, having a larger misfit with austenite (~22%) and considerable elastic strain energy due to its lower precipitation temperature, the cube-on-cube orientation relationship with respect to the austenite matrix may not always be maintained. Thus, the precipitate morphology is expected to become more irregular (see reference [21,22]). In the present study, the misfit between carbide and austenite was determined

as ~18% (lattice parameter equals ~0.43 nm) by SAD and assuming that the austenite lattice parameter is 0.365 nm [9]. This value lies in between that of TiN and NbC. Moreover, the precipitation temperature of the carbide in the present work is close to that of NbC reported in references [21,22], so that the elastic strain energy cannot be ignored under this condition. Therefore, the carbide in the present study is expected to exhibit a shape that lies in between that of TiN and NbC. Of course, accurately predicting the morphology of this carbide needs more work, including calculating interfacial energy, elastic strain energy and their particle size dependences, etc. However, this is beyond the scope of the present work.
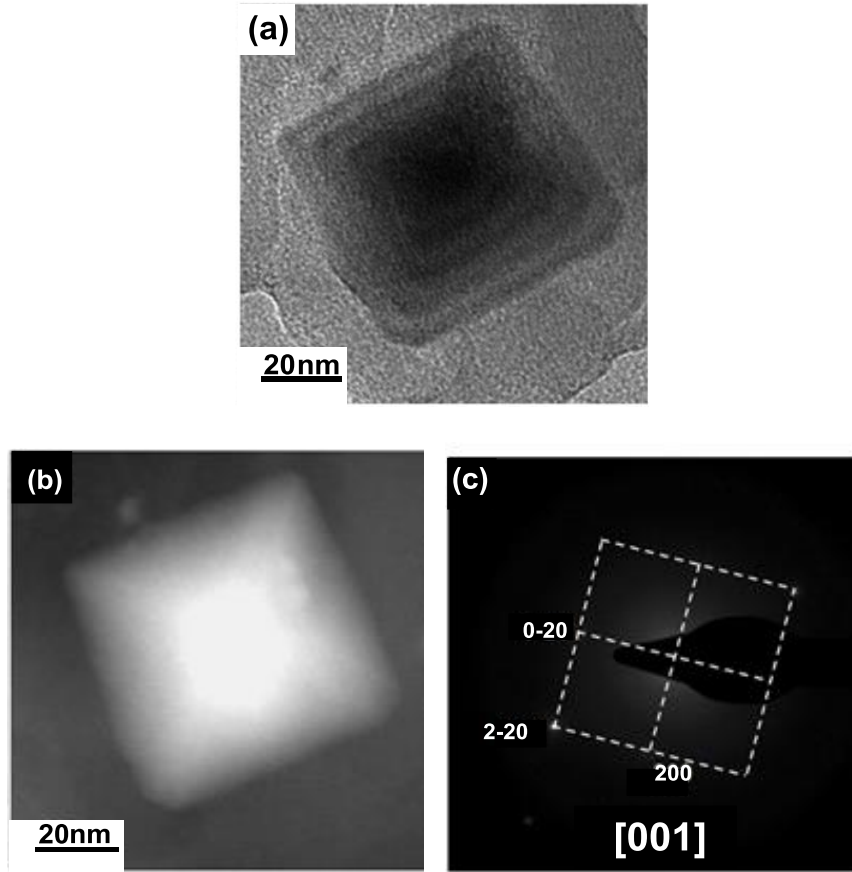

Figure 7. A carbide particle formed in the specimen deformed at 925 ℃ and held for 1800 seconds; (a) TEM image, (b) HAADF-STEM image and (c) the corresponding selected area electron diffraction (SAD). It should be noted that the shape of this precipitate is a rectangular pyramid or an octahedron as observed in (b) rather than a cube as seen in (a). In addition, the two diagonals of this pyramid or octahedral-shaped precipitate are on plane {200}, which is identified by SAD in (c).

A high-resolution transmission electron microscopy (HRTEM) investigation of the carbides formed in the Ti-Mo microalloyed steel was performed in this study, and an example of the lattice image of a carbide is presented in Figure 8(a). It was identified as a (Ti,Mo)C particle with a NaCl-type crystal structure using a two-dimensional fast Fourier transformation (FFT) analysis, which is consistent with the SAD result (see Figure 5). The lattice image obtained by an inverse fast Fourier transformation (IFFT) as shown in Figure 8(b) has been identified to have a lattice parameter of 0.43 nm, which is very close to that (0.423-0.430 nm) of the inter-phase precipitated (Ti,Mo)C particles reported by Yen et al. [7] and Funakawa et al. [1].
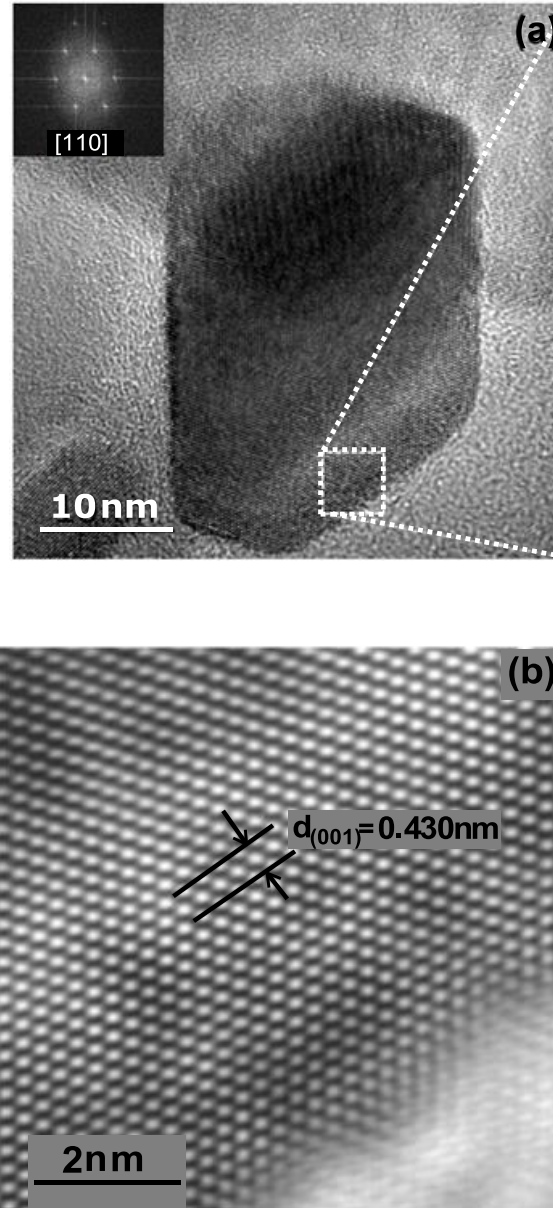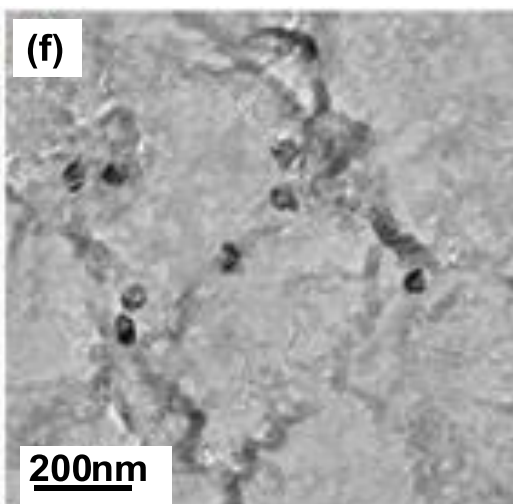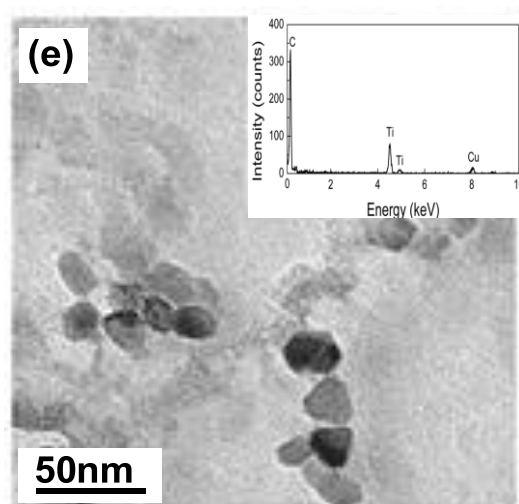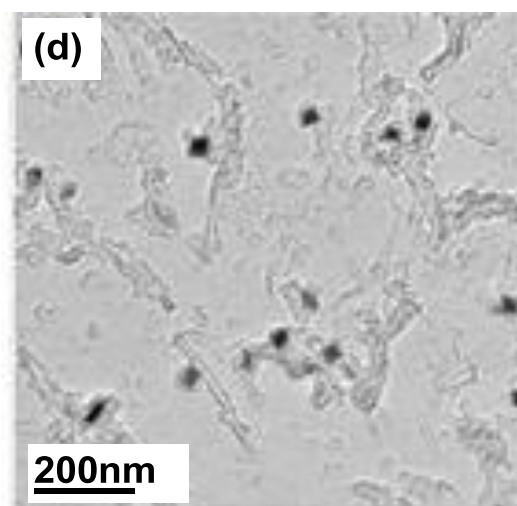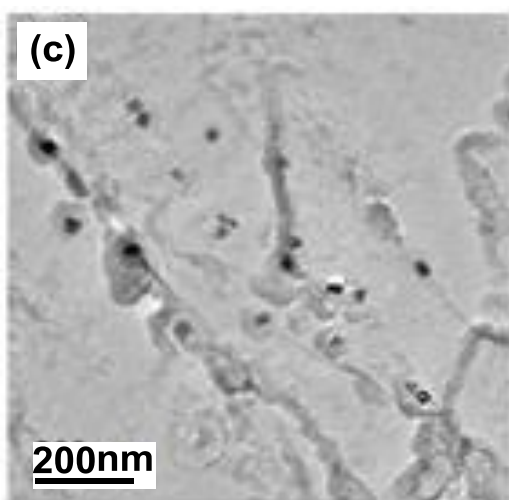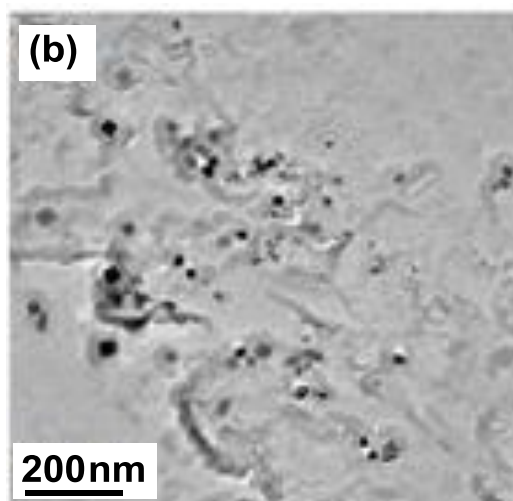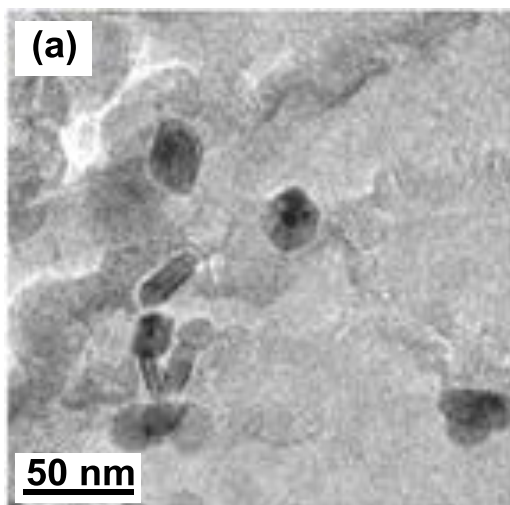

Figure 8. (a) HRTEM image showing a carbide particle in the specimen deformed at 925 ºC and held for 3000 seconds and (b) IFFT lattice image of the area marked by a white-line frame on the carbide particle in (a).

Growth and Coarsening of Precipitates

In the present work, the particle size evolution of (Ti,Mo)C particles in the Ti-Mo microalloyed steel and TiC in the reference Ti steel, as a function of isothermal holding time, were investigated, and the results at the testing temperature of 925 ºC are presented in Figure 9. It can be clearly seen that the carbide sizes in both steels were very close to each other for a 200 seconds holding time (see Figures 9(a) and (e)). However, with an increase of holding time to 600 seconds, to 1800 seconds and to 3000 seconds, (Ti,Mo)C particles in the Ti-Mo steel exhibited a smaller size and higher density than TiC in the Ti steel (see Figure 9(b), (c), (d), (f), (g) and (h)). In order to better understand the growth and coarsening behavior of carbides in the two steels, the average particle sizes for various holding times at 925 ºC were measured and plotted in Figure 10. During the initial stage of precipitation, the carbides in both steels grow very quickly, and show almost the same growth rate. The growth of carbides at this stage approximately followed a parabolic law, ie. $d = \alpha\sqrt{Dt}$, where d is the size of the particle, α is the growth coefficient and D is the diffusion coefficient of the element which controls the growth rate. With an increase of holding time, the growth rate of the carbides slowed down in both steels, especially for the (Ti,Mo)C particles in the Ti-Mo steel, the average particle size being almost unchanged from 200 seconds to 1800 seconds. During this stage, precipitate development lies in the coarsening stage, ie. Ostwald ripening. The transition time from growth to coarsening was ~200 seconds for (Ti,Mo)C particles and ~600 seconds for TiC. It should be noted that the transition time from growth to coarsening for (Ti,Mo)C particles is roughly comparable with the P_f time (~400 seconds) given in the stress relaxation curve (see Figure 1). More importantly, (Ti,Mo)C particles in the Ti-Mo steel exhibit a superior coarsening resistance compared to TiC particles in the Ti steel during this stage, as shown in Figure 10. This phenomenon has often been observed [1,5,6-8] for (Ti,Mo)C particles precipitated in ferrite or during the γ→α phase transformation.
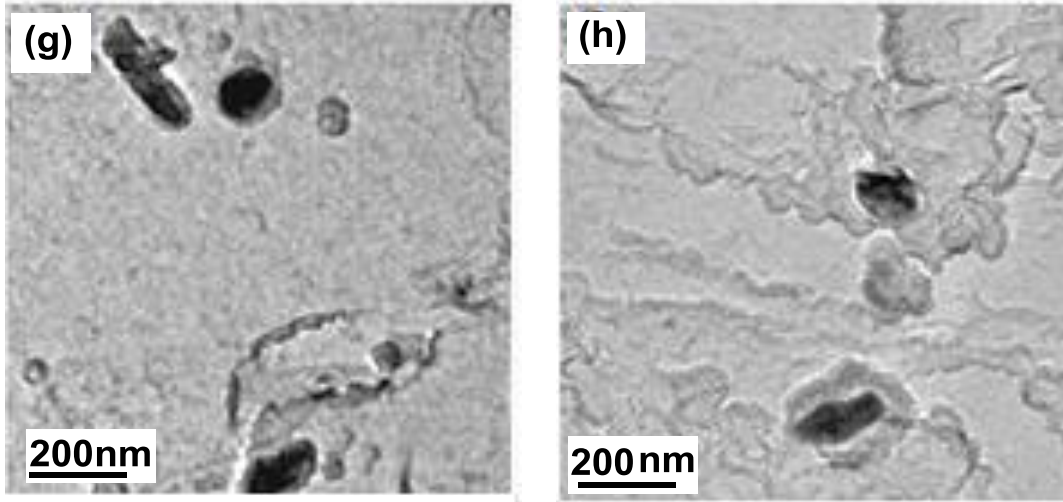
Figure 9. (a)-(d) TEM images showing carbide particles formed at 925 ℃ for various holding times in Ti-Mo microalloyed steel; (a) 200 seconds, (b) 600 seconds, (c) 1800 seconds and (d) 3000 seconds. (e)-(h) TEM images showing carbide particles formed at 925 ℃ for various holding times in Ti microalloyed steel; (e) 200 seconds, (f) 600 seconds, (g) 1800 seconds and (h) 3000 seconds.
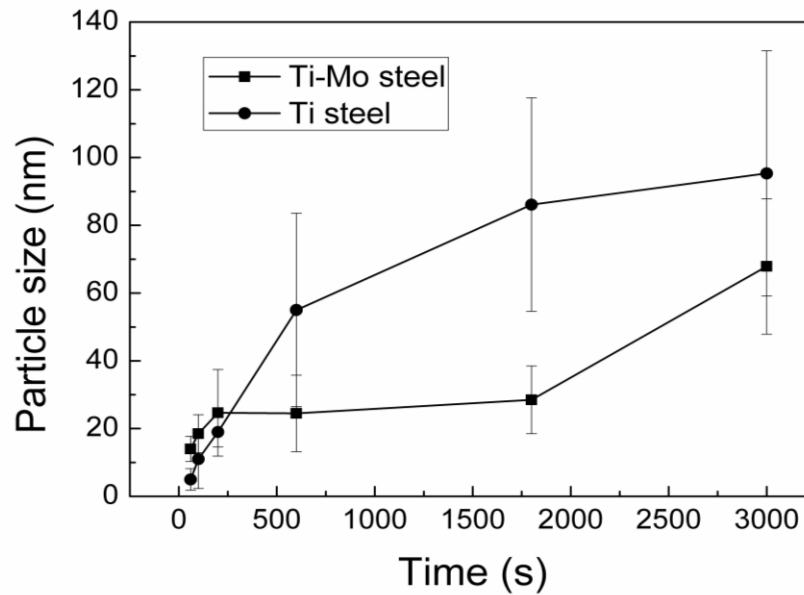
Figure 10. Average particle sizes of carbides at 925 °C as a function of isothermal holding time.

The relationship between average particle size and holding time during the initial stage of precipitation, before 200 seconds, for the Ti-Mo steel and before 600 seconds for the Ti steel, is roughly determined as $d = kt^{\frac{1}{2}}$, where d is the average size of the particle, k is a constant and t is the isothermal holding time.

According to Ostwald's ripening theory:

$$d_t^n - d_0^n = \frac{k}{RT}V_m^2 CD\gamma t \tag{3}$$

where d_t is average particle size at a given time, d_0 is the initial average particle size, n is 3 for volume diffusion controlled coarsening, k is a constant, V_m is the molar volume of the precipitate, C is the concentration of solute in the matrix that is in equilibrium with the precipitate, D is the diffusivity of the solute, γ is the interfacial energy per unit area between the precipitate and the matrix, R is the gas constant and T is the absolute temperature. The coarsening rate of a carbide at a given temperature T is mainly dependent on the interfacial energy γ, the diffusivity D and the concentration C of the rate controlling element in austenite [8,9].

Since interstitial atoms diffuse much faster than substitutional atoms in austenite, the coarsening process is considered to be controlled by the diffusion of substitutional elements Ti or Mo. According to Yong's theory [9], the coarsening process of ternary (Ti,Mo)C particles depends on the product of D and C of substitutional solute atoms in austenite. The element that has a smaller product of D and C is considered as the controlling element. As discussed in a previous section, (Ti,Mo)C particles are rich in Ti rather than Mo, so that the concentration of Ti in solution is much lower than that of Mo during the coarsening stage. In addition, the diffusivity of Ti in austenite is a little larger (~1.1-1.2 times) than that of Mo over the investigated temperature range [9]. Therefore, on balance, the controlling element in the coarsening process of (Ti,Mo) carbides in the Ti-Mo steel is determined as Ti, which is also the controlling element for the TiC coarsening process in the Ti steel. In another work that will be published [23], the effect of Mo on the kinetics of carbide precipitation in Ti microalloyed steel was investigated by hot rolling experiments. Figure 11 is the physical-chemical phase analysis result showing the precipitated amount of Ti in carbide (TiC or (Ti,Mo)C) for 600 seconds and 1800 seconds isothermal holding at ~925 ℃ in Ti and Ti-Mo steels. The results show that the addition of Mo into a Ti steel can increase the amount of Ti precipitated as carbide from the austenite. Therefore, the remaining Ti solute in austenite for the Ti-Mo steel is lower than for the Ti steel during the coarsening process. Consequently, the decreased Ti concentration caused by the Mo addition is considered to result in the decrease of the coarsening rate of (Ti,Mo)C particles according to Equation (3). On the other hand, the lattice parameters of carbides were identified by TEM/SAD as ~0.430 nm for both (Ti,Mo)C and TiC. Therefore, the lattice misfit between carbide and austenite matrix is almost the same for the two steels, indicating that the structural interfacial energy of (Ti,Mo)C particles approximately equals that of TiC particles if the cube-on-cube orientation relationship is maintained between the carbide and austenite [9]. However, the partial replacement of Ti by Mo in the TiC crystal lattice results in a decrease of the contributions of chemical binding to the interfacial energy of carbide/austenite according to our calculation result [23] and Yang's DLP/NNBB theory [24,25]. Thus, the chemical interfacial energy is possibly reduced by the partial replacement of Ti by Mo in the TiC lattice, although the exact chemical interfacial energy depends on the spread over which the interface is defined. As a result, the total interfacial energy of a (Ti,Mo)C particle with austenite is possibly reduced as compared with that of TiC, and this in turn decreases the coarsening rate of (Ti,Mo) carbides according to Equation (3).
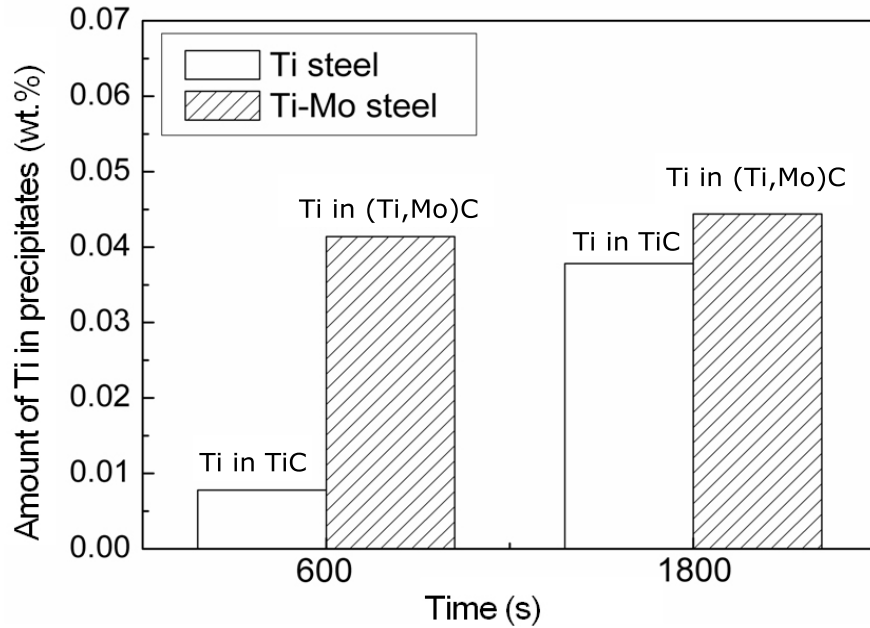
Figure 11. Physical-chemical phase analysis showing the precipitated amount of Ti in carbide (TiC or (Ti,Mo)C) for 600 seconds and 1800 seconds isothermal holding time after one pass rolling with a reduction of 20% at ~925 ℃ in Ti and Ti-Mo microalloyed steels. It should be noted that the total Ti content is 0.1 wt.% for both steels [23].

Thermodynamic and Kinetic Analysis for (Ti,Mo)C Phase

In this paper, the compositional evolution of (Ti,Mo)C particles in a Ti-Mo steel was studied at the testing temperature of 925 ℃. As shown in Figure 12, the atomic ratio of Ti/Mo in (Ti,Mo)C particles increased with isothermal holding time or particle growth. This phenomenon seems to indicate that, on the one hand, the incorporation of Mo into TiC favors the nucleation and growth during the early stages of precipitation, but on the other hand, the high level of Ti replacement by Mo in the TiC lattice is "metastable" with respect to equilibrium precipitation of (Ti,Mo)C phase. Figure 13 shows the variations of the equilibrium atomic fractions of Ti, Mo and C in MC phase, with temperature, calculated by Thermo-calc, (Figure 13(a) – Ti, Figure 13(b) – Mo, Figure 13(c) – C). FCC and BCC phases were selected for the Thermo-calc calculations. This meant that the MC phase was in equilibrium with austenite at higher temperatures and with ferrite at lower temperatures. In addition, the calculated MC phase contained a small amount of Fe and Mn, thus leading to the sum of atom factions of Ti and Mo not being 0.5 as shown in Figures 13(a) and (b), especially at lower temperatures. In Figure 13, the equilibrium chemical composition of the MC phase with FCC structure approaches pure TiC at temperatures above 800 ℃. As the temperature decreases, the equilibrium atomic fraction of Mo in the MC phase increases. When the temperature decreases to below 700 ℃, the rate of increase of the atomic fraction of Mo with temperature becomes larger. The atomic ratio of Mo/Ti is about 1.0 in the temperature range of 500-600 ℃. The measured atomic fractions of Mo by EDS in MC phase at different temperatures for 1800 seconds isothermal holding time are also shown (black circles) in Figure 13(b). Here, it is assumed that no vacancies are present at C atom positions in the MC lattice, namely a perfect NaCl-type MC phase. In this case, the atomic fraction of Mo in MC reaches the minimum

66

because the partial replacement of Ti by Mo in the TiC lattice possibly produces a certain amount of vacancies at C atom positions according to reference [8]. In addition, the experimental result (shown as black diamond) from Funakawa et al [1], for a Ti-Mo microalloyed steel with a similar chemical composition to that of the present steel was given in Figure 13(b) for comparison, (specimen held at 620 °C for 3600 seconds after finish rolling and furnace cooled to room temperature) As the temperature decreases, the measured atomic fraction of Mo in MC phase increases. However, the values are much higher than those calculated by Thermo-calc, and the difference becomes larger with decreasing temperature, for example, ~3% at 950 °C, but up to ~8% at 875 °C. The steel from Funakawa et al, showed a difference of ~11%. As discussed above, the site fraction of Mo in the (Ti,Mo)C lattice decreases with isothermal holding time or with particle growth. Such a finding, together with the comparison between the experimental results and theoretical calculations, indicates that the greater replacement of Ti by Mo in the TiC lattice is energetically unfavorable with respect to the equilibrium precipitation, when the other energy conditions, including interfacial energy and elastic strain energy, between precipitate and matrix are not considered.
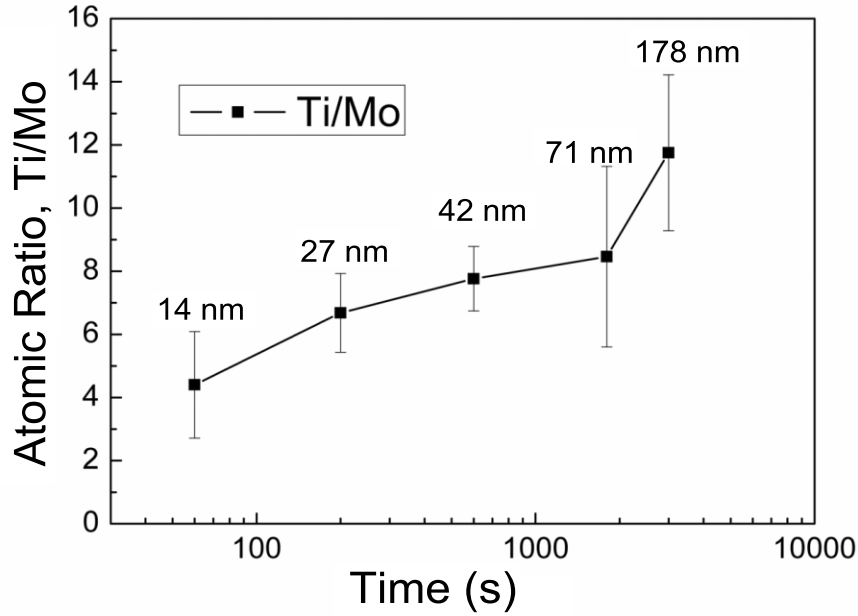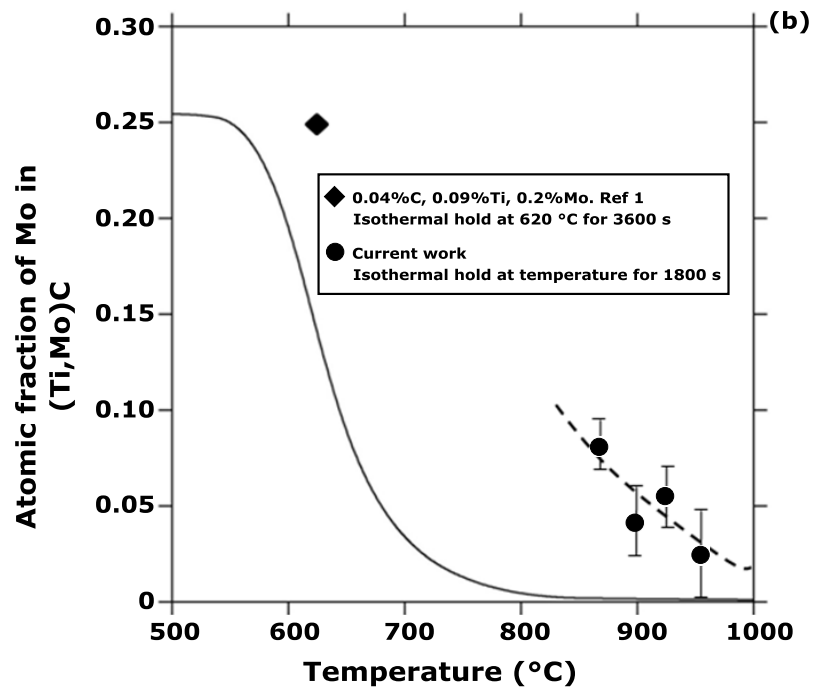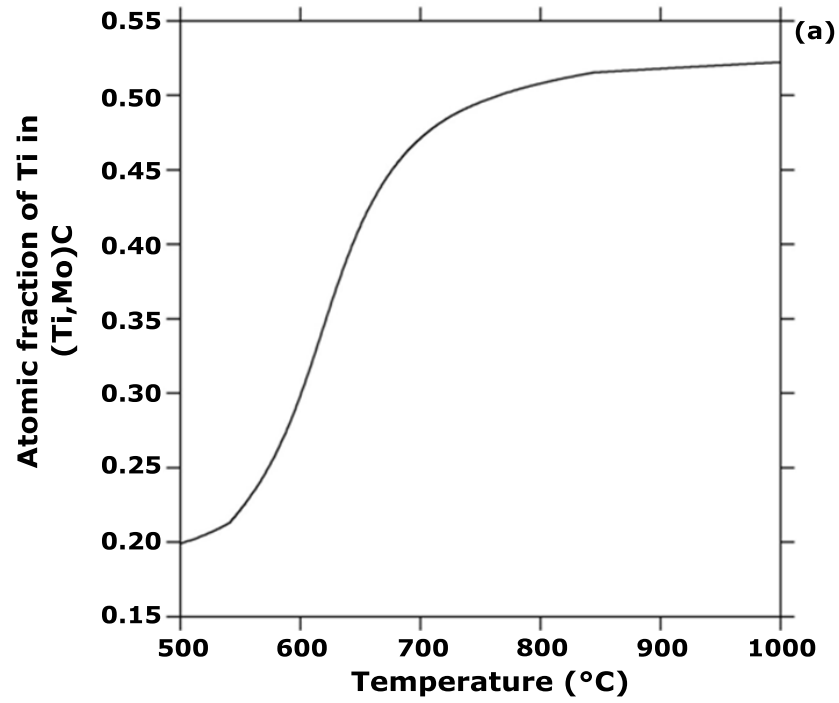

Figure 12. Atomic ratio of Ti/Mo in carbide as a function of isothermal holding time at 925 °C. The figures above the Ti/Mo-*log*(time) curve represent the average particle sizes of the measured precipitates.

(a)

(b)

0.04%C, 0.09%Ti, 0.2%Mo. Ref 1
Isothermal hold at 620 °C for 3600 s

Current work
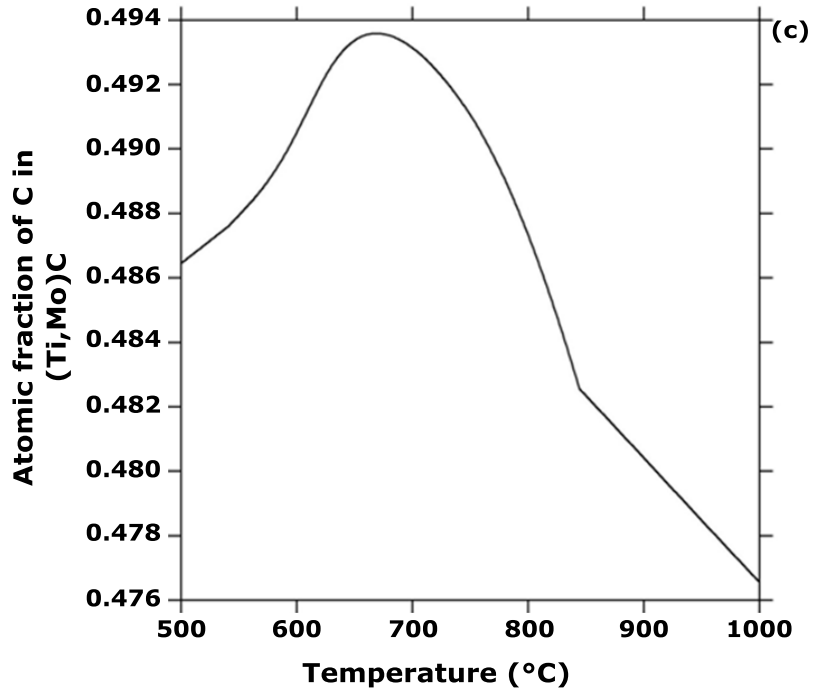Isothermal hold at temperature for 1800 s

68

Figure 13. Variations of equilibrium atomic fractions of; (a) Ti, (b) Mo and (c) C in MC carbide particle with temperature as calculated using Thermo-calc with database TCFE6.
(The datapoints shown as black circles in Figure 13(b) are from the current work for an isothermal hold of 1800 s).

As discussed in a previous section, the partial replacement of Ti by Mo in the TiC lattice possibly decreases the chemical interfacial energy between (Ti,Mo)C and austenite [23]. Therefore, this effect, in fact, favors the decrease of the nucleation energy barrier, thus enhancing the nucleation of (Ti,Mo)C phase during the early stages of precipitation. Accordingly, smaller (Ti,Mo)C particles contain more Mo as shown in Figure 12. However, with particle growth, the surface area to volume ratio of the particle becomes less significant, ie. the interface effect becomes not so significant. Thereupon, the incorporation of Ti into (Ti,Mo)C phase becomes more beneficial to the decrease of the total free energy of the system, thus resulting in the decrease of the fraction of Mo in the (Ti,Mo)C phase, as shown in Figure 12. However, the incorporation rate of Ti atoms into (Ti,Mo)C phase depends on the diffusivity of Ti in austenite, which is a function of isothermal temperature. The diffusion rate of Ti atoms is slower at lower temperatures, thus leading to the larger difference, in terms of the fraction of Mo in (Ti,Mo)C phase, between the experimental measurements and the equilibrium results calculated by Thermo-calc at lower temperatures.

Conclusions

The precipitation-time-temperature diagram for the kinetics of carbide precipitation in Ti-Mo microalloyed steel determined by a stress relaxation method exhibited a typical "C" shape curve, and its nose was located at ~925 ℃. The precipitates formed during stress relaxation in the Ti-Mo microalloyed steel were identified as polyhedral Ti-rich (Ti,Mo) carbides possessing a NaCl-type crystal structure that contains a certain amount of Mo. The (Ti,Mo)C precipitates were heterogeneously distributed in a cell-like manner, implying that the precipitates nucleated on dislocations or on dislocation sub-structures, which were produced by deformation. The growth of carbide particles in the Ti-Mo microalloyed steel approximately followed a parabolic law during the growth stage. During the coarsening stage, (Ti,Mo)C particles in the Ti-Mo microalloyed steel exhibited a higher coarsening resistance as compared with TiC particles in the Ti microalloyed steel, which is attributed, on the one hand, to the decrease of Ti concentration in austenite by the accelerating effect of Mo on Ti precipitation as carbide and, on the other hand, possibly to the decrease in the chemical interfacial energy of carbide/austenite by the incorporation of Mo into the TiC lattice.

References

1. Y. Funakawa et al., "Development of High Strength Hot Rolled Sheet Consisting of Ferrite and Nanometer-sized Carbides," *The Iron and Steel Institute of Japan International*, 44 (2004), 1945-1951.

2. T. Shimizu, Y. Funakawa and S. Kaneko, "High Strength Steel Sheets for Automobile Suspension and Chassis Use – High Strength Hot Rolled Steel Sheets with Excellent Press Formability and Durability for Critical Safety Parts," *JFE Technical Report*, 4 (2004), 25-31.

3. K. Yamada, K. Sato and H. Nakamichi, "Analysis of Nanometer-sized Precipitates using Advanced TEM," *JFE Technical Report*, 9 (2007), 5-11.

4. M. Nagoshi, T. Kawano and K. Sato, "Quantitative Chemical State Analysis of Ti and Mo in a High Strength Steel Using X Ray Absorption Fine Structure (XAFS)," *JFE Technical Report*, 9 (2007), 12-15.

5. Y. Funakawa and K. Seto, "Coarsening Behavior of Nanometer-sized Carbides in Hot Rolled High Strength Sheet Steel," *Materials Science Forum,* 539 (2007) 4813-4818.

6. C.Y. Chen et al., "Precipitation Hardening of High Strength Low Alloy Steels by Nanometer-sized Carbides," *Materials Science and Engineering A,* 499 (2009) 162-166.

7. H.W. Yen, C.Y. Huang and J.R. Yang, "Characterisation of Interphase Precipitated Nanometer-sized Carbides in a Ti-Mo Bearing Sheet," *Scripta Materialia,* 61 (2009), 616-619.

8. J.H. Jang et al., "Stability of (Ti,M)C (M=Nb,V,Mo and W) Carbide in Steels using First Principles Calculations," *Acta Materialia,* 60 (2012), 208-217.

9. Q.L. Yong, Secondary Phases in Steels. Metall Industry Press, Beijing (2006).

10. H.S. Zurob et al., "Modelling Recrystallisation of Microalloyed Austenite: Effect of Coupling Recovery, Recrystallisation and Precipitation," *Acta Materialia,* 50 (2002), 3075-3092.

11. B. Dutta, E.J. Palmiere and C.M. Sellars, "Modelling the Kinetics of Strain Induced Precipitation in Nb Microalloyed Steels," *Acta Materialia,* 49 (2001), 785-794.

12. W.J. Liu and J.J. Jonas, "A Strain Relaxation Method for Following Carbonitride Precipitation in Austenite at Hot Working Temperatures," *Metallurgical Trans*actions, 19A (1988), 1403-1413.

13. Z.Q. Wang et al., "Strain Induced Precipitation in a Ti Microalloyed HSLA Steel," *Materials Science and Engineering A,* 529 (2011), 459-467.

14. M.G. Akben et al., "Dynamic Precipitation and Solute Hardening in a Titanium Microalloyed Steel Containing Three Levels of Manganese," *Acta Metallurgica,* 32 (1984), 591-601.

15. A. Pandit et al., "Strain Induced Precipitation of Complex Carbonitrides in Nb-V and Ti-V Microalloyed Steels," *Scripta Materialia,* 53 (2005), 1309-1314.

16. W.J. Liu and J.J. Jonas, "Ti(CN) Precipitation in Microalloyed Austenite During Stress Relaxation," *Metallurgical Transactions,* 19A (1988), 1415-1424.

17. X.P Mao et al., *Acta Metallurgica Sinica*, 42 (2006), 1091-1095. (In Chinese)

18. J. Moon and C.H. Lee, "Pinning Efficiency of Austenite Grain Boundary by a Cubic Shaped TiN Particle in Hot Rolled HSLA Steel," *Materials Characterization,* 73 (2012), 31-36.

19. M. Enomoto and Z.G. Yang, "Calculation of the Equilibrium Shape of TiN Particles in Iron," *The Iron and Steel Institute of Japan International*, 44 (2004), 1454-1456.

20. R. Shi, N. Ma and Y. Wang, "Predicting Equilibrium Shape of Precipitates as Function of Coherency State," *Acta Materialia*, 60 (2012), 4172-4184.

21. S.G. Hong, K.B. Kang and C.G. Park, "Strain Induced Precipitation of NbC in Nb and Nb-Ti Microalloyed HSLA Steel," *Scripta Materialia,* 46 (2002), 163-168.

22. J.S. Park, Y.S. Ha and Y.K. Lee, "Comparison of Experimental Methods to Measure the Isothermal Precipitation Kinetics of Nb(C,N) in Austenite of a Nb Microalloyed Steel," *Metallurgical and Materials Transactions,* 40 A (2009), 1515-1519.

23. Z.Q. Wang et al., "Effect of Mo Addition on the Kinetics of Carbide Precipitation in Ti Microalloyed Steel. (unpublished work)

24. Z.G. Yang and M. Enomoto, "A Discrete Lattice Plane Analysis of Coherent FCC/B1 Interfacial Energy," *Acta Materialia,* 47 (1999), 4515-4524.

25. Z.G. Yang and M. Enomoto, "Calculation of the Interfacial Energy of B1-type Carbides and Nitrides with Austenite," *Metallurgical and Materials Transactions,* 32 A (2001), 267-274.

EFFECT OF MOLYBDENUM ON PRECIPITATION BEHAVIOR IN TITANIUM MICROALLOYED HSLA STEELS
PART II - PRECIPITATION DURING γ→α PHASE TRANSFORMATION

Wang Zhenqiang

Central Iron and Steel Research Institute (CISRI), Beijing, China

Keywords: Phase Transformation, Microhardness, Interphase Precipitation, Titanium, Molybdenum

Abstract

The effects of Mo on the isothermal γ→α phase transformation and precipitation behavior were investigated. Addition of 0.2 wt.%Mo to a Ti microalloyed steel results in a fully ferritic microstructure at higher isothermal transformation temperatures. The microhardness of the microstructure, isothermally transformed at all temperatures, in a Ti-Mo steel was higher than that in a Ti steel. This is attributed to the superior coarsening resistance of MC carbide in the Ti-Mo steel as compared with that in a Ti steel.

Introduction

Currently, an increasing number of Ti microalloyed steels are being or have been developed by many researchers, and the microstructures mainly consist of ferrite and a little pearlite. The strengthening mechanisms for these steels include grain refinement and precipitation hardening. The γ→α phase transformation process was fully used to obtain a refined ferrite grain size and a dispersion of nano-sized carbides. This microstructure exhibited a superior combination of high strength and ductility. Adding a certain amount of Mo to a Ti microalloyed steel influences the precipitation behavior of carbides during phase transformation. Firstly, the addition of Mo has an effect on the phase transformation, and then on the precipitation behavior; secondly, Mo influences the precipitation by changing the activities and diffusivities of the carbide formers; thirdly, Mo can enter the crystal lattice of MC, so leading to a complex phase transformation and precipitation process. In this paper, isothermal phase transformation experiments were conducted to study the effect of Mo on the precipitation behavior of MC type carbides.

Experimental

The chemical compositions of the studied steels are given in Table I. The Ti steel was the reference steel used to determine the role of Mo in a Ti-Mo steel. The two experimental steels were prepared by vacuum melting, and then hot forged to 20 mm diameter rods. After homogenization in the austenite phase field for 300 minutes at 1200 °C followed by water quenching, the cylindrical specimens with 8 mm diameter and 12 mm length to be used for Gleeble simulation were cut from the center of the as-homogenized rods using an electrical discharge machine. An illustration of the isothermal treatment is shown in Figure 1. The specimens were initially heated up to 1200 °C, held for 3 minutes, and then cooled to the isothermal temperature, ranging from 550 to 750 °C. The isothermal holding time was

30 minutes. After isothermal holding, the specimens were directly water quenched to room temperature. The optical metallography specimens were cut from the center of the isothermally treated specimens. The hardness of selected microstructures was measured. The hardness was measured only on the ferrite grains, when the proeutectoid ferrite was formed at higher temperature. The hardness of bainite or massive ferrite was measured under the condition that there was no ferrite formed at lower temperature. The hardness load used was 100 g and the loading time was 10 seconds. Five measurements were carried out. The precipitates were analyzed using H-800 TEM analytical and high-resolution transmission electron microscopy. EDS analysis and quantitative electron diffraction were also carried out.

Table I. Chemical Composition of Tested Steels (wt.%)

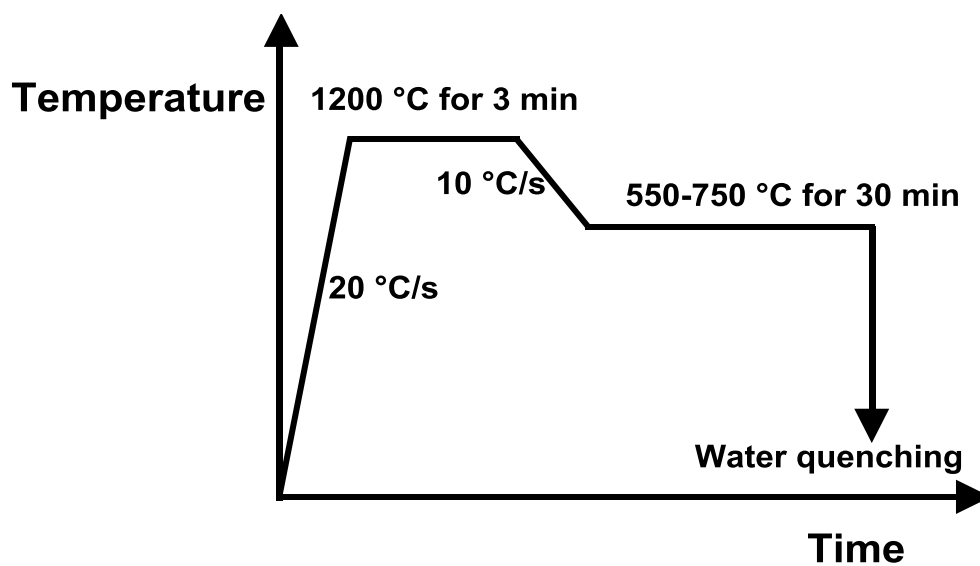| Steel	C	Mn	Si	Ti	S	P	N	Mo
Ti	0.046	1.47	0.12	0.097	0.0060	0.0073	0.0024	—
Ti-Mo	0.042	1.51	0.20	0.100	0.0028	0.0052	0.0018	0.21

Figure 1. Illustration of isothermal treatment process.

Results and Discussion

Microstructure

Figures 2 and 3 show the isothermally transformed microstructures of the Ti and Ti-Mo steels respectively. It can be seen that the addition of Mo has a significant effect on the isothermal phase transformation of the Ti-containing steel. In the case of the Ti only steel, the transformed microstructure from 750 °C to 550 °C was: F+M(untransformed austenite) →F→M→B. In the case of Ti-Mo steel, a fully ferrite microstructure was obtained at temperatures above 725 °C. When the temperature was decreased to 700 °C, the fraction of ferrite decreased significantly. This result was opposite to that in the Ti steel. Firstly, adding Mo to the Ti steel increased the possibility of obtaining a fully ferritic microstructure. The ferrite+MC phase field was enlarged by the addition of Mo to the Ti steel, as shown in Figure 4. On the other hand, adding Mo to the Ti steel accelerates the MC precipitation during phase transformation. According to previous researchers, the addition of Mo can decrease the interfacial energy between MC and the ferrite matrix, and thus favor the nucleation and growth of precipitates during initial stages of precipitation. At higher temperatures, Mo accelerates the MC precipitation during phase transformation, thus decreasing the C content in the austenite near the γ/α interface. The decrease of C content results in the acceleration of the $\gamma \rightarrow \alpha$ transformation. When the temperature was decreased to 650-675 °C, only a little ferrite was formed. This is because the diffusivity of elements at lower temperatures is very slow, resulting in the decrease of the MC precipitation rate. Under this condition, the role of Mo in delaying ferrite transformation becomes more significant. When the temperature was decreased to 625 °C or below, bainite and massive ferrite were formed.
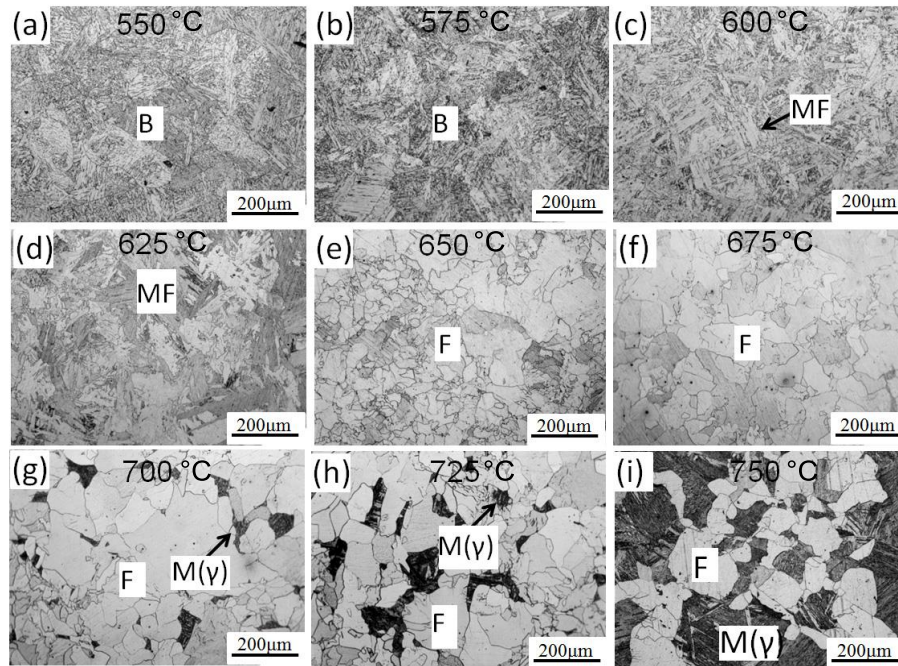

Figure 2. Transformed microstructure of Ti steel after isothermal treatment.
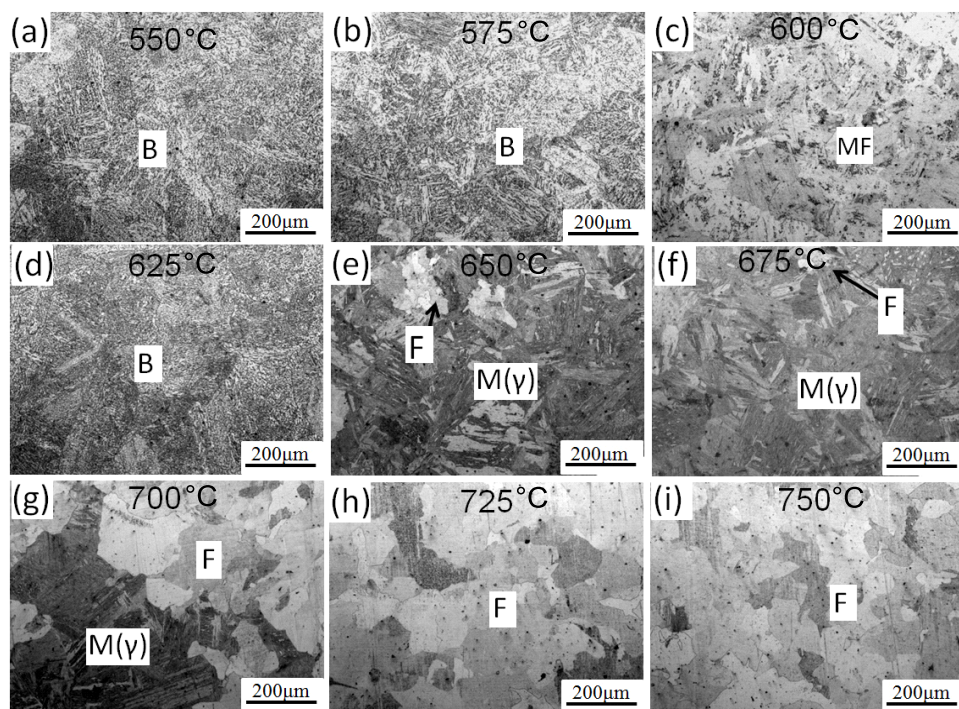
75

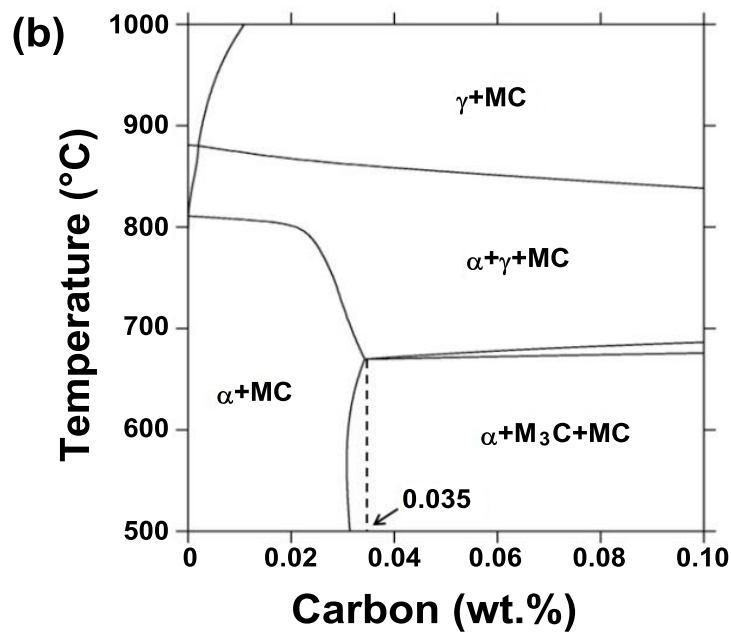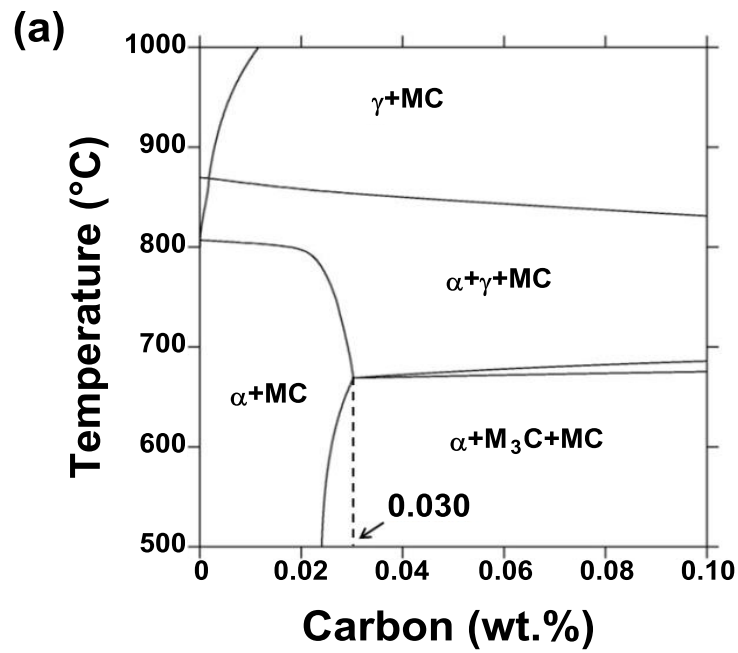Figure 3. Transformed microstructure of Ti-Mo steel after isothermal treatment.

Figure 4. Phase diagram calculated using Thermo-calc (TCFE6 database);
(a) Ti steel (b) Ti-Mo steel.

Effect of Mo on the Hardness of Selected Microstructures

Figure 5 shows the hardness variation of selected microstructures of the Ti and Ti-Mo steels with isothermal temperature. It can be seen that the hardness of the Ti-Mo steel was higher than that of the Ti steel within the studied temperature range, which is evidence of increased precipitation hardening in the Ti-Mo steel.
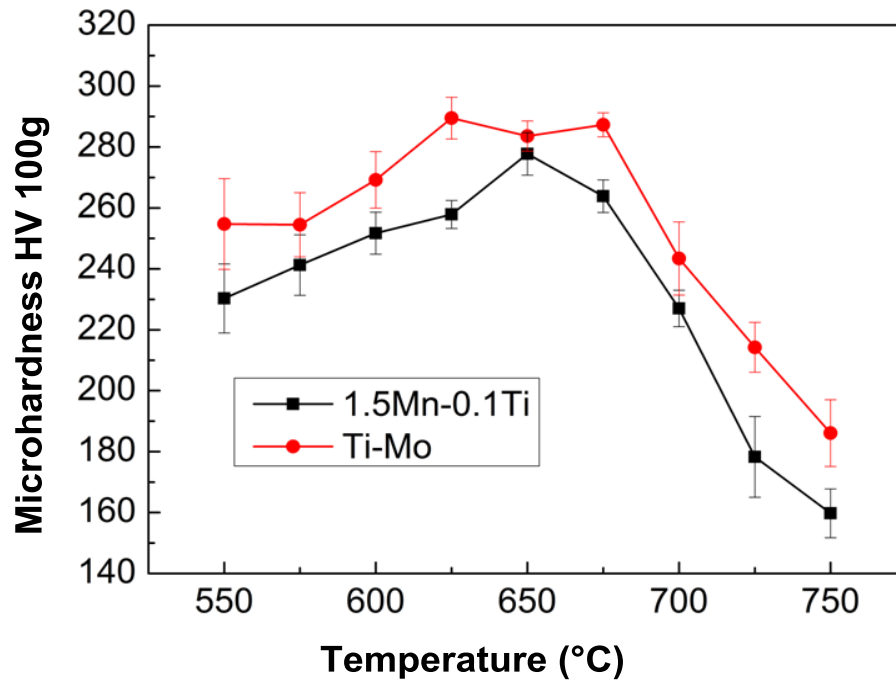

Figure 5. Effect of Mo on the microhardness of selected microstructures produced at different isothermal treatment temperatures.

Precipitates in Ti-Mo Steel and the Role of Mo

Figure 6 shows TEM images exhibiting the interphase precipitation in the Ti-Mo steel formed after an isothermal treatment at 750 °C. It can be seen that the interphase precipitation was not uniform within a ferrite grain. The finer planar-like precipitation shown in Figure 6(a) can be clearly observed. Coarser precipitates were also observed in the same grain as shown in Figure 6(b). In Figure 6(c), the interphase precipitation in a grain, having different orientations, can be observed. In addition, the precipitate size decreases with decreasing isothermal temperature, as shown in Figures 7 and 8.
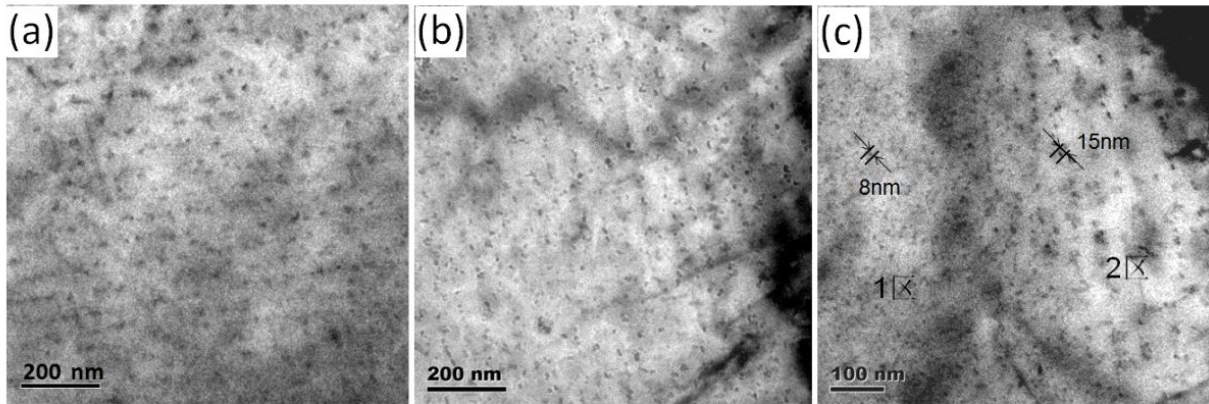

Figure 6. TEM image showing the interphase precipitation in Ti-Mo steel at 750 °C; (a) planar interphase precipitation, (b) coarser precipitates, (c) non-uniform precipitation in a grain (Area 1: fine precipitate, area 2: coarse precipitate).
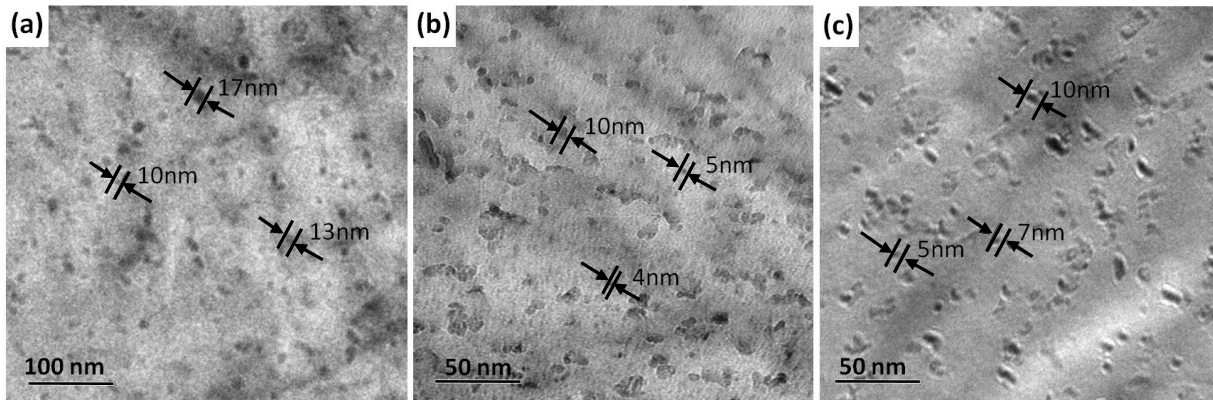

Figure 7. MC precipitate size variation with isothermal temperature; (a) 750 °C, (b) 675 °C, (c) 650 °C.
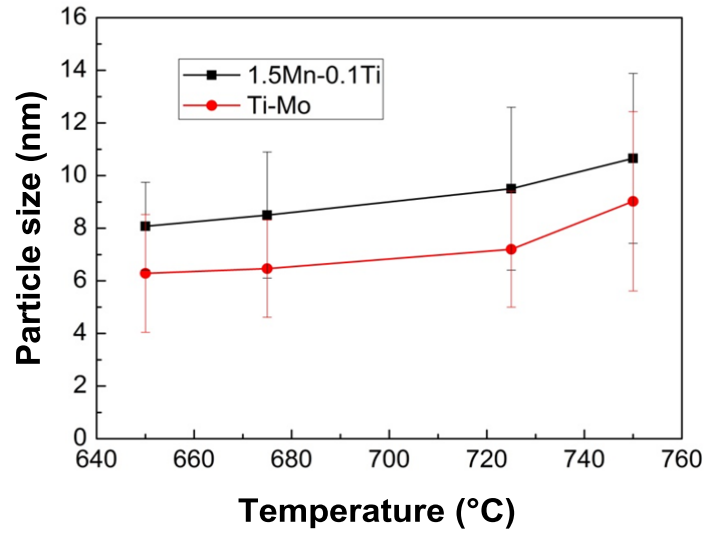
Figure 8. The effect of Mo on the precipitate size of MC carbide with variation in isothermal treatment temperature.

The selected area diffraction pattern in Figure 9(a) has been analyzed. The result indicates that (Ti,Mo) carbides forming during the isothermal transformation adopt the Baker–Nutting (B–N) orientation relationship with respect to the ferrite matrix, ie. {001}carbide//{001}ferrite and <110>carbide//<010>ferrite. The EDX spectrum shown in Figure 9(d) indicates that the content of Ti and Mo in (Ti,Mo)C was almost the same.
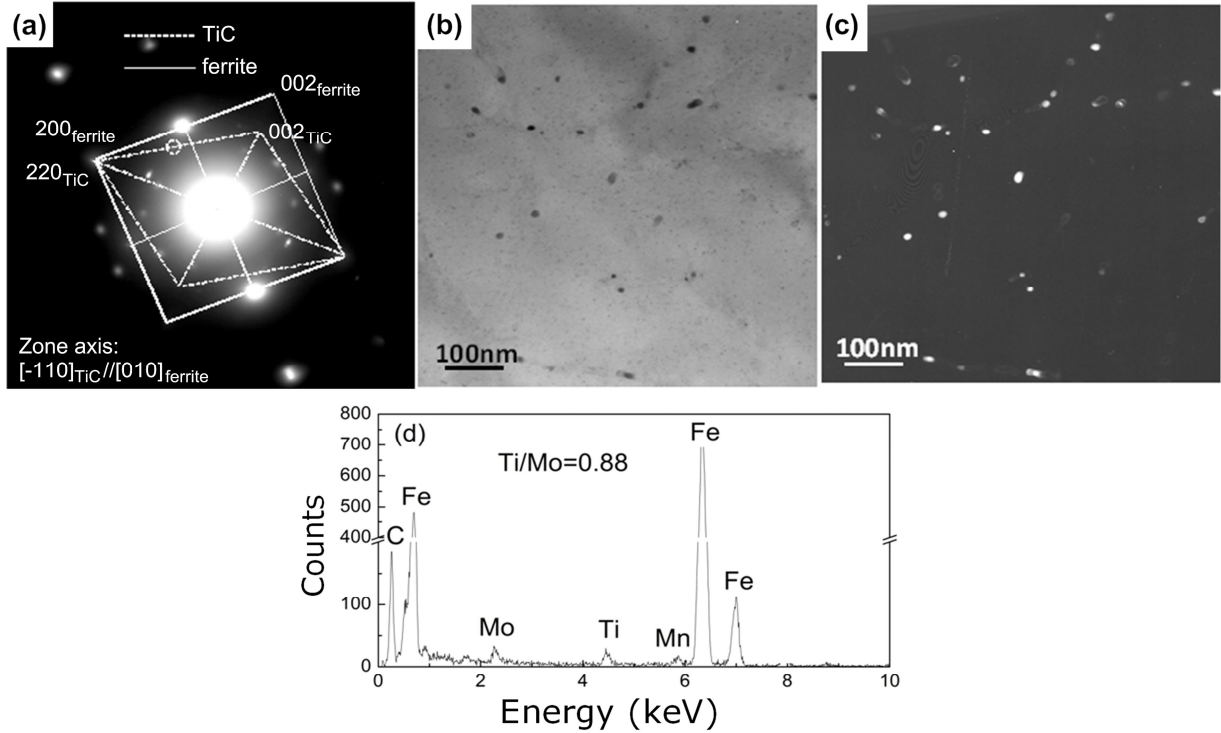
Figure 9. Crystal structure, orientation relationship with respect to the ferrite matrix and composition analysis.

Precipitation Hardening

The increase in yield strength due to the precipitation hardening can be calculated by using the following equation:

$$\Delta\sigma_p = \frac{K}{d} f^{1/2} \ln\frac{d}{b} \tag{1}$$

Where K is a constant, 5.9 N/m, b is the burger vector, f is volume fraction of precipitate and d is the average particle size. Figure 10 shows the relationship between the increase in yield strength and precipitate size. By approximate calculation, the increase in yield strength due to (Ti,Mo)C particles in the Ti-Mo steel was about 200 MPa, which is about twice the effect of TiC in the Ti steel, owing to a larger volume fraction of smaller particles.

81

Figure 10. The relationship between the increase in yield strength and precipitate size.

Conclusions

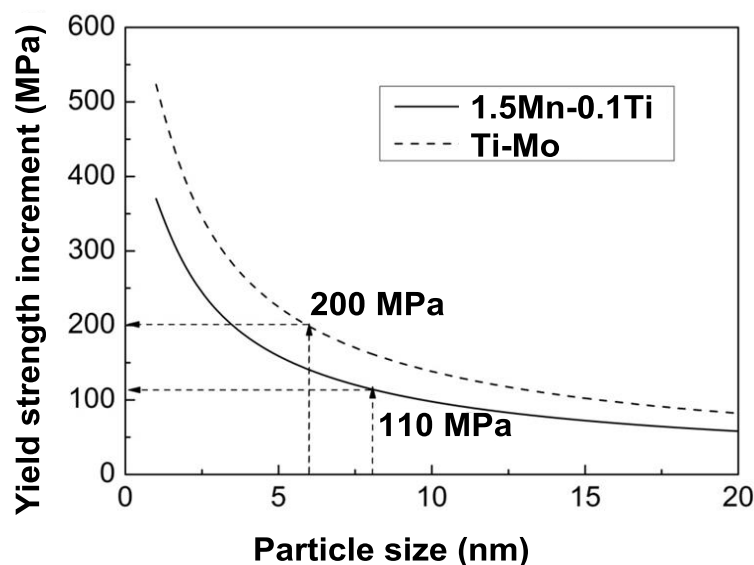The effects of Mo on the isothermal phase transformation and precipitation behavior in a Ti bearing steel were investigated. Addition of 0.2 wt.%Mo to a Ti microalloyed steel results in a fully ferrite microstructure at higher isothermal transformation temperatures. The microhardness of the microstructure isothermally transformed at all temperatures in the Ti-Mo steel was higher than that in the Ti steel. This is attributed to the superior coarsening resistance of MC type carbides in the Ti-Mo steel as compared with that in the Ti steel. The Ti-Mo steel exhibited an increased precipitation hardening contribution to the overall strength of the steel compared to the Ti only steel.

References

1. Y. Funakawa et al., "Development of High Strength Hot Rolled Sheet Steel Consisting of Ferrite and Nanometer-sized Carbides," *The Iron and Steel Institute of Japan International*, 44 (2004), 1945-1951.

2. T. Shimizu, Y. Funakawa and S. Kaneko, "High Strength Steel Sheets for Automobile Suspension and Chasis Use – High Strength Hot Rolled Steel Sheets with Excellent Press Formability and Durability for Critical Safety Parts," *JFE Technical Report,* 4 (2004), 25-31.

3. Y. Funakawa and K. Seto, "Coarsening Behaviour of High Strength Low Alloy Steels by Nanometer-sized Carbides," *Materials Science Forum,* 539 (2007), 4813-4818.

4. C.Y. Chen et al., "Precipitation Hardening of High Strength Low Alloy Steels by Nanometer-sized Carbides," *Materials Science and Engineering A*, 499 (2009), 162-166.

5. H.W. Yen, C.Y. Huang and J.R. Yang, "Characterisation of Interphase Precipitated Nanometer-sized Carbides in a Ti-Mo Bearing Steel," *Scripta Materialia*, 61 (2009), 616-619.

6. J.H. Jang et al., "Stability of (Ti,M)C (M=Nb,V,Mo and W) Carbide in Steels using First Principles Calculations," *Acta Materialia,* 60 (2012), 208-217.

7. Z.Q. Wang et al., "Strain Induced Precipitation in a Ti Microalloyed HSLA Steel," *Materials Science and Engineering A,* 529 (2011), 459-467.

8. X.P. Mao et al., *Acta Metallurgica Sinica*, 42 (2006), 1091-1095. (In Chinese).

SOLUBILITY AND PRECIPITATION OF CARBIDES CONTAINING NIOBIUM AND MOLYBDENUM IN LOW ALLOY STEELS

J.G. Speer[1], C.M. Enloe[2], K.O. Findley[1], C.J. Van Tyne[1] and E.J. Pavlina[3]

[1]ASPPRC, Colorado School of Mines, Golden, CO 80401, USA
[2]Severstal N.A., Dearborn, MI, USA
[3]Institute for Frontier Materials, Deakin University, Waurn Ponds, Victoria 3216, Australia

Abstract

Niobium and molybdenum have been critically important alloying additions in steels for several decades. Niobium typically contributes through careful control of niobium carbide precipitation in austenite and ferrite, which enables grain refinement and precipitation strengthening, although solute effects on recrystallization and transformation kinetics can also be important. Molybdenum is a powerful hardenability agent and is extensively used to influence austenite decomposition kinetics and microstructure development in many steels. Molybdenum and niobium have been employed together in steels, and more recent investigations suggest that interactions associated with combined niobium plus molybdenum additions may provide synergistic enhancements beyond the separate effects of the individual elements. Molybdenum can enhance the benefits of NbC precipitates by reducing the carbide coarsening kinetics. This behavior has been suggested to be important in fire-resistant constructional steels, and high strength, formable automotive hot-rolled sheet steels. More recently, similar effects have been obtained in austenite, where enhanced grain refinement during high temperature carburizing simulations has been confirmed in Nb+Mo modified alloys. The objective of the present paper is to provide some perspective on the physical metallurgy fundamentals influencing a variety of such applications, including solubility of niobium and molybdenum carbides in ferrite and austenite, and the precipitation and coarsening behavior of mixed (Nb,Mo) carbides.

Introduction

Niobium and molybdenum are common alloying elements in many steels and as small additions contribute important enhancements to microstructure and properties. These two elements may be added individually or in combination, along with other important alloying additions in steels. Their individual effects are due to solute effects on grain boundaries or transformation interfaces, and through precipitation-related phenomena. More recently, "synergistic" effects of combined additions of niobium and molybdenum have been reported to provide additional benefits in some applications.

Niobium "microalloying" is employed in a variety of steels, such as thermomechanically processed high-strength, low-alloy (HSLA) steels where substantial grain refinement and precipitation strengthening are achieved. Niobium is dissolved before hot deformation, and subsequent rolling temperatures are designed so that niobium precipitates as niobium carbide (or

carbonitride) on the deformation substructure of the austenite, suppressing subgrain migration and thus delaying recrystallization. During transformation upon subsequent cooling, ferrite nucleation from the deformed or "pancaked" austenite is accelerated, leading to grain refinement. Niobium remaining in solution prior to transformation may enhance hardenability (ie. suppress diffusional transformation) due to solute drag, and then subsequently precipitate as a carbonitride at lower temperature in ferrite, where its solubility is lower, and provide dispersion strengthening. Niobium carbonitrides can also provide important boundary pinning effects during conventional heat treatments, leading to ferrite grain refinement upon annealing of cold-worked steels, or microstructure refinement of a variety of steels following austenitization, including such processes as quenching and tempering, normalizing, carburizing, etc. Formation of stable carbonitrides may also be employed to reduce solute interstitial concentrations in applications such as "interstitial-free" steels or stainless steels.

Molybdenum is also employed in a broad range of steels, often because of its potent effects (as a solute) on hardenability, suppressing the formation of diffusional transformation products such as ferrite or pearlite, in favor of bainite or martensite. Molybdenum also participates in various carbide precipitation reactions, and contributes temper resistance or secondary hardening in a number of steels. Finally, molybdenum is an important addition in pitting-resistant stainless steels, contributing to performance through chemical rather than microstructural effects.

Solubility Considerations

The solubility of alloy carbides or carbonitrides is an important consideration in understanding driving forces for precipitation or dissolution behavior and has a critical influence on whether the alloying elements are in solution or precipitated. The solubility is strongly influenced by temperature and a variety of compositional variables. Consequently, solubility considerations are critical in tailoring the various interactions between key processing temperatures and alloy chemistry to enable precipitation and avoid dissolution/coarsening, etc. for a particular application and processing configuration. Solubility thus represents the basis for design of some important aspects of steel alloying and processing.

The solubility of important carbide and nitride forming species is typically greater in austenite than in ferrite. Solubilities are frequently represented in the form of "solubility products" for MX compounds such as niobium carbide or niobium nitride, and solubility products of mixed precipitates such as carbonitrides have also been addressed.

Niobium carbide equilibrium solubility products have been published by a variety of investigators, and examples are shown in Figure 1 using the following solubility product expressions for NbC in ferrite (α) and austenite (γ) [1,2].

$$\log_{10}[Nb_\alpha][C_\alpha] = 3.90 - (9930/T_K) \qquad (1)$$

$$\log_{10}[Nb_\gamma][C_\gamma] = 2.26 - (6770/T_K) \qquad (2)$$

In these expressions, [Nb] and [C] represent the solute niobium and carbon concentrations (wt.%) in austenite or ferrite, respectively, in equilibrium with NbC at a given temperature (T_K in Kelvin). The curves in Figure 1 are "solubility isotherms" that represent the loci of niobium and carbon solubilities for different temperatures. The change in scale between Figures 1(a) and 1(b) should be noted, and illustrates the much lower levels of niobium and carbon concentrations that are soluble in ferrite as compared to austenite. The strong temperature dependence of solubility is clear in both austenite and ferrite (solubilities of the order of hundreths of a weight percent are common in austenite, while thousanths of a weight percent are typical in ferrite), as well as the strong influence of carbon concentration on the niobium solubility. These composition and temperature dependencies provide the means (and constraints) for alloy and process design. Niobium may precipitate or dissolve in austenite depending on composition and processing, but precipitates should usually be expected at temperatures in the ferritic regime for typical alloys.
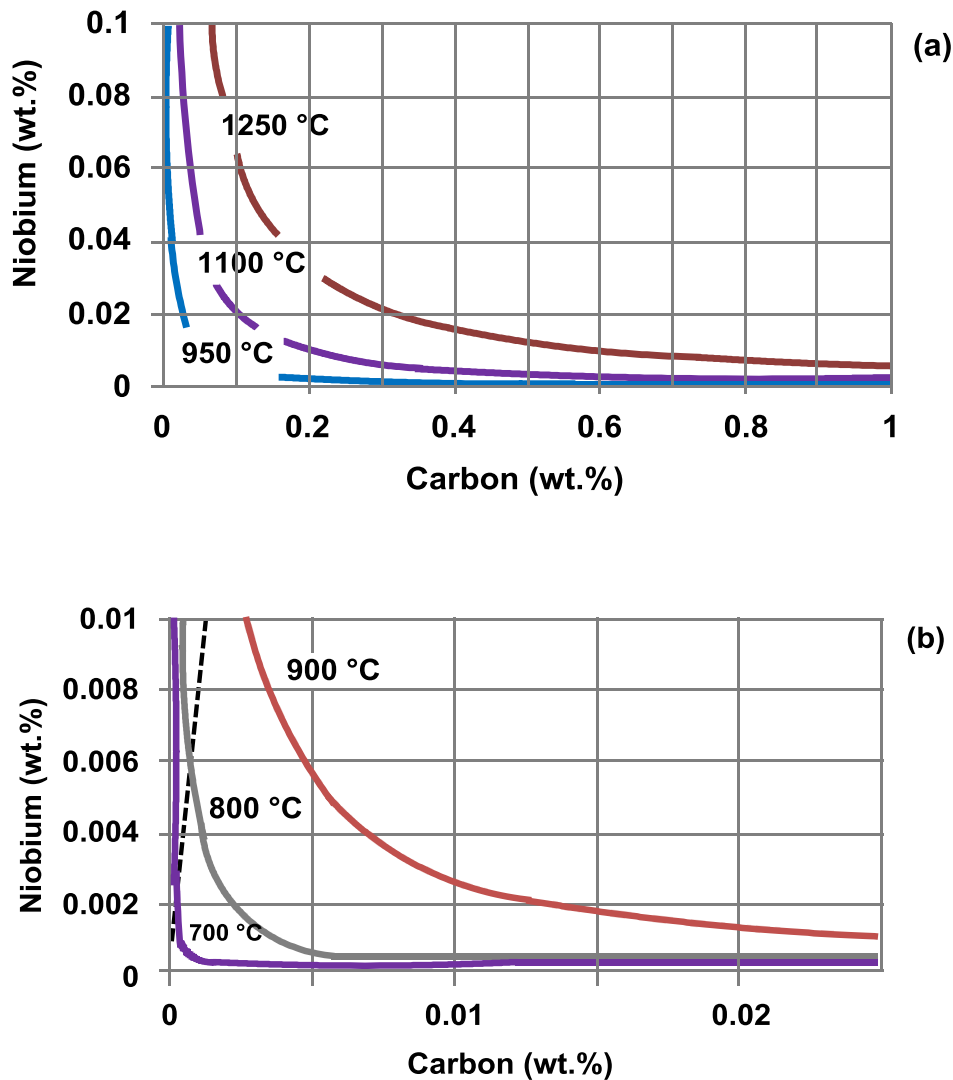

Figure 1. NbC equilibrium solubility isotherms at selected temperatures in austenite (a) and ferrite (b). The dashed stoichiometric line is shown in (b).

In comparison to niobium carbide, molybdenum carbide solubilities have been less well documented. Molybdenum forms an M_2C-type carbide in tempered martensitic steels containing substantial molybdenum additions, but also participates in the precipitation of carbides of MC-type stoichiometry that commonly form in microalloyed HSLA steels. Equilibrium solubility products in ferrite and austenite for these carbides have recently been calculated by Pavlina *et al.* [3], and are given by the following relationships:

For Mo₂C

$$\log_{10}[Mo_\alpha][C_\alpha]^{1/2} = 4.00 - (5088/T_K) \qquad (3)$$

$$\log_{10}[Mo_\gamma][C_\gamma]^{1/2} = 3.04 - (2814/T_K) \qquad (4)$$

For MoC

$$\log_{10}[Mo_\alpha][C_\alpha] = 3.19 - (4649/T_K) \qquad (5)$$

$$\log_{10}[Mo_\gamma][C_\gamma] = 1.29 - (523/T_K) \qquad (6)$$

Definition of terms similar to equations (1 and 2)

The solubilities of these Mo-carbides are higher than typical microalloy carbides such as NbC, TiC and VC [3], and Mo-carbides are also much more likely to precipitate in ferrite than in austenite (due to their high solubility in austenite). While Mo_2C is somewhat more stable than MoC, the solubility of MoC in ferrite is of greater interest in microalloyed steels; Figure 2 shows solubility isotherms for MoC in ferrite for temperatures of 500, 600 and 700 °C. Even in ferrite, it is clear that molybdenum solubility is quite high, of the order of tenths of a weight percent in low carbon steels. Molybdenum solubility is reduced when molybdenum precipitates with other species such as niobium in a mixed carbide or carbonitride. The solubility of such a mixed carbide, $(Nb_xMo_{1-x})C$, has recently been addressed by Enloe *et al.*, and will be discussed further below, with respect to precipitation behavior recently reported in Nb-Mo steels [4-6].
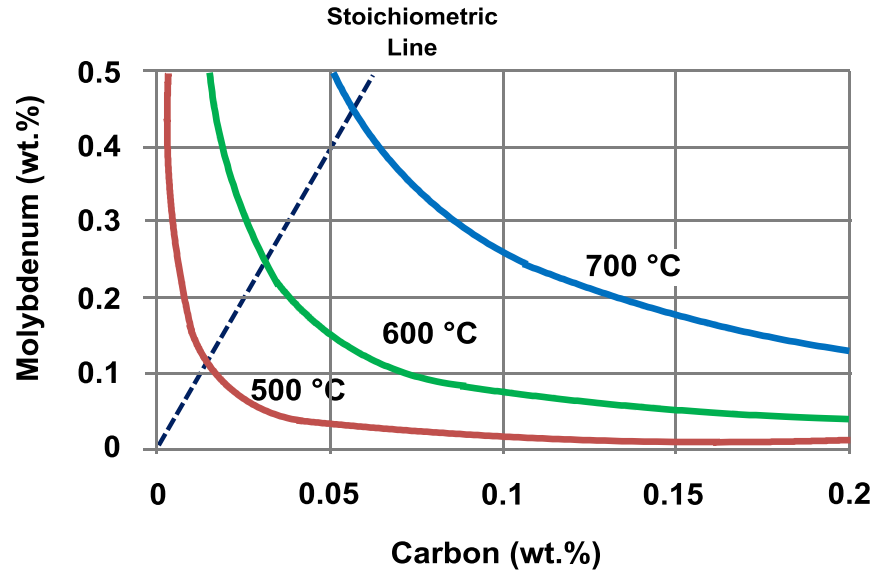
Figure 2. MoC solubility isotherms in ferrite at 500, 600 and 700 °C, calculated based on the recent solubility product analysis of Pavlina *et al.* [3]. The dashed line indicates stoichiometric (1:1 atomic basis) ratios of Mo to C.

Applications of Combined Nb+Mo Alloying Additions

Niobium and molybdenum are added individually or in combination to many families of steels to exploit the various benefits of these important elements. The synergistic effects of combined additions are of special interest here, wherein molybdenum influences the behavior of niobium carbide. Early work [7] reported a greater fraction of (Nb,Mo)(C,N) precipitates and precipitate refinement during tempering of steels containing both niobium and molybdenum. Molybdenum is now believed to reduce the coarsening kinetics of NbC, and it is this effect that has led to some recent applications in steel development. These applications have included fire-resistant constructional steels, where resistance to precipitate coarsening improves high temperature strength [8]. Molybdenum additions to Nb- or Ti-microalloyed steels are also being employed in high-strength hot-rolled sheet products having high hole expansion performance and enhanced precipitation strengthening [9-11], and more recently have been investigated for high temperature carburizing of gears, used herein to illustrate physical metallurgy principles in Nb+Mo steels.

Vacuum carburizing is growing in importance, and Nb-microalloying has been employed to develop a fine array of NbC precipitates to suppress austenite grain growth at the elevated temperatures associated with vacuum processing, since the fatigue properties of carburized (martensitic) gears are well known to benefit from a refined PAGS (prior-austenite grain size) [12]. A series of studies in the authors' laboratories have been undertaken in this area, [eg. 13,14], and Figure 3 presents bending fatigue properties (S-N curves) for three Nb-modified SAE 8620 steels that were vacuum carburized at 1050 °C. The benefit of niobium additions on the low-cycle fatigue life and particularly the endurance limit is clear from the figure, resulting from enhanced austenite grain refinement due to NbC precipitates. More recent work has begun

to explore the potential for enhancing the grain refining effect of niobium during high temperature carburizing by a further addition of Mo, and early results are promising [5,6].
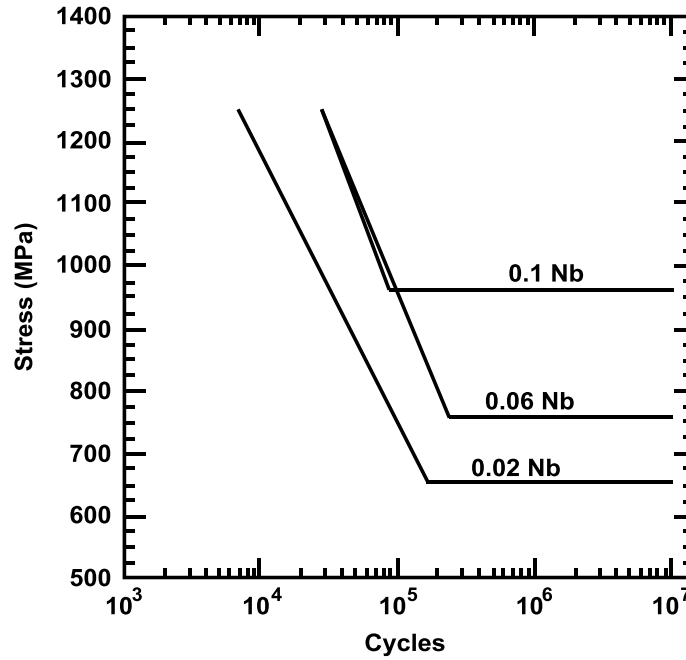

Figure 3. Stress versus cycles to failure in bending fatigue (min./max. stress ratio = +0.1) for Nb-modified SAE 8620 steel, control-rolled, reheated at 114 °C/min to 1050 °C and vacuum carburized [14].

Enloe *et al*. examined NbC precipitation and austenite grain coarsening behavior in a series of SAE 4120 alloys with low (~0.04%) and high (~0.1%) levels of niobium and with or without a molybdenum addition [5,6]. A small titanium addition was also included to provide an additional contribution from TiN pinning [15]. Table I presents the chemical compositions of the modified 4120 alloys investigated by Enloe *et al.* The steels were reheated to 1250 °C, hot-rolled and air cooled to room temperature prior to the simulated carburizing thermal treatment (ie. "pseudocarburizing") at 1100 °C. The MoLNb alloy was also subjected to a solution treatment at 1250 °C and quenched prior to pseudocarburizing to modify the initial precipitate distribution. Figure 4 shows NbC precipitate size distributions that were measured using transmission electron microscopy (TEM) of extraction replicas, and indicates the precipitate coarsening kinetics at the elevated carburizing temperature. The results are plotted as the cube of the particle radius, r, versus time, reflecting the well-known LSW (Lifshitz-Slyozov-Wagner) relationship for particle coarsening, where r^3 is proportional to time. A dashed line is superimposed on the figure reflecting LSW kinetics (straight line) with a slope estimated using parameters identified in the literature [5].

Table I. Chemical Compositions wt.% of Modified 4120 Experimental Alloys [5]

wt.%	C	Mn	Cr	Mo	Ti	Nb	V	Al	N	Ti/N
LNb	0.21	0.89	0.50	0.00	0.015	0.044	-	0.025	0.008	1.9
HNb	0.21	0.83	0.49	0.01	0.012	0.104	-	0.022	0.009	1.3
MoLNb	0.21	0.86	0.50	0.29	0.013	0.043	-	0.024	0.008	1.6
MoHNb	0.21	0.86	0.50	0.30	0.015	0.118	-	0.021	0.008	1.9

L = Low
H = High

The results in Figure 4 suggest some important implications. Most importantly, the molybdenum addition to both the low and high niobium steels reduces the NbC coarsening rate at 1100 °C, as emphasized by the vertically descending arrows in the figure, confirming the benefit of the combined Nb+Mo addition. The higher niobium level is associated with greater coarsening, as expected based on LSW kinetic theory, where the solute concentration of the diffusing species plays an important role, and due to a greater fraction of larger Nb-rich precipitates after hot rolling. Despite the faster particle coarsening kinetics, the high-Nb steel maintains superior grain coarsening resistance due to its increased volume fraction of particles [5,6]. While the coarsening behavior of the solution treated alloy fits the LSW model rather closely, the coarsening rates of the hot-rolled steels are greater than the model predictions. This behavior is attributed to a bi-modal particle size distribution in the hot-rolled condition, due to the presence of coarser particles formed in austenite and finer particles formed in ferrite during cooling after rolling [5]. Grain coarsening studies have confirmed the beneficial influence of adding both niobium and molybdenum [6], and additional studies are needed to verify the corresponding improved fatigue behavior that would be expected.
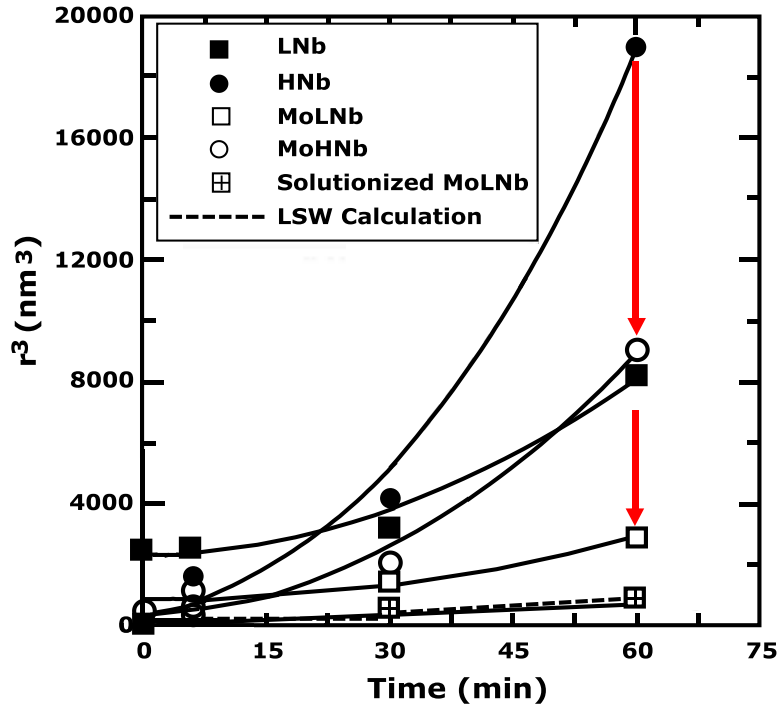
Figure 4. NbC particle radius cubed (r^3) vs. holding time at 1100 °C for four hot-rolled experimental steels, and MoLNb steel after 1250 °C solution treatment and quench. Dashed line indicates coarsening rate calculated based on LSW theory [5]. Arrows emphasize the influence of Mo on NbC coarsening kinetics.

Precipitation of Mixed (Nb,Mo)C

The influence of molybdenum on microalloy carbide coarsening has been ascribed to a variety of potential factors including, (1) Mo-segregation to the particle/matrix interface, reducing interfacial energy, (2) reduced misfit strains at the interface, due to effects of molybdenum on lattice parameters, or (3) reduced niobium diffusivity due to the presence of solute molybdenum [4,5,16,17]. Evolution of the mixed (NbMo) carbide precipitates was examined in the Nb-Mo modified SAE 4120 alloys discussed above, using TEM/STEM (with energy dispersive characteristic X-ray spectroscopic chemical analysis, EDS) and 3-D atom probe tomography (APT). These recent studies have contributed new understanding of (Nb,Mo) carbide precipitation behavior, and a few highlights are included below.

Figure 5(a) shows a composition profile for niobium, molybdenum and titanium determined using STEM-EDS from the surface toward the center of a small carbide on an extraction replica shown in an annular dark field STEM image (Figure 5(b)) for the hot-rolled and air cooled MoHNb specimen. The results indicate the presence of niobium, molybdenum and titanium in the precipitate, with molybdenum enrichment near the surface, and titanium present near the center. The increased X-ray counts for these elements near the center are due to the increased interaction volume in this location. The molybdenum enrichment near the surface could be due to segregation to the interface, or low-temperature precipitation during cooling.
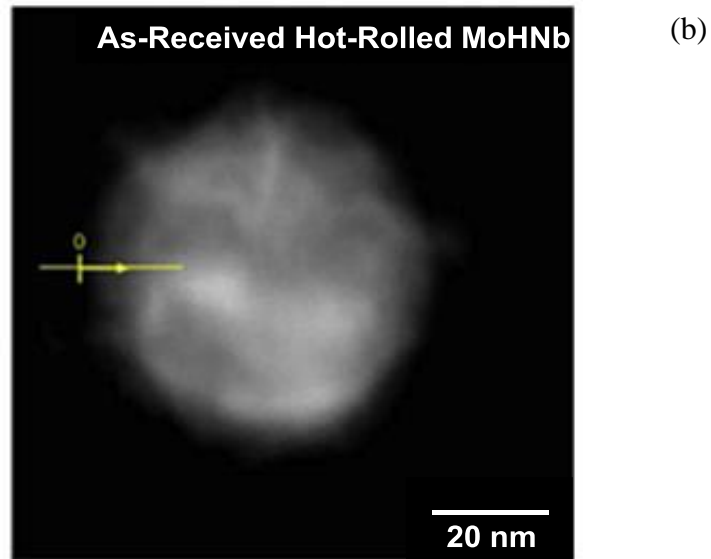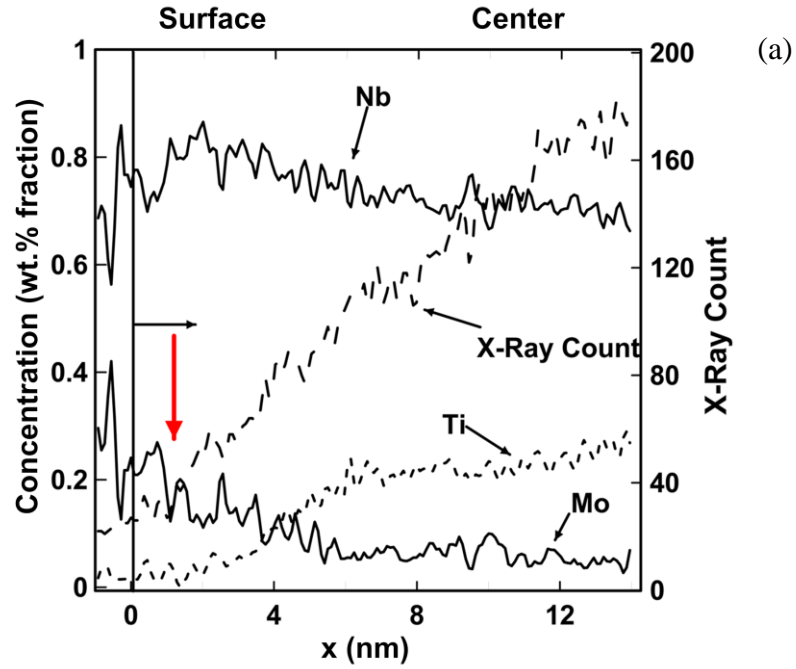
Figure 5. STEM EDS composition profiles (a) for niobium, molybdenum and titanium for microalloy carbide with reference location shown in the dark field STEM image in (b), for hot-rolled steel MoHNb [4]. Mo enrichment near the particle/matrix interface is highlighted by the red arrow in (a).

Calculations of particle compositions in mixed $(Nb_xMo_{1-x})C$ have been made for these steels using a regular solution model enabled by the MoC solubility product expressions recently made available from Pavlina *et al*., as discussed above [3,4,18]. Figure 6 shows predicted molybdenum atom fractions on the metallic sublattice for alloys containing 0.2%C, 0.3%Mo, and 0.043 or 0.118%Nb, corresponding to the nominal MoLNb and MoHNb alloy compositions. The figure indicates that substantial molybdenum incorporation into the niobium carbides is expected at temperatures in the ferritic regime, and much less so in austenite. As expected, the molybdenum fractions are also reduced when the overall niobium concentration is increased in the alloy.
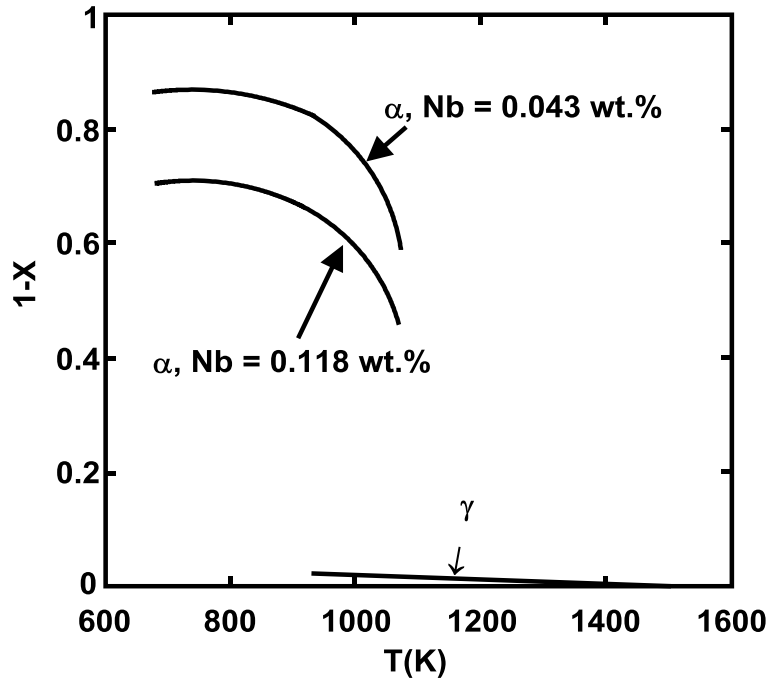

Figure 6. Predicted Mo concentrations in $(Nb_xMo_{1-x})C$ for 0.2%C, 0.3%Mo steels in ferrite and austenite at various temperatures [4].

Particle compositions in specimens heated to a low temperature (900 °C) within the austenite regime (and quenched) retain a mixed character, and are found to be dependent on alloy composition and particle size, as shown in Figure 7 for the MoLNb and MoHNb. The smaller particles contain greater molybdenum fractions, while larger particles contain higher titanium concentrations, particularly in the lower-Nb steel. Presumably, the finer particles may have formed at lower temperature (with greater molybdenum enrichment expected, as per Figure 6), or may have been influenced by re-precipitation during quenching from the austenite.
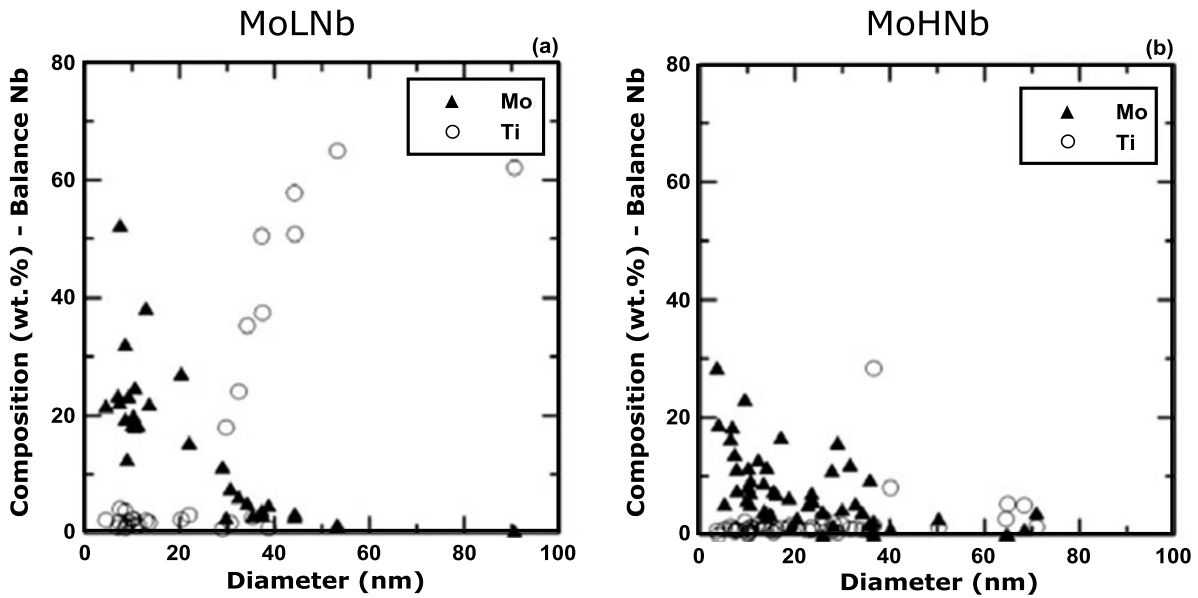
Figure 7. Molybdenum and titanium metallic sublattice compositions (balance niobium) versus particle diameter determined by STEM EDS in mixed carbides for MoLNb (a) and MoHNb (b) steels hot-rolled, reheated to 900 °C and water quenched [4].

As the STEM-EDS results are unable to distinguish molybdenum enrichment near the surface from segregation at the interface, 3-D APT, (atom probe tomography), with high spatial resolution, was used to examine small precipitates in specimens quenched from austenite. Figure 8(a) shows a 3-D reconstructed image of the specimen tip in the MoHNb sample heated to 900 °C and water quenched (with red dots indicating individual carbon atoms, and blue dots indicating areas of niobium atoms), and Figure 8(b) shows a corresponding composite profile or "proximity histogram" (a profile of local atomic concentration as a function of proximity to an interface [19]) centred on the 10% niobium iso-concentration surfaces (blue surfaces in Figure 8(a)) for four particles in the reconstruction. The profile shows molybdenum incorporation in the carbide, but does not indicate any substantial enrichment of the interface with molybdenum. This result does not support the hypothesis that molybdenum's contribution to NbC coarsening resistance in austenite results from segregation to the interface, but does not preclude the possibility that such a mechanism may operate in ferrite.
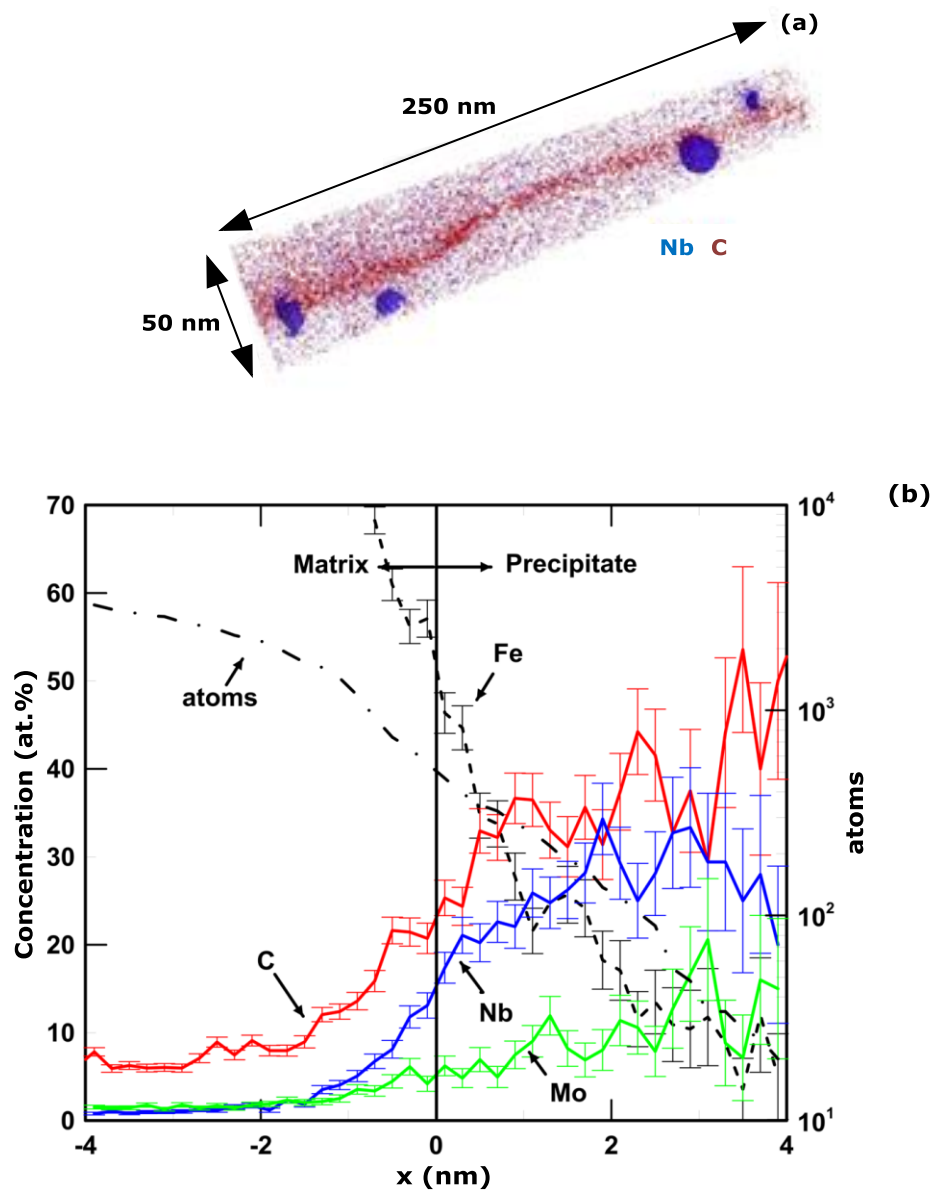
Figure 8. Three dimensional atom-map reconstruction (a) of hot-rolled MoHNb sample heated to 900 °C and water quenched. Proximity histogram (b) for the four particles showing atom count and atomic concentrations of Fe, C, Nb and Mo as a function of distance from a 10 at.% Nb iso-concentration surface [4].

Summary

Niobium and molybdenum are important elements in many steels due to their specific individual effects: predominantly grain refinement and precipitation in the case of Nb-microalloyed HSLA steels, and predominantly hardenability and temper resistance in Mo-added structural steels. When added in combination, some additional synergy is also possible from a contribution of molybdenum to reduced NbC coarsening kinetics. The understanding of the associated mechanism remains incomplete, however. Precipitate coarsening resistance enhances precipitation strengthening in ferrite in some applications, and has been shown recently to provide austenite refinement during high temperature carburizing simulations. Molybdenum is incorporated in the microalloy carbides, particularly at lower temperature, and recent analysis of Mo-carbide solubility has provided solubility products for MoC and Mo_2C in ferrite and austenite enabling better understanding of the mixed (Nb,Mo)C carbides. Atom probe tomography has not confirmed enrichment of the particle/matrix interface for small particles quenched from austenite, although this mechanism cannot be ruled out in ferrite.

Acknowledgements

References

1. K.A. Taylor, "Solubility Products for Titanium-Vanadium, and Niobium Carbide in Ferrite," *Scripta Metallurgica et Materialia*, 32 (1995), 7.

2. K.J. Irvine, F.B. Pickering and T. Gladman, "Grain Refined C-Mn Steels," *The Journal of the Iron and Steel Institute*, 205 (1967), 161.

3. E.J. Pavlina, J.G. Speer and C.J. Van Tyne, "Equilibrium Solubility Products of Molybdenum Carbide and Tungsten Carbide in Iron," *Scripta Materialia,* 66 (2012), 243.

4. C.M. Enloe et al., "Compositional Evolution of Microalloy Carbonitrides in a Mo-bearing Microalloyed Steel," *Scripta Materialia,* 68 (2013), 55.

5. C.M. Enloe et al., "The Effect of Molybdenum on Niobium, Titanium Carbonitride Precipitate Evolution and Grain Refinement in High Temperature Vacuum Carburizing Alloys," *Proceedings of the 3rd International Symposium on Steel Sciences,* May 27-30th, 2012, Kyoto, Japan, *The Iron and Steel Institute of Japan*, 163.

6. C.M. Enloe, "The Effect of Molybdenum on Niobium, Titanium Carbonitride Precipitate Evolution and Grain Refinement in High Temperature Vacuum Carburizing Alloys" (Ph.D. thesis, Colorado School of Mines, 2012).

7. S. Kanazawa et al., "On the Behaviour of Precipitates in the Nb-Mo Heat Treated High Strength Steel with 80 kg/mm^2 Strength Level," *Transactions of the Japan Institute of Metals*, 8 (1967), 113.

8. J.G. Speer, D.K. Matlock and S.G. Jansto, "Nb-microalloyed Fire-resistant Construction Steels: Recent Progress," *Proceedings of the Value-added Niobium Microalloyed Construction Steels Symposium*, November 5-7, 2012, Singapore, in press.

9. K. Seto, Y. Funakawa and S. Kaneko, "Hot Rolled High Strength Steels for Suspension and Chassis Parts "NANOHITEN" and "BHT" Steel," *JFE Technical Report*, 10 (2007), 19.

10. Y. Funakawa and K. Seto, "Coarsening Behaviour of Nanometer-sized Carbides in Hot-rolled High Strength Steel Sheet," *Materials Science Forum,* 539-543 (2007), 4813.

11. W.B. Lee et al., "Influence of Mo on Precipitation Hardening in Hot Rolled HSLA Steels containing Nb," *Scripta Materialia*, 43 (2000), 319.

12. J.P. Wise and D.K. Matlock, "Bending Fatigue of Carburizing Steels: A Statistical Analysis of Microstructural and Process Parameters," (SAE Technical Paper Series No. 2000-01-0611), (2000).

13. K.A. AlOgab et al., "The Influence of Niobium Microalloying on Austenite Grain Coarsening Behavior of Ti-modified SAE 8620 Steel," *The Iron and Steel Institute of Japan International,* 47 (2007), 307.

14. R.E. Thompson, D.K. Matlock and J.G. Speer, "The Fatigue Performance of High-temperature, Vacuum-carburized Nb-modified 8620 Steel," *SAE Transactions - Journal of Materials and Manufacturing,* 116 (5) (2008), 392.

15. S.G. Davidson, J.P. Wise and J.G. Speer, "The Influence of Titanium on Grain Size in High-temperature Carburized Steels," *Proceedings of the ASM 20th Heat Treating Conference*, (2000), 1144.

16. R. Uemori et al., "AP-FIM Study on the Effect of Mo Addition on Microstructure in Ti-Nb Steel," *Applied Surface Science*, 76 (1994), 255.

17. J.H. Jang et al., "Stabilility of (Ti,M) (M = Nb, V, Mo and W) Carbides in Steels using First-principles Calculations," *Acta Materialia,* 60 (2012), 208.

18. J.G. Speer, S. Mehta and S.S. Hansen, "Composition of Vanadium Carbonitride Precipitates in Microalloyed Austenite," *Scripta Metallurgica,* 18 (1984), 1241.

19. O.C. Hellman et al., "Analysis of Three-dimensional Atom-probe Data by the Proximity Histogram," *Microscopy and Microanalysis*, 6 (2000), 437.

DESIGN OF A MODULAR ALLOYING CONCEPT FOR HDG LOW-CARBON DP STEEL, ITS INDUSTRIAL IMPLEMENTATION AND EXPERIENCES WITH OEM PARTS

M. Calcagnotto[1], V. Flaxa[1], T. Schulz[1], S. Schulz[2] and H. Mohrbacher[3]

[1]Salzgitter Mannesmann Forschung GmbH, Salzgitter, Germany
[2]Salzgitter Flachstahl GmbH, Salzgitter, Germany
[3]NiobelCon bvba, Schilde, Belgium

Keywords: Hot Dip Galvanizing, Dual Phase Steel, Bake Hardening, Press Stamping

Abstract

The application of higher strength multiphase steels (AHSS) in automotive body construction can significantly contribute to an increased crash safety level and at the same time reduce body weight. However, frequently encountered difficulties during body manufacturing, due to reduced formability, enhanced crack formation at trim edges, increased spring-back or deteriorated fracture behavior of weld joints, are typically related to unfavorable microstructures. The strict limitation of the C content to below 0.1 wt.% across all strength classes ranging from 500 to 1000 MPa allowed the development of hot dip galvanized dual phase steels which avoided the mentioned manufacturing difficulties. Key to the successful development was a well-tuned addition of Nb for grain refinement, in combination with Mn and Cr bulk alloying on the one hand and adjusted cold rolling reductions, as well as annealing and cooling conditions on the other hand. This modular alloying concept not only brings about advantages for the steel user but it also simplifies sequencing during production in the steel mill when producing various strength grades. For instance, the transition between heats of two strength classes during continuous casting can be shortened and also coil welding between continuous processes such as pickling, tandem rolling and hot dip galvanizing becomes simpler and safer.

Extended annealing simulations were utilized to optimize the combination of alloying elements during the design of the modular alloy concept. These were helpful to fine-tune the temperature profile with regard to the transformation behavior, which in turn is influenced by cold reduction and chemical composition. These simulations were performed under boundary conditions reflecting the process parameters in the industrial annealing lines. By that approach, swift industrial implementation became possible. The resulting trial coils rapidly satisfied general customer demands and in particular concerning surface quality with regard to roughness and zinc adhesion. Consequently, a quick production release by OEMs could be achieved.

Introduction

Within the large group of multiphase steels available worldwide, dual phase (DP) steels in the thickness range of 0.8 to 2.5 mm find the widest application in car body construction. DP steels are mostly used as hot dip galvanized (HDG) sheet. In Europe, these steels currently are standardized within EN10346. However, to guarantee a global availability of automotive sheet with identical properties, the OEMs AUDI, BMW, Daimler, Ford, GM and VW have defined

characteristic properties of these steels in the new standard VDA239 [1]. The requirements of VDA239 with regard to chemical compositions and mechanical properties are applicable, irrespective of the surface treatment and are explained in detail in [2]. Tables I and II display the mechanical properties to be determined by tensile testing along the sheet rolling direction and the chemical composition of cold rolled DP steel, respectively. In the grade designation, "Y" and "T" refer to the minimum yield and tensile strength, respectively.

Table I. Mechanical Properties of Cold Rolled Dual Phase Steels (Testing along Rolling Direction) According To VDA239 [1]

	CR290Y490T-DP	CR330Y590T-DP	CR440Y780T-DP	CR590Y980T-DP	CR700Y980T-DP
Yield Strength $R_{p0.2}$ MPa	290 - 380	330 - 430	440 - 550	590 - 740	700 - 850
Tensile Strength Rm MPa	490 - 600	590 - 700	780 - 900	980 - 1130	980 - 1130
Elongation A_{50mm} %	min. 26	min. 21	min. 15	min. 11	min. 9
Elongation A_{80mm} %	min. 24	min. 20	min. 14	min. 10	min. 8
n-value n_{4-6}	min. 0.19	min. 0.18	min. 0.15	-	-
n-value $n_{10-20/Ag}$	min. 0.15	min. 0.14	min. 0.11	-	-
Bake hardening index BH_2 MPa	min. 30	min. 30	min. 30	min. 30	min. 30

n_{4-6} strain hardening exponent determined between 4 and 6% plastic strain
$n_{10-20/Ag}$ strain hardening exponent determined between 10 and 20% plastic strain or Ag if Ag<20%

Table II. Chemical Composition of Cold Rolled Dual Phase Steels According To VDA239 [1]

	CR290Y490T-DP	CR330Y590T-DP	CR440Y780T-DP	CR590Y980T-DP	CR700Y980T-DP
max. C %	0.14	0.15	0.18	0.20	0.23
max. Si %	0.50	0.75	0.80	1.00	1.00
max. Mn %	1.80	2.50	2.50	2.90	2.90
max. P %	0.080	0.040	0.080	0.080	0.080
max. S %	0.015	0.015	0.015	0.015	0.015
Al %	0.015-1.00	0.015-1.50	0.015-2.00	0.015-2.00	0.015-2.00
max. (Cr+Mo) %	1.00	1.40	1.40	1.40	1.40
max. (Nb+Ti) %	0.15	0.15	0.15	0.15	0.15
max. B %	0.005	0.005	0.005	0.005	0.005

The well known designations DP600 and DP780 can be used instead of CR330Y590T-DP or CR440Y780T-DP. Accordingly, the specification allows chemical compositions over a wide range of alloying elements as long as the requirements regarding mechanical properties are fulfilled and cold forming properties (including edge stretching or bending in some applications) are not restricted by martensite lines, slag inclusions or segregations. At first sight a steady increase of the C content from 0.05% to around 0.20% within the allowed range of VDA239 appears appropriate for realizing increasing strength levels from 490 MPa to 980 MPa. Other elements such as Mn, Si, Cr and P, which increase strength and hardenability, complete the analysis. Pursuing the strategy of continuously increasing the C content, however, bears a process related risk as casting of melts in the peritectic range causes problems. In order to avoid these problems, alloying strategy-1 excludes the peritectic range, ie. lower strength DP grades are being produced with C content < 0.1% whereas a higher C content is used for higher strength grades (Figure 1). In the case of DP600, two principal alloys are possible. In a low C variant, an increased Mn content has to be selected, whereas the high C variant requires a lower Mn addition. Generally for the higher strength DP grades, the Mn content is raised up to a level of around 2.2%. Practical experience revealed in this case that the applicable processing windows could vary considerably, depending on the chemical analysis. Even small deviations from the ideal processing route of such DP steels result in inhomogeneous microstructure, banding, varying mechanical properties and severe anisotropy. Consequently, stringent limitations in the manufactured properties (sometimes directionally dependent) and premature damage are being observed. The optimum microstructure and hence properties of cold rolled hot-dip galvanized DP steels require an exact adjustment, not only for the chemical analysis, but also for the hot rolling conditions, cold reduction and annealing conditions.
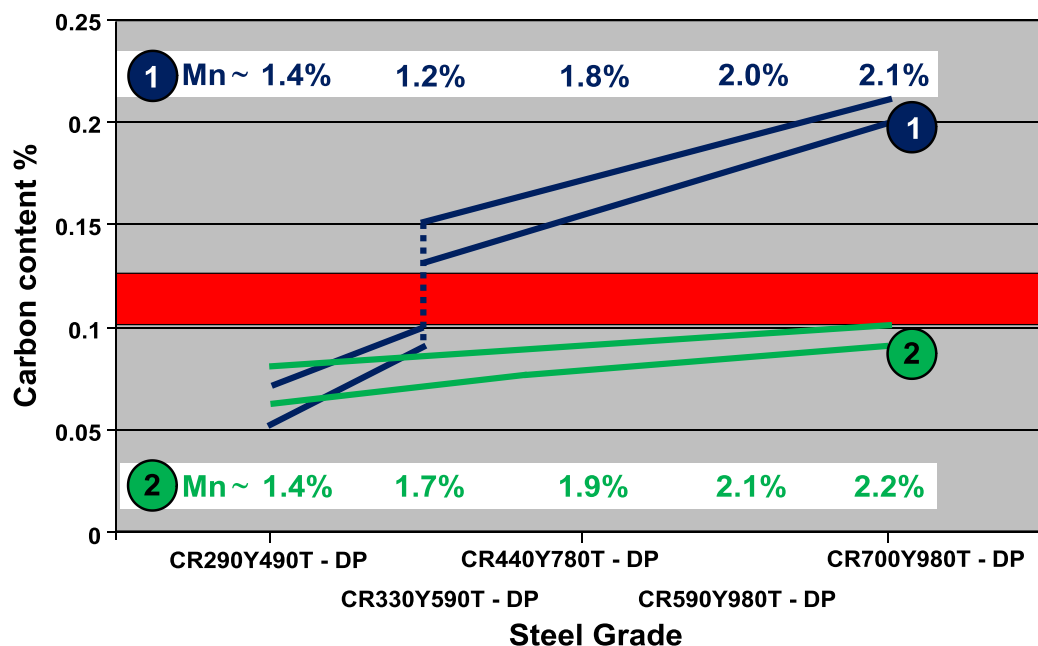

Figure 1. C and Mn alloying strategies for DP grades defined by VDA239 (the peritectic C range preferably to be avoided is indicated in red).

Table III reveals several examples of alloying concepts for DP600 and DP780 grades being commercially supplied by major European steelmakers. It is evident that some DP600 concepts are indeed designed to avoid the peritectic reaction, whereas several others are in the unfavorable peritectic C range (the element C has the strongest influence on the peritectic of steel). The Mn level is typically on the high side for sub-peritectic DP600 concepts. Additional hardenability is achieved by either an increased Cr content (A.1, B.2, D.1, E.2, F.1, F.3) or by Mo alloying (B.1, C.2, E.1, E.3, F.2) in combination with a reduced Cr (and sometimes Mn as in E.3, F.2) content. In one approach, (E.2), B microalloying is used to increase hardenability. This concept implies a small Ti addition to fix interstitial N.

The alloy concepts for DP780 generally apply C additions in the peritectic range and high Mn levels. In the majority of cases Cr is used as a second hardenability element whereas Mo is rarely used for this grade. It is apparent that several DP780 concepts use Nb microalloying and in one case Ti microalloying, while B microalloying is not being applied in these examples.

The considerable variation in alloying concepts, especially for DP600 grades, has in some part arisen historically. On the other hand, in several cases limitations within the production route mandate certain alloying elements. More precisely, the cooling power in the hot-dip galvanizing line is one of the most decisive issues in determining the bulk-alloying concept (Figure 2). Lines having limited cooling power require either rather high alloying contents of Mn and Cr, or alternatively, a relatively smaller Mo addition. Due to the significant amount of HDG DP600 being produced, steelmakers often have to employ several coating lines flexibly, so that usually the line with the weakest capability determines the overall alloy concept.

Table III. Commercialized Alloy Concepts for DP600 and DP780 by European Steel Mills
(alloy additions in wt.%)

| Producer	Concept	C	Si	Mn	P	Al	Cr	Mo	Ti	Nb	B
		DP600									
A	A.1	0.09	0.13	1.49	0.014	0.05	0.75	-	-	-	-
B	B.1	0.07	0.02	1.85	0.014	0.05	0.21	0.18	-	-	-
	B.2	0.09	0.24	1.78	0.013	0.04	0.56	-	-	-	-
C	C.1	0.09	0.25	1.88	0.019	0.04	0.21	-	-	-	-
	C.2	0.12	0.32	1.38	0.013	0.03	0.25	0.07	-	-	-
D	D.1	0.11	0.19	1.62	0.012	0.05	0.46	-	-	-	-
E	E.1	0.11	0.18	1.39	0.011	0.04	0.15	0.20	-	-	-
	E.2	0.11	0.21	1.51	0.012	0.03	0.46	-	0.03	-	0.007
	E.3	0.10	0.07	1.24	0.014	0.91	0.03	0.20	-	-	-
F	F.1	0.10	0.21	1.78	0.010	0.03	0.44	-	-	-	-
	F.2	0.11	0.11	1.23	0.014	0.88	0.04	0.20	-	-	-
	F.3	0.11	0.23	1.49	0.009	0.03	0.66	-	-	-	-
		DP780									
A	A.2	0.15	0.18	2.08	0.011	0.04	0.26	-	-	0.02	-
C	C.3	0.15	0.21	1.97	0.023	0.03	0.25	-	-	-	-
	C.4	0.15	0.21	1.91	0.016	0.03	0.19	-	0.03	-	-
D	D.2	0.14	0.30	1.75	0.012	0.04	0.52	-	-	0.02	-
F	F.4	0.16	0.17	1.72	0.013	0.03	0.32	0.16	-	-	-
	F.5	0.14	0.30	1.76	0.010	0.03	0.50	-	-	0.02	-
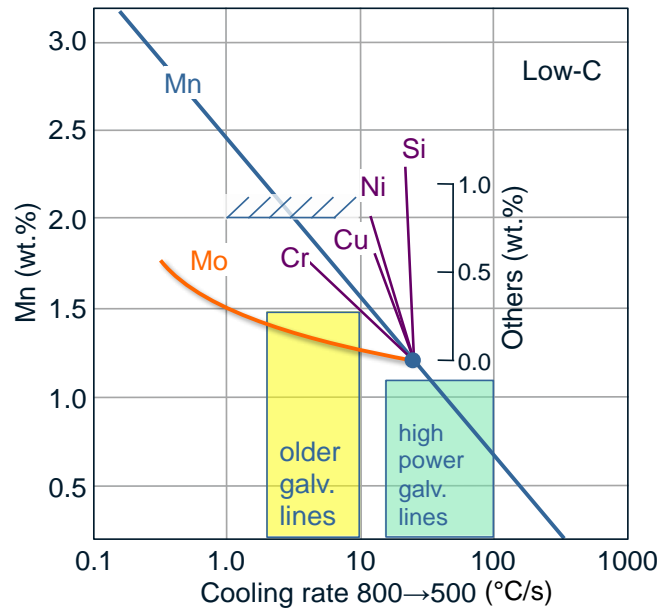
Figure 2. Influence of Mn and other bulk alloying elements on the critical cooling rate for producing low-C dual phase steel on galvanizing lines [3].

A particular advantage of adding Mo to hot dip galvanized DP steels refers to the coating quality. Elevated amounts of Mn, Si or Cr can cause problems of surface wetting and adhesion of the zinc layer. This is related to the fact that these elements can enrich at the surface during intercritical annealing, forming surface oxides. The presence of an oxide layer lowers the wettability of the surface. Mo on the contrary shows no tendency to enrich and form an oxide layer at the surface. Therefore, Mo alloyed concepts such as E-I, E-III and F-II with significantly reduced Mn and Cr additions are superior concepts for hot-dip galvanizing processes.

The bulk alloying concepts of DP780 grades are much more similar throughout the supplier base. This is because the quantities of HDG DP780 demanded by the market thus far have been quite limited. Therefore, steelmakers can run the production exclusively on the more capable galvanizing lines allowing a reduction in the amount of hardenability alloys.

Microalloying with Nb, providing microstructural refinement, has been found to significantly improve bendability, particularly of DP780 steel [3]. This aspect will be detailed in a later section. Basically, it is sufficient to add a small amount of Nb to the otherwise unchanged alloy concept (A.2) to enable the improvement, as is indicated in Figure 3.
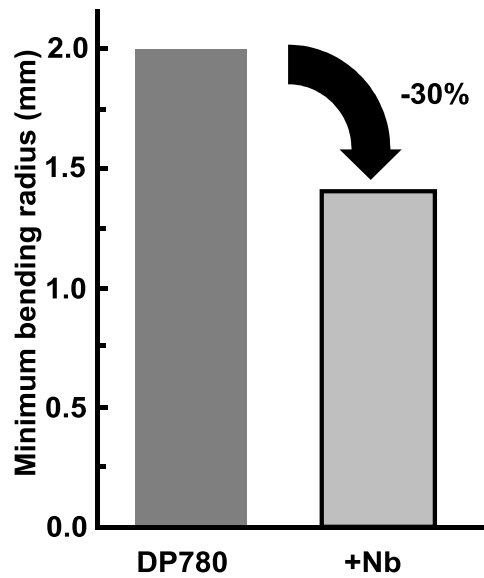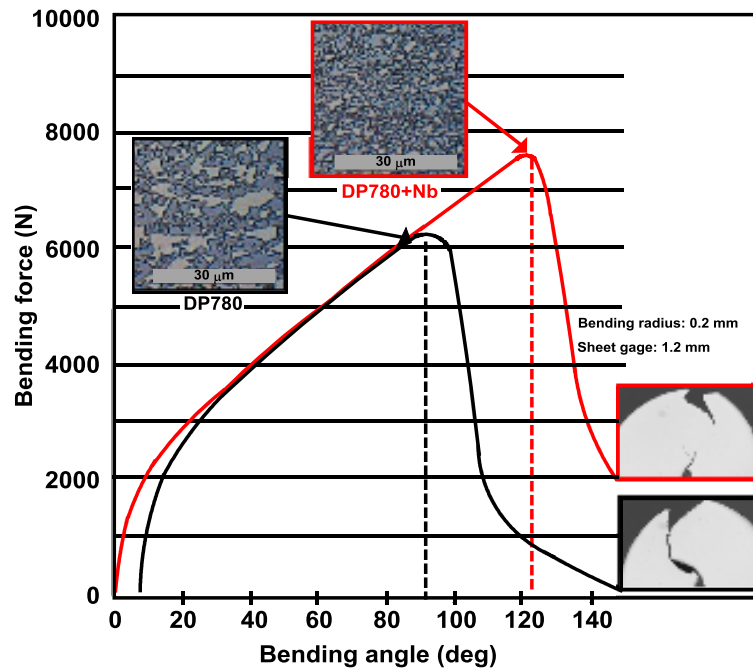
Figure 3. DP780 steel under 3-point bending conditions (acc. to VDA238) and 180°-bending before and after microstructural refinement (corresponds to steel A.2 in Table III) [4].

Cornerstones of a Novel Platform - Alloying Concept for Low-C DP Steels

An alternative to current mainstream alloy concepts for DP steels is indicated by strategy 2 in Figure 1, wherein the C content is principally limited to a maximum of 0.1% for the entire strength range. When pursuing such a low-C approach, it is important to consider the hardenability concept in detail. Reducing the C content brings the bainite nose forward, increasing the risk of forming bainite during holding at the zinc bath temperature, as is schematically demonstrated by Figure 4. It has been discussed already that increased additions of Mn and Cr, as well as a smaller addition of Mo, can delay bainite formation. Furthermore, microstructural refinement by Nb microalloying can assist the rapid formation of ferrite during cooling, thus promoting C enrichment in austenite. A higher austenite C content facilitates transformation into martensite rather than into bainite.

Based on these ideas, it was decided to develop an alloy platform concept that is strictly limited to a maximum of 0.1%C. The hardenability concept to be defined should provide:

- high robustness against process variations, resulting in low scatter of the specified mechanical properties;
- the possibility of producing the grade on galvanizing lines with somewhat different time-temperature characteristics;
- the possibility of producing increased sheet gages up to 2.5 mm;
- good quality of the galvanized surface;
- high resistance against edge cracking (high hole expansion ratio).
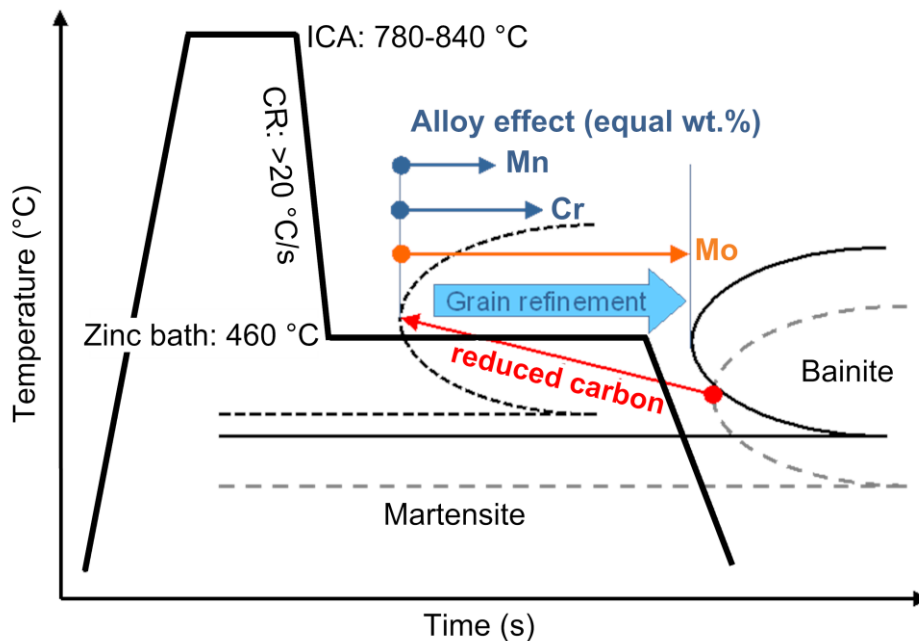

Figure 4. Alloying effects on bainite formation in low-C DP steel during a hot dip galvanizing cycle.

The qualification of respective alloy concepts has been done initially by laboratory simulation for the DP600 and DP780 grades. Thereafter, industrial trials have been initiated to verify the alloy concept under realistic production conditions in the two hot-dip galvanizing lines available at Salzgitter Flachstahl GmbH. Subsequently, the established industrial concept was tested regarding press shop performance by stamping various parts in serial production dies.

Microstructural Refinement in DP Steels and the Essence of Nb Microalloying

Several prior research efforts have indicated that microstructural refinement in DP steels not only enhances strength, but also is beneficial to secondary (ie. non-specified) cold forming properties, such as bending, stretch flanging or hole expansion.

For instance, Calcagnotto et al. [5] demonstrated that severe grain refinement in DP steel could raise yield as well as tensile strength by about 20%. This strength surplus provides a higher safety margin with respect to the minimum specified values on the one hand and on the other hand, the strength surplus provided by grain refinement allows a reduced martensite content in the dual phase microstructure and hence increased elongation.

Grain refinement of the dual phase microstructure was shown to have a considerable positive effect on the bending behavior of cold rolled DP steel. Figure 3 demonstrates that the grain-refined steel (A.2) supports a higher bending force at an increased bending angle. The non-grain-refined steel fails at a bending angle of around 90° so that the production of typically U-shaped profiles is problematic. The grain-refined steel on the contrary offers a sufficient margin for the forming process thus offering clearly improved process robustness. Furthermore, the grain-refined DP steel allows a tighter minimum radius for 180°-bending showing an improvement of around 30% (Figure 3).

Grain refinement of the final dual phase microstructure is for a large part inherited from the hot rolled microstructure. The prior hot rolled strip microstructure can be principally adjusted to be either ferritic-pearlitic or bainitic. The occurrence of either is mainly related to the coiling temperature. Bainitic hot rolled strip will be typically finer grained than ferritic-pearlitic hot rolled strip. Yet Nb microalloying provides microstructural refinement, irrespective of the coiling temperature.

Irrespective of whether or not the processing route for producing DP steel is adapted to Nb microalloying, the effect of Nb is always noticeable. Therefore, it is important to perform a holistic consideration of possible effects of Nb during the entire process chain and then to optimize individual processing steps.

The most prominent effect of Nb is recrystallization delay during hot rolling leading to pancaking of the austenite. The pancaked austenite transforms into a fine-grained polygonal ferrite and dispersed pearlite islands under conventional coiling conditions. This condition is usually chosen if the hot strip is destined for further cold rolling followed by intercritical annealing. This refined ferritic-pearlitic microstructure is inherited by the final material producing a finer grained ferrite matrix embedding smaller martensite islands, as shown in Figure 5, where a Nb microalloyed variant is compared to a Nb-free one for a coiling

temperature of 680 °C. Comparing these microstructures, one has to state that the effect of Nb is partly overlaid by the effect of Si, the Si content being higher in the non microalloyed steel and thus promoting ferrite formation.
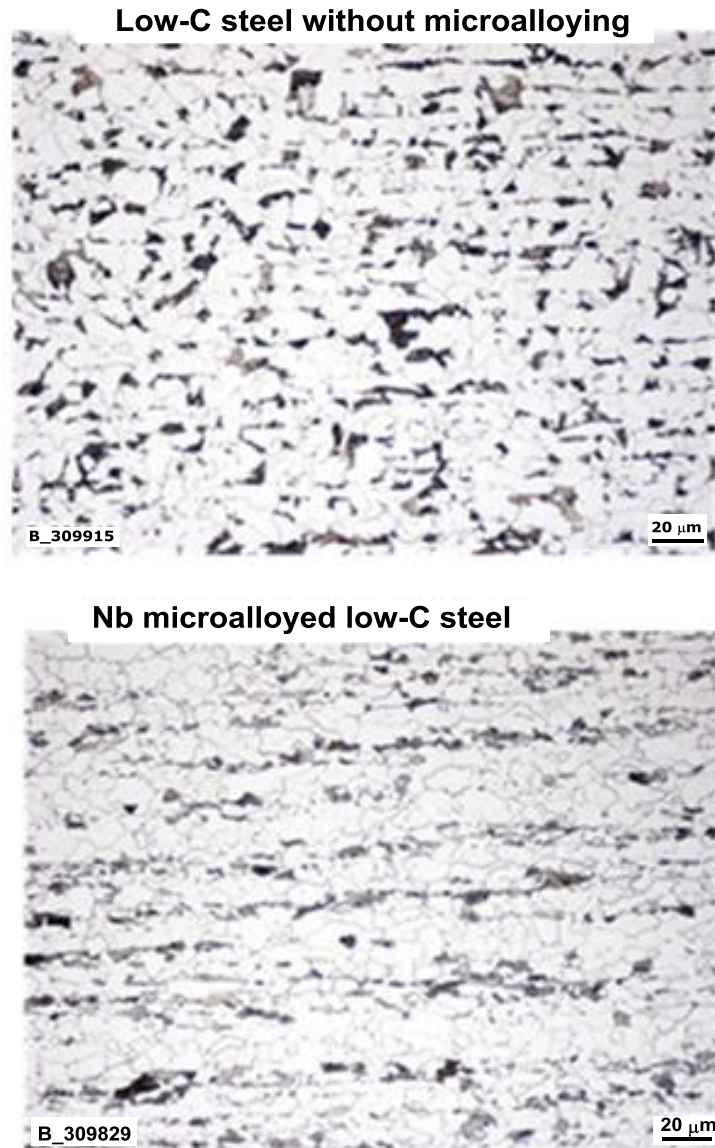
Low-C steel without microalloying

Nb microalloyed low-C steel

Figure 5. Effect of Nb microalloying on ferritic-pearlitic microstructure of low-C DP steel after coiling at 680 °C.

Low-C steel without microalloying

Nb microalloyed low-C steel

Figure 6. Effect of Nb microalloying on bainitic microstructure of low-C DP steel
after coiling at 500 °C.

As mentioned earlier, an option for producing cold rolled DP steel is coiling the hot strip in the temperature range of 500 to 550 °C. This results in a bainitic microstructure of the hot strip, as shown in Figure 6, for the same low-C chemistry. This observation agrees with results published by Pichler et al. [6] and was also reported by [7]. For example, the CCT diagram shown for the Nb microalloyed variant in Figure 7 demonstrates the resulting microstructures for two coiling temperatures. Because a significant portion of Nb remains in solid solution under this coiling condition, it is available for precipitation during subsequent intercritical annealing [8].

108

When the coiling condition is set directly to produce DP steel from the rolling heat (ie. hot rolled DP steel), the effect of the pancaked austenite is to enhance ferrite nucleation, due to the larger total austenite grain boundary area [9]. This allows obtaining the desired amount of ferrite in a shorter time and thus helps optimizing the cooling path on the run-out table. Naturally, ferrite as well as martensite grain sizes are also refined. Such grain refinement has been found to increase the tensile strength of hot rolled DP steel by around 150 MPa and thus provides an efficient possibility for upgrading DP600 towards DP780.

Grain refinement and particularly bainitic transformation lead to a significant increase of yield strength of the hot strip, which has to be taken into consideration with respect to the subsequent cold rolling operation. Since the addition of Nb leads to grain refinement, the yield strength of conventional ferritic-pearlitic hot strip will be increased [6]. The yield and tensile strength of the cold rolled full hard strip are also increased compared to Nb-free material and depends on the cold roll reduction. When the hot strip is coiled for a bainitic microstructure, the yield strength can become so high that typical cold reduction schedules might exceed the rolling force limits of the mill. Therefore, hot strip with bainitic microstructure is not recommended when a high level of cold reduction is targeted. However, such strip could be directly hot dip galvanized, ie. either without any or with a limited cold reduction.
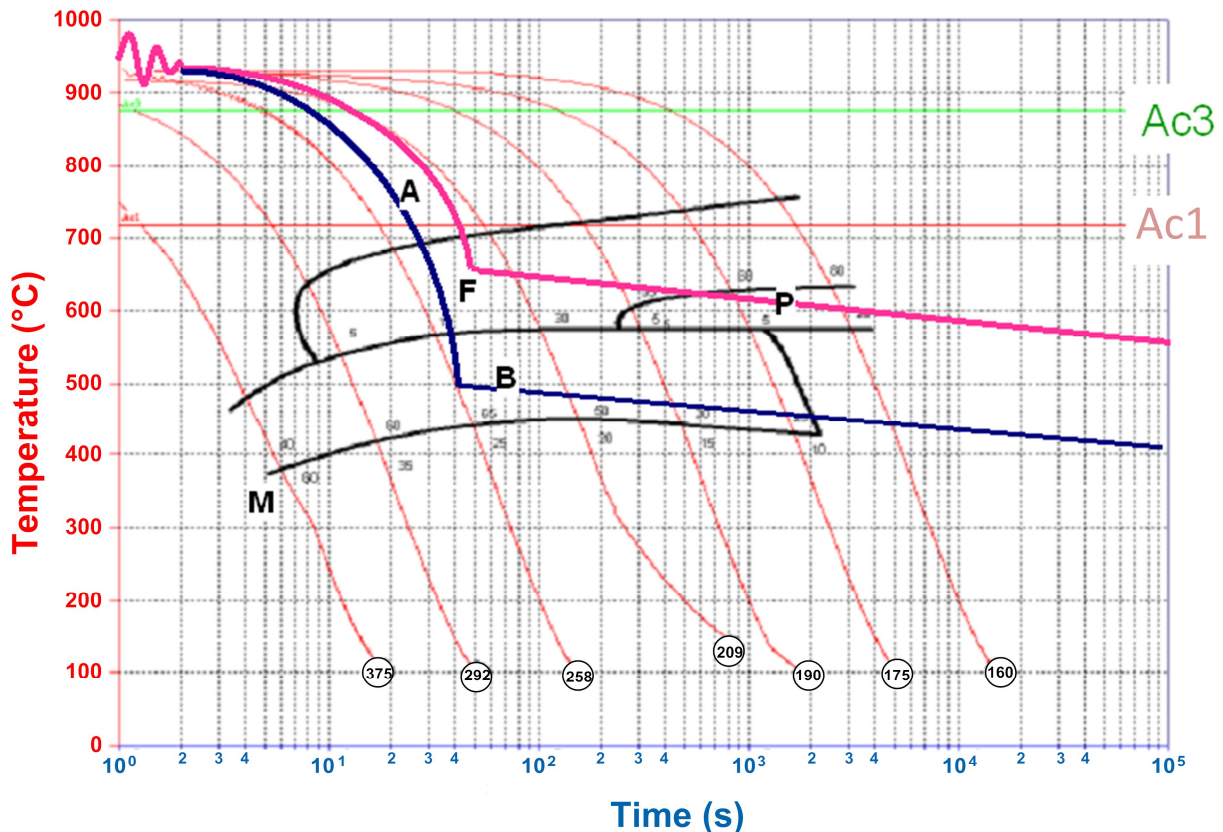

Figure 7. CCT diagram of the Nb microalloyed low-C steel and cooling curves after finishing.

Nb microalloying has multiple effects with regard to the metallurgical mechanisms occurring during the intercritical annealing cycle [6,9]. Nb precipitates usually exist in the hot rolled strip when coiling at conventional temperatures in the range of 600-650 °C. Any Nb remaining in solid solution has the potential to precipitate *in situ* during the annealing cycle. The precipitation potential is enhanced when coiling temperature is lowered to 500-550 °C as more Nb is retained in solid solution [8]. This coiling condition also results in a very fine-grained bainitic microstructure. Experiments have shown that in either case Nb precipitation is practically complete after reaching the intercritical soaking phase. For the bainitic coiling condition most of the Nb is retained in solid solution, which then precipitates during the heating cycle as very fine particles with a relevant contribution to strengthening. The existing precipitates produced in larger amounts after conventional coiling conditions are subjected to some degree of coarsening during the heating phase of the annealing cycle and are hence less strength effective.

Nb delays the recrystallization during reheating of cold deformed ferrite either by precipitation or by solute drag of Nb on the grain boundaries. Experience with Nb alloyed DP steel indicated that the recrystallization temperature is typically raised by around 20 °C as compared to the same base analysis without Nb addition. The retarded recrystallization also preserves dislocation networks that act as nucleation sites for austenite. Hence austenite formation should be accelerated in Nb alloyed DP steel [10]. Furthermore, the grain-refined microstructure of an Nb microalloyed strip additionally provides an increased grain boundary area for nucleation sites for austenite when annealing in the intercritical temperature range. Measurements have indeed confirmed that at a given intercritical annealing temperature, the amount of austenite in the Nb added alloy is higher compared to the Nb-free base alloy [10]. During the soaking phase, C partitioning is accelerated and is more homogeneous within the austenite from the finer grained microstructure of the Nb alloyed strip, due to the shorter diffusion distances in the smaller grains.

By slow cooling to the (sub-Ae_3) quenching temperature, a defined amount of new ferrite is being nucleated from the existing austenite. Again, the refined microstructure of Nb microalloyed steels exhibits quicker kinetics for this ferrite formation. A consequence of the enhanced amount of ferrite is that the remaining austenite phase is further enriching in C. This means that the hardenability of the C-enriched and smaller grained austenite is improved. With regard to mechanical properties, Nb microalloyed DP steel should have less but stronger martensite as a second phase when subjected to a given annealing cycle, as compared to the Nb-free base alloy.

Laboratory Development and Pre-qualification of Low-C DP Platform Concepts

The development stages described here have the purpose of qualifying different alloy concepts which all have low C content (max. 0.1%) in common. The various trial concepts have an increased addition of Nb, partly in combination with other microalloying elements such as Ti and B (Table IV). The content of bulk alloying elements such as Si (0.25%), Mn (1.85%) and Cr (0.4%) were kept constant. Other elements were not employed. The aim was to clarify how these alloy concepts, in combination with adapted hot and cold rolling conditions, as well as annealing parameters, influence the microstructure and processing properties of DP steel.

All five microalloyed concepts, as well as a microalloy-free reference variant, were finish rolled at 920 °C to a hot rolled sheet gage of 3 mm. Subsequently, all samples were coiled at both 500 °C and 680 °C, resulting in a bainitic or ferritic-pearlitic microstructure, respectively. The strength data and microstructural characteristics for all combinations are summarized in Table V. It is evident that increasing the Nb content from 0 to 0.03% results in the expected microstructural refinement, irrespective of the coiling temperature. The consequence is an increase of the flow stress by about 50 MPa (see also Figure 8). Further addition of Ti and/or B to the higher Nb alloyed variant does not lead to significant changes in the hot strip properties. Comparing W-3, W-4 and W-6, one has to consider that the effective B content (B in solid solution) of alloy W-4 is significantly lower than 0.003 due to the absence of Ti, ie. some of the B will be tied up with N.

Table IV. Base Alloy Concept and Microalloying Options for Laboratory Trials and Industrial Pre-qualification (wt.%)

Base alloy	Microalloy option	Nb	Ti	B
<0.1%C	W-1	0.00	0.00	0.000
0.25%Si	W-2	0.015	0.00	0.000
1.85%Mn	W-3	0.030	0.00	0.000
0.40%Cr	W-4	0.030	0.00	0.003
50 ppm N	W-5	0.030	0.030	0.000
100 ppm P	W-6	0.030	0.030	0.003

Each of the hot rolled variants was stepwise cold rolled on a laboratory rolling mill to a total cold reduction of 60%. The yield strength was determined by tensile testing for the different reduction stages. The flow curves are shown in Figure 9. Generally, strong work hardening is observed with increasing cold reduction. The group of flow curves originating from the bainitic coiled material (cooling option HR1) is consistently at least 150 MPa higher than the ferritic-pearlitic material (cooling option HR2). Only the flow curves of option HR2 were finally used to calculate cold reduction schedules for industrial trials since the material coiled under option HR1 was too strong for efficient cold rolling.

Table V. Properties and Microstructural Characteristics of Hot Strip (3 mm)
Under Two Coiling Conditions

HR1 (FRT: 920 °C CT: 500 °C)	W-1 (Nb free)	W-2 (+Nb)	W-3 (++Nb)	W-4 (++Nb+B)	W-5 (++Nb+Ti)	W-6 (++Nb+Ti+B)
YS (MPa)	480	512	533	564	553	525
TS (MPa)	612	645	679	706	682	741
Grain size (ASTM)	12.5	13.5	13	13	12.5	13.5
Ferrite (%)	25	15	25	15	15	10
Pearlite (%)	15	5	5	5	5	5
Bainite (%)	60	75	65	70	75	70
Martensite (%)	0	5	5	10	5	15
HR2 (FRT: 920 °C CT: 680 °C)	W-1 (Nb free)	W-2 (+Nb)	W-3 (++Nb)	W-4 (++Nb+B)	W-5 (++Nb+Ti)	W-6 (++Nb+Ti+B)
YS (MPa)	310	345	363	348	386	366
TS (MPa)	464	485	495	483	497	496
Grain size (ASTM)	10	11	11	10	11	10
Ferrite (%)	75	85	78	78	78	85
Pearlite (%)	25	15	22	22	22	15
Bainite (%)	0	0	0	0	0	0
Martensite (%)	0	0	0	0	0	0

In a separate development project, a processing route allowing the direct annealing and galvanizing of bainitic coiled (~ 500 °C) hot strip has been designed using a modified analysis of variant W-6. By this route hot dip galvanized DP steels in the gage range of 2 to 3 mm, having minimum yield and tensile strength of 330 MPa and 580 MPa, respectively could be successfully produced. The details of this development will be published elsewhere.
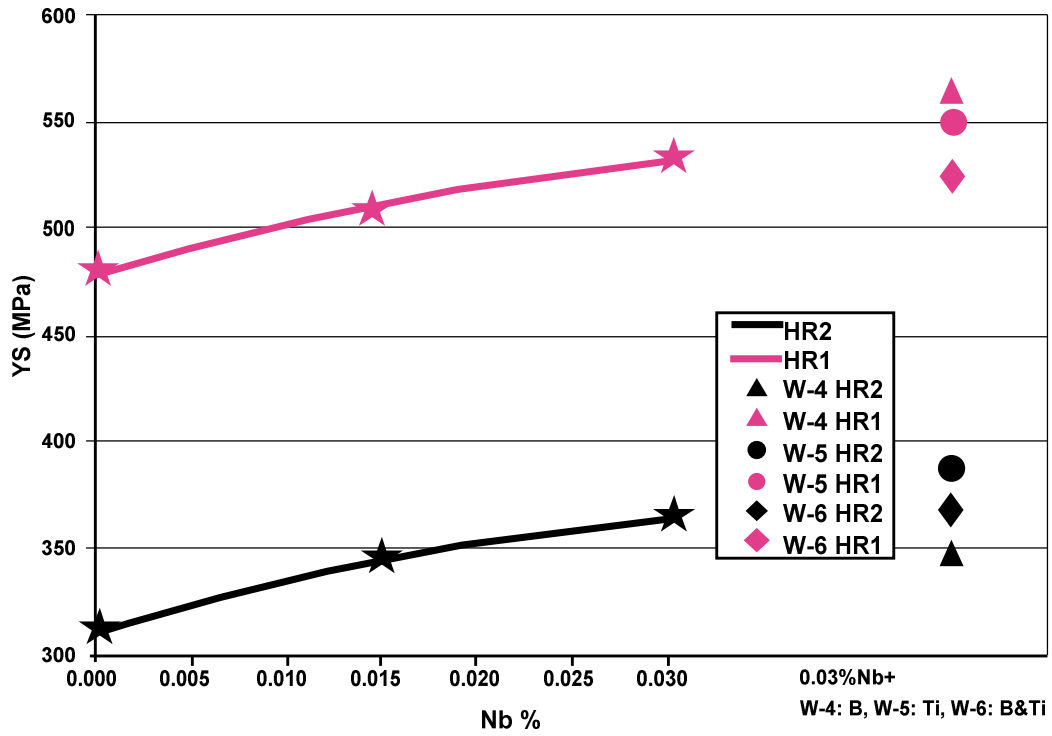
Figure 8. Effect of Nb and other microalloying elements on the yield strength of hot rolled 3 mm strip using different coiling temperatures.
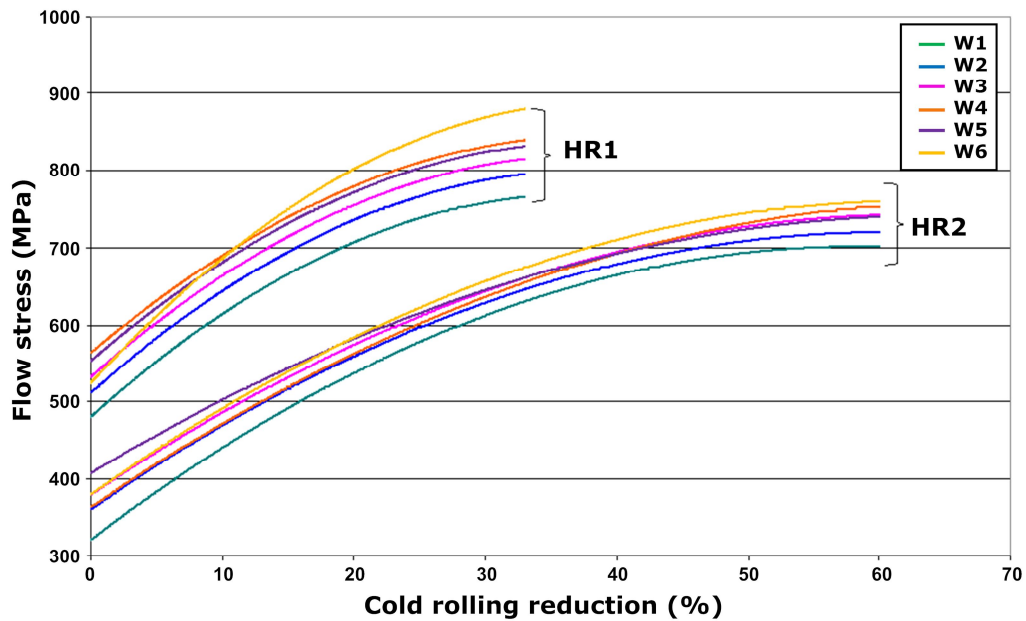
Figure 9. Influence of cold reduction on flow stress for two coiling conditions.

113

The further development process considered only cooling variant HR2 in combination with the analytical variants W-2 (0.015%Nb) and W-6 (0.030%Nb +Ti+B), as well as the non-microalloyed reference variant W-1. With these it had to be clarified which cold reduction and which annealing temperature program would deliver the best properties. However, one has also to consider that, due to the strong cold working, the tandem mill is exposed to higher loads. Thus, the cold roll reduction has to be kept as small as possible.

Figure 10 shows two CCT diagrams which were calculated using JMatPro® [11]. It demonstrates schematically for the Nb microalloyed variant W-3 that cold reduction (in this case 57%) results in an accelerated formation of ferrite. As an approach to simulate this influence, the grain size was varied from ASTM no. 9 to ASTM no. 14 for the cold-rolled material. In order to reasonably study this effect, samples of 2.0 mm thickness (33% cold reduction) as well as 1.3 mm thickness (57% cold reduction) were annealed by time-temperature cycles that correspond to the characteristics of the available two (horizontal and vertical) galvanizing lines. According to Figure 11 these lines are characterized by:

- High annealing temperature, short holding period and moderate cooling rate (horizontal line, HDG1);
- Lower annealing temperature, long holding time and accelerated cooling (vertical line).

In the vertical line (HDG2) there is the additional possibility of cooling the strip to below 300 °C before the zinc pot. By rapid induction heating, the strip can then be reheated to the required zinc bath temperature.

It turned out that a cold reduction of 57% is sufficient to obtain the desired microstructure as well as mechanical properties when the annealing and cooling strategy is appropriately adjusted. This applies for both time-temperature cycles, ie. those for the vertical as well as horizontal lines.
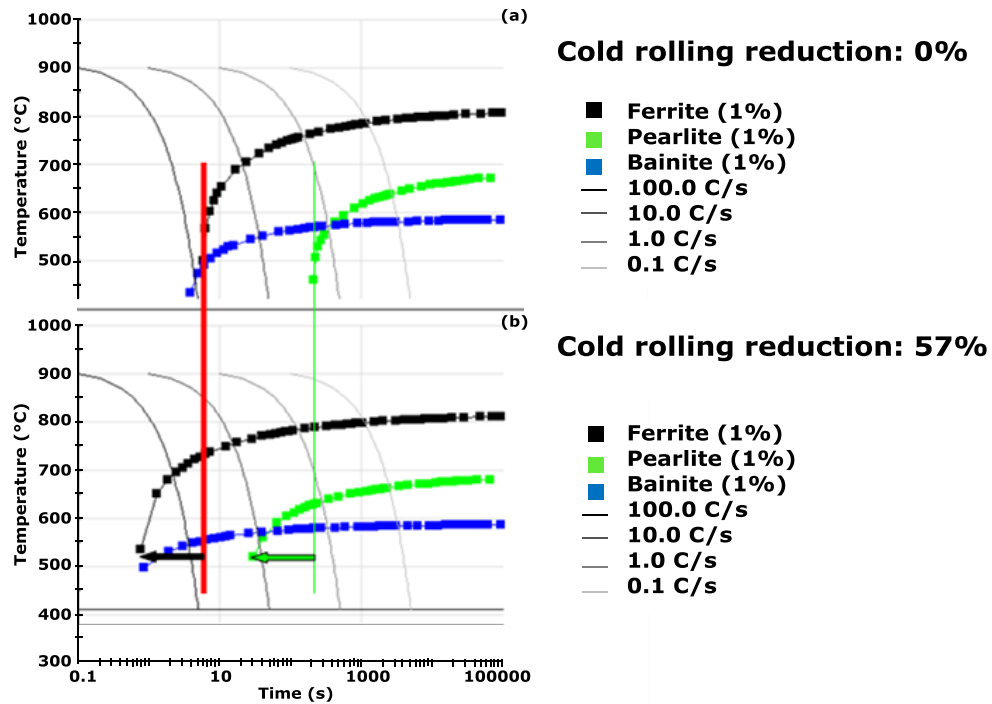
Figure 10. Influence of cold reduction on phase formation in variant W-3, calculated using JMatPro® [11].
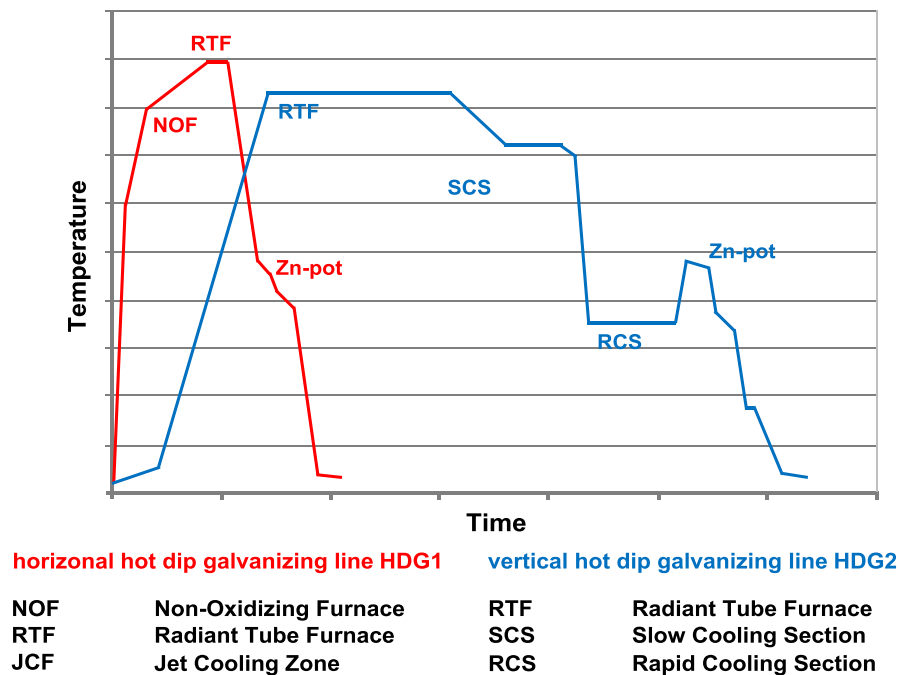

Figure 11. Typical annealing cycles of the two hot dip galvanizing lines used by Salzgitter Flachstahl GmbH for production of DP steel.

Industrial Implementation and Results

Large-scale trials were conducted on both hot dip galvanizing lines using strip gages between 1 and 2 mm and strip widths up to 1500 mm. The hot rolling was according to condition HR2 and the cold reduction varied between 40 and 60%. With regard to the chemical composition, the coils represented concepts W-1, W-2 and W-6. Particularly, the adaption of furnace operation conditions, as well as cooling intensity to the line speed, assured that the simulated optimum parameters could be achieved. The obtained results, with respect to mechanical properties and microstructural characteristics, are summarized in Table VI.

Table VI. Properties and Microstructural Characteristics of Cold Rolled Strip
(Cold Reduction 57%) for the Two Different Galvanizing Cycles

Mech. properties in Transverse direction	HDG1			HDG2		
	W-1 (Nb free)	W-2 (+Nb)	W-6 (++Nb+Ti+B)	W-1 (Nb free)	W-2 (+Nb)	W-6 (++Nb+Ti+B)
YS (MPa)	336	392	537	317	384	497
TS (MPa)	560	655	856	525	626	783
A80 (%)	26	22	15	28	23	18
n-value	0.17	0.16	0.12	0.17	0.15	0.11
Grain size (ASTM)	13	13	13	11	11	12
Ferrite (%)	70	60	65	80	75	65
Bainite (%)	10	20	0	5	15	0
Martensite (%)	20	20	35	15	10	35
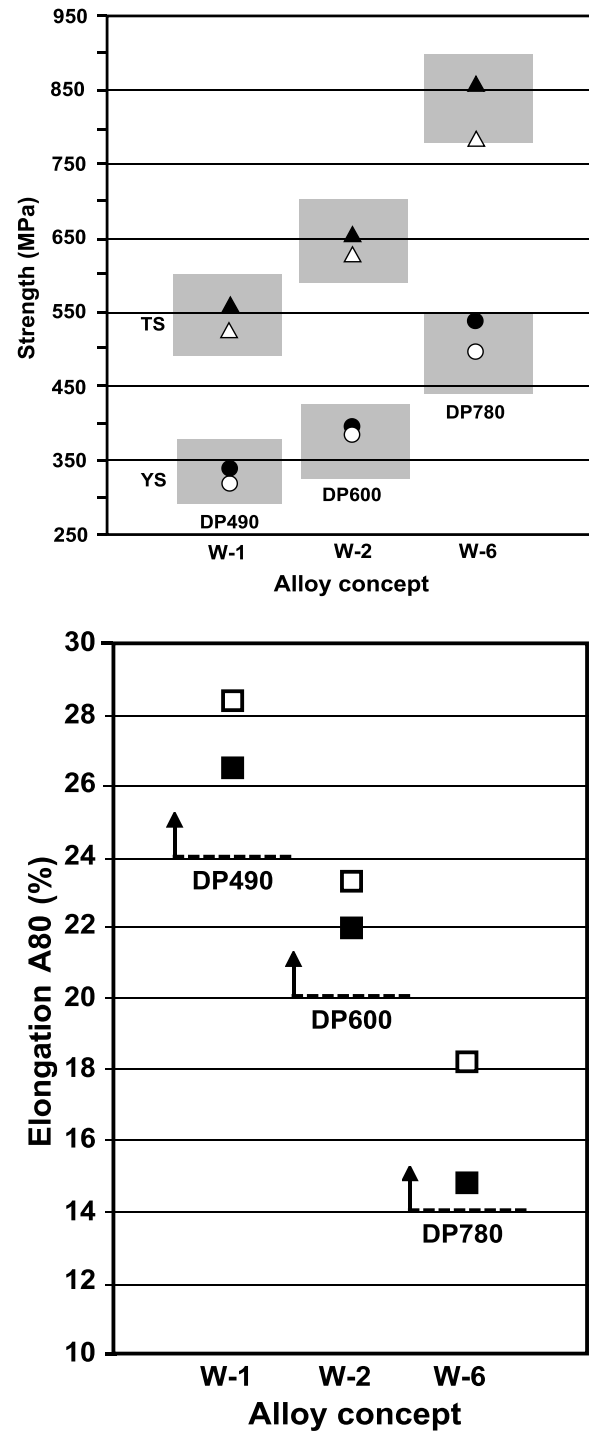
Figure 12. Mechanical properties of produced coil materials in relation to property ranges specified by VDA239 (filled symbols: horizontal HDG1, open symbols: vertical HDG2).

Figure 12 summarizes the obtained strip properties after treatment in the vertical hot dip galvanizing line. The base analysis consisting of 0.09%C, 0.25%Si, 1.85%Mn and 0.4%Cr in combination with stepwise increased addition of Nb, as well as Ti and B (W-6), succeeds in generating the strength classes of 500, 600 and 800 MPa. Using the process provided by the horizontal galvanizing line, a similar gradation of strength is obtained whereby the actual strength is approximately 40 MPa higher in each grade as compared to the vertical line.

Press Shop Performance

The performance of the industrially produced material was verified for several commercial car body parts having gages between 1 and 2 mm, as described in Table VII. The press shop trials were performed using production dies that were not specifically tuned to the new material. Although in regular production, softer HSLA steels with somewhat increased gage are being stamped, the majority of the trial material could be successfully formed into parts. Due to the increased base strength of the trial material being further enhanced by cold working and bake hardening, a weight reduction potential in the range of 10 to 20% is achievable compared to the HSLA material.

Two examples of a successful trial part made from the grade DP600 (option W-2) are shown in Figure 13 and 14. In the formed part the actual strength after drawing, as well as after drawing and baking, was determined. Therefore, small tensile samples with a gage length of 15 mm were taken at appropriate positions taking the original rolling direction into account. Figure 14 indicates this procedure, as well as the sample geometry for another trial part, representing a seat cross member that was manufactured from DP600 in 1 mm gage.

Table VII. Die Trial Schedule for Various Press Parts and Strength Options
(Thickness Reduction Compared to the HSLA Material as Indicated)

Option	Grade acc. to VDA239	Gage (mm)	Press part	OEM	Configuration	Original material (mm)
W-1	CR290Y490T-DP	1.0	Seat cross member	VW Golf PQ35	Double attached	HSLA 1.25
W-2	CR330Y590T-DP	1.0	Seat cross member	VW Golf PQ35	Double attached	HSLA 1.25
W-2	CR330Y590T-DP	2.0	A-pillar lower outside	Audi A5 Cabriolet	Double attached	HSLA 2.25
W-2	CR330Y590T-DP	1.0	Reinforcement D-pillar	Audi A6 Avant	Double attached	HSLA 1.20
W-3	CR440Y780T-DP	2.0	Rail front	N.N.	Single part	HSLA 2.00

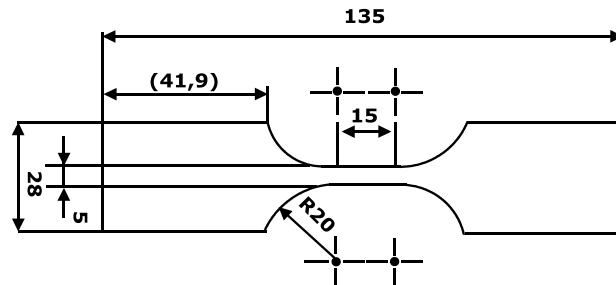Figure 13. A-Pillar lower outside made from 2 mm CR330Y590T-DP (option W-2).

Figure 14. Seat cross member made from 1 mm CR330Y590T-DP with marked samples for tensile tests and schematic tensile test specimen showing dimensions.

Comparison of actual mechanical properties, ie. after forming and baking versus the original properties in the as delivered sheet, is provided in Table VIII for three different trial parts. The following observations can be made:

1. The as-delivered material reveals a very high isotropy for both yield and tensile strength, which is particularly favorable for stretch forming operations;
2. After forming, yield strength is significantly increased by work hardening. The amount of work hardening depends on the severity of deformation and the direction. The magnitude of the work hardening effect can bring an increase of over 200 MPa in yield strength and of around 50 MPa in tensile strength;
3. The bake hardening effect was also found to be rather high as is typical for DP steels. In some cases the yield strength increase by this effect is in the order of 100 MPa while its influence on the tensile strength is rather limited.

Table VIII. Actual Measured Properties in Trial Parts after Stamping (Work Hardening) and Baking Compared to the Original Sheet Properties

Stamped part	Condition	Yield strength (MPa)		Tensile strength (MPa)	
	Orientation to rolling direction	transverse	parallel	transverse	parallel
Seat cross member	As delivered sheet (1 mm)	377	374	660	658
	Pressed part (PP)	570	563	669	731
	PP after baking (180 °C / 20 min)	658	622	687	697
A-pillar lower outside	As delivered sheet (2 mm)	362	363	620	622
	Pressed part (PP)	447	385	626	622
	PP after baking (180 °C / 20 min)	566	560	644	641
Reinforcement D-pillar	As delivered sheet (1 mm)	377	374	660	658
	Pressed part (PP)	605	580	702	645
	PP after baking (180 °C / 20 min)	639	659	678	695

Resistance against Edge Cracking

DP steels generally allow forming of complex shapes due to their high elongation. However, practical experience repeatedly revealed unexpected failure, such as sheared edge splitting during flanging operations, as indicated in Figure 15. Highly localized strain leads to the initiation of micro damage at the ferrite-martensite phase boundary. The induced micro damage subsequently grows into a propagating crack under the applied stress. The larger the size of an initial damage site, the smaller is the critical stress required for crack propagation. A crack typically propagates along the ferrite-martensite interface. Hence, a refined microstructure and non-agglomerated martensite islands, in particular, should characterize optimized DP steel.

Another significant influence on the hole expansion ratio of DP steel originates from the difference in hardness between the soft ferrite phase and the hard martensite phase. Hosoya et al. [12] have demonstrated this effect by performing different low temperature tempering treatments to quenched DP steel in the strength range of 800 to 1000 MPa. Their results suggest a linear relationship between the hardness difference and the hole expansion ratio. Therefore, the volume fraction of martensite in the steel appears to be of less significant impact, provided that its distribution is homogeneous.

The developed low-C microalloyed DP steel concept principally provides all the mentioned prerequisites for high resistance against edge cracking:

- Nb microalloying provides general refinement of ferrite and martensite, resulting in relatively short hard-to-soft interfaces;
- Reduced segregation and pearlite banding due to sub-peritectic alloy design in combination with optimized coiling conditions after hot rolling avoid martensite agglomeration;
- The low overall C content leads to reduced C enrichment in austenite during intercritical annealing (for a given austenite fraction, which in a lower C steel will occur at a higher annealing temperature) and hence softer martensite after quenching resulting in a smaller hardness difference between ferrite and martensite phases.

Benchmarking of the newly developed Nb microalloyed DP600 grade (variant W-2) versus non-optimized reference materials of the same grade using hole expansion testing according to ISO-TS 16630 indeed revealed a clearly superior performance. The hole expansion ratio of the developed low-C steel is above 60%, while that of existing non-optimized DP steels of 590 MPa strength level shows only values of around 40% (Figure 16). Although the hole expansion ratio is currently not specified by VDA239, it is an important criterion in several automotive markets. Accordingly, it can be expected that the hole expansion ratio may be included in VDA239 during a future revision of this specification.
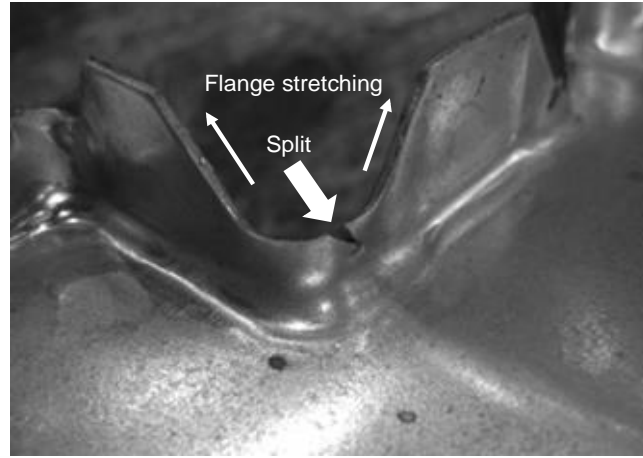
Figure 15. Sheared edge cracking phenomenon in DP steel under stretch flanging conditions [13].
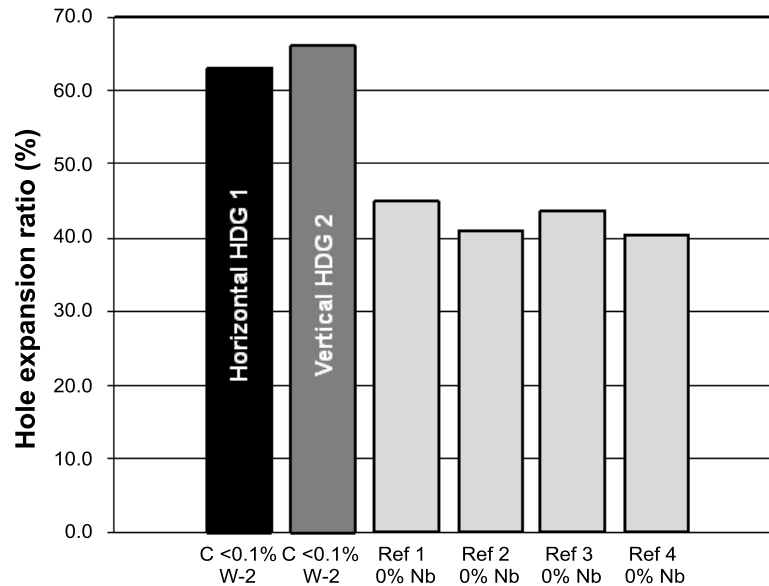
Figure 16. Performance of newly developed low-C Nb microalloyed DP steel in ISO-TS 16630 hole expansion test in comparison to non-optimized reference material.

Conclusions

A low C based modular alloying concept for hot dip galvanized DP steels has been developed and successfully tested on press stamped parts using commercial dies.

Based on laboratory simulations, a common alloy platform based on low C, Si, Mn and Cr was defined. Systematic variation of the Nb microalloy content, as well as selective additional microalloying of Ti and B allowed producing DP steels in the strength range of 500 to 800 MPa.

The concept was shown to be robust under greatly varying processing conditions in the cold rolling and galvanizing operation. This allows running the same alloy concept through two rather different galvanizing lines. It is also possible to produce galvanized DP steel with a large thickness. The mechanical properties of all grades safely meet the requirements of the VDA239 specification. Very good isotropy of properties could be also verified. Cold working and bake hardening were observed to provide a substantial strength increase in finished press stamped parts.

The developed DP steel furthermore exhibited a substantially improved hole expansion behavior. This enhances the resistance against cracking under particular forming operations such as stretch flanging or bending.

References

1. Anonymous, VDA 239-100 Sheet Steel for Cold Forming, Publication "Verband der Autoindustrie VDA," 20.08.2011, www.vda.de.

2. T. Dettinger et al., VDA Werkstoffblatt 239: "An Approach for a Global Sheet Steel Specification," *Proceedings of the 3rd International Conference on Steels in Cars and Trucks,* Salzburg (2011), 273.

3. K. Hashiguchi et al., "Effects of Alloying Elements and Cooling Rate After Annealing on Mechanical Properties of Dual Phase Steel Sheet" (Kawasaki Steel Technical Report No. 1, September 1980), 70.

4. P. Larour et al., "Influence of Post Uniform Tensile and Bending Properties on the Crash Behaviour of AHSS and Press-hardening Steel Grades," *Proceedings of the IDDRG 2010 Biennial Conference*, Graz, Austria, (2010).

5. M. Calcagnotto, "Ultrafine Grained Dual-phase Steels" (Ph.D. thesis, Verlag Shaker, Aachen, 2010).

6. A. Pichler et al., "Advanced High Strength Thin Sheet Grades: Improvement of Properties by Microalloying Assisted Microstructure Control," *Proceedings of the International Symposium on Niobium Microalloyed Sheet Steel for Automotive Applications*, TMS, (2006), 245.

7. Y. Granbom, "Influence of Niobium and Coiling Temperature on the Mechanical Properties of a Cold Rolled Dual Phase Steel," *La Revue de Métallurgie,* 4 (2007), 191.

8. H. Mohrbacher, "Effects of Nb in Galvanized Advanced High Strength Steels for Automotive Applications," *Proceedings of Galvatech '07*, Osaka, (2007), 386.

9. W. Bleck, A. Frehn and J. Ohlert, "Niobium in Dual Phase and TRIP Steels," *Proceedings of the International Symposium Niobium 2001*, TMS, Orlando, (2001), 727.

10. O. Girina, N. Fonstein and D. Bhattacharya, "Effect of Nb on the Phase Transformation and Mechanical Properties of Advanced High Strength Dual Phase Steels," *Proceedings of New Developments on Metallurgy and Applications of High Strength Steels,* Buenos Aires (2008).

11. JMatPro® developed by Sente Software Ltd. http://www.jmatpro.com.

12. K. Hasegawa et al., "Effects of Microstructure on Stretch-Flange-Formability of 980 MPa Grade Cold-rolled Ultra High Strength Steel Sheets," *The Iron and Steel Institute of Japan International*, 44 (3) (2004), 603.

13. T. Hebesberger et al., "Dual-phase and Complex-phase Steels: AHSS Material for a Wide Range of Applications," in: *SCT 2008, Future Trends in Steel Development, Processing Technologies and Applications: Bringing the Automotive, Supplier and Steel Industries, Proceedings of the 2nd International Conference on Steels in Cars and Trucks*, 1st–5th June, 2008, Wiesbaden, ed. by Bernhard Fuchsbauer and Hans J. Wieland, (Düsseldorf: Verlag Stahleisen, 2008), 456-463.

THE EFFECT OF LOW LEVELS OF MOLYBDENUM IN HIGH STRENGTH LINEPIPE STEELS

C. Stallybrass[1], J. Konrad[1] and H. Meuser[2]

[1]Salzgitter Mannesmann Forschung GmbH, Ehinger Straße 200, 47259 Duisburg, Germany
[2]Salzgitter Mannesmann Grobblech GmbH, Wiesenstrasse 36, 45473 Mülheim, Germany

Keywords: Alloy Design, Low Alloy Steel, High Strength, Large-diameter Pipe, Molybdenum

Abstract

Heavy plates for large-diameter linepipes are produced using low-carbon microalloyed steels by thermomechanical rolling. In combination with accelerated cooling, this processing strategy has made it possible to achieve yield strength levels of 690 MPa and above in combination with attractive technological properties. While the focus in the case of high strength grades above the 485 MPa yield strength level was initially on heavy plate with moderate wall thickness, improved low-temperature toughness and weldability at higher wall thicknesses have gained importance in recent years. This has made it necessary to adapt the steel composition and the processing parameters in order to maintain the balance of properties.

The microstructure that is obtained after accelerated cooling from the homogeneous austenite depends on the steel composition and the cooling conditions. Alloying additions that retard ferrite formation are used in order to obtain a predominantly bainitic microstructure. Molybdenum is well known to be especially effective in this respect and is, therefore, used frequently in high strength linepipe grades at a level of 0.2% or higher. However, this leads to an increase of the carbon equivalent which impairs weldability. In an experimental investigation that was carried out at Salzgitter Mannesmann Forschung GmbH, three laboratory heats were cast with a variation of the molybdenum content up to 0.2%. Coupons were rolled down to a wall thickness of 25 mm followed by accelerated cooling. The plates were characterized with regard to their microstructure, tensile properties and low-temperature toughness. In addition, welding trials were carried out in order to assess the toughness in the heat affected zone and the influence of the molybdenum content. It was found that an addition of 0.1% molybdenum led to a strength increase while excellent levels of low-temperature toughness were maintained in the base material and in the heat affected zone.

Introduction

High strength linepipe steels offer an economic advantage compared to lower strength grades as they allow a reduction in wall thickness of the pipe at the same operating pressure. This leads to savings with regard to raw materials, transportation and field welding. Conversely, they allow an increase of the operating pressure at the same wall thickness. Since the first application of X80 large-diameter pipes more than 25 years ago, the combination of mechanical properties required by customers has become increasingly complex, due to the strong worldwide interest to develop remote natural gas resources in hostile environments. These can include pipeline operation under arctic conditions or in areas with ground movement. High deformability and low-temperature

toughness are therefore critical requirements in order to ensure pipeline safety. The optimization of the toughness has, therefore, been a strong focus of development.

Since the beginning of the 1980s, heavy plates, pipes and pipe bends of X80 with a minimum yield strength of 555 MPa have been developed and produced by Salzgitter Mannesmann Grobblech GmbH (SMGB) and EUROPIPE and have become daily business for both companies as long as the requirements are merely according to EN 10208-2 [1], API 5L [2] or equivalent. In recent years, however, the complexity of requirements for linepipe materials has increased steadily with regard to toughness and weldability. SMGB has reacted to these demands with continuous alloy and process development in cooperation with Salzgitter Mannesmann Forschung GmbH (SZMF) in order to offer economically feasible solutions and guarantee safe operation for these scenarios.
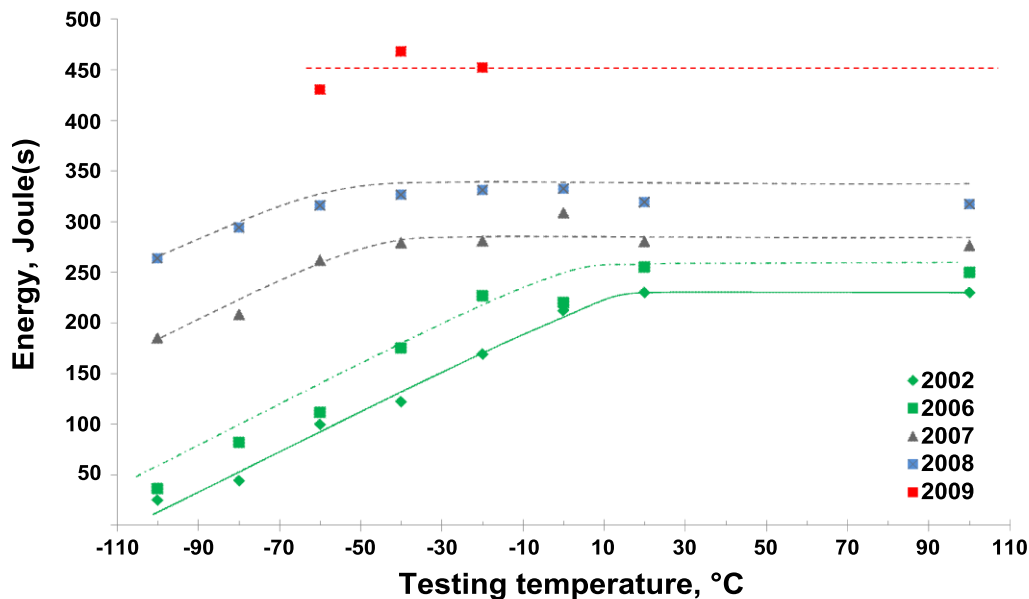
Figure 1. Development of Charpy properties and requirements for SMGB X80 plates since 2002 for a plate thickness between 25 and 30 mm.

The first X80 pipes were developed and produced according to specifications with a focus on elevated strength level with no specific requirements for low-temperature toughness in the base metal or the heat affected zone (HAZ). Since then, more and more emphasis has been placed on toughness [1-4]. Since 2002, SMGB has produced X80 plates above 25 mm wall thickness, which presented an additional challenge compared to the first X80 plates with lower wall thickness. The toughness development for X80 heavy plates since 2002 is illustrated in Figures 1 and 2. The requirements regarding minimum Charpy impact energy, as well as the shear area fraction in drop-weight-tear (DWT) tests, increased constantly. As shown in Figure 1, the upper shelf energy was raised from a level of 230-250 J at a testing temperature of 10 °C in 2002 to 2006 to 450 J at -60 °C in 2009. This went hand in hand with an improvement of the shear area in the DWT test, where the 85% shear area transition temperature was lowered from 0 °C down to -50 °C in 2009.
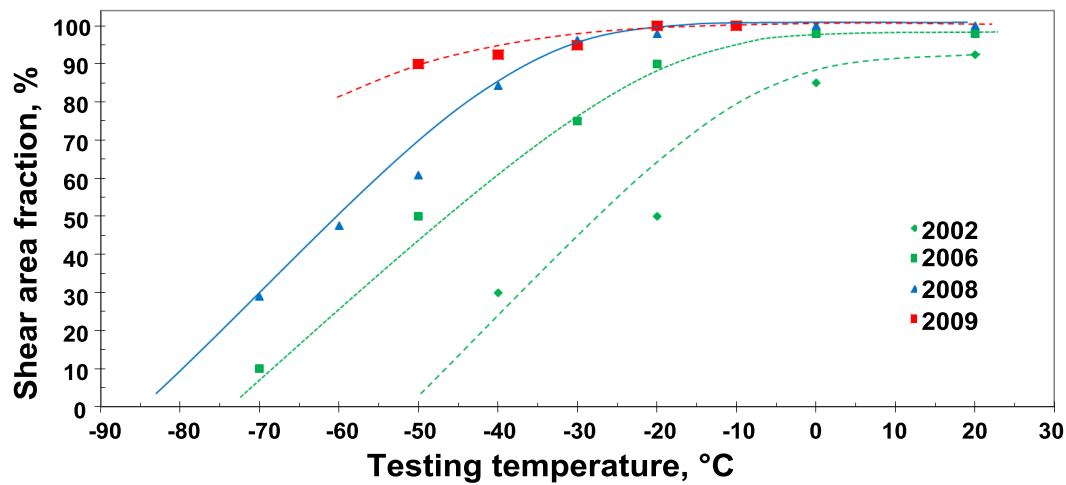
Figure 2. Development of shear area in the DWT-test for SMGB X80 plates since 2002 for a plate thickness between 25 and 30 mm.

Submerged-arc welding of large-diameter pipes requires a high heat input in order to achieve the welding speeds necessary for practical production. This leads to significant changes in the microstructure in the heat affected zone (HAZ) [5]. These include grain coarsening and the formation of carbon-rich constituents in a bainitic matrix in the vicinity of the fusion line. It has been demonstrated that the alloy design of the plate material in combination with the processing parameters during welding plays a key role for achieving a high level of HAZ toughness at low temperatures [6].

Continuous alloy and process development made it possible to achieve the X80 strength level and reduce the level of alloying elements at the same time. This is illustrated in Figure 3 which shows the reduction of the carbon equivalent range (CE_{IIW}) of X80 since 1990. The reduction of the CE_{IIW} improved the weldability while material costs were maintained in a reasonable range. Achieving the right balance of all material properties places tight restrictions on the alloy design and processing strategy at all stages of production.
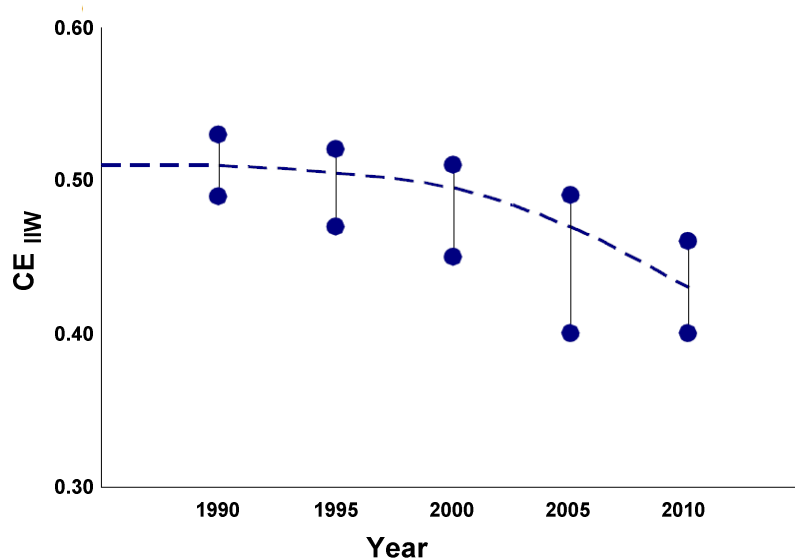
Figure 3. Development of the carbon equivalent CE_{IIW} of X80 since 1990.

Modern high strength heavy plates for large-diameter pipes are produced using low-alloy, low carbon steels which are microalloyed with niobium. They are generally produced by thermomechanical rolling (TMCP) followed by accelerated cooling. This processing route results in a microstructure that predominantly consists of bainite. The combination of high strength and high toughness in these steels is a result of the microstructure realized by TMCP and is strongly influenced by the alloy design and the processing conditions during heavy plate production.

In order to generate a predominantly bainitic microstructure, accelerated cooling has to begin above the temperature at which austenite transforms to ferrite, ie. above the Ar_3 temperature. This is a function of the steel composition and it has been shown that the addition of molybdenum lowers the Ar_3 temperature more effectively than the addition of the same level of copper, nickel or chromium [7]. Classically, molybdenum levels of 0.2% or above are used in high strength linepipe steels. This has a significant effect on alloying costs and on the weldability of high strength heavy plates compared to lower strength grades. However, it has also been shown that a combined addition of chromium and molybdenum is more effective in promoting bainite formation than an addition of only one of these elements [8]. It is also well known that molybdenum can lower the sensitivity to temper embrittlement of steels by reducing the enrichment of tramp elements at austenite grain boundaries. The aim of the present investigation was, therefore, to examine the effect of molybdenum additions of 0.1% and 0.2% in combination with 0.2% chromium on the mechanical properties and the weldability.

128

Production of Laboratory Heats and Rolling Trials

100 kg laboratory heats were produced by vacuum induction melting with a variation in the molybdenum content from 0 to 0.2%, as shown in Table I. The carbon equivalent (IIW) varied between 0.42 and 0.46. The ingots were sectioned into coupons and were rolled on a two-high rolling mill down to a wall thickness of 25 mm. Final rolling temperatures above the Ar_3 temperature were selected for all three compositions in order to ensure a predominantly bainitic microstructure after accelerated cooling, which was interrupted above the martensite start temperature at around 450 °C.

Table I. Composition of the Investigated Laboratory Heats (wt.%)

Steel	C	Si	Mn	Cr	Mo	Others	CE_{IIW}	Pcm
0 Mo	0.07	0.3	1.8	0.2	0.0	Nb, Ti	0.42	0.18
0.1 Mo	0.07	0.3	1.9	0.2	0.1	Nb, Ti	0.45	0.19
0.2 Mo	0.07	0.3	1.9	0.2	0.2	Nb, Ti	0.46	0.20

The reheating temperature was selected above the equilibrium dissolution temperature of Nb(C,N) precipitates based on thermodynamic calculations. Once these are dissolved, only Ti(N,C) particles can inhibit grain coarsening, because these precipitates are stable over the whole range of feasible reheating temperatures.

Reheating at excessively high temperatures leads to grain coarsening, which can have a detrimental effect on the toughness of the product, because the grain size of the final product increases as well [9]. On the other hand, it has been shown that increasing the reheating temperature leads to an increase in the strength of the heavy plate [10]. Finding the right balance between the dissolution of Nb(C,N) and austenite grain coarsening during reheating is, therefore, important in order to achieve the desired combination of mechanical properties in the final plate product.

Microstructure Characterization

Longitudinal sections of the plates were characterized by scanning electron microscopy (SEM) in combination with electron backscatter diffraction (EBSD), since light-optical microscopy offers only limited possibilities to characterize the microstructure in detail, because of the low magnification and resolution possible with this technique. It was found that a predominantly bainitic microstructure with small volume fractions of ferrite and carbon-rich constituents was achieved in all cases. SEM images of the samples taken close to the plate surface and at the mid-wall position are shown in Figure 4. Carbon rich constituents with a size below 3 μm were observed either along grain boundaries or between bainite sheaves. They varied in character from retained austenite to martensite and carbon-rich bainite. During the bainitic transformation, carbon is continuously redistributed to the austenite which leads to a significant enrichment in these regions which can reach levels that stabilize the austenite down to room temperature. The transformation product that is formed then depends on the local composition and the cooling rate.

EBSD-measurements were carried out close to the plate surface and at the mid-wall position. These make it possible to characterize the microstructure quantitatively in more detail, eg. with regard to the cell size, the local misorientation or the texture. The correlation of these properties with the alloy composition and processing parameters has been the focus of materials development at the SZMF [11,12]. Maps of the kernel average misorientation (KAM) of the investigated plates close to the surface and at the mid-wall position are shown in Figure 5, which illustrate orientation gradients between 0° and 3° within domains. These domains or cells are defined as areas with a minimum misorientation of 15° with respect to neighboring domains. Blue areas denote regions of lower misorientation, ie. lower local strength, and green or yellow areas are regions of higher local misorientation, ie. higher local strength. The average cell size was found to be below 2.6 µm in all three steels and did not vary significantly with the molybdenum content or the position through the wall thickness.

All three steels showed roughly similar distributions of the local misorientation close to the plate surface. However, the fraction of the areas with low misorientation increased significantly from the plate surface to the mid-wall position in the case of the steels with 0%Mo and 0.1%Mo, while the steel with 0.2%Mo showed the weakest increase of areas of low misorientation. The qualitative observation of the decrease of areas with low misorientation was confirmed by a quantitative analysis of the distributions of the kernel average misorientation for the three steels at the mid-wall position, as shown in Figure 6. These distributions typically have a positive skew. It was found that the position of the peak or mode of the distribution was shifted to higher values with increasing molybdenum content from 0.34° (0 Mo) to 0.44° (0.1 Mo) and 0.53° (0.2 Mo). The median values increased from 0.54° (0 Mo) to 0.59° (0.1 Mo) and 0.68° (0.2 Mo).

Since the rolling and cooling conditions were held constant within experimental limits in the trials, the observed variation of the local misorientation, depending on the position, can be attributed to the difference in the molybdenum content of the steels and is related to the inherent decrease of the cooling rate from the surface to the centre of the plate during accelerated cooling. Those regions with a lower misorientation originate from phase transformation at higher temperature, while regions of higher misorientation, on the other hand, were transformed at a lower temperature. This shows that the addition of molybdenum inhibits the transformation at higher temperatures effectively and improves the homogeneity of the microstructure over the wall thickness.
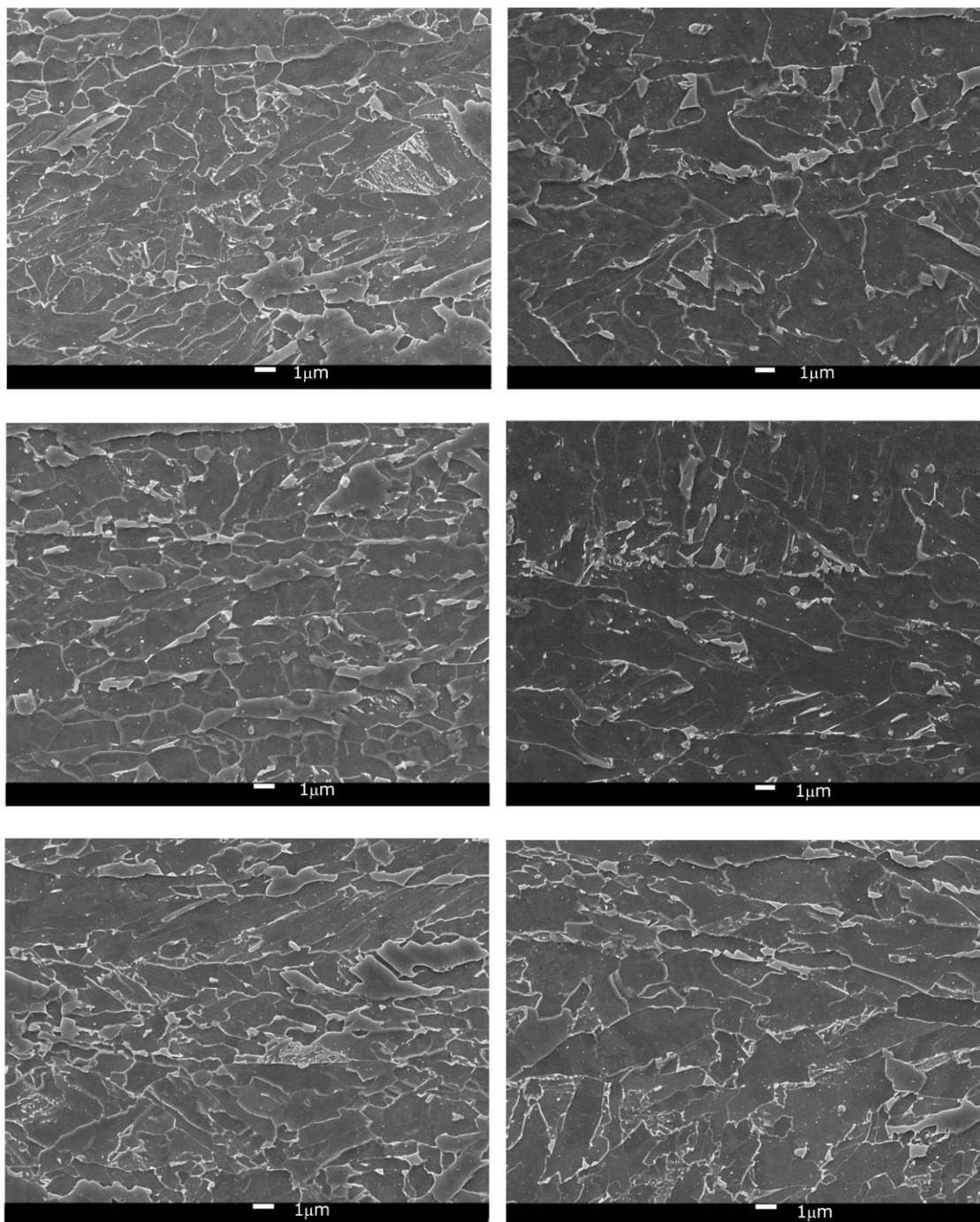
Figure 4. SEM-images of the microstructure of the laboratory-rolled plates close to the surface (left) and at the mid-wall position (right) of steel 0 Mo (top), 0.1 Mo (center) and 0.2 Mo (bottom).
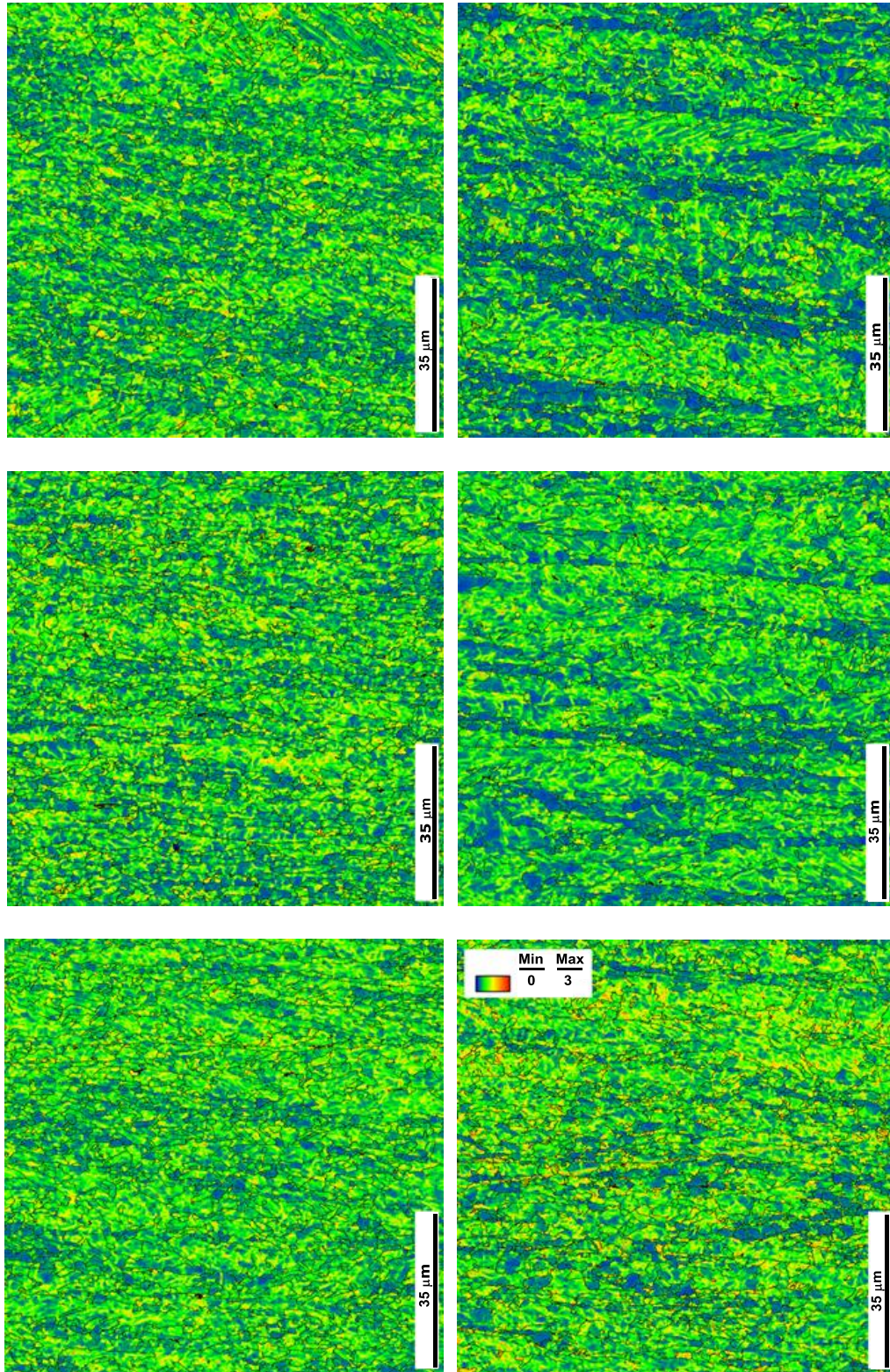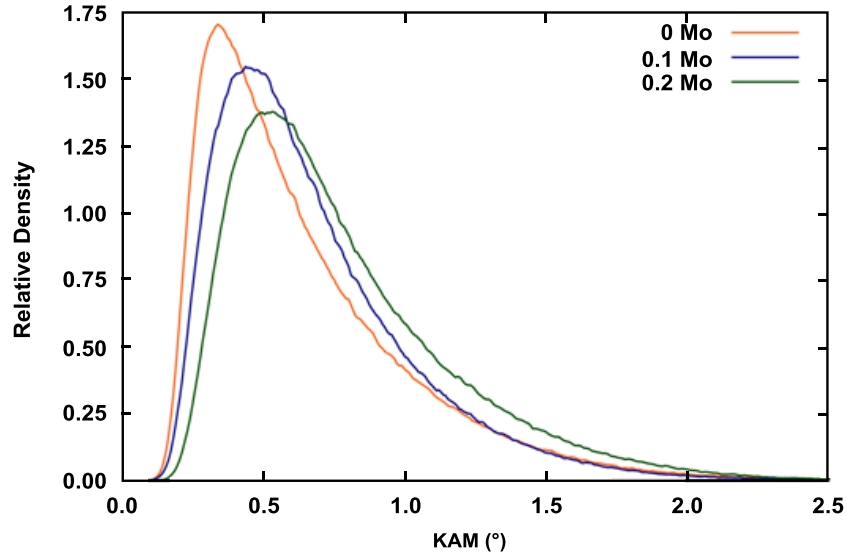
Figure 5. Kernel average misorientation between 0° and 3° of the laboratory-rolled plates close to the surface (left) and at the mid-wall position (right) of steel 0 Mo (top), 0.1 Mo (center) and 0.2 Mo (bottom).

Figure 6. Distribution of the kernel average misorientation (KAM) of the laboratory-rolled plates at the mid-wall position.

Mechanical Properties

Materials testing consisted of tensile tests on round bar specimens, Charpy impact tests and pressed-notch (PN) Battelle drop-weight-tear tests at -20 °C in the transverse direction using specimens with the full wall thickness.

The transverse tensile results from the plates (see Figure 7) showed that the X80 requirements (SMYS 555 MPa, SMTS 625 MPa) in the transverse direction with regard to the yield strength and tensile strength were fulfilled by all three compositions. The yield strength increased continuously with increasing molybdenum content from 610 MPa to 676 MPa and the tensile strength increased from 672 MPa to 729 MPa. The increase of strength was concomitant with an increase of the yield to tensile ratio from 0.91 to 0.93.
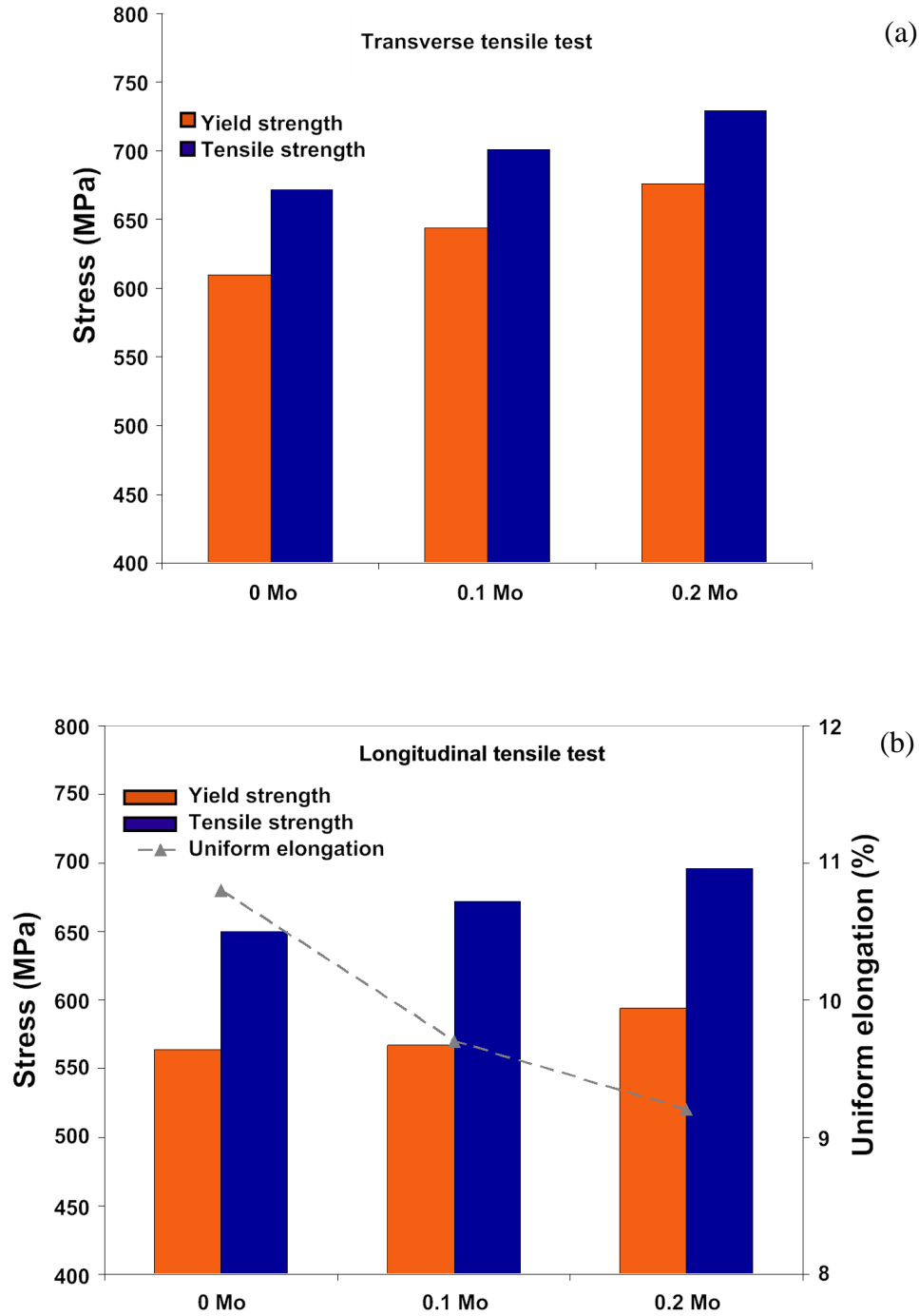
Figure 7. Results of tensile tests in transverse (a) and longitudinal direction (b).

In the longitudinal direction, the yield strength increased with increasing molybdenum content from 564 MPa to 594 MPa and the tensile strength increased from 650 MPa to 696 MPa, ie. the X80 specification minimum values were also fulfilled in the longitudinal direction. The yield to tensile ratio was between 0.87 and 0.84. The uniform elongation decreased with increasing molybdenum content from 10.8% to 9.2%.
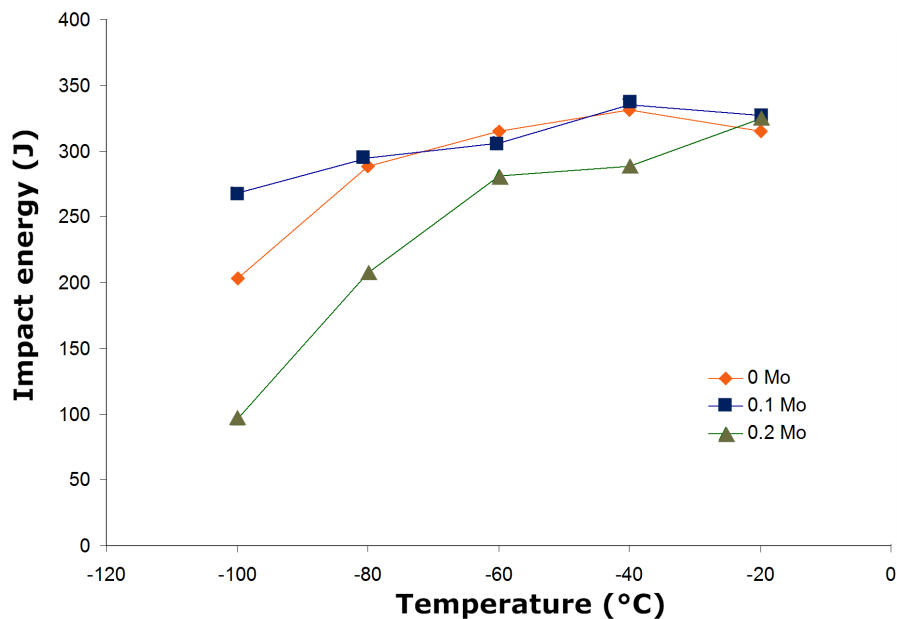
Figure 8. Average impact energy of samples in transverse direction.

Charpy impact tests were carried out in the transverse direction between -20 °C and -100 °C. The average impact energy is presented in Figure 8 as a function of the testing temperature. Down to -60 °C, an excellent level of impact energy, in the range from 250 J up to 350 J with little scatter of individual values, was observed. There was no significant difference in this range between the 0 Mo and 0.1 Mo steels with values around 300 J, while slightly lower values were found for the 0.2 Mo steel which showed a decrease of the impact energy below -60 °C. At -100 °C, the 0.1 Mo steel showed the highest average energy value with purely upper shelf behavior, whereas the 0 Mo and 0.2 Mo steels showed considerable scatter of individual values. While the impact energy at testing temperatures below -60 °C may not be relevant for a specification, the results indicate differences in the potential for low-temperature application. In this respect, the 0.1 Mo steel is clearly superior to the 0.2 Mo steel.

Drop-weight-tear tests (DWTT) were carried out at a testing temperature of -20 °C in the transverse direction using pressed-notch specimens with the full wall thickness. The average shear area and minimum-maximum range is shown in Figure 9. Typical acceptance criteria are an average value of ≥85% and a lowest single value of 75% shear area fraction. The results show that these criteria were not fulfilled in the case of the 0 Mo steel which only attained an average shear area of 84%. The 0.1 Mo and 0.2 Mo steels, on the other hand, fulfilled the criteria with average values of 90%.
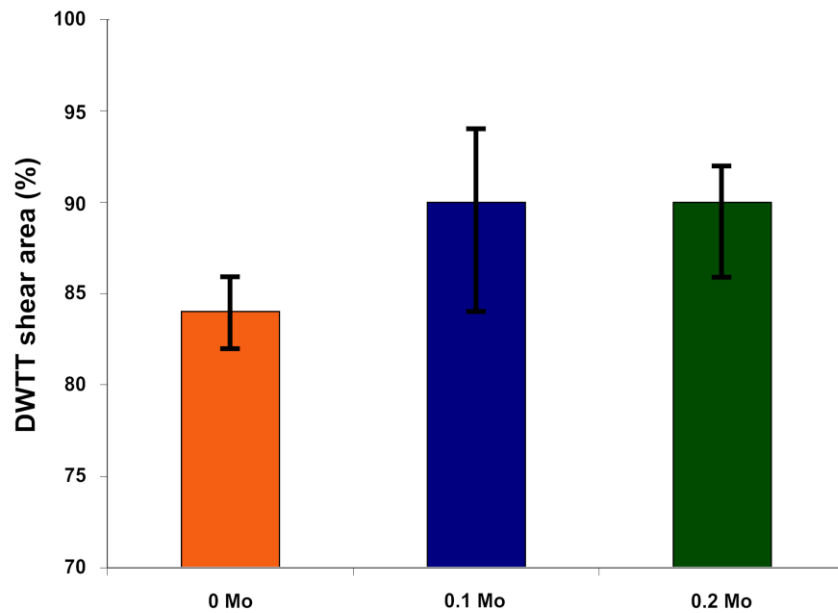
Figure 9. Average DWTT shear area and minimum-maximum range at -20 °C.

Submerged Arc Welding Trials

Double-layer submerged arc welding trials were carried out on the laboratory-rolled plates. The welding parameters were held constant and resulted in a heat input of 50-60 kJ/cm for the inner and outer weld seams. The same welding consumables were used in these trials for all welds. The welding conditions that were used are realistic for the production of large-diameter pipes with a 25 mm wall thickness. Macrographs of the welds are presented in Figure 10.
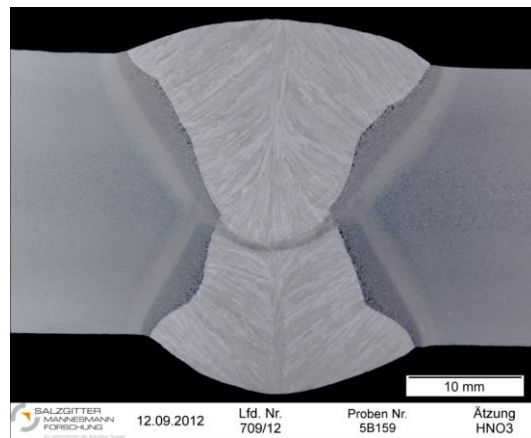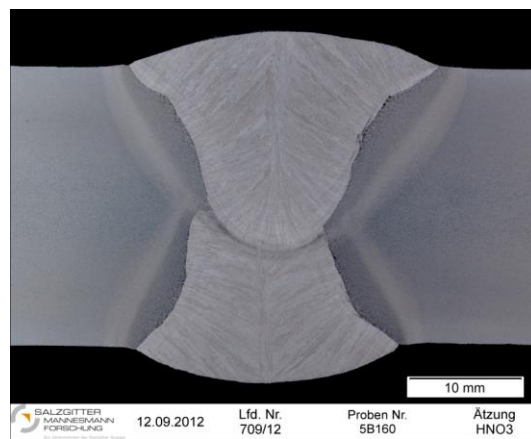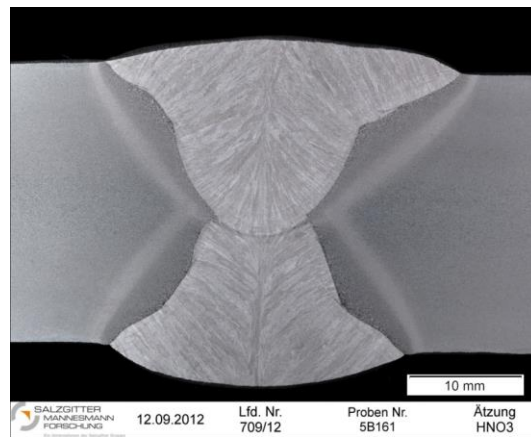
Figure 10. Macrographs of the laboratory welds produced using the steels
0 Mo (a), 0.1 Mo (b) and 0.2 Mo (c).

Charpy V-notch tests were carried out between 0 °C and -20 °C on six samples per testing temperature in the HAZ of the outer weld seam, 2 mm below the plate surface, in order to compare the HAZ toughness of the investigated materials. The notches of the Charpy specimens were positioned so that the tested cross section contained 50% weld metal and 50% HAZ (FL 50/50). At a testing temperature of 0 °C, the 0 Mo and 0.1 Mo steels showed similar average impact energies around 190 J, whereas the average for the 0.2 Mo steel was 130 J, see Figure 11. At a testing temperature of -10 °C, the average value of the 0.1 Mo steel (117 J) dropped below the level observed in the case of the 0 Mo steel (159 J), but was still slightly above the value for the 0.2 Mo steel (100 J). At -20 °C, all three steels showed similar average values of between 90 J and 100 J.

The three steels fulfilled typical requirements for toughness in the heat affected zone, eg. 56 J average and 45 J minimum, within the investigated temperature range. However, the results confirm that the HAZ toughness decreases with increasing molybdenum content. In the case of lower design temperatures, measures have to be taken to improve the toughness. Possible strategies have been outlined recently and could include a reduction in the silicon content or the carbon content [6]. The positive effect of a reduction of the silicon content has been noted previously and attributed to the reduced stability of retained austenite [13,14]. Since the 0.2 Mo steel showed the lowest toughness, a combination of both steps may be necessary in order to achieve a sufficient improvement. Both measures would, however, lead to a decrease of the strength level. This could be compensated for by an increase of the niobium content above 0.06% which has been found to improve the strength without impairing the HAZ properties significantly [15,16].
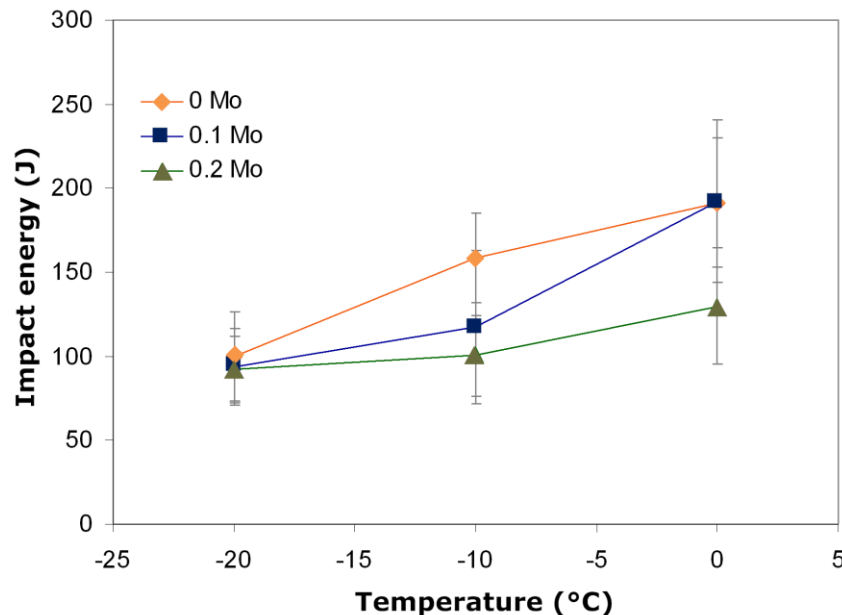
Figure 11. Average impact energy and standard deviation at the FL 50/50 position.

Conclusions

A laboratory trial was carried out with the aim to investigate the effect of the molybdenum content on the microstructure, mechanical properties and HAZ toughness of linepipe steels at the X80 strength level. Thermomechanical rolling down to a wall thickness of 25 mm in combination with accelerated cooling from above the Ar_3 temperature resulted in a predominantly bainitic microstructure. In EBSD investigations, the 0 Mo and 0.1 Mo steels showed a significant variation in the local misorientation from the plate surface to the mid-wall position, whereas only a minor variation was observed in the case of the 0.2 Mo steel, ie. the homogeneity of the microstructure was improved with increasing molybdenum content. The variation of the local misorientation is related to a decrease in the cooling rate from the surface to the mid-wall position. The extent of this effect is higher as the plate thickness increases.

The tensile tests showed that all three steels fulfilled X80 requirements, that both the yield strength and the tensile strength increased with increasing molybdenum content and that an addition of only 0.1% molybdenum has a strengthening effect in combination with 0.2% chromium. The Charpy tests showed that a higher level of impact energy at low temperatures can be reached if a molybdenum addition of 0.1% is used while all other alloying elements are held constant. A beneficial effect of a molybdenum addition was also found in DWT tests at -20 °C.

The effect of the molybdenum content on the HAZ toughness was investigated by submerged arc welding trials. The toughness level was sufficient for all three steels down to -20 °C. The lowest level of toughness in the HAZ was found for the 0.2 Mo steel, while the 0.1 Mo steel showed a higher toughness at 0 °C and -10 °C. It is possible that higher levels of toughness can be realized if the alloy design is improved, eg. by a reduction of the silicon or carbon content. The concomitant drop in strength could be compensated for by an addition of niobium above 0.06%.

References

1. EN10208-2: Steel Pipes for Pipelines for Combustible Fluids – Technical Delivery Conditions – Part 2: Pipes of Requirement Class B10208-2.

2. ANSI/API Specification 5L, 44th ed., 1 October, 2007.

3. G. Wilkowski et al, "Effect of Grade on Ductile Fracture Arrest Criteria for Gas Pipelines," *Proceedings of the Sixth International Pipeline Conference*, Calgary (2006), IPC2006-10350.

4. M. Erdelen-Peppler et al., "Investigations on the Applicability of Crack Arrest Predictions for High Strength Linepipe at Low Temperatures," *Proceedings of the 2nd International Conference on Super-High Strength Steels*, Peschiera del Garda, Italy (2010).

5. A.D. Batte, P.J. Boothby and A.B. Rothwell, "Understanding the Weldability of Niobium-bearing HSLA Steel," *Proceedings of the International Symposium Niobium* (2001), Orlando, 931.

6. C. Stallybrass et al, "Influence of Alloying Elements on the Toughness in the HAZ of DSAW-Welded Large-diameter Linepipes," *Proceedings of the 9th International Pipeline Conference,* Calgary (2012), IPC2012-90118.

7. C. Ouchi, T. Sampei and I. Kozasu, "The Effect of Hot Rolling Condition and Chemical Composition on the Onset Temperature of γ-α Transformation after Hot Rolling," *Transactions of the Iron and Steel Instititue of Japan,* 22 (1982), 214.

8. A.M. Llopis, " Effect of Alloying Elements in Steels on the Kinetics of the Austenite to Bainite Transformation" (DOE Technical Report, DOI 10.2172/7283325, California University, 1975).

9. M. Militzer and E.B. Hawbolt, "Austenite Grain Growth in Microalloyed Low Carbon Steels," *Corrosion,* 37 (5) (1981), 247-256.

10. C. Stallybrass et al, "Development of High Strength Heavy Plate Optimised for Low Temperature Toughness for Linepipe Applications," *Proceedings of the Pipeline Technology Conference,* Ostend (2009), Ostend 2009-003.

11. C. Stallybrass et al., "High Strength Heavy Plate Optimised for Application in Remote Areas and Low-temperature Service," *Proceedings of the 8th International Pipeline Conference*, Calgary (2010), IPC2010-31227.

12. J. Konrad et al., "Characterisation of the Microstructure of X80 Heavy Plate for Pipeline Applications using the EBSD Method," *Proceedings of the 3rd International Conference on Thermomechanical Processing of Steels*, Padua (2008).

13. R. Taillard et al., "Effect of Silicon on CGHAZ Toughness and Microstructure of Microalloyed Steels," *Metallurgical and Materials Transactions A*, 26A (1995), 447.

14. M. Gräf and K. Niederhoff, "Properties of HAZ in Two-pass Submerged Arc Welded Large-diameter Pipe, *Proceedings of the 3rd International Pipeline Technology Conference*, Brugge, May (2000), 553.

15. K. Hulka and F. Heisterkamp, "Physical Metallurgy, Properties and Weldability of Pipeline Steels of Various Niobium Contents," *Proceedings of International Conference on Technology and Applications of HSLA Steels,* Philadelphia, (1983), 915-924.

16. B. Bersch and K. Kaup, "Effect of Niobium on the Welding Behavior of Thermo-mechanically Rolled Steels," *3R international*, 10 (1983), 484-492.

HIGH STRENGTH PIPELINE STEELS WITH OPTIMIZED HAZ PROPERTIES

S. Brauser, C. Stallybrass, W. Scheller and J. Konrad

Salzgitter Mannesmann Forschung GmbH,
Ehinger Strasse 200, 47259 Duisburg, Germany

Keywords: HAZ, Linepipe Steels, Submerged Arc Welding, Niobium, Toughness, Carbon-rich Constituents, M/A Phase

Abstract

Large diameter linepipes for long-distance transport of natural gas are produced using either heavy gauge coil or heavy plate material. The combination of high strength and excellent low-temperature toughness of modern linepipe steels is a direct result of the thermomechanically controlled processing (TMCP), which leads to a fine grain size after rolling. Because TMCP allows attainment of high levels of strength by reducing the grain size, it was possible to lower the C content and to improve the weldability significantly. Addition of Nb is an effective measure to inhibit recrystallization during finish rolling, which is the key to obtaining a fine-grained microstructure. The temperature threshold below which recrystallization is severely retarded between rolling passes depends on the level of the Nb addition and accumulated strain. Thus, the level of the Nb content can be adjusted to the limitations of the rolling mill. Double submerged arc welding during the production of large-diameter linepipes leads to severe changes in the microstructure of the heat-affected zone (HAZ), including grain coarsening by more than one order of magnitude, as well as different transformation products. Because of the large austenite grain size close to the fusion line, the phase transformation during cooling is retarded and C-rich particles can form. This can have a negative effect on the toughness in the HAZ. An experimental investigation was carried out at Salzgitter Mannesmann Forschung GmbH (SZMF), in which the Nb content of laboratory heats was varied between 0.02% and 0.10%. These heats were thermomechanically rolled to a wall thickness of 25 mm and subsequently used for double-layer submerged arc welding trials. The processing parameters during rolling and welding were held constant in order to ensure that the effect of the alloying elements could be isolated. The fusion line toughness was determined at -20 °C as well as -40 °C and the microstructure was investigated by high-resolution scanning electron microscopy. It was found that high levels of toughness in the heat-affected zone could be achieved across the full range of Nb studied.

Introduction

Modern high-strength heavy plates used in the production of UOE pipes are generally produced by thermomechanical rolling, followed by accelerated cooling (TMCP/AC). This processing route results in a microstructure that consists predominantly of bainite. The combination of high strength and high toughness of these steels is a result of the microstructure realized by TMCP and is strongly influenced by the steel composition and rolling and cooling conditions. Continuous alloy and process development has made it possible to achieve high strength levels at C levels below 0.1% in combination with Mn levels below 2.0%, which led to a significantly improved weldability. These steels are typically microalloyed with Ti and Nb, in order to inhibit grain growth during reheating and recrystallization during rolling, which leads to a fine grain size after TMCP. The temperature threshold below which recrystallization is severely retarded between rolling passes depends on the level of the Nb addition and accumulated strain. Thus, the level of the Nb content can be adjusted to facilitate heavy plate production [1]. The level of other alloying elements strongly depends on the desired strength level and the wall thickness.

For the production of UOE pipes, submerged arc welding (SAW) in two passes is the most economic solution. However, the thermal cycles during high heat input SA welding induce a significant modification of the microstructure in the heat affected zone (HAZ) and, therefore, can lead to a critical change of local mechanical properties in terms of toughness and strength.

In order to investigate the impact of Nb on the HAZ properties, welding trials were carried out on laboratory heats with Nb contents of up to 0.105% using high heat input SAW. Charpy V-notch tests, as well as hardness tests, were performed to clarify the correlation between the Nb content and HAZ properties. Finally, the fusion line microstructure was investigated in terms of the volume fraction of C-rich constituents by high resolution scanning electron microscopy, to correlate the microstructure in the HAZ with the HAZ toughness.

Requirements on Linepipe Steels and HAZ Properties

High strength linepipe steels offer an economic advantage compared to lower strength grades as they allow a reduction in wall thickness of the pipe at the same operating pressure. This leads to savings with regard to raw materials, transportation and field welding. Conversely, they allow an increase of the operating pressure at the same wall thickness. Since the first application of X80 large-diameter pipes more than 25 years ago, the combination of mechanical properties required by customers has become increasingly complex, due to the strong worldwide interest to develop remote natural gas resources in hostile environments. These can include pipeline operation under arctic conditions, ie. at temperatures of -40 °C or below, or in areas with ground movement. High deformability and low-temperature toughness are therefore critical requirements in order to ensure pipeline safety. The optimization of the toughness has therefore been a strong focus of development, both in the case of the base metal and the HAZ.

In pipe manufacturing, special attention has to be paid to the welding as an essential aspect for the whole pipeline safety. From the economic point of view, multi-wire submerged arc welding in two passes (DSAW) is the most sensible welding technique for medium and high wall thicknesses. However, besides the economic advantage, the DSAW process leads to various challenges in terms of weld properties. The high heat input induces long cooling times which are associated with unfavorable microstructure modifications and reduced HAZ toughness [2]. The essential parameter for characterization of the HAZ properties is the cooling condition after welding, or more exactly the cooling time between 800 °C and 500 °C ($t_{8/5}$ time). In general, the impact energy of the HAZ decreases and the transition temperature is shifted to higher values with increasing $t_{8/5}$ time [3,4]. For DSAW of large diameter pipes, heat input values above 4 kJ/mm are employed, which corresponds to a $t_{8/5}$ time in the HAZ above 50 seconds. Figure 1 shows an example of a numerically calculated temperature-time cycle for the HAZ of the second weld layer. Apart from the cooling conditions, the microstructure and toughness of the HAZ are strongly influenced by the peak temperature. With regard to the resulting microstructure modifications, the HAZ can be divided into four different zones [5]:

- Sub-critically reheated HAZ (SCHAZ) – temperature below A_{c1};
- Inter-critically reheated HAZ (ICHAZ) – temperature between A_{c1}-A_{c3};
- Grain-refined HAZ (GRHAZ) – temperature above A_{c3}, with no extensive grain growth;
- Coarse-grained HAZ (CGHAZ) – temperature above A_{c3}, with significant grain growth.

Generally, the critical part of the weld in terms of toughness measurement is represented by the CGHAZ. Here, a significant austenite grain coarsening occurs which retards the phase transformation during cooling, as the nucleation density is reduced [6]. As a result, coarse upper bainite can be formed. To inhibit this unfavorable γ-grain coarsening, Ti and Nb are added, which form stable precipites that exert a pinning force on grain boundaries [6]. However, during high heat input SA welding, partial or complete dissolution of these precipitates takes place in regions with peak temperatures above 1200 °C combined with low cooling rates, so that the γ-grain coarsening cannot be suppressed, resulting in a coarse microstructure. This is one reason why multi-wire SAW is critical in terms of HAZ toughness. In addition, C-rich constituents between bainite lath boundaries can be formed during cooling. The volume fraction, size and morphology of these C-rich constituents have a negative effect on the toughness in the HAZ of SA welds [7,8]. This is even more critical in the case of the area of the weld overlap between the first and second layer, where the peak temperature during SA welding is between A_{c1} and A_{c3}, see Figure 2. In this intercritically reheated coarse-grained (ICCG) HAZ, only a certain fraction of the material transforms to austenite. Because of the higher solubility, these γ-phase portions have substantially higher C content than the matrix [6]. This stabilizes the intercritical austenite by shifting the A_{r3} temperature to lower values, which promotes the formation of M-A constituents to a significant extent.

Because of these interactions between heat input, cooling time and resulting microstructures during DSA (Double Submerged Arc) welding of large diameter pipes, special attention has to be paid to the HAZ properties, in particular to the absorbed impact energy values. Requirements concerning acceptable CVN values are given by specifications such as DNV-OS-F101 and API 5L for a broad range of steel grades and wall thicknesses. More than these standards, customer requirements define the desired weld properties. These requirements strongly depend on the loading and environmental conditions in the field and can therefore differ from the specifications.
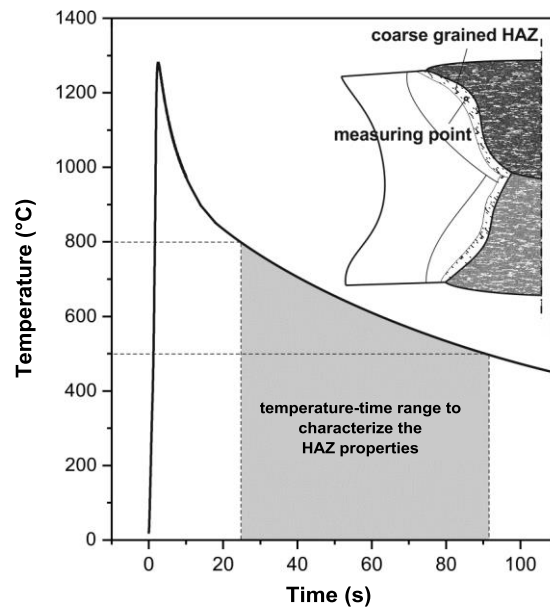
Figure 1. Temperature-time behavior in the CGHAZ of SA welds (outside layer) determined with FE simulation.
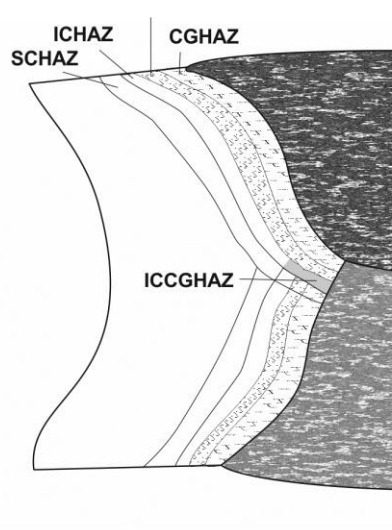
Figure 2. HAZ microstructure regions within two pass SA weld.

144

As mentioned above, Nb is an essential alloying element to generate a favorable fine-grained base metal microstructure. However, concerning the HAZ properties some inconsistent aspects have been reported in the literature. Thus, many researchers have investigated the influence of Nb content on HAZ toughness. Some investigators have found that low additions of Nb decrease toughness [8,9] while others [10] have demonstrated that there is no significant effect of Nb. Kawano et al. [11] have found that small additions of Nb (0.02%) lower the toughness in low C steel, especially for high heat input welds. Hulka and Heisterkamp [12] have shown that for a submerged arc welded 0.08%C-1.5%Mn steel (heat input of 2 kJ/mm) increasing Nb content up to a level of 0.08%Nb results in a deterioration of HAZ toughness, while further increase of Nb content leads to improved toughness. Similar results were presented by Bersch and Kaup [13] for a 0.09%C- steel for various welding processes, see Figure 3. The authors pointed out that first a reduction in toughness was observed, followed by an improved toughness behavior with increasing Nb content for both the multilayer technique, as well as double submerged arc welding.

The metallurgical phenomena in the HAZ are connected with the solubility of Nb-carbonitride precipitates [14]. If the temperature during welding reaches a level at or above the solubility of Nb carbonitride precipitates, dissolution will occur with the consequence of austenite grain growth. Additionally, it was mentioned in [15] that at intermediate cooling rates the solute Nb will depress the $\gamma \rightarrow \alpha$ transformation by decreasing the A_{r3} temperature [16]. This promotes the formation of upper bainite as well as the development of martensite-austenite (M-A) constitutes. Thus, Koseki [9] showed that Nb increases the M-A area fraction in low (0.03%C) and high (0.16%C) C steels. However, Shams [17] has demonstrated for a 0.07%C – 1.4%Mn steel grade that the extent of A_{r3} temperature reduction depends strongly on the dissolved Nb content and the cooling conditions, see Figure 4. Nb content in solution by up to 0.05% lowers the A_{r3} temperature significantly, while a further increase in dissolved Nb content tends to increase the A_{r3} temperature.
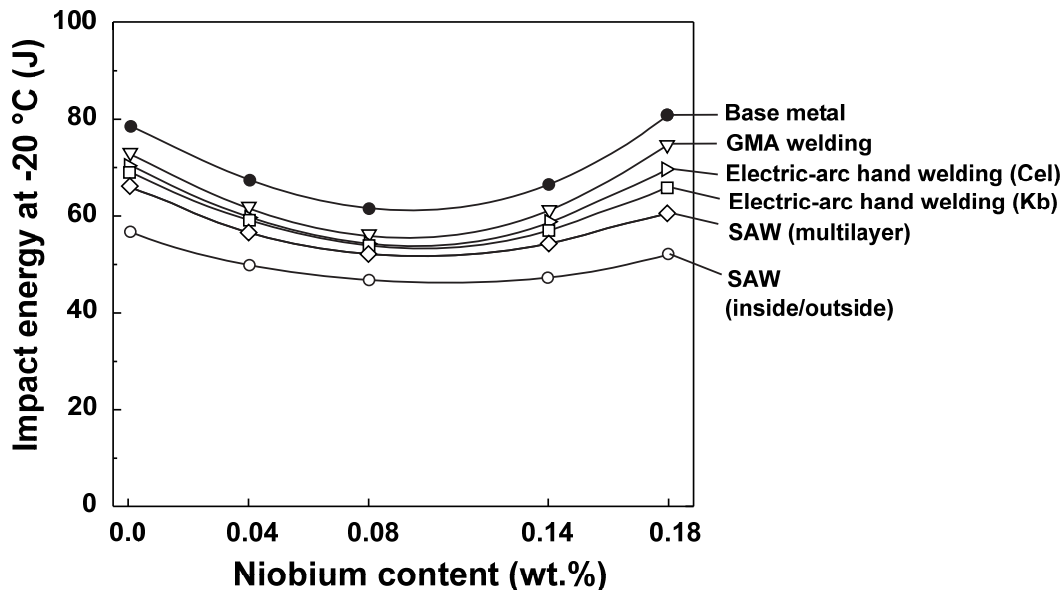
Figure 3. HAZ impact energy values depending on the Nb content for 0.09%C- steel [13].
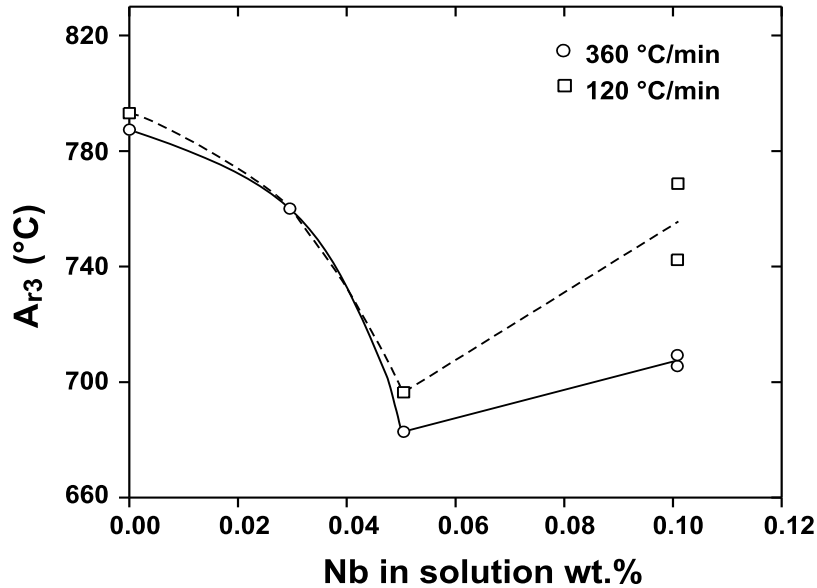
Figure 4. Effect of Nb in solution on A_{r3} temperature of 0.07 C- 1.5 Mn steel [17].

Alloy Design for Optimized HAZ Properties

The improvement of the HAZ toughness of heavy wall linepipes at low temperatures has been the focus of alloy development at SZMF for several years. Solutions for optimizing HAZ properties have been presented recently for Grades X65 to X80 [6]. It was found that the CE_{IIW} does not correlate well with the HAZ toughness and that the Pcm-value is a more suitable measure. Microstructural investigations have shown that the decrease of toughness is related to an increase in the volume fraction of C-rich constituents. These can include M/A-constituents, bainite and pearlite. The volume fraction of these C-rich constituents in a given position of the HAZ is related to the base metal composition if the welding parameters and the wall thickness are held constant. Higher levels of HAZ toughness were achieved by reducing the C and Si content, which naturally led to a drop in base metal strength. Strategies to compensate for this drop were identified that did not affect the HAZ properties significantly. Especially a slight increase of the Mn content from 1.6% to 1.8% did not have a detrimental effect. The influence of a variation in the level of Nb was, however, not investigated. For this reason, laboratory trials with a systematic variation of the Nb content between 0.02% and 0.10% were carried out.

Four 100 kg laboratory heats were produced by vacuum induction melting, see Table I. The carbon equivalent (IIW) and Pcm values were constant for all four heats. The ingots were sectioned into coupons and were rolled on a two-high rolling mill down to a wall thickness of 25 mm. Final rolling temperatures above the A_{r3}-temperature were selected for all three compositions in order to ensure a predominantly bainitic microstructure after accelerated cooling, which was interrupted above the martensite-start temperature at around 450 °C.

146

Table I. Composition of the Investigated Laboratory Heats (wt.%)

Steel	C	Si	Mn	Cr	Nb	Ti	CE$_{IIW}$	Pcm
0.022 Nb	0.04	0.1	1.8	0.1	0.022	0.014	0.36	0.14
0.046 Nb	0.04	0.1	1.8	0.1	0.048	0.014	0.36	0.14
0.071 Nb	0.04	0.1	1.8	0.1	0.071	0.014	0.36	0.14
0.105 Nb	0.04	0.1	1.8	0.1	0.105	0.014	0.36	0.14

The same reheating temperature was selected for all four steels, above the equilibrium dissolution temperature of Nb(C,N) precipitates based on thermodynamic calculations. Once these are dissolved, only Ti(N,C) particles can inhibit grain coarsening, because these are stable over the whole range of feasible reheating temperatures.

DSA Welding of Optimized HAZ Alloys: Welding Conditions and Destructive Tests

In order to determine the effect of a variation of the Nb content on the HAZ properties for high heat input welding, welding trials were carried out using multi wire double submerged arc welding (DSAW) which is extensively used for longitudinal welding in large diameter pipe production [18]. For both inside and outside welding, high heat inputs above 5 kJ/mm were achieved at welding speeds typically used in production. The welding parameters as well as bevel preparation were chosen based on mill production values. In the welding trials, a slightly basic flux was used in combination with filler wires following the TiB concept.

The toughness of the HAZ, as the key parameter, was determined by Charpy V-notch tests. In order to obtain statistically relevant results regarding the correlation between chemical composition of the base metal and the HAZ toughness, these Charpy tests were performed at two significant temperatures (-20 °C/-40 °C) on nine samples for each temperature. The notch positions were selected according to DNV-OS-F101 [19] and ISO 3183 [20], respectively, Figure 5. However, it can be assumed that the notch position according to DNV-OS-F101 represents the more critical case, because a higher fraction of the notch is located in the brittle coarse-grained HAZ, Figure 6. In addition, hardness tests were carried out according to DNV-OS-F101, in order to investigate the effect on the hardness in the vicinity of the weld.
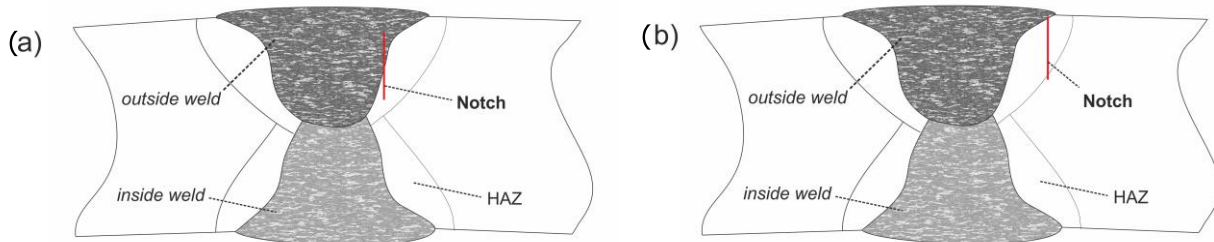
Figure 5. Notch positions according to; (a) DNV-OS-F101 and (b) ISO 3183.
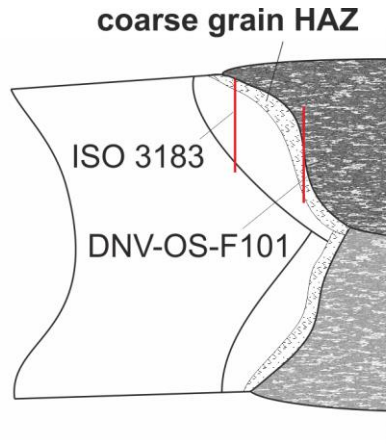
Figure 6. Schematic representation of the impact of the notch position on the portion of coarse grain HAZ sampled by the Charpy notch.

Results and Discussion

The base metal was characterized in the as-rolled condition by light-optical microscopy and tensile tests in the transverse direction. An example of the microstructure that was realized by accelerated cooling is shown in Figure 7. In all four cases, a predominantly bainitic microstructure was achieved. The results of the transverse tensile tests are shown in Figure 8. The yield strength and tensile strength were found to increase continuously with increasing Nb content. The steels with Nb levels of 0.022% and 0.048% achieved values that are in the range of Grade X70, while the steels with the higher Nb content were at the X80 strength level.
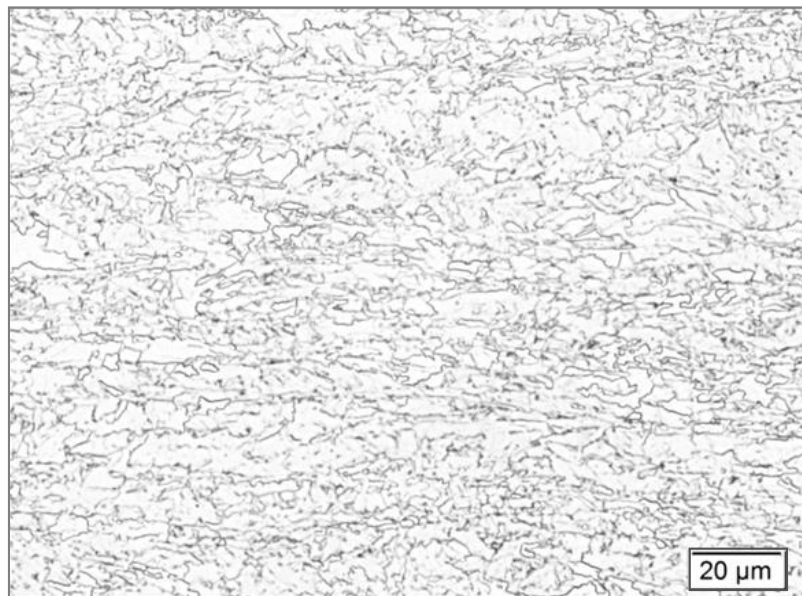
Figure 7. Microstructure of the laboratory rolled plate with 0.105%Nb.
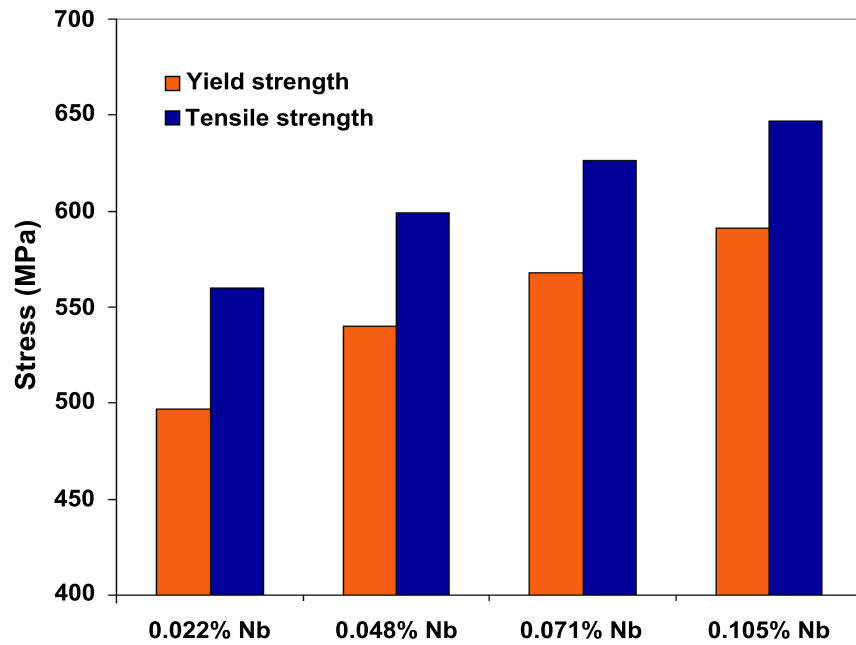
Figure 8. Results of transverse tensile tests on the base metal in the as-rolled+AC condition.

Figure 9 shows an example of a produced weld seam. All welds show typical shapes with no anomalies.

Figure 9. Cross section of SA weld, Nb content 0.022%.

In Figure 10, the hardness profiles of the SA welds, depending on the Nb content for the different areas of the weld, are presented. A typical hardness curve was found for thermomechanically rolled (+AC) microalloyed steels with a hardness reduction of the HAZ and an increasing hardness of the weld metal compared to the base metal. In general, a rise in base metal hardness was observed with increasing Nb content up to 0.071%. However, a further increase in Nb content did not have a significant impact on the hardness. This is in contrast to the base metal strength values, where a rise in Nb content was connected with continuously increasing strength properties.

The lowest hardness was found at the transition from the base metal to the HAZ independent of the Nb content. In this area of the weld, a peak temperature during welding below 600 °C occurred, which leads to softening.

Based on Figure 10(b), which shows the hardness profiles of the overlap areas of the inside/outside welds, it appears that welding of the second (outside) layer leads to the lowest HAZ hardness. This behavior is well known for DSA welding of thermomechanically rolled steels and is caused by the annealing of the HAZ during welding of the second layer.
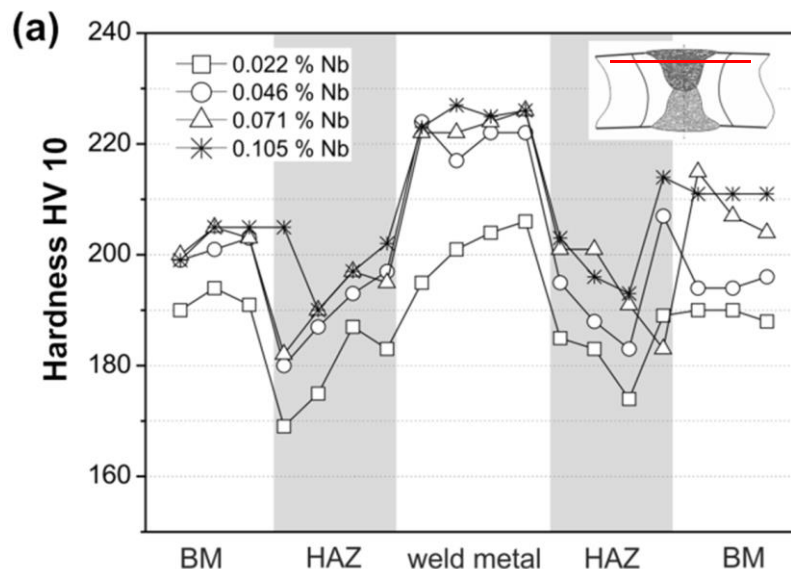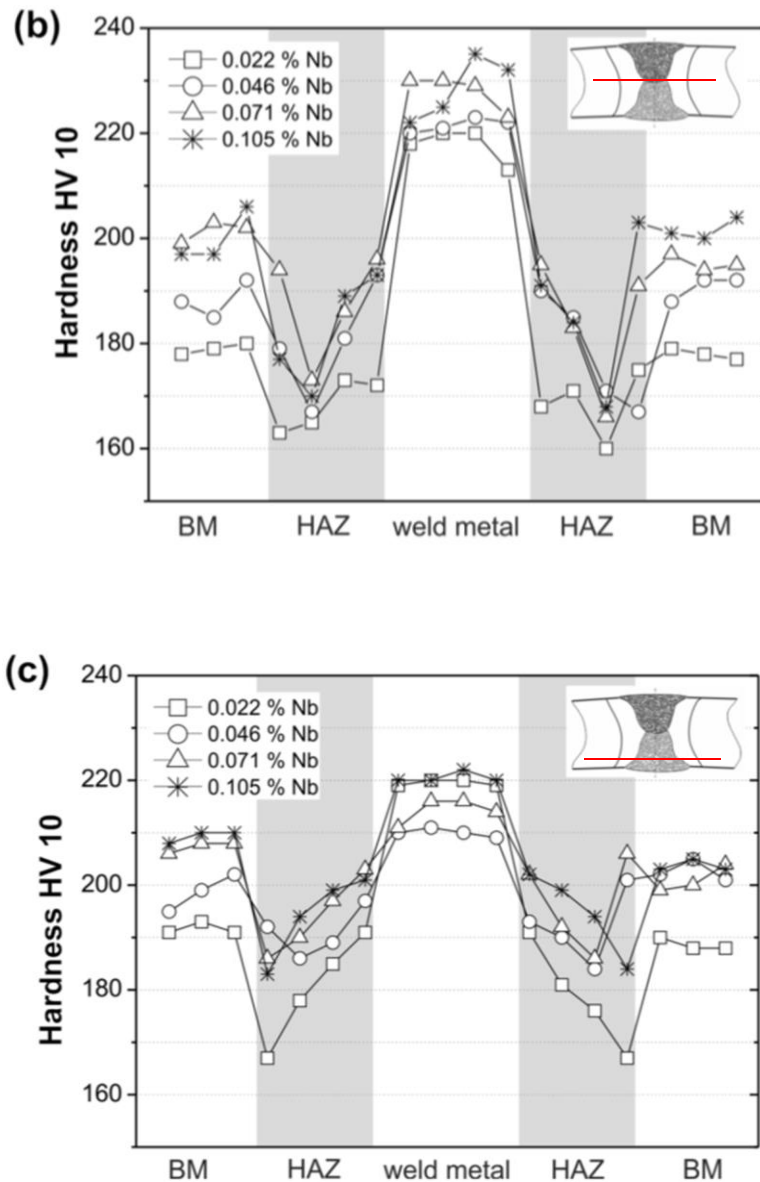
Figure 10. Hardness distribution of the inside/outside SA welds; (a) outside weld, (b) overlap area, (c) inside weld.

The weld metal showed an inconsistent behavior with regard to the hardness depending on the Nb content. Thus, for the outside weld, base metal with a low Nb content of 0.022% led to the lowest hardness, while a further increase up to 0.105% Nb in the base metal resulted in comparable weld metal hardness in all cases, Figure 10(a). In contrast, for the overlap area (Figure 10(b)) as well as for the inside layer (Figure 10(c)) the impact of Nb is not pronounced. This result is surprising in light of the extensive dilution during welding (around 60% to 70%). It appears that other parameters such as the composition of the filler wire play a major role for the weld metal hardness. In this context, it can be summarized that a high Nb content does not have a significant effect on the weld metal hardness.

The results of Charpy V-notch tests are presented in Figure 11. A slight reduction in impact energy with increasing Nb content was found for the notch position according to DNV-OS-F101 at -20 °C, see Figure 11(a). However, all mean values are relatively high and exceed the toughness requirements in [19,20] considerably.

(a) T= -20 °C

(b) T= -40 °C
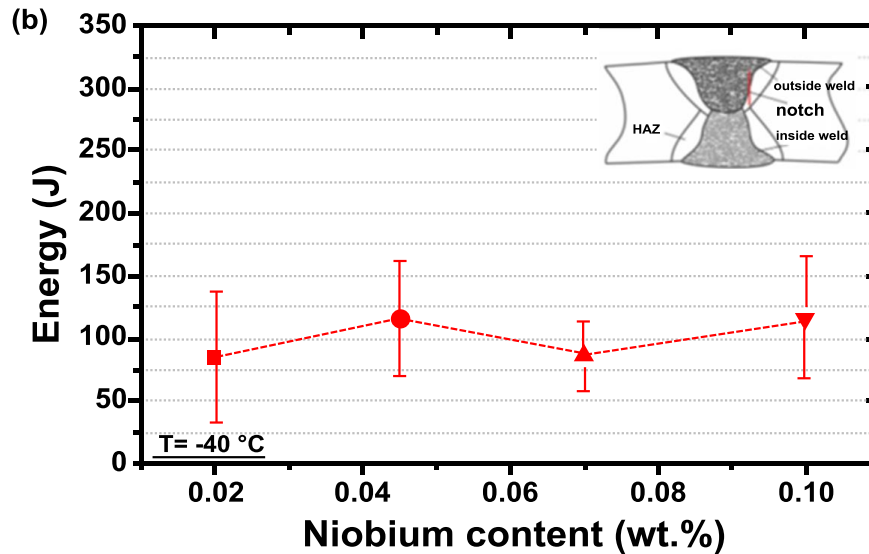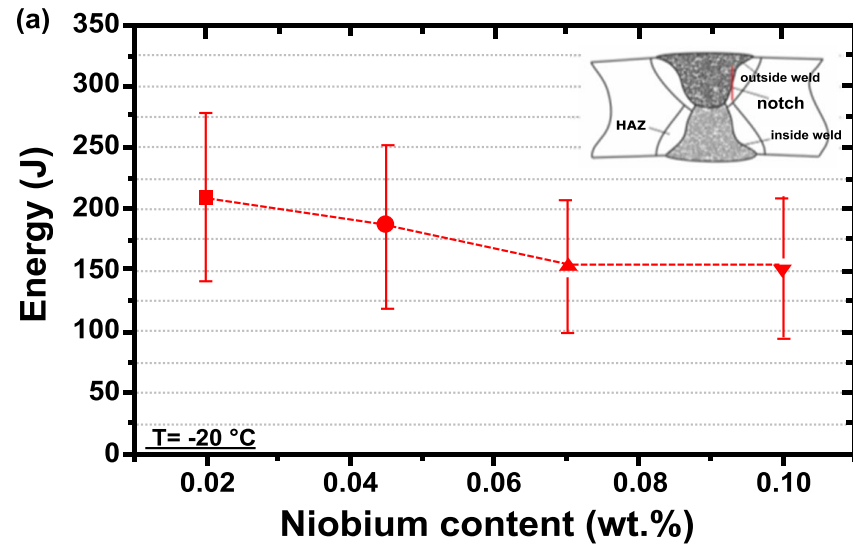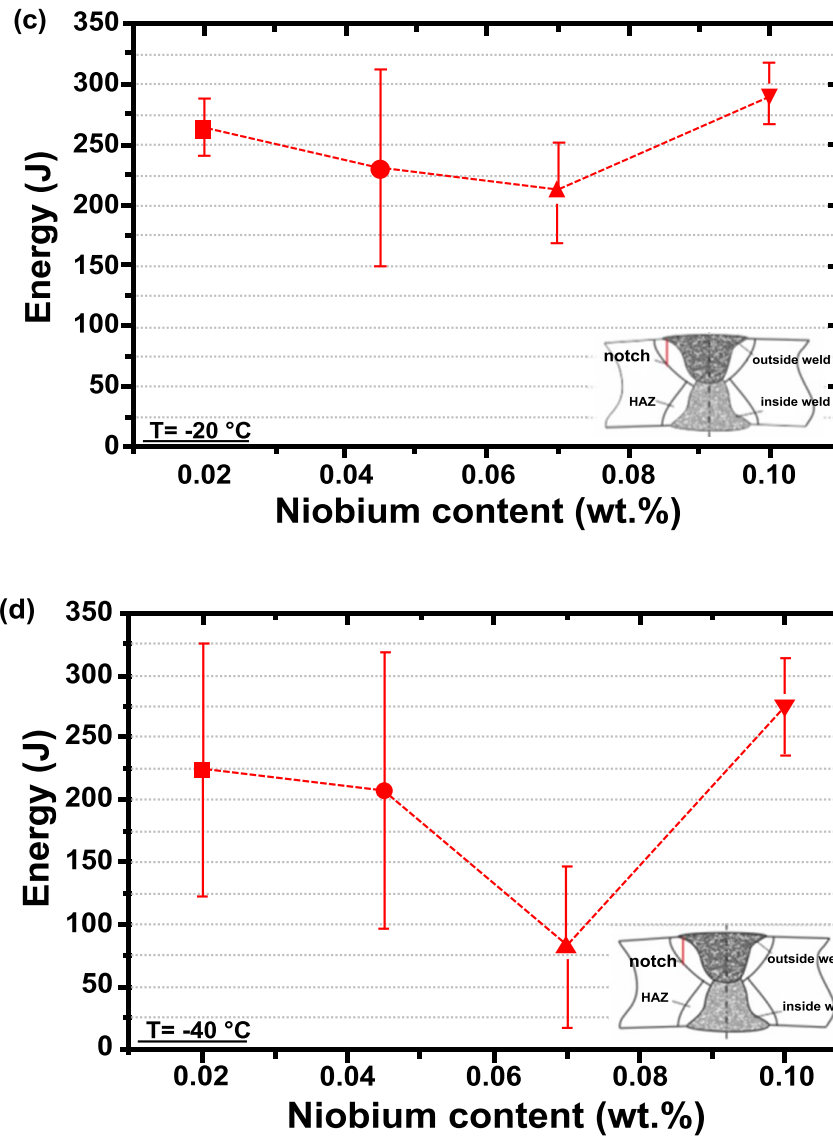
Figure 11. Evolution of Charpy impact energy depending on the Nb content for test temperatures; (a) -20 °C and (b) -40 °C, notch position according to DNV-OS-F101, as well as (c) -20 °C and (d) -40 °C, notch position according to ISO 3183.

At a test temperature of -40 °C and a notch position at the fusion line according to DNV-OS-F101, an increase of the Nb content did not have a negative impact on the toughness, see Figure 11(b). For a notch position according to ISO 3183, for both test temperatures (-20 °C/-40 °C), an increase of the Nb content up to 0.071% led to a reduction in impact energy. However, a further increase in Nb content to 0.105% led to the highest impact toughness values for both test temperatures. This trend of high impact toughness values at a high Nb content (0.105%) was observed previously in similar investigations [12,13].

The decrease of the impact energy at 0.071%Nb could be related to unfavorable weld geometry. Generally, the notch position specified by ISO 3183 results in a notch that is located in the HAZ including sub-critically reheated HAZ and a low fraction of the base metal, see Figure 12(a). The fractions of base metal and sub-critically reheated HAZ potentially lead to a mechanical support effect. However, the notches for most of the specimens with 0.071%Nb at -40 °C were positioned completely in the HAZ with a lower fraction of sub-critically reheated HAZ and no base metal fraction, ie. little support effect is expected, see Figure 12(b).
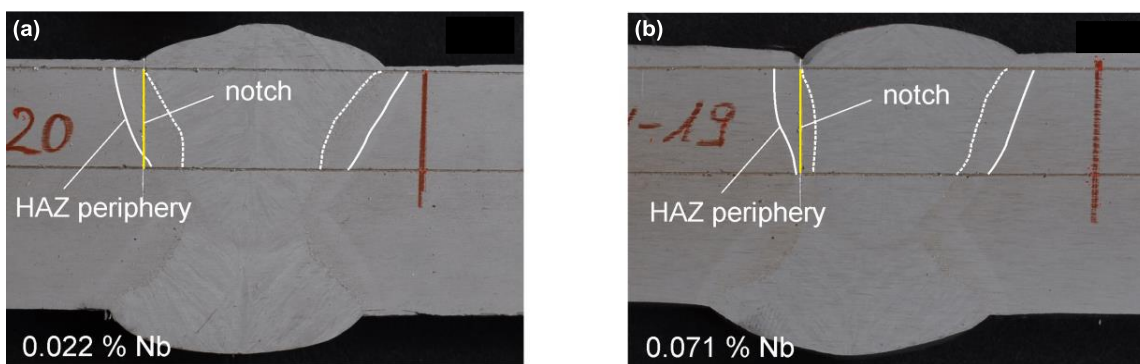
Figure 12. Difference in weld geometry leads to deviating notch position in the HAZ periphery.

It was found that the scatter of the measured impact energy values for the notch position according to DNV-OS-F101 is comparable for all alloy types and is nearly independent of the test temperature. For the notch position according to ISO 3183, the CVN test results for alloys with 0.046%Nb and 0.071%Nb show a high scatter at both test temperatures. In contrast, the high Nb steel (0.105%) exhibits low scatter at -20 °C and -40 °C, which is evidence that the observed high level of impact energy for this steel is genuine.

The comparison in Figure 13 shows that the notch position affects the impact values considerably. As discussed above, the notch position according to DNV-OS-F101 tends to be more critical in all cases in terms of HAZ toughness measurement. Thus, differences in notch position result in changes above 25% at a test temperature of -20 °C and above 40% at a test temperature of -40 °C, respectively. Because of the discussed critical interaction between notch position and weld geometry for the steel with 0.071%Nb, the difference at -40 °C represents an exception which, therefore, should not be taken into account in this context.
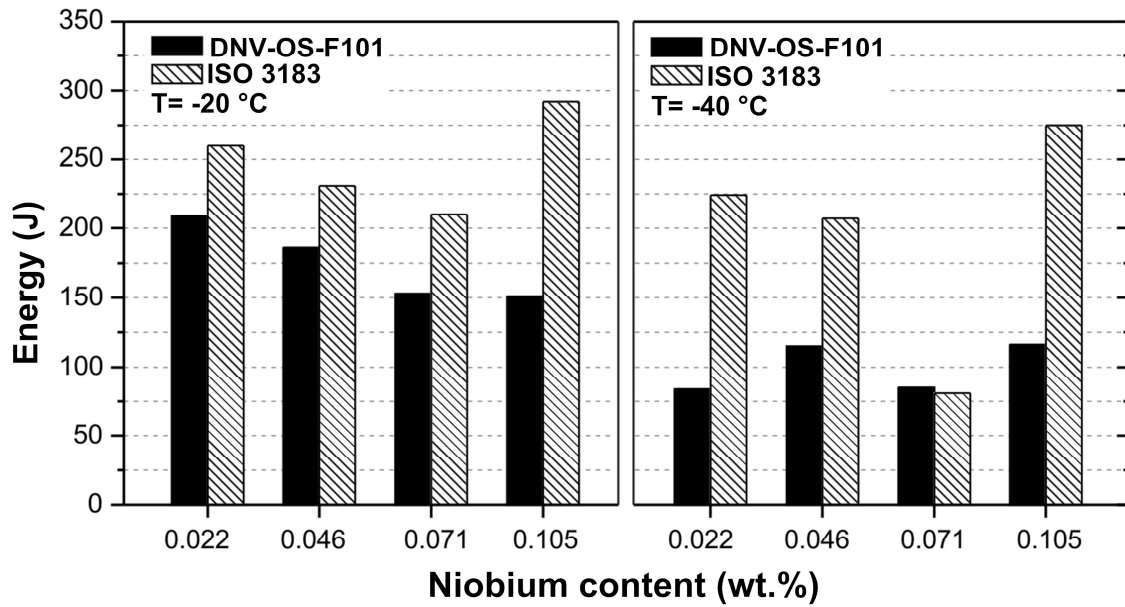
Figure 13. Effect of the notch position on CVN test results for test temperature of -20 °C (left) and -40 °C (right).

In summary, it can be stated that a Nb content of 0.105% does not have a negative impact on the toughness of the HAZ compared to a material with low Nb content (0.02%), see Figure 14. On the contrary, a trend towards higher toughness was observed.
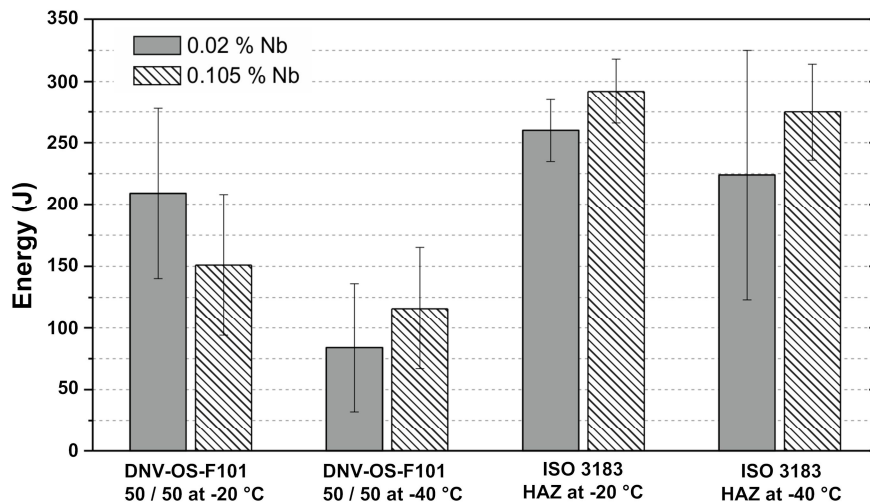

Figure 14. Comparison of the Charpy impact energy of the investigated steels containing low and high levels of Nb.

The microstructure in the CGHAZ was investigated by high-resolution scanning electron microscopy (SEM) of cross sections of the welds produced using the laboratory heats, in order to relate the HAZ-toughness to the microstructure. The samples were etched for a few seconds using a solution of nitric acid. Fifteen images were taken per sample at a magnification of 2000x within the CGHAZ in the position where the notches of the FL50/50 Charpy specimens intersect the fusion line. These were subsequently used for point analysis in order to measure the volume fraction of C-rich microstructure constituents. An example of microstructure, as observed by SEM, is shown in Figure 15. The microstructure consists of M/A-constituents and pearlitic and C-rich bainitic islands in a low-C bainitic matrix.

The average volume fraction of C-rich constituents in the CGHAZ and standard deviation obtained from the point analysis of 15 SEM images per weld are shown in Figure 16. It was found that the mean volume fraction of C-rich constituents was below 2.5% in all cases. This is lower than the level reported for any of the steels in a similar investigation [6] and is believed to be a result of the low C content of only 0.04%. In addition, the Nb content did not affect the volume fraction of the C-rich constituents significantly. A minor increase of the volume fraction of M/A-constituents with increasing Nb content was concomitant with a decrease of the volume fraction of pearlitic/bainitic islands.
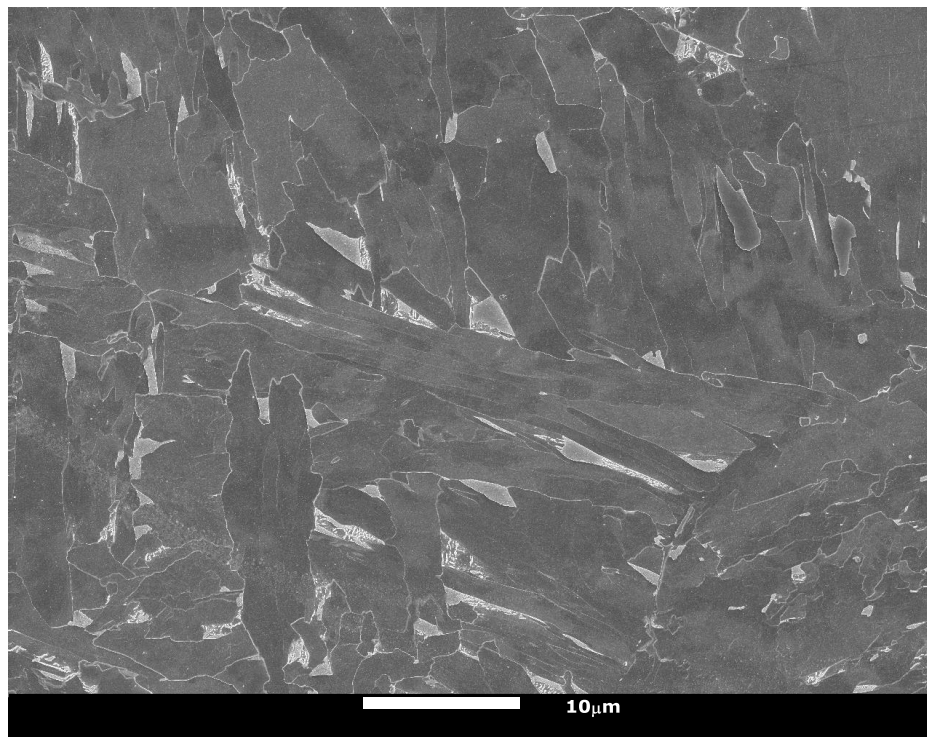
Figure 15. Example of the microstructure in the CGHAZ.
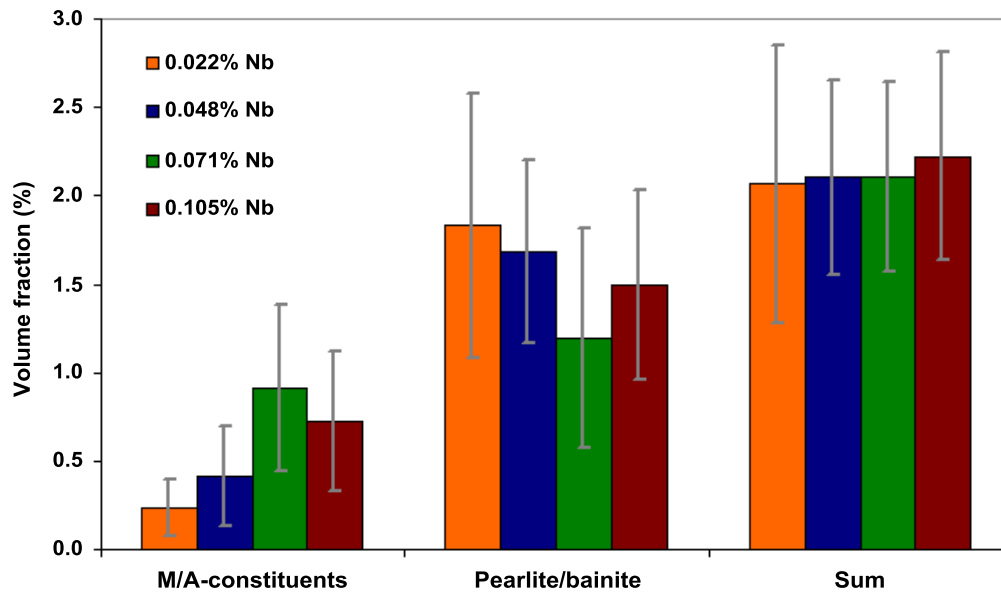
Figure 16. Volume fraction of C-rich constituents in the HAZ.

The impact of the different Nb contents with regard to the sensitivity to test temperature variations is shown in Figure 17. For the notch position according to DNV-OS-F101, all alloys exhibit decreased CVN values at the lower test temperature (-40 °C). The 0.022%Nb containing alloy demonstrated the highest drop (>50%), while the 0.105%Nb containing alloy type showed the lowest drop (around 20%). The highest CVN values at -40 °C were obtained at Nb contents of 0.046% and 0.105%, respectively.

For the notch position according to ISO 3183, a minor drop (<20%) of impact energy with decreasing test temperature was observed. However, the steel with 0.071%Nb constitutes an exception and could be related to the above mentioned unfavorable weld geometry (Figure 12). Again, the lowest drop was found for the steel containing 0.105%Nb.

(a)

(b)
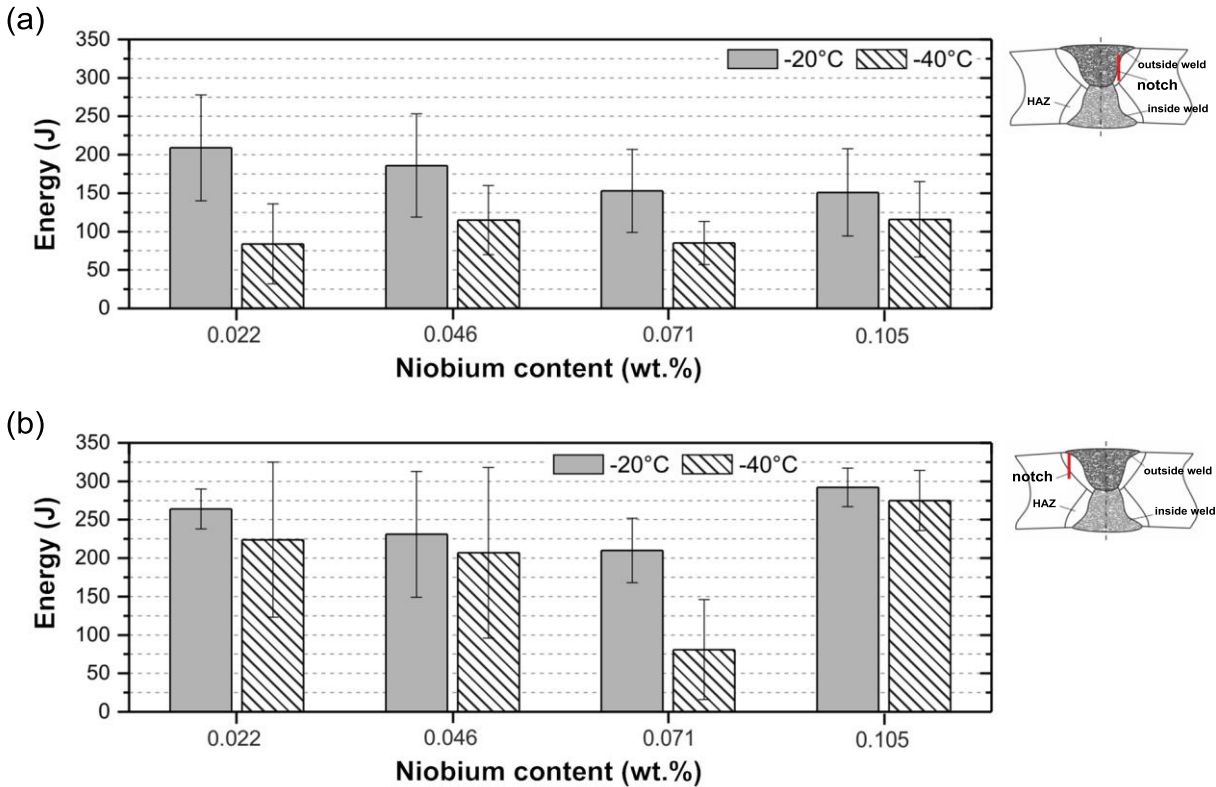
Figure 17. Influence of the test temperature on the CVN test results of the investigated steels with different Nb contents; (a) notch position according to DNV-OS-F101, (b) notch position according to ISO 3183.

Summary

Laboratory DSA welding trials were carried out on four laboratory heats with a Nb content between 0.022% and 0.105% with the aim to investigate the effect of Nb on the HAZ toughness of steels suitable for large diameter pipes. Tensile tests in the as-rolled condition showed that the strength increased from the X70 to the X80 level above a niobium content of 0.07%.

SA welding trials with high heat input (>5 kJ/mm) were carried out in order to quantify the impact of Nb on the HAZ properties under production conditions. It was demonstrated within this investigation that the influence of Nb up to 0.105% on HAZ toughness of SA welds is not pronounced. The impact energies for the 0.07%Nb steel were a bit lower than the others, the reasons for which were not clear, though possibly due to unfavorable weld geometry. In addition, the impact of the test temperature on the HAZ toughness was analyzed depending on the Nb content. The lowest decrease in CVN values between -20 °C and -40 °C was observed in the case of a Nb content of 0.105%. The microstructure of the HAZ was investigated by scanning electron microscopy and did not vary significantly depending on the Nb content. Finally, it was shown that the notch position has a significant effect on the observed impact energy.

References

1. K. Hulka and J.M. Gray, "Niobium Science and Technology," *Proceedings of International Symposium Niobium 2001* (2001), 587.

2. R. Maksuti et al., "Correlation of Microstructure and Toughness of the Welded Joint of Pipeline Steel X65," *Damage and Fracture Mechanics*, *2009*, 315.

3. J. Wiebe et al., "Influence of Heat Input during GMAW on the Mechanical Properties of Seamless Line Pipe Steels up to X80," *Proceedings of the Twenty-first (2011) International Offshore and Polar Engineering Conference,* Maui, Hawaii, USA, June 19-24, (2011), Volume 4, 187.

4. DIN EN 1011-2:2001-05: Welding - Recommendation for Welding of Metallic Materials - Part 2: Arc Welding of Ferritic Steels, 2001.

5. R.C. Cochrane, "HAZ Microstructure and Properties of Pipeline Steels," *Proceedings of the International Seminar on Welding of High Strength Pipeline Steels,* Araxa, Brazil, (2011), CBMM/TMS 2014, 153.

6. C. Stallybrass et al., "Influence of Alloying Elements on the Toughness in the HAZ of DSAW-welded Large Diameter Linepipes," *Proceedings of the 9th International Pipeline Conference (2012),* Calgary, Alberta, Canada, September 19-24, (2012), ASME, New York, volume 3, 105.

7. F. Matsuda et al., "Review of Mechanical and Metallurgical Investigations of M-A Constituent in Welded Joint in Japan," *Transactions of the Japan Welding Research Institute,* 24 (1) (1995), 1.

8. Y. Li et al., "The Effect of Vanadium and Niobium on the Properties and Microstructure of the Intercritically Reheated Coarse Grained Heat Affected Zone in Low Carbon Microalloyed Steels," *The Iron and Steel Institute of Japan International*, 41 (1) (2001), 46.

9. E. El-Kashif and T. Koseki, "Effect of Niobium on HAZ Microstructure and Toughness of HSLA Steels," Thermec 2006, *Materials Science Forum,* 539 – 543 (2007), 4838-4843 (11).

10. H. Yasuhara et al., "Carbon-Manganese Wrought Steel with Inoculated Acicular Ferrite Microstructure," *CAMP-The Iron and Steel Institute of Japan*, (12) (6) (1999), 120.

11. H. Kawano et al., "TMCP Steel Plate with Excellent HAZ Toughness for High-rise Buildings," (R&D Kobe Steel Engineering Report Tokyo, 54 (2004), 110).

12. K. Hulka and F. Heisterkamp, "Physical Metallurgy, Properties and Weldability of Pipe Line Steels with Various Niobium Contents," *Proceedings of the HSLA Steels Technology and Applications Conference,* Philadelphia, (1983), 915.

13. B. Bersch and K. Kaup, "Effect of Niobium on the Welding Behaviour of Thermomechanically Rolled Steels", *3R International*, 10 (1983), 484.

14. A.D. Batte, P.J. Boothby and A.B. Rothwell, "Understanding the Weldability of Niobium-bearing HSLA Steel," Niobium Science and Technology: *Proceedings of the International Symposium Niobium* (2001), Orlando.

15. T. Abe, K. Tsukada and I. Kozasu, "Role of Interrupted Accelerated Cooling and Microalloying," Metallurgy and Applications: *Proceedings of the International Conference HSLA Steels '85*, (1985), Beijing/China, 103.

16. D. Webster and J.H. Woodhead, "Effect of 0.03% Niobium on the Ferrite Grain Size of Mild Steel," *Journal of the Iron and Steel Institute*, 202 (1964), 987.

17. N. Shams, "Microstructure of Continuous Cooled Niobium Steels," *Journal of Metals,* (37) (12) (December 1985), 20.

18. A. Liessem et al., "Essential Welding Aspects for High Strength Linepipe," *Proceedings of the International Seminar on Welding of High Strength Pipeline Steels*, Araxa, Brazil, (2011), CBMM/TMS 2014, 189.

19. Offshore Standard DNV-OS-F101 Submarine Pipeline Systems, October 2007.

20. ISO 3183 Petroleum and Natural Gas Industries - Steel Pipe for Pipeline Transportation Systems, 2007.

STEEL ALLOY DESIGNS FOR CONTROL OF WELD HEAT AFFECTED ZONE PROPERTIES

F.J. Barbaro[1], Z. Zhu[1], L. Kuzmikova[1], H. Li[1] and J.M. Gray[2]

[1]University of Wollongong, NSW, Australia.
[2]Microalloyed Steel Institute, LP, Houston, Texas, USA.

Keywords: Titanium, Niobium, Precipitation, HAZ, TMCP, Weldability, Mechanical Properties, Toughness, HTP Steel, Thermal Simulation

Abstract

This paper reviews the current technology related to the control of weld HAZ properties in high strength steels. The debate related to the appropriate balance of Ti and N is addressed and it is concluded that a stoichiometric ratio provides optimum fracture toughness. Although the control of the Ti/N ratio is difficult, this paper now provides guidance in terms of alloy design to achieve optimum fracture toughness in the HAZ.

The enhanced resistance to grain coarsening behaviour in higher Nb steels has now provided another incremental improvement in the weldability of these steels for critical applications, such as high pressure gas transmission pipelines. The role of Mo in the alloy design of these new steels is a further activity to be undertaken in the design concept to further improve the performance and safety of modern steel structures.

Introduction

Modern high strength steels are manufactured using tailored alloy designs and processed using advanced thermomechanically controlled processes. The final mechanical properties of the steel are controlled through development of specific microstructures which are characterised by a fine ferrite grain size and a dispersion of alloy precipitates that optimise strength, ductility and toughness.

The process of welding inherently subjects the steel to elevated temperatures, which significantly modifies microstructures and therefore the mechanical properties. The region immediately adjacent to the weld, where the temperature approaches the melting point, can be significantly degraded by the extreme grain coarsening that can occur in the austenite phase region. Although many parameters control the microstructure and mechanical properties of the HAZ, it is control of the austenite grain size that is critical in terms of the performance of these steels.

Ti microalloying produces a dispersion of stable TiN precipitates which retard austenite grain coarsening by a grain boundary pinning action [1-5], as shown in Figure 1. Other methods of HAZ microstructural control have been developed [6] but Ti microalloying, following complete deoxidation, to ensure formation of nitride precipitation, is currently the dominant method employed.
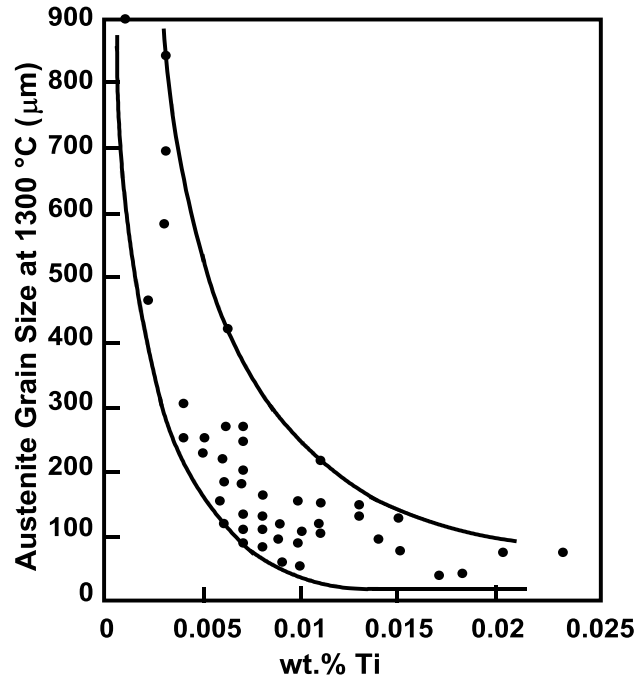
Figure 1. The effect of Ti content on austenite grain size at 1300 °C [4].

It is true to say that the use of Ti in steels is by far the most complex and least understood of all the microalloying elements. Ti is a strong oxide, sulphide, nitride and carbide former and it is the chemical balance of impurities and processing that determines the final form of the Ti compounds and the resulting properties.

A very fine dispersion of TiN precipitates is required to exert a grain boundary pinning action in opposition to the driving force for grain growth. Maximum pinning force (Z) has been shown by Zener [7], to be directly proportional to the volume fraction of precipitates (f) and inversely proportional to the precipitate size or radius (r), as defined in Equation (1). Therefore, a large volume fraction of small precipitate is beneficial for grain size control.

$$Z \propto f/r \qquad (1)$$

The approach to achieving the optimum dispersion of precipitates is the basis of ongoing debate amongst steelmakers and specifiers. Different approaches have been proposed to control the precipitate dispersion but the reported results are generally clouded by the influence of secondary effects associated with base alloy design and processing, including casting condtions.

This paper details the technology of TiN precipitation and recent research that clarifies the current debate regarding appropriate alloy designs of Ti bearing high strength steel grades. The issues associated with the current Ti alloy design are discussed and an alternative incremental approach using increased levels of Nb to improve the weld HAZ properties of these steels is presented.

Background

An addition of Ti, following deoxidation and in the presence of N, results in the formation of TiN precipitates which have high thermal stability [8]. As discussed above, the effectiveness of such precipitates is dependent on their size distribution and volume fraction and is related to the solubility product data, as shown in Figure 2.

$$\log [\%Ti] \cdot [\%N] = \frac{-14,400}{T} + 5.0$$
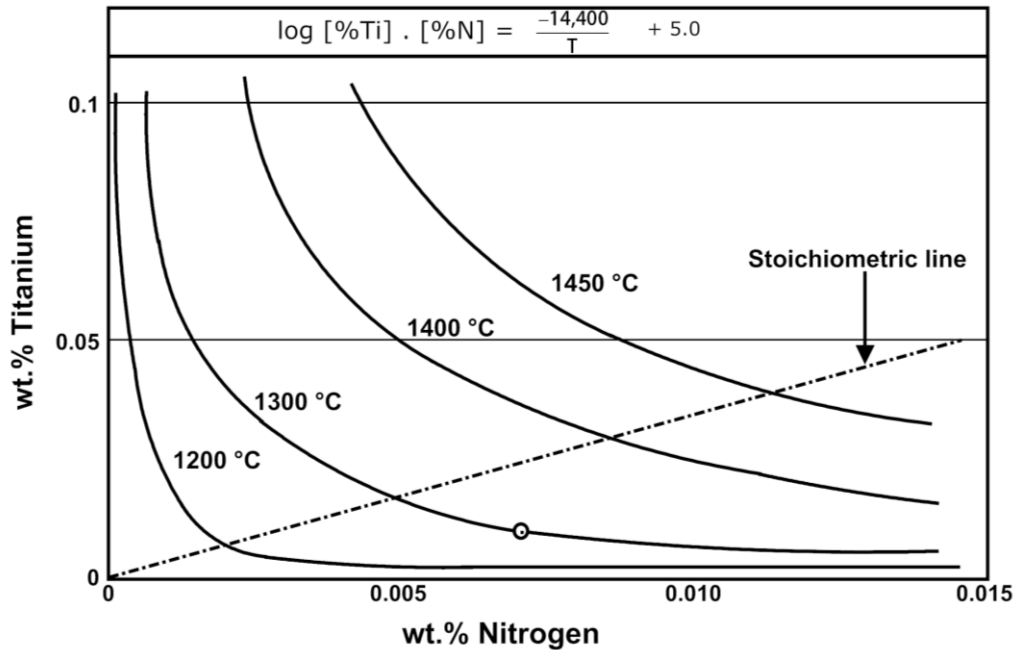
Figure 2. Solubility isotherms for TiN in austenite [9].

As the concentration of Ti and N increase, the temperature at which precipitation forms increases and results in the formation and/or growth of large TiN precipitates. Large TiN precipitates which are primarily cubiodal in shape are not only ineffective in grain boundary pinning [7] but also provide sites for the initiation of cleavage fracture [10,11]. An optimum dispersion of TiN precipitates can be achieved by limiting the overall concentration of both Ti and N, to reduce the temperature of formation and minimise thermally activated diffusion processes that lead to precipitate growth, as shown in Figure 2. In other words, a large number of very small precipitates are required to achieve maximum grain size control. The grain coarsening temperature increases when there is a maximum volume fraction of small pinning particles.

Therefore, a certain volume fraction of precipitation is required to effect grain boundary pinning and a minimum level of Ti is essential to ensure optimum grain size control. Unfortunately, however, current steelmaking practice struggles to accurately control the final level of N and so a specific stoichiometric ratio can be difficult to achieve. A non-stoichiometric ratio not only results in a non optimal size distribution but also results in either excess Ti or N, which generates the formation of TiC in the former and excess N in the latter. There is also controversy about the role of excess N as some claim that free N is detrimental to toughness [12-15] while others suggest beneficial effects as the N retards precipitate dissolution [16].

163

It should however be emphasised that the overall performance of the steel is defined by the range of Ti and N levels as well as the casting conditions and the slab cooling rates. The latter processing conditions are also critical, as the as-cast precipitates, especially the detrimentally large precipitates, are difficult to modify because of their high thermal stability.

In terms of procurement of steel for critical applications, such as pipelines, it is appropriate to evaluate steel performance and production capability, with respect to weld HAZ properties. Reliance solely on an alloy design or specification is insufficient when specific mechanical property performance is essential to ensure structural integrity and public safety.

More recently, the work of Zhu et al. [17] has now demonstrated, using detailed quantitative metallography, a more complete understanding of the influence of Ti/N ratio on weld HAZ microstructure. This work utilised a set of samples from commercial API 5L X70 grade pipe, which were produced using identical processing conditions and contained the same base chemistry, but most importantly a range of Ti/N ratios, for critical evaluation of weld HAZ microstructure and mechanical properties.

As experienced by previous investigators, the inherent difficulty in accurately evaluating a narrow weld HAZ necessitated the use of a Gleeble weld thermal simulator to provide sufficient, suitably sized specimens containing the critical CGHAZ region of the welds. The peak temperature and cooling rate employed directly reflected real welding conditions to ensure that the microstructures and importantly the austenite grain size were identical to those of the real weld.

Metallographic examination revealed the simulated microstructures to primarily consist of an aligned bainitic ferrite with small amounts of interlath M-A islands. Hardness values were consistent with the peak hardness values recorded in HAZ profiles from the real welds and so confirmed the suitability of the weld simulation conditions.

Although qualitative evaluation of the austenite grain size indicated minor variations in average grain size, the significant observable difference was revealed using quantitative metallographic techniques. The results presented in Figure 3 confirm that a distinct difference in distribution of grain size was observed which suggested that both an increased volume fraction of fine austenite grains and less coarsened austenite grains were present in the steel with a Ti/N ratio close to the stoichiometric combination of Ti and N. This was further supported by the results of Charpy impact tests, shown in Figure 4, which demonstrated a "measurable" improvement in impact toughness.
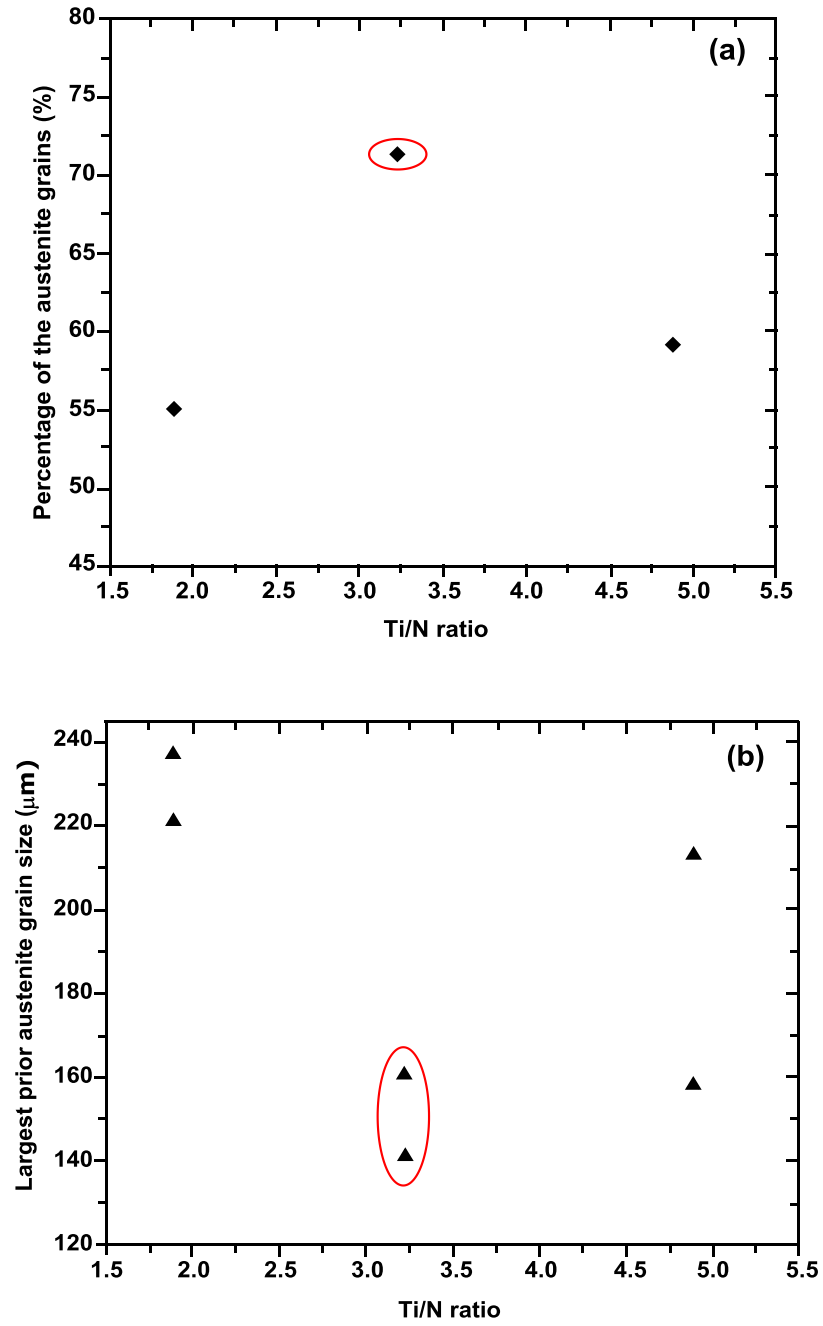
Figure 3. Results of statistical analysis of prior austenite grains size in steels with different Ti/N weight ratios; (a) percentage of fine grains (smaller than 80 μm), (b) largest grain size [18].
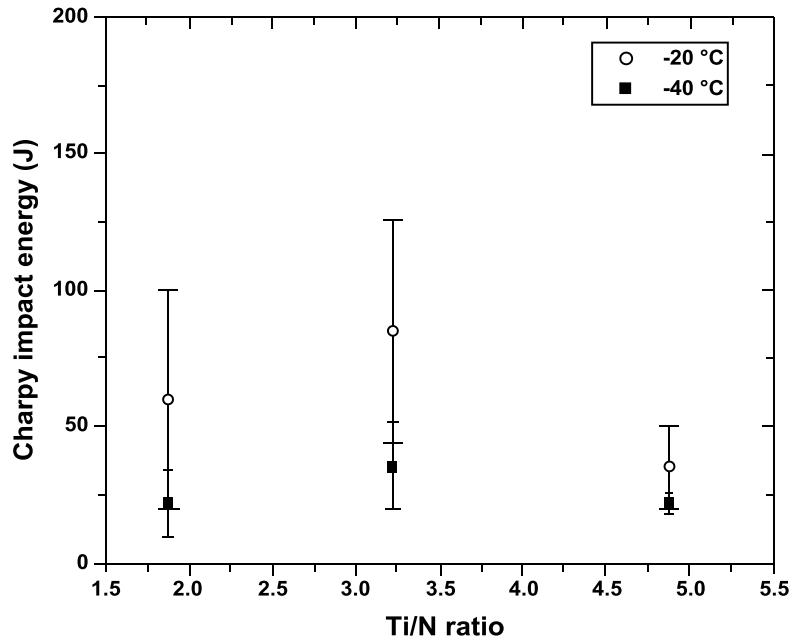
Figure 4. Mean Charpy impact energy of the simulated CGHAZ of samples with different Ti/N weight ratios. Each point is an average of three measurements [18].

Such a fine difference in microstructure and toughness performance would not have been discernible in evaluation of real welds because of the difficulties in evaluating and testing the sharp gradient of microstructures immediately adjacent to the weld fusion line.

It is reasonable to assume that based on these results, the practice of first tier steel producers [19] and thermodynamic considerations, that the optimum combination of Ti and N exists around the stoichiometric ratio, at levels that restrict initial formation of TiN in the liquid steel, ie above the solidus.

High Temperature Processed Steel

A new alloy design, although reported many decades ago [20], has only now been commercially developed and successfully utilised in a number of large international pipeline projects [21,22]. The steel design typically contains a low C content, microalloyed with Ti but with a Nb content in the range 0.08-0.11 wt.%, which enables the full capability of Nb microalloying to be effectively utilised in steel manufacture and service performance [23].

It has been clearly demonstrated that Nb provides a number of benefits to the mechanical properties of steels: grain size refinement; lowering the γ to α transition temperature (A_{r3}), precipitation hardening and retardation of austenite recrystallisation [24,25].

It is pertinent to point out the salient features of the higher Nb alloy design and the improvements to processing conditions that also provide economic benefits to the steelmaker. Key features of this higher Nb alloy design include:

Reduced C Content:

(a) Minimises elemental partitioning, ie segregation, during casting, as schematically shown in Figure 5 [26]. Avoidance of the peritectic reaction eliminates the involvement of enriched interdendritic liquid during transformation and furthermore provides an extended solidification range in delta ferrite that enhances homogenisation of the newly formed solid prior to further transformation on cooling;

(b) Maintains and enhances the solubility of the Nb to assist in the benefits outlined above, Figure 6 [26]. Most notable is the delayed precipitation of carbonitrides that enhances the hot ductility and increases the operating window for hot rolling, and therefore reduces mill operating loads. The consequential benefits to available mill uptime and maintenance downtime should also be considered;

(c) Reduces carbon equivalent and therefore improves the weldability for reduced susceptibility to hydrogen assisted cold cracking.

Controlled Ti Addition which provides control of N thus allowing optimum NbC precipitation, and avoids the formation of mixed carbonitride precipitates which occur over a larger temperature range.
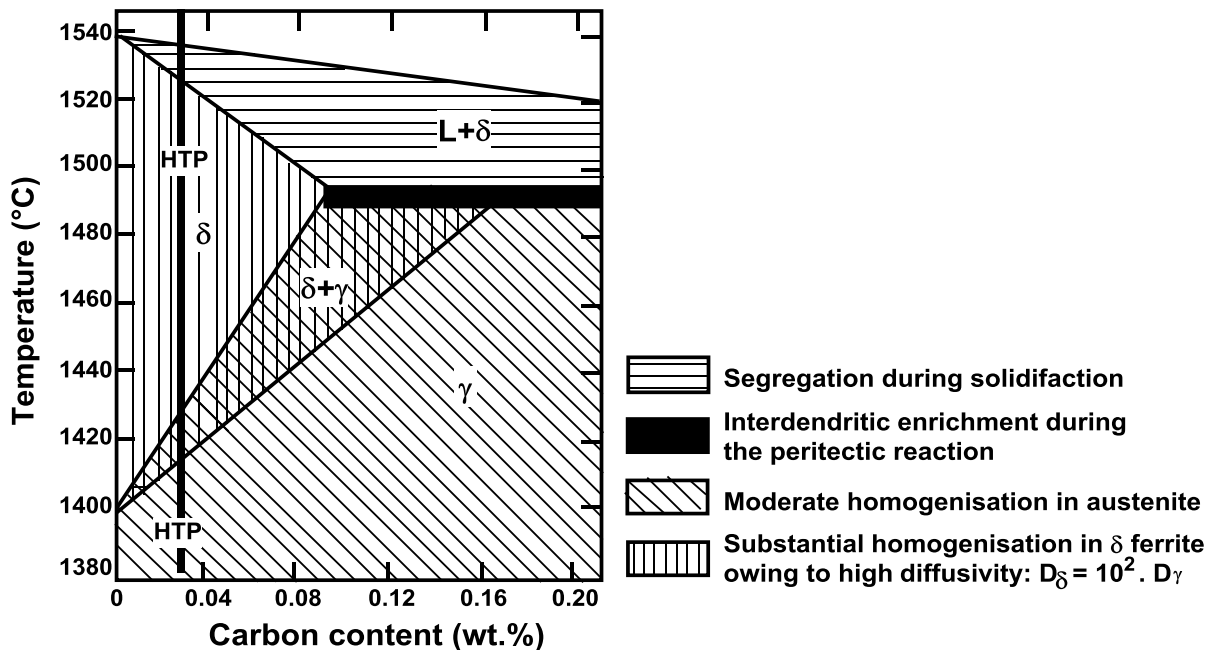
Figure 5. Part of the Fe-C diagram with classification of the segregation severity.
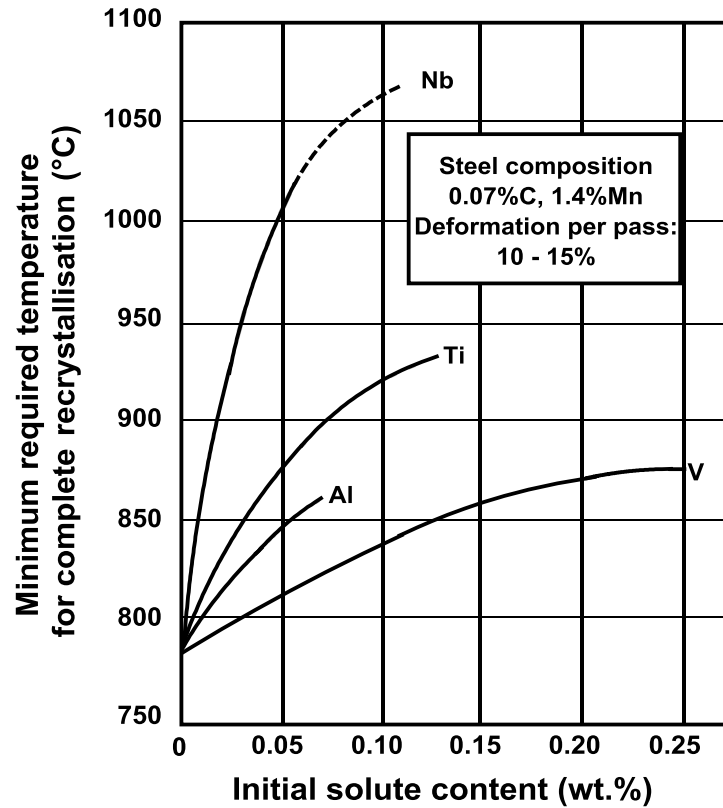
Figure 6. Retardation of recrystallisation by the microalloying elements.

This alloy design therefore offers a number of economical processing advantages over traditional grades, particularly API high strength grades, as pointed out by Ouaissa et al.[27]:

(a) Continuous casting can be successfully achieved over an increased slab width range providing greater tonnage throughput at the slab making operation stage;

(b) Hot ductility is improved and so slab-cracking issues are avoided. This not only avoids the necessity for slab inspections and reconditioning but also provides the opportunity to reduce energy consumption by direct hot charging;

(c) Increased thermal processing window enables more significant slab width reductions at the sizing press;

(d) Finish rolling temperature is increased, ie T_{nr} is raised, and so entry to the finishing mill is increased by roughly 100 ℃ and so provides latitude for increased reductions and/or reduced mill loadings, thus minimising mill wear and tear.

In summary, the alloy design permits steel mills with low tolerable rolling forces to produce high strength steel grades with enhanced toughness [26]. The weldability performance of these steels therefore needs to be more thoroughly understood.

Despite the wide ranging research [28-30] carried out on the role of Nb in steel, there is relatively limited work on the effect of increased Nb levels on weld HAZ grain size control in these low C steels. Therefore, this experimental work was conducted to investigate the effect of Nb and C content on austenite grain coarsening during thermal cycles similar to those experienced in the HAZ of a typical fusion weld. The chemical composition of the studied steels is presented in Table I.

Table I. Chemical Composition (Key Alloy Elements) of the Investigated Steels, wt.%

Steels	C	Mn	Si	Mo	Cr	Nb	Ti	V	N
Steel 1	0.140	1.20	0.27	0.002	0.020	0.001	0.0140	0.006	0.0021
Steel 2	0.085	1.44	0.30	0.010	0.030	0.033	0.0160	0.066	0.0060
Steel 3	0.047	1.59	0.23	0.150	0.031	0.055	0.0077	-	0.0031
Steel 4	0.050	1.61	0.16	0.002	0.240	0.110	0.0120	0.003	0.0048

Three different Nb bearing steels were selected, along with a Nb free steel, all of which contained Ti, and subjected to four different peak temperatures (1050, 1150, 1250 and 1350 ˚C) using a Gleeble 3500 thermalmechanical simulator. The heating rate, dwell time and cooling rate, which are presented in Figure 7, were selected to duplicate typical thermal conditions experienced during actual weld fabrication, but in any case were identical for each steel.
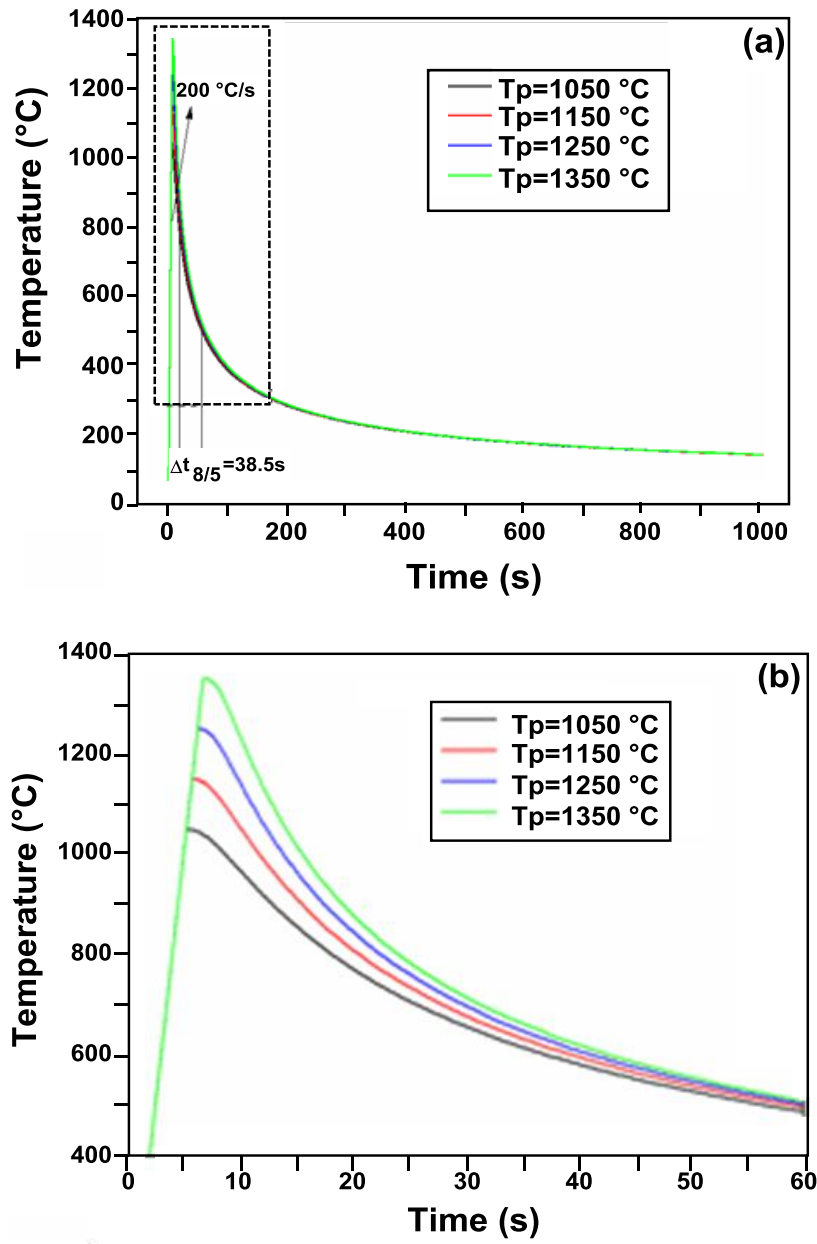
Figure 7. Thermal cycles used for the HAZ simulation of the studied steels;
(a) overview, (b) close-up. Tp is peak temperature.

The average austenite grain size values of the four investigated steels are presented in Figure 8. The measured grain size of the samples subjected to a thermal cycle with a peak temperature of 1050 ˚C was fairly uniform with an average value of ~10 μm. Increasing the peak temperature to 1150 ˚C resulted in significant grain growth in the Nb free steel. A peak temperature of 1250 ˚C stimulated grain growth in all four steels but interestingly, the high Nb steel experienced a rapid increase in grain size, in comparison to 1150 ˚C. As the peak temperature increased to 1350 ˚C, significant coarsening occurred in all the steels except the high Nb steel, where only a slight increase occurred.

Overall, the Nb-containing steels exhibited greater austenite grain size control compared to the Nb free grade while the high Nb, low C steel demonstrated remarkable control at the peak temperature of 1350 ˚C.
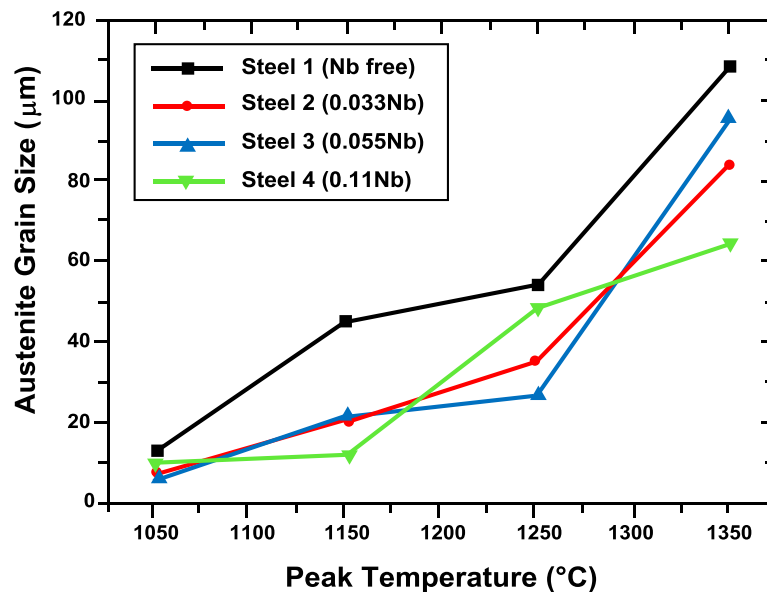
Figure 8. Grain size measurements of the investigated steels at different peak temperatures.

Charpy data from weld thermal simulation trials, where the $\Delta t_{8/5}$ cooling time was varied to simulate differences in weld heat input, is shown in Figure 9. The data confirmed that the extent of toughness degradation in the higher Nb steel was significantly less than that in the more conventional Nb bearing steel 3. Further evidence of the remarkable performance of the high Nb steel is revealed in Figure 10 where the Charpy impact transition temperature is approximately 20 ℃ lower than Steel 3 which can be attributed to the finer grain size and uniform CGHAZ microstructure as shown in Figure 11.

These results demonstrate the ongoing technical development that underpins the increasing versatility of steels in our society and the diligent use of microalloying to improve steel performance.
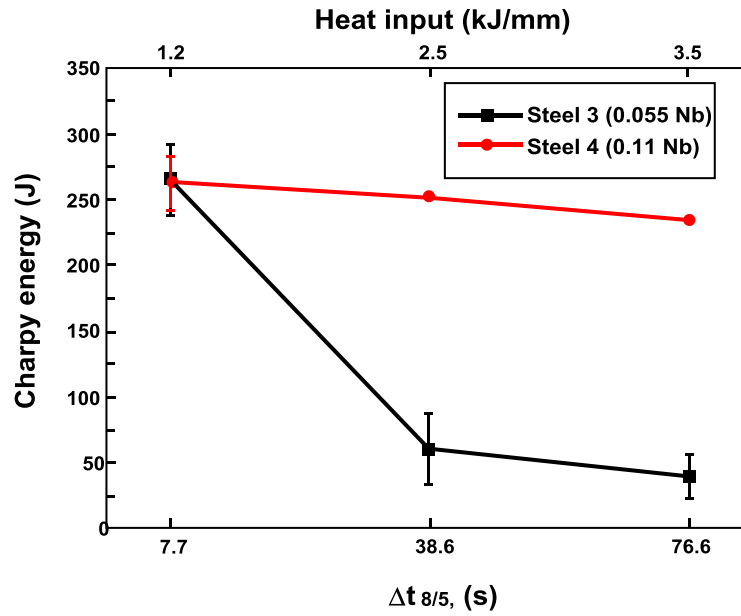
Figure 9. Comparison of Charpy impact toughness (at -20 ˚C) for Steels 3 and 4 as a function of (Δt8/5) weld cooling time, which can be correlated with weld heat input.
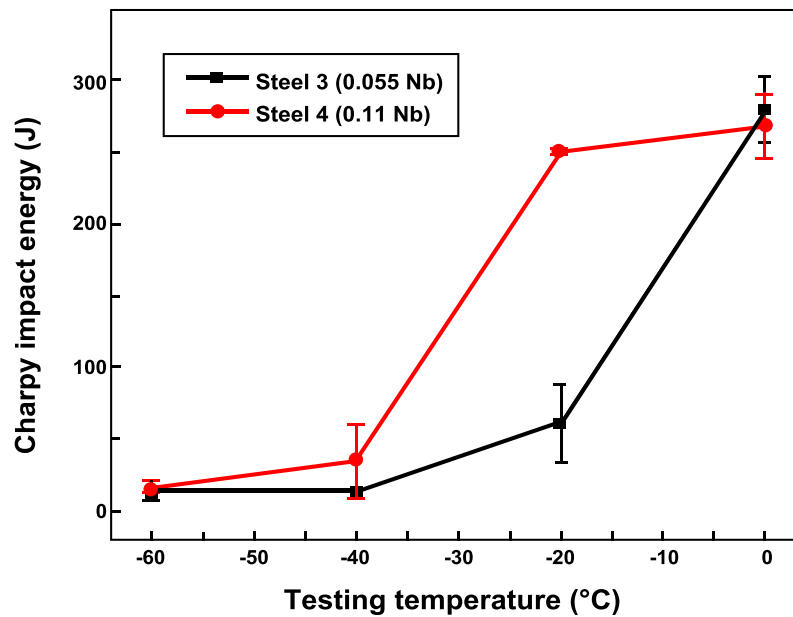
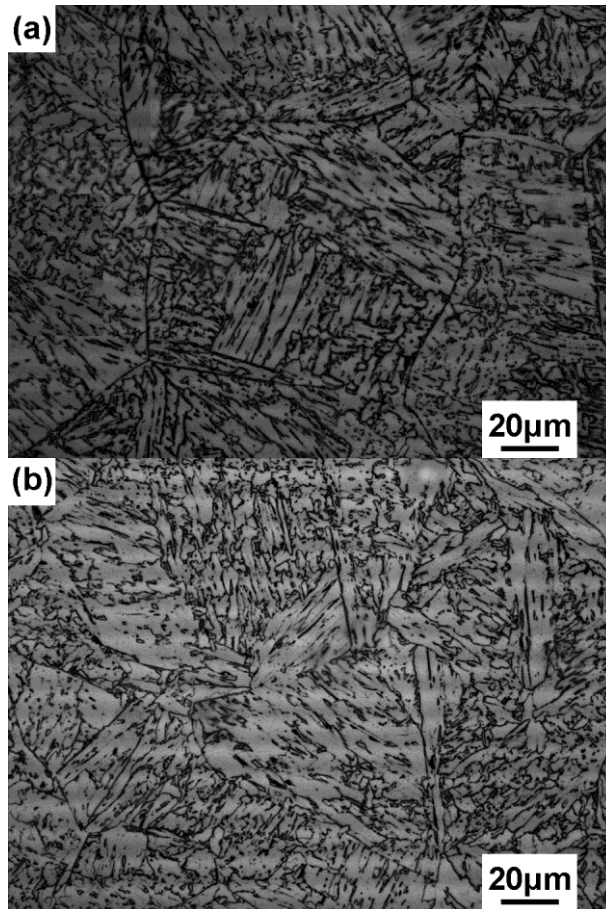Figure 10. Ductile brittle transition curves for Steel 3 and Steel 4.

Figure 11. Representative micrographs of simulated CGHAZ;
(a) Steel 3 (0.055 Nb), (b) Steel 4 (0.11 Nb).

Conclusions

This paper has reviewed the current technology related to the use of Ti in control of weld HAZ properties in high strength steels. The additional results presented have served to highlight the influence of Nb content on HAZ grain coarsening characteristics and weldability.

Interestingly, all investigated steels contained a deliberate addition of Ti which is known to restrict austenite grain coarsening at high temperatures but the role of higher Nb and low C in this work has demonstrated an unexpected beneficial effect.

Nb-Ti microalloyed steels are known to contain complex precipitates which can include (Ti,Nb)(C,N), some can exist as a Ti-rich core and Nb-rich shell structure [31] and others as separate precipitates.

It is also well known that the dissolution of Nb rich precipitates in these steels occurs at a lower temperature than that of Ti, particularly when TiN exists. The fact that the high Nb steel demonstrated superior austenite grain size control at 1350 °C and enhanced Charpy impact toughness in simulated coarse grained HAZ samples, presents an exciting opportunity that could further incrementally improve the weldability and structural integrity of fabricated structures produced from high strength steels.

The mechanism for this performance could be related to a number of different effects which include, but are not limited to:

- Solute drag effects from the presence of Nb in solid solution, from dissolution of NbC and NbCN;
- The role of the Nb rich shell surrounding TiN precipitates, forming a barrier to the coarsening of TiN precipitates;
- Segregation of Nb to austenite grain boundaries [32] and/or decreasing grain boundary energy [33], which can thus retard grain growth.

It is clear that these recent results present an exciting opportunity to further improve the reliability of modern high strength steels and warrants further investigation which is the subject of ongoing studies at the University of Wollongong.

Acknowledgements

References

1. F. Pickering, "Titanium Nitride Technology," *Proceedings of the 35th Mechanical Working and Steel Processing Conference (1993)*, Pittsburgh, Pennsylvania, USA, 477- 494.

2. T. Gladman and D. Dulieu, "Grain-Size Control in Steels," *Metal Science*, 8 (1) (1974), 167-176.

3. A. Batte, P. Boothby and A. Rothwell, "Understanding the Weldability of Niobium-bearing HSLA Steels," *Proceedings of the International Symposium Niobium (2001)*, Orlando, Florida, 2 - 5 December, 2001, 931-958.

4. P. Bateson et al., "Development of TMCR Steel for Offshore Structures," *Proceedings of Structural Materials in Marine Environments (1994),* London, 226-243.

5. T. George and J. Irani, "Control of Austenitic Grain Size by Additions of Titanium," *Journal of Australian Institute of Metals,* 13 (2) (1968), 94-106.

6. F.J. Barbaro and P. Krauklis, "Intragranular Ferrite in Inoculated Low-carbon Steels," invited review paper, *Materials Forum*, 23 (1999), 77-104.

7. C.S. Smith, "Grains, Phases and Interfaces: as Interpretation of Microstructure," *Metallurgical Research and Technology*, 15 (4) (1948), 1-37.

8. B. Loberg et al., "The Role of Alloy Composition on the Stability of Nitrides in Ti-Microalloyed Steels during Weld Thermal Cycles," *Metallurgical and Materials Transactions A*, 15 (1) (1984), 33-41.

9. S. Matsuda and N. Okumura, "Effect of Distribution of Ti Nitride Precipitate Particles on the Austenite Grain Size of Low Carbon and Low Alloy Steels," *Transactions of the Iron and Steel Institute of Japan*, 18 (4) (1978), 198-205.

10. D. Fairchild, D. Howden and W.A.T. Clark, "The Mechanism of Brittle Fracture in a Microalloyed Steel: Part I. Inclusion-induced Cleavage," *Metallurgical and Materials Transactions A*, 31 (3) (2000), 641-652.

11. D. Fairchild, D. Howden and W.A.T. Clark, "The Mechanism of Brittle Fracture in a Microalloyed Steel: Part II. Mechanistic Modeling," *Metallurgical and Materials Transactions A*, 31 (3) (2000), 653-667.

12. K.S. Bang and H.S. Jeong, "Effect of Nitrogen Content on Simulated Heat Affected Zone Toughness of Titanium Containing Thermomechanically Controlled Rolled Steel," *Materials Science and Technology*, 18 (2002), 649-654.

13. J.S. Smaill, S.R. Keown and L.A. Erasmus, "Effect of Titanium Additions on the Strain-aging Characteristics and Mechanical Properties of Carbon-manganese Reinforcing Steels," *Metallurgical Research and Technology*, 3 (1976), 194-201.

14. K.S. Bang, C. Park and S. Liu, "Effects of Nitrogen Content and Weld Cooling Time on the Simulated Heat-affected Zone Toughness in a Ti-containing Steel," *Journal of Materials Science*, 41 (18) (2006), 5994-6000.

15. S.C. Wang, "The Effect of Titanium and Nitrogen Contents on the Microstructure and Mechanical Properties of Plain Carbon Steels," *Materials Science and Engineering A*, 145 (1) (1991), 87-94.

16. J.K. Choi, "Development of High Strength and High Performance Steels at POSCO through HIPERS-21 Project," *Proceedings of the 1st International Conference on 'Super-high Strength Steels' (2005),* 2nd-4th November, Rome, Italy: Associazione Italiana di Metallurgia.

17. Z. Zhu et al., "Influence of Ti/N Ratio on Simulated CGHAZ Microstructure and Toughness in X70 Steels," *Science and Technology of Welding and Joining*, 18 (1) (2013), 45-51.

18. Z. Zhu et al., "Role of Ti and N in Line Pipe Steel Welds," *Science and Technology of Welding and Joining,* 18 (1) (2013), 1-10.

19. G.F. Bowie, R.M. Smith and F.J.Barbaro, "The Influence of Micro Titanium Additions on the Weld Heat Affected Zone Hardness of C-Mn Structural Steels," *Proceedings of the International Conference Welding 90 (1990),* Geestacht, 219.

20. J.M. Gray, "Transformation Characteristics of Very-Low-Carbon Steels," ed. F.J. Barbaro, (Wollongong, 1969).

21. L. Ji et al., "Research on Key Technology and Production Quality of X80 Linepipe for the 2nd West-East Gas Pipeline," *Proceedings of the International Seminar on X80 and Higher Grade Line Pipe Steel (2008)*, Xi'an, China.

22. W.J. Fazackerley, P.A. Manuel and L. Christensen, "First X-80 HSLA Pipeline in the USA," *Proceedings of the International Symposium on Microalloyed Steels for the Oil and Gas Industry (2006),* Araxá, Brasil.

23. K. Hulka and J.M. Gray, "High Temperature Processing of Line Pipe Steels," *Proceedings of the International Symposium Niobium (2001),* Orlando, Florida, 2 - 5th December, 2001.

24. H. Mohrbacher, "Grain Size Control by Niobium Microalloying in Gear Steel during High Temperature Carburizing" (NiobelCon bvba, 2970-Schilde, Belgium).

25. S. Vervynckt et al., "Study of the Austenite Recrystallization - Precipitation Interaction in Niobium Microalloyed Steels," *The Iron and Steel Institute of Japan International,* 49 (6) (2009), 911-920.

26. K. Hulka, P. Bordignon and J.M. Gray, "Experience with Low Carbon HSLA Steel Containing 0.06-0.10 Percent Niobium," *Proceedings of the International Seminar The HTP Steel Project (2003),* Araxá, Brasil.

27. B. Ouaissa et al, "Investigations on Microstructure, Mechanical Properties and Weldability of a Low-carbon Steel for High Strength Helical Linepipe," *Proceedings of the 17th Joint Technical Meeting (2009),* Milan, Italy.

28. E. Palmiere, C. Garcia and A. De Ardo, "Compositional and Microstructural Changes which Attend Reheating and Grain Coarsening in Steels Containing Niobium," *Metallurgical and Materials Transactions A*, 25 (2) (1994), 277-286.

29. L. Cuddy and J. Raley, "Austenite Grain Coarsening in Microalloyed Steels," *Metallurgical and Materials Transactions A*, 14 (10) (1983), 1989-1995.

30. K.A. Alogab, D.K. Matlock and J.G. Speer, "Abnormal Grain Growth During Heat Treatment of Microalloyed-Carburizing Steel," *Proceedings of the Conference on New Developments on Metallurgy and Applications of High Strength Steels,* Buenos Aires, Tenaris Center for Industrial Research, 2008.

31. A. Craven et al., "Complex Heterogeneous Precipitation in Titanium-niobium Microalloyed Al-killed HSLA Steels--I.(Ti, Nb)(C, N) Particles," *Acta Materialia*, 48 (15) (2000), 3857-3868.

32. E. Essadiqi and J.J. Jonas, "Effect of Deformation on the Austenite-to-ferrite Transformation in a Plain Carbon and Two Microalloyed Steels," *Metallurgical and Materials Transactions A*, 19 (3) (1988), 417-426.

33. B. Vynokur, "Influence of Alloying on the Free Energy of Austenitic Grain Boundaries in Steel," *Materials Science*, 32 (2) (1996), 144-157.

PRACTICAL ADVANTAGES OF NIOBIUM AND MOLYBDENUM ALLOYING IN THE PRODUCTION AND PROCESSING OF FORGED ENGINEERING STEELS

F. Hippenstiel

BGH Edelstahl Siegen GmbH
Industriestraße 9, 57076 Siegen
Amtsgericht Siegen, HRB 3578, Germany

Abstract

Ever-increasing quality demands on forged engineering steels require specific modifications of the chemical composition of existing alloys or even necessitate the development of new steel grades. The current paper mainly focuses on the metallurgical principles of addition of niobium and molybdenum to forged case carburising and quenched and tempered steel grades. The influence of niobium alloying on the grain size stability after carburising at high process temperatures, in combination with further development of the typical chemistry of case-hardening steels, has been worked out. An additional practical study shows the effects of microalloying on the grain size of heavy-duty forgings.

Introduction

Forged engineering steels are nowadays used for diverse applications in the automotive and machine building sector. A special feature of this group of products is that steelmakers produce both forged steel bar and open-die forgings for direct use in machine building, as well as forged or rolled billets for conversion in forging shops or ring rolling mills to manufacture finished components. The products therefore have to meet different requirements, giving rise to widely differing demands on the engineering steels and their manufacturing process. In the case of forged steel bar and open-die forgings, as used in machine building and plant engineering, the principal focus is on:

- mechanical properties, and
- testability (especially ultrasonic testing).

Since some particular applications require machining followed by additional heat treatment (eg. case-hardening) or surface finishing, it is desirable to ensure process stability when designing a steel product. It is also an important point in applications of products made from billets, since they undergo further hot forming including (preliminary) heat treatment, and the batch frequency is sometimes high. These factors are now considered in relation to niobium and molybdenum alloyed engineering steels.

Technical Rules for Selecting Forged Engineering Steels

There are various sets of rules for designing machine components, and each manufacturer also draws on its own experience. The principal factors when selecting steel at the engineering design stage are tensile strength and yield strength and also the toughness of the material concept. One of the core questions relates to assessing through-hardenability. In the case of complex, highly stressed components, the aim is to achieve a uniform martensitic/bainitic heat-treated structure throughout the cross-section. Toughness is a measure of the material's potential crack arresting capability, and, in the case of engineering steels, depends on the microstructure or the microstructure homogeneity, and the grain size. When selecting a steel it is therefore necessary to consider that appropriate tempering temperatures can be used to achieve the required strength. There should also be a uniform, homogeneous grain structure. Figure 1 shows the relationship for various steel concepts between the yield strength and the nominal diameter of relevance for heat treatment purposes. This shows that as the alloy content increases, the dimensions associated with through-hardenability increase. With the special grades it should be borne in mind that in some cases other elements, such as niobium, are added as microalloys, and there can also be a reduction in the tramp elements. Metallurgical process engineering measures are also necessary, since high steel purity is required to generate excellent mechanical properties [1].
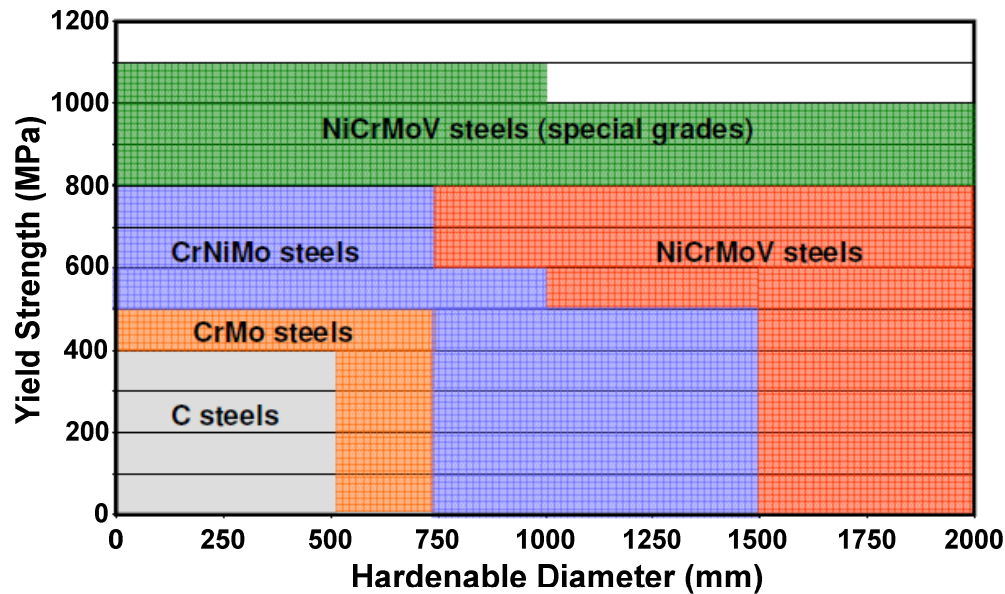
Figure 1. Diagram of the yield strength to be expected across the hardenable diameter for heat treatment purposes for various steel grade concepts.

This paper examines the various alloying concepts in greater detail, using the example of a plastic mould steel, Figure 2. Two fundamental trends are evident in the case of this material. Firstly, the tools for plastics processing are becoming ever larger, and, secondly, steel users specify a relatively high hardness, since this improves machinability (eg. HSC, milling, polishing) [2].
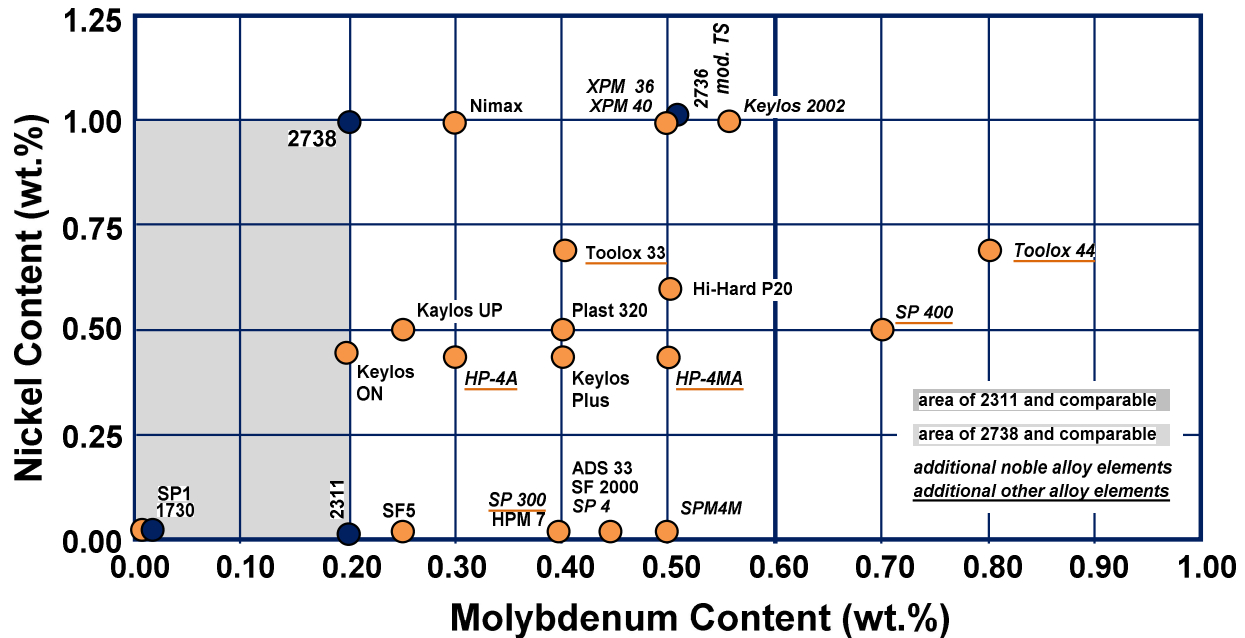
Figure 2. Diagram of the currently available material concepts or steel grades for plastic moulds ("Noble elements": V, Nb, Ti).

Development of the original materials DIN 1.2311 and 1.2738 was therefore pursued in two directions. The nickel and molybdenum content was raised to increase through-hardenability for larger moulds, and the molybdenum content was increased to ensure sufficiently high tempering temperatures, despite high hardness requirements; microalloying elements such as niobium were also added when appropriate.

Optimisation of Case-hardening Steels

Case-hardening steels constitute a special group of steels, since the heat treatment process to chemically influence the surface layer (case-hardening) that follows machining also has to be considered when seeking to achieve the desired optimisation of material properties. This process gives the component (usually a toothed component) a hard surface with a carbon content of around 0.8 wt.% and a tough core with the base carbon content of around 0.2 wt.% that is typical for case-hardening steels. The carburisation process depends on the temperature and time, so it is in the interests of economic efficiency to choose the highest carburising temperatures. Component sizes have also increased over time, so that quite long carburising times are sometimes needed in machine building to achieve the case-hardening depths required by the engineering design.

When optimising case-hardening steels, it is also necessary to consider that process stability is a prime consideration in automotive applications because of the batch frequencies and/or the chain of linked production steps, whereas in applications in machine building and plant engineering the focus is on the material's reliability, especially because of the different load cycles and unit sizes. Analysis of the cost structure of a middleweight goods vehicle revealed that the axle and engine/drive elements make up around 50% of the production cost [3]. There is therefore great potential for reducing manufacturing costs if full use is made of the available properties, or if these can be further improved.

The main parameters of case-hardening steels can be summarised as follows:

- Hardenability and homogeneity;
- Microscopic and macroscopic purity;
- Mechanical properties (strength and toughness);
- Wear resistance at roller contact surfaces;
- Dimensional change and distortion behaviour during and after heat treatment;
- Treatment and machining properties (hot and cold forming and machinability).

Most of these properties are associated with the grain size of the steels. Figure 3, for example, shows the relationship between grain size and the service life of a case-hardened component. This shows that both mixed grain and coarse grain sizes significantly reduce service life [4]. In this example there is a reduction in load capacity of 40% between a fine-grain steel (generally defined by a grain size figure of ASTM = 5 or finer) and a coarse-grain steel.
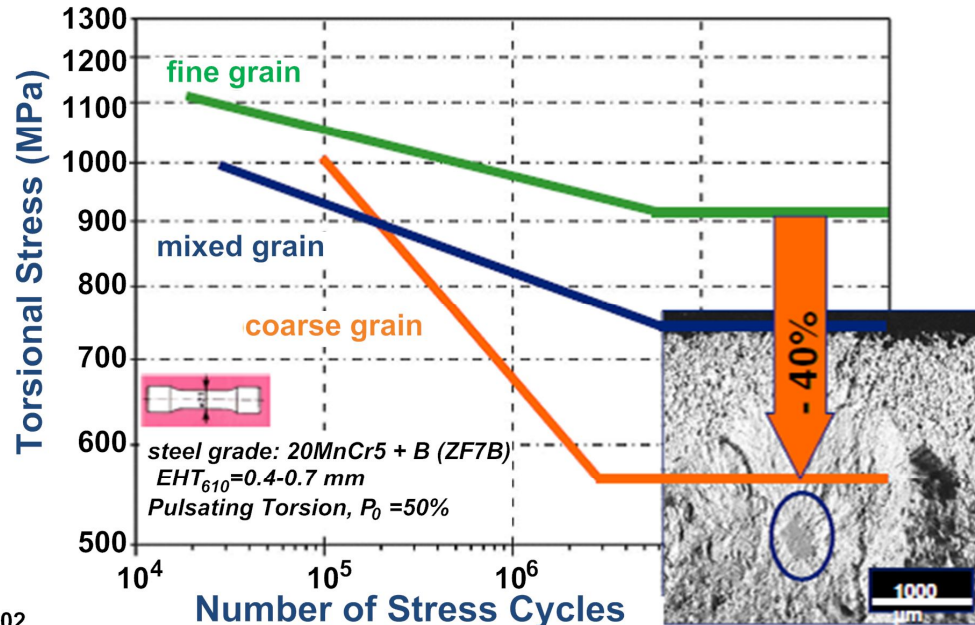
source: Hock, 2002

Figure 3. Relationship between grain size and service life of a case-hardened component.

Some work has been carried out in the past to improve the fine grain stability of case-hardening steels. Aluminium nitrides are generally used to ensure fine grain stability in the case of standard case-hardening steels, but aluminium nitrides dissolve above 950 °C, (or somewhat lower or higher temperatures depending on the steel grade and preliminary heat-treatment condition), and grain growth sets in. Microalloying elements can be added to achieve higher dissolution temperatures making it possible to achieve more economic carburising at higher temperatures. For example, adding niobium causes niobium carbo-nitrides to form in addition to the aluminium nitrides, and the dissolution temperature of these niobium carbo-nitrides is significantly higher than 1050 °C. Another finding is that additional grain refinement can generally be achieved even at lower temperatures by adding microalloying elements. Figure 4 shows this finding in the case of a MoCr steel [5]. Another important factor to consider is the nitrogen content in the steel. In order to create optimum conditions, a minimum nitrogen content of around 100 ppm should be maintained. As already mentioned, fine-grain stability in the case of the classic case-hardening steels also depends on the production conditions and heat-treatment cycles. A further reason for adding microalloying elements in case-hardening steels is to ensure fine-grain stability regardless of process route.
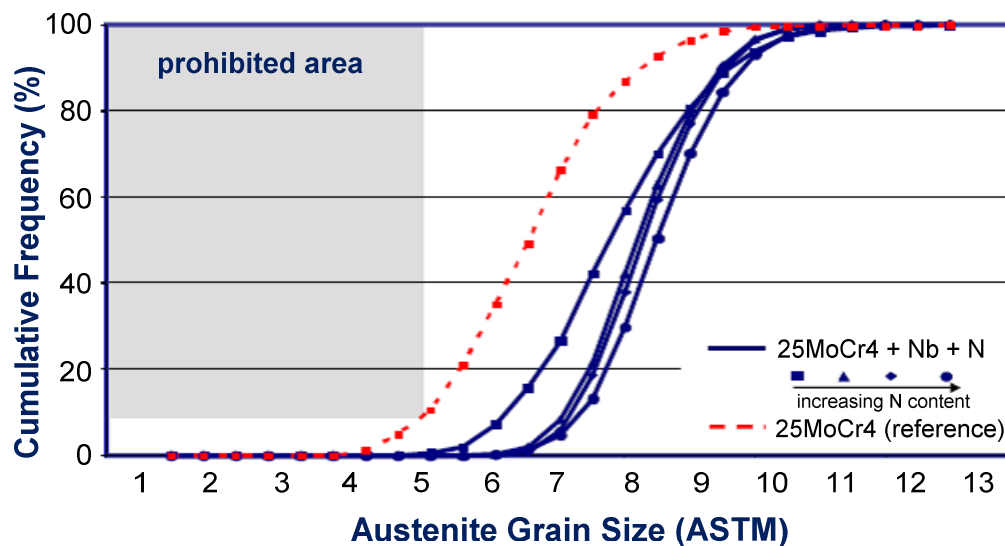
Figure 4. Grain growth tests of microalloyed melts of a MoCr steel in the ferrite-pearlite annealed pre-condition after 950 °C and 25 hours holding time [5].

Figure 5 shows the result of a test on a melt of material 25MoCr4 [6]. Here too, around 300 ppm of niobium was added as an alloy, and grain growth tests conducted on samples taken from rolled billets (as rolled) and from drop forgings subsequently produced (FP annealed). It is evident that the fine-grain stability with a grain size of ASTM 5 or finer is guaranteed in both cases at 1050 °C and a holding time of 30 hours. This example indicates no correlation with the production route or the process route selected.
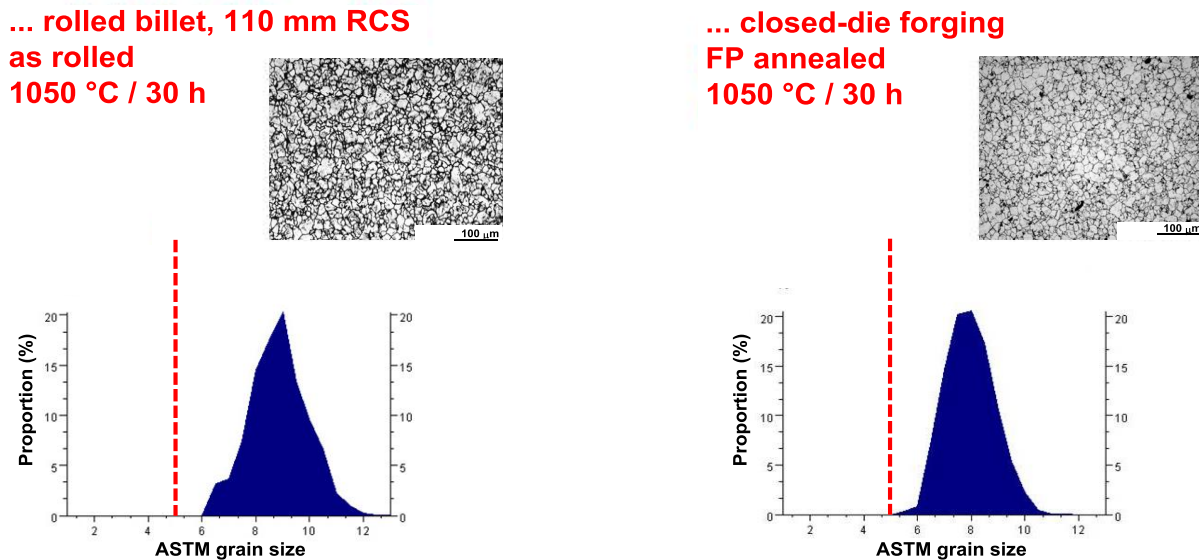
Figure 5. Fine grain stability of a microalloyed 25MoCr4 steel in two different product forms (rolled billet and closed-die forging, same melt) 30 hours holding time at 1050 °C [6].

A further advantage of microalloying in case-hardening steels arises from a process stability improvement in downstream processing of the steel. Due to the reduced spread of grain sizes observed, a lower spread of dimensional changes and distortion can be expected. A seminal study by Randak [7] was supplemented by further studies on components made of forged steel bar; these studies likewise illustrated a positive effect with the observed grain being achieved by adding microalloying elements, Figure 6 [8].
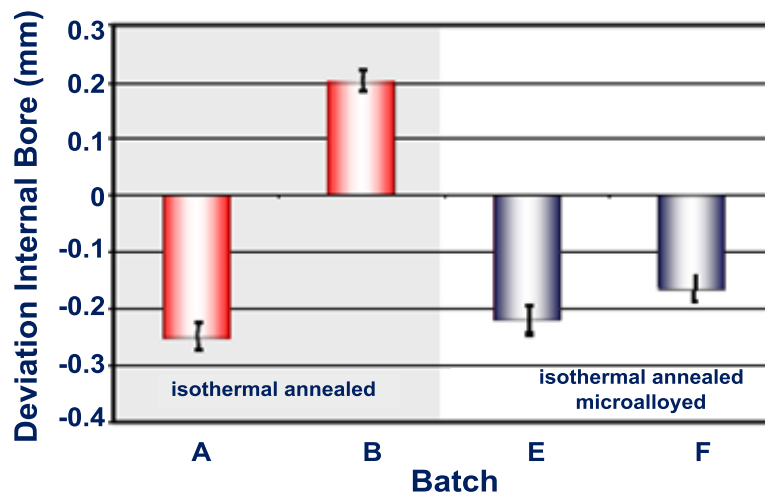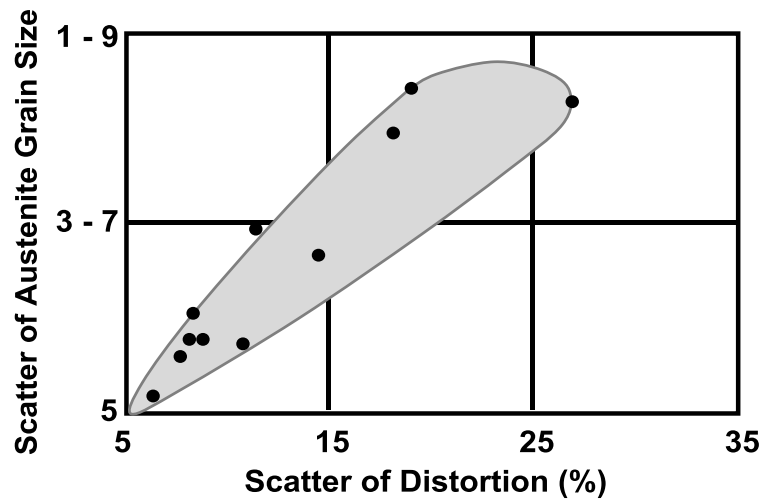
Figure 6. Relationship between grain size and microstructure on the dimensional change and distortion of case-hardened components [7,8].

Increasingly stringent quality requirements for steel grades resulting from new challenges in machine building and plant engineering are also leading to a constant ongoing development of existing materials. For case-hardening steels, the scope for development is principally as follows:

- Increase core strength and toughness;
- Increase fatigue strength under reverse bending stresses;
- Increase hardenability;
- Reduce or homogenise dimensional change and distortion.

Table I shows the chemical composition and the mechanical properties of more recent material concepts compared to the 18CrNiMo7-6 grade to DIN EN 10084/9/. The first concept seeks to satisfy the future requirements for larger gear units, and represents a higher strength variant of the case-hardening steels (new steel concept 1). Hardenability has basically been increased compared to the standard steel 18CrNiMo7-6 by increasing the manganese and molybdenum content. The nickel and chromium content was reduced for reasons of alloying efficiency. It would in principle also be possible to add niobium to promote grain refinement. The second concept shows an economic variant of the standard steel 18CrNiMo7-6, which is designed to achieve alloying efficiency without significantly changing the properties required. For example, hardenability was increased by increasing manganese and chromium, based on a molybdenum chromium steel. In order to achieve toughness comparable to a nickel alloyed case-hardening steel, niobium was added as an alloy. The intention is to form stable special carbides with molybdenum, promoting the steel concept's fine-grain stability. There is also a comparison of the mechanical properties of the two new steel concepts after blank hardening at 880 °C/2 hours/oil quench/180 °C/2 hours. The enhanced hardenability of the new steel concept 1 is also expected to be evident in the figures for tensile strength, and in rotating-bending fatigue tests. It also shows that the toughness values are still at quite a good level despite the high strength achieved. It was observed as regards the new steel concept 2 that strengths comparable to the alloy-efficient concept can be achieved with only a moderate loss of toughness. Further characteristics of the two materials are currently being studied in a publicly funded project [10].

Table I. Overview of Chemical Composition and Mechanical/Technological Characteristics of More Recent Steel Concepts for Case-hardened Components [10].

Steel Grade	C	Si	Mn	Cr	Mo	Ni	Nb
20MnCr5 mod.	0.26	0.12	1.46	1.23	0.54	0.91	-
20CrMo5 mod.	0.21	0.25	1.17	1.15	0.21	0.22	0.04
18CrNiMo7-6 (1.6587)	0.15/0.21	≤ .40	0.50/0.90	1.50/1.80	0.25/0.35	1.40/1.70	-

content (wt.%)

	Concept 1 20MnCr5 mod.	Concept 2 20CrMo5 mod.	18CrNiMo7-6
Tensile strength, R_m (MPa)	1758	1182	1182
Impact energy, A (J)	47	55	80
Rotating fatigue limit $\sigma_{(50\%)}$ at $N=10^7$(MPa)	722	491	510
Hardenability at 11 mm (HRC)	51	44	41
Hardenability at 25 mm (HRC)	50	36	36

Grain Size Control in Heavy Forgings

Large open-die forgings for power generation plant construction are considered particularly challenging. Ever larger forgings are needed as power densities increase, also necessitating the processing of very large ingots that now reach weights of up to 650 tonnes. But there are nevertheless still high expectations as to their mechanical properties (strength and toughness) and through-transmission characteristics in ultrasonic testing which also makes grain size an important factor in this steel application. Niobium can also be used as a microalloying element to enhance grain sizes in the case of heavy forgings. Figure 7 shows a result of a study carried out on a plastic mould steel. The grain sizes were simulated for a relevant nominal diameter for heat-treatment purposes of 1130 mm. Despite the addition of niobium as a microalloying element, it is evident that after the forming process proper, grain sizes increase again as the forging cools [11].
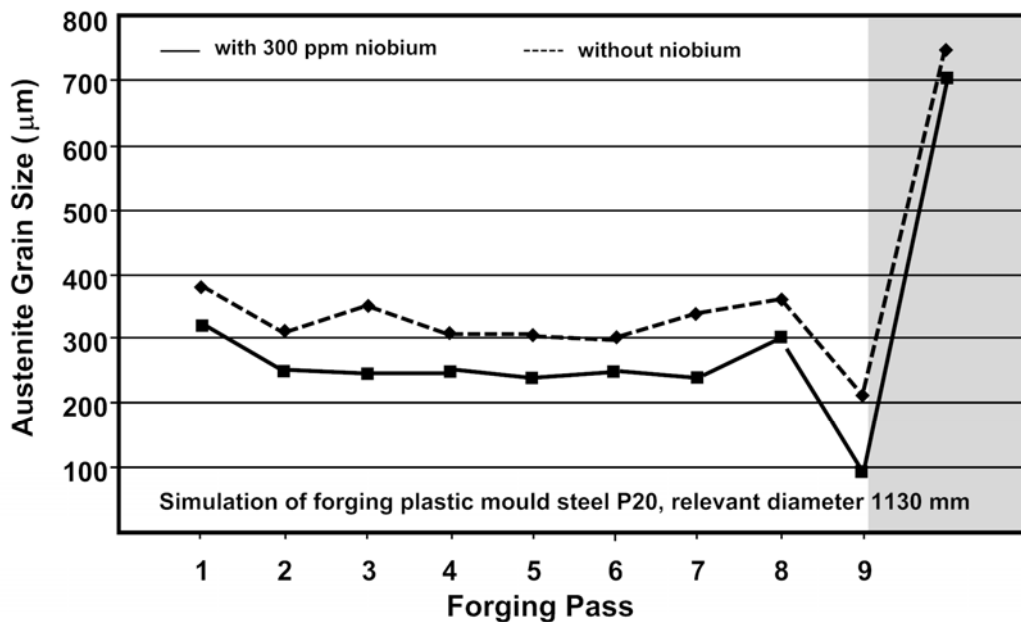
Figure 7. Effect of niobium on the austenite grain size in the core of a forging during and after the forging process and cooling in air to 800 °C [11].

The results of the simulations carried out are consistent with the results of tests using a hot-forming simulator. Figure 8 shows the grain sizes determined using metallographic methods for samples forged in the laboratory with similar parameters to the industrial production process. The grain size tends to be somewhat finer in the case of the niobium alloyed variant. It should however be noted that in the example quoted, the hot-forming temperature was above the solution temperature of the niobium carbo-nitrides. A further study is therefore required to determine the effect of the forging temperatures [11].
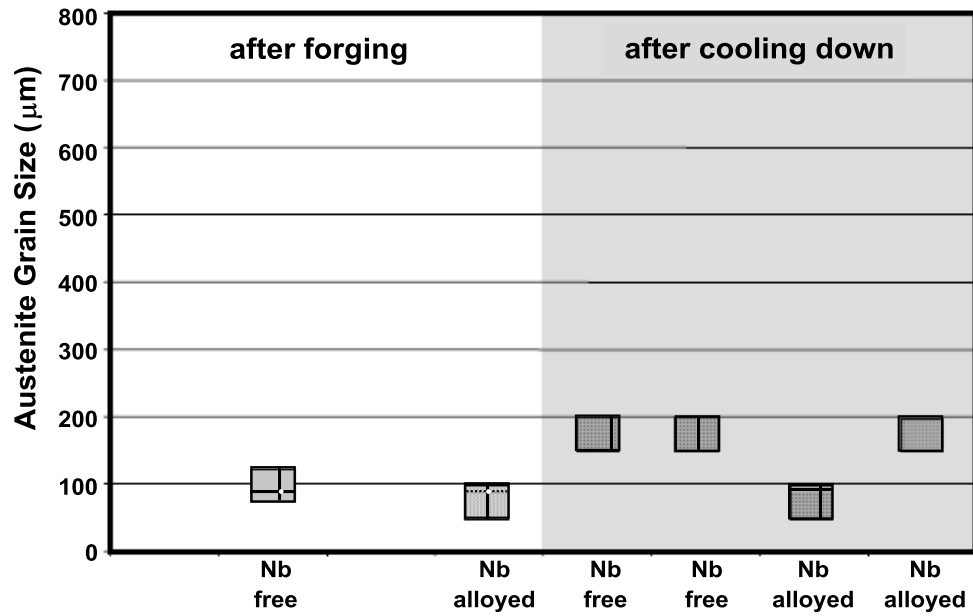
Figure 8. Austenite grain size in the surface layer of a forging after the forging process and cooling in air determined by hot forming tests [11].

Figure 9 summarises this study; in this case upsetting tests were carried out with two different melts of material 27NiCrMoV11-6. The aim was to compare the grain sizes of a conventional melt with a microalloyed melt at various forging temperatures, decreasing through A, B and C. As the result shows, there is a significant difference between the worst and best case.

It is, therefore, possible to have a beneficial effect on the grain sizes of a forging by adding niobium and selecting a temperature range [12].
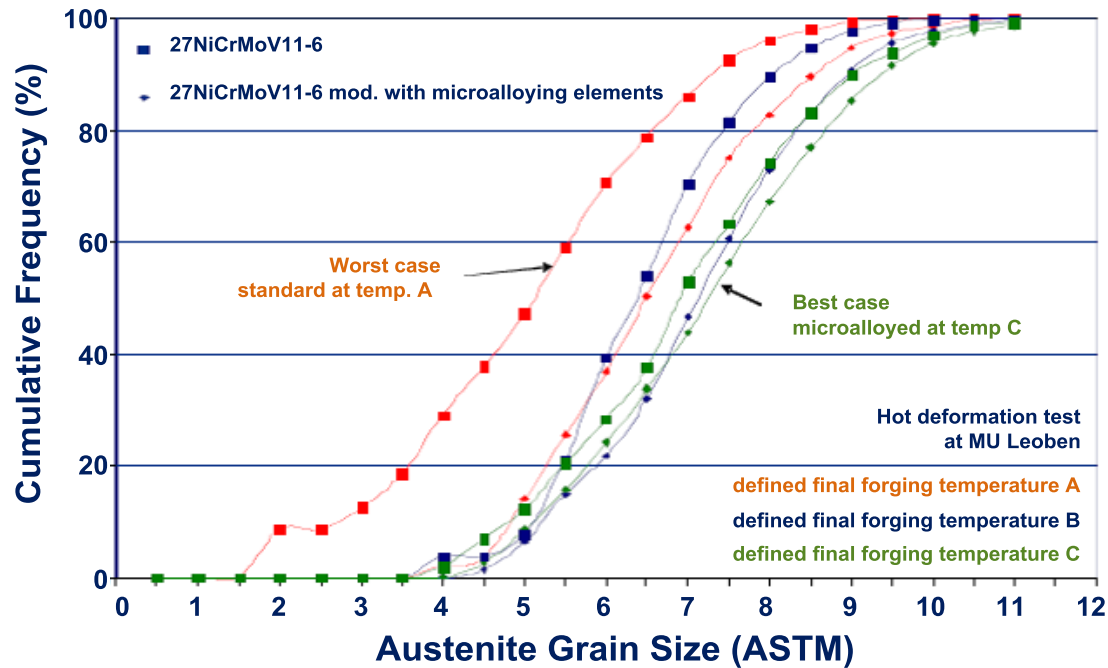
Figure 9. Grain size distribution of upsetting tests as a function of chemical composition and process parameters in forging [12].

Conclusions

The alloying elements molybdenum and niobium offer numerous practical benefits for forged engineering steels on tempering. Molybdenum contributes principally to increasing through-hardenability and hardness retention, thus steel grades for larger components in particular are alloyed with molybdenum. An additional point here is also that molybdenum suppresses temper brittleness in forgings. Adding niobium provides a way forward in the development of existing steels. Especially in steels with molybdenum, very fine and stable special carbides form because of the synergistic interaction between molybdenum and niobium, which can be used to improve the mechanical and technological properties. In case-hardening steels, this can be used to homogenise the grain size, also improving the fine grain structure and stability, regardless of process routes. Niobium can furthermore affect grain sizes at the production stage, which is of particular relevance in the case of heavy forgings made from large blooms with a corresponding solidification cross-section. This may also provide a route to simplifying the heat-treatment sequence in the case of large forgings, without having to accept constraints on ultrasonic inspection.

References

1. W. Grimm, A. Mukhoty and D. Römpler, "Einfluss verschiedener Schmelzvarianten auf die Mechanischen Eigenschaften von Einsatzstählen," *Zeitschrift für Wirtschaftliche Fertigung*, 4 (77) (1982), 194.

2. F. Hippenstiel et al., Handbook of Plastic Mould Steels, (Edelstahlwerke Buderus AG, 2004).

3. M. Keppel, MAN, private communication, 7th December, 2007.

4. S. Hock et al., "Einfluss von Umform- und Wärmebehandlungsfolgen auf Korngröße und Schwingfestigkeit von Einsatzgehärteten Bauteilen," *Harterei-Technische Mitteilungen (HTM),* 1 (54) (1999), 45.

5. F. Hippenstiel, "Improvement Working and Utility Properties of Classical and New Mo Alloyed Carburizing Steels," *Proceedings of 3rd International Conference on Steels in Cars and Trucks, SCT* (2011), 314.

6. F. Hippenstiel and R. Caspari, "Einsatzstähle für die Hochtemperaturaufkohlung in der Praxis," Heat Treatment Colloquium 2005, Wiesbaden.

7. A. Randak and R. Eberbach, "Einfluß der Austenit-Korngröße auf einige Eigenschaften des Stahles 16MnCr5," *Harterei-Technische Mitteilungen (HTM),* 3 (24) (1969), 201.

8. F. Hippenstiel, "Metallurgical and Production-related Protocols to Reduce Heat-treatment Distortion in the Manufacture of Gear Components," *Proceedings of the International Conference on Distortion Engineering, IDE* (2005), 57.

9. DIN EN 10084:2008: Case Hardening Steels – Technical Delivery Conditions.

10. H. Mohrbacher and F. Hippenstiel, "Optimization of Molybdenum Alloyed Carburizing Steels by Nb Microalloying for Large Gear Applications," *Proceedings of the Materials Science and Technology (MS&T) Conference* (2011), Columbus, Ohio, 446.

11. W. Grimm and F. Hippenstiel, "Controlling Grain Size in the Manufacture of Large Open-die Forgings" (Paper presented at the International Forgemasters' (IFM) Meeting 2003, Kobe), 310.

12. F. Hippenstiel and S. Schramhauser, "Forging our Future, Capabilities – Challenges – Opportunities," 18th International Student's Day of Metallurgy 2011, Leoben, 106.

SLIP-ROLLING RESISTANCE AND LOAD CARRYING CAPACITY OF 36NiCrMoV1-5-7 STEEL

C. Scholz[1,2], M. Woydt[1] and H. Mohrbacher[3]

[1]BAM Federal Institute for Materials Research and Testing, 12200 Berlin, Germany
[2]KYB Corp., 252-0328 Sagamihara, Japan
[3]NiobelCon bvba, 2970 Schilde, Belgium

Keywords: Molybdenum, Steel, Slip-rolling Resistance, High Contact Pressure, Oil

Abstract

The approaching CO_2 targets have now forced automotive OEMs to direct R&D efforts in the powertrain to reduce friction and increase lifetime as well as load carrying capacities of running systems. Martensitic steels such as 36NiCrMoV1-5-7 have a great potential to be used in automotive powertrain applications owing to their favorable mechanical properties. In order to realize lightweighting strategies it is essential that steels with improved fracture toughness values, as well as higher annealing temperatures with regard to higher contact pressures and possible thin film coating application, should be considered. State-of-the-art steels, like 16MnCr5, 21NiCrMo2, 30CrMoV9 and 100Cr6, are not able to sustain a further increase in torque or load during use, as well as annealing effects under higher oil or deposition temperatures. Therefore, recent research has explored the slip-rolling resistance, frictional and wear behavior of steels, such as 36NiCrMoV1-5-7, Cronidur 30 (AMS 5898), 20MnCr5 (SAE 5120) and 100Cr6H (SAE E52100), and this has shown that possible lean alloying concept alternatives with promising performance characteristics are already available.

Introduction

Highly concentrated or loaded contacts in powertrain, bearing and gear applications offer significant savings in CO_2 emissions. Today, thin film coatings, alternative base oils and new additives are popular as fields of work. In order to meet the CO_2 target of 2020 for passenger cars (95 g.CO_2/km), determined by the European Union [1], there is still a need for optimization of driving concepts. Although in public, the internal combustion engine is seen as the focus of efficiency gains, the whole powertrain offers at least the same scope for improvements. There are two reasons:

  (a) Lightweight design;
  (b) Reduction in friction without reducing the lifetime.

Lightweighting strategies increase the contact stresses above P_{0max} of 2.14 GPa (or FZG load stage 14) due to the reduction of component sizes. These demands directly raise questions about the suitability of the most promising technical solution. Steels with improved mechanical properties, ie. toughness values, which are offering a reduced coefficient of friction, resistance to high contact pressure and potential to apply a low friction surface coating represent a valid alternative to conventional gear and bearing steels. Traditional bearing steels, like 100Cr6

(SAE E52100) have reached their mechanical limits at contact pressures above FZG load stage 14. Furthermore, increased torques or contact pressures push the oil film temperatures on the gear tooth flanks to 200 °C, exceeding the tempering temperatures of state-of-the-art steels used in gear technology, like 20MnCr5 (SAE 5120), 21NiCrMo2 (1.6523), 30CrMoV9 (1.7707) or similar. In addition, the same tempering effect on steel surfaces can be observed during the deposition of thin film coatings, like DLCs or comparable coatings [2]. Figure 1 shows the influence of temperature on hardness values of different steels used for slip-rolling contacts. The real temperatures on surfaces during coating exceed in most cases 180 °C during deposition times ranging from five to eight hours. Both factors trigger metallurgical changes.

Nitrogen alloyed steels, like Cronidur 30 (AMS 5898, 1.4108) or XD15NW, which have a high annealing resistance of above 380 °C, are globally not widely available and are expensive due to their special manufacturing process, heat treatment and the N_2 furnaces needed. Embargo and Dual Use Regulations limit the direct and indirect use of some alloys, including Maraging steels. Therefore, alternative steels are required offering annealing temperatures far above 250 °C using simple production processes and heat treatment cycles. Higher deposition temperatures would be desired for enhancing metallurgical bonding of thin films through diffusion.
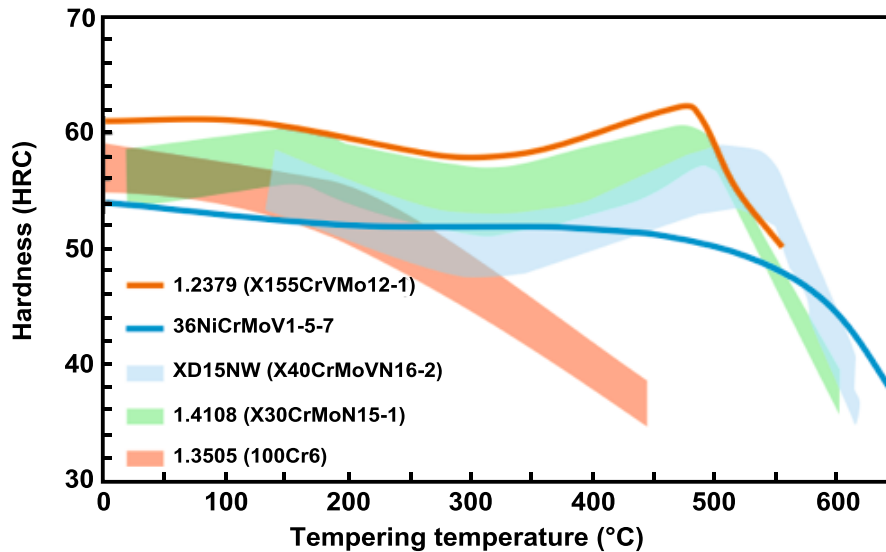
Figure 1. Tempering charts of different bearing and gear steels showing the influence of temperature on hardness.

Recent investigations on the slip-rolling resistance of silicon alloyed steels with improved toughness values and low contents of high-cost alloying elements showed promising test results [3,4]. Silicon alloyed steels V300 (1.8062) and NC310YW (40SiNiCrMo10) displayed also a load carrying capacity in the mixed/boundary lubrication regime up to 2.5 GPa. Furthermore, the steel V300 can offer a friction reduction of approximately 40% compared to commonly used steel-steel combinations.

The design recommendations in DIN 3990, part 5 and ISO 6336-5 mention only surface hardness and allowable stress. Gear applications, which require high toughness and long fatigue life at the very high loads impacting tooth flanks and toes of the gear teeth, cannot be realized by using the aforementioned low-alloy case hardening steels, such as 20MnCr5 (1.7147) or 27MnCr5 [5,6]. Distortion of parts, as well as grain growth, are enhanced by case hardening and thermochemical treatments.

Currently the molybdenum alloyed steel 18CrNiMo7-6 (<0.25 wt.%Mo) is used as standard for windmill gearbox applications. Alloying steels with higher molybdenum contents such as 2% instead of the standard 0.25% provides a hardness value above 700 HV even after tempering at 300 °C (see Figure 2). Thus, the tempering resistance of steel can be strongly improved by adding significant contents of molybdenum as well as optionally niobium, Figure 3. The effects of molybdenum and niobium alloying are shown in more detail in [7].
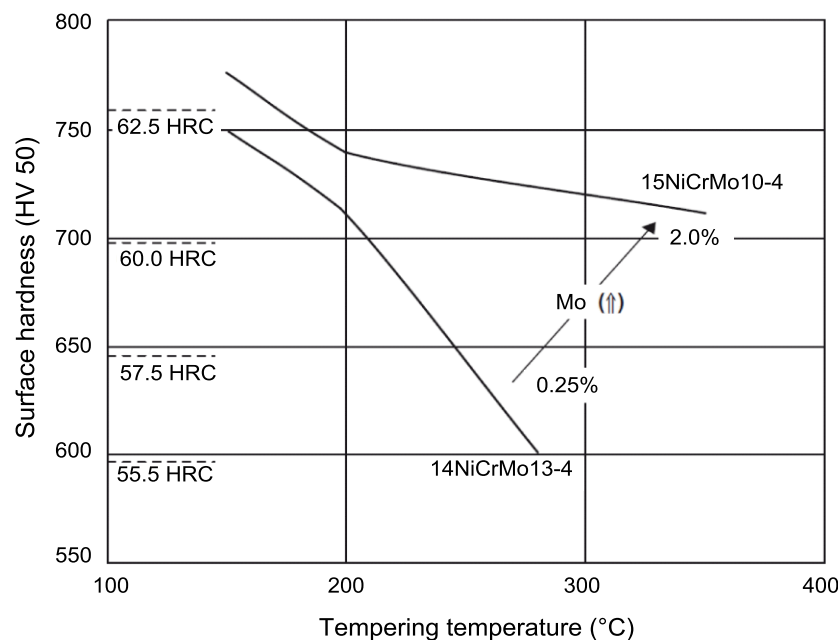
Figure 2. Effect of molybdenum alloying on the tempering resistance of case carburized, quenched and tempered steels [5].
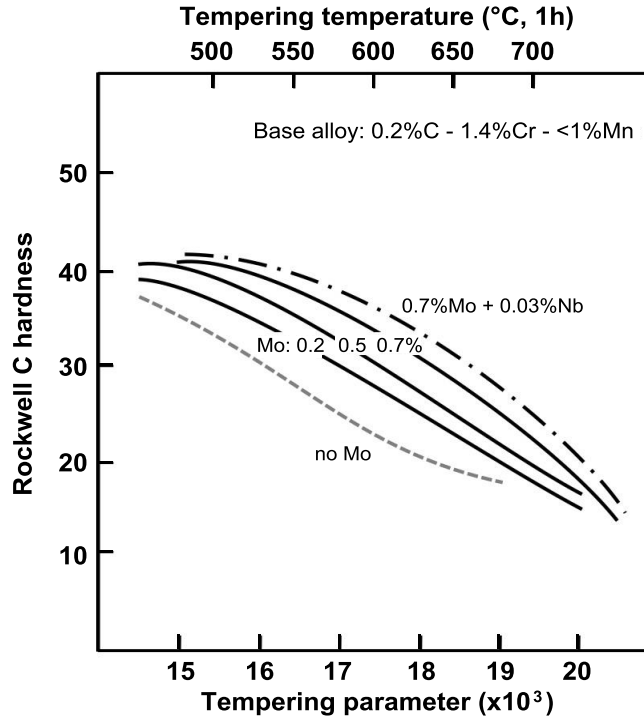
Figure 3. Effect of increasing Mo additions and Nb micro-alloying on the tempering resistance. (Tempering Parameter = $(T(20+\log(t))$ where T is in Kelvin and t in hours) [7].

The present study investigates the slip-rolling resistance and load carrying capacity of the molybdenum alloyed steel 36NiCrMoV1-5-7 in comparison to 20MnCr5, Cronidur 30 and 100Cr6 for contact pressures (P_{0max}) of up to 3.8 GPa, in order to investigate its potential as an alternative steel for bearing or gear components.

Experimental Details

Material Selection

In previous investigations on the slip-rolling resistance of thin film coatings [8,9,10,11], the substrates were mainly made of the well-known bearing steels 100Cr6H (OVAKO PBQ, double remelted) and Cronidur 30 which is a martensitic cold working steel melted under pressurized nitrogen. Due to use of a PESR process (Pressure Electroslag Remelting) in combination with sophisticated rolling technology, extremely high cleanliness and a homogeneous structure with increased lifetime properties can be obtained in comparison to 100Cr6, at a maximum hardness of 60 HRC. Better corrosion and wear resistance can be achieved by partially replacing carbon with nitrogen which is retained in solution. Another positive aspect of this steel grade is its high temper resistance up to 500 °C [12]. Both steels 100Cr6H and Cronidur 30 are widely used in the bearing industry and were therefore selected as reference materials to 36NiCrMoV1-5-7.

194

Table I. Room Temperature Mechanical Properties of Materials Tested After Heat Treatment

Material	100Cr6H (SAE E52100)	Cronidur 30 (AMS 5898)	20MnCr5 (1.7147)	36NiCrMoV1-5-7
Density ρ (g/cm^3)	7.8	7.67	7.85	-
Young's Modulus E (GPa)	210	213	210	215
Elongation (%)	n.d.a.	<5	~ 10	~ 12.5
Hardness (HRC)	65.8	62.2	~ 47	~ 54
Fracture Toughness K_{IC} (MPa√m)	~ 16.5	~ 21	n.d.a.	120
Charpy Toughness KV (J)	-	-	25	30
Ultimate Strength R_m (MPa)	~ 2300	~ 2300	~ 900	1474
Residual Austenite (vol.-%)	6.8	22.5	6.3	<2.5
Maximum Service Temperature (°C)	150	475	180	510

n.d.a. = no data available

Table I summarizes the mechanical properties of the steels tested after heat treatment. The residual austenite contents of all tested materials were determined by means of X-ray diffraction (XRD) directly after receiving the samples from heat treatment.

Table II. Chemical Composition Determined by Spark Emission Spectroscopy of 100Cr6H, Cronidur 30, 20MnCr5 and 36NiCrMoV1-5-7 (wt.%)

Material	C	Si	Mn	P	S	Cr	Mo	Ni	N	V
100Cr6H	1.0	0.25	0.35			1.50				
20MnCr5	0.17-0.23	0.15-0.40	1.10-1.40	≤0.035	≤0.035	1.00 - 1.30				
Cronidur 30	0.25-0.35	<1.0	<1.0			14.0-16.0	0.85-1.1	<0.5	0.3-0.5	
36NiCrMoV1-5-7	0.3	0.25	0.2	0.002	0.002	1.50	0.8	3.0		0.3

Case-carburized 20MnCr5 is, in effect, a reference alloy for gear applications, comparable to AISI 52100 for bearings. In comparison to the other steels, 20MnCr5 is the only one which received a thermochemical treatment (case-carburization). Carburizing steels for gear components is a standard procedure in order to guarantee a hard and failure resistant material surface. It has to be noted that the carbon concentration in the surface region of 20MnCr5, ranging to slightly above 1.0 wt.% carbon, exceeds those stated in Table II due to case hardening. In ISO 6336-5 it is stated that the carbon content of the case area after carburization should lie in the range of 0.7 to 1.0 wt.%. The elemental concentrations in the carburized surface regions of 20MnCr5 were determined by SEM-EDX, spark emission spectroscopy and electron microprobe analysis. The carbon concentration ranged between 0.90 to 1.20 wt.%C. Finally, the surface of the case hardened 20MnCr5 is from a metallurgical point of view only slightly different from 100Cr6H (SAE E52100). The chemical composition of Cronidur 30, as well as 100Cr6H and 36NiCrMoV1-5-7, used as tribological test materials, are summarized in Table II. Using spark emission spectroscopy, the amounts of alloying elements in comparison to standard specifications were determined before tribological tests were conducted in order to guarantee the required quality of the materials. As mentioned in [9], the use of high quality substrate materials, ie. without segregation or porosity, impurities and defects due to the production process, is necessary for applications in highly loaded contacts to ensure the highest possible lifetime. With regard to a possible coating of the substrates, the selected steel has to withstand temperatures up to 300 °C without decreasing its hardness or changing its structural constitution.

Contrary to other state-of-the-art slip-rolling steels, 36NiCrMoV1-5-7 is a cost-attractive alternative offering several benefits, including:

- Elevated tempering temperatures above 300 °C, favoring the application of thin film coatings, such as diamond-like carbon or Zr(C,N) without causing microstructural changes in the substrate during deposition (see heat treatment chart in Figure 4);
- Simplified heat treatment cycles and manufacturing routes;
- Reduced friction for uncoated steel under mixed/boundary conditions;
- High load carrying capacity;
- Straightforward and simple heat treatment;
- Low wear as uncoated steel, similar to thin films;
- Tribological compatibility with state-of-the-art lubricants.
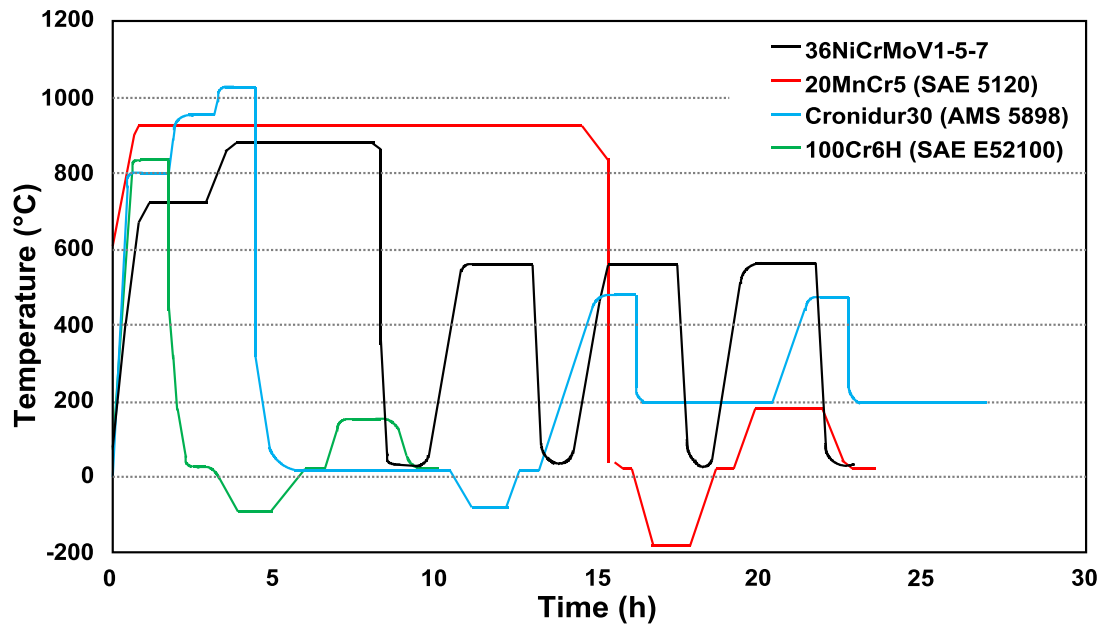
Figure 4. Schematic heat treatment curves of the steels 36NiCrMoV1-5-7, 20MnCr5, Cronidur 30 and 100Cr6H.
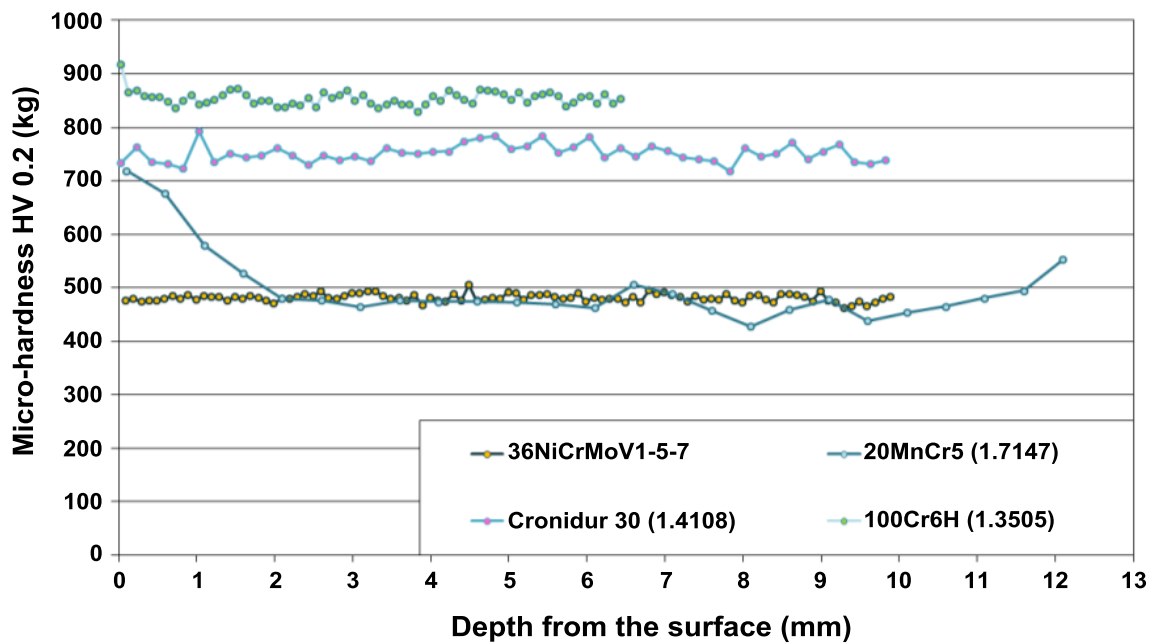

Figure 5. Hardness profiles of bearing and gear steels after heat treatment.

The hardness of the steels after heat treatment is shown in Figure 5. The high hardenability of the steels means there is little fall off in hardness below the sample surface except in the case of the 20MnCr5 which has received a case hardening treatment.

According to Figure 6, the metallographic analysis of the material structure, it can be stated that all steels show a broadly fine, martensitic structure. According to the aforementioned XRD analysis, Table I, Cronidur 30 contains a residual austenite content of 22.5 vol.%, which is not clearly visible in the micrograph. Inclusions within the structure were detected only in the case of 36NiCrMoV1-5-7. The influence of these inclusions in relation to the slip-rolling resistance will be considered below. Due to PESR (Cronidur 30) and VIM-VAR (100Cr6) procedures during the steelmaking process, nonmetallic inclusions could be minimized. 20MnCr5 revealed low amounts of manganese(II) sulfides within its structure.
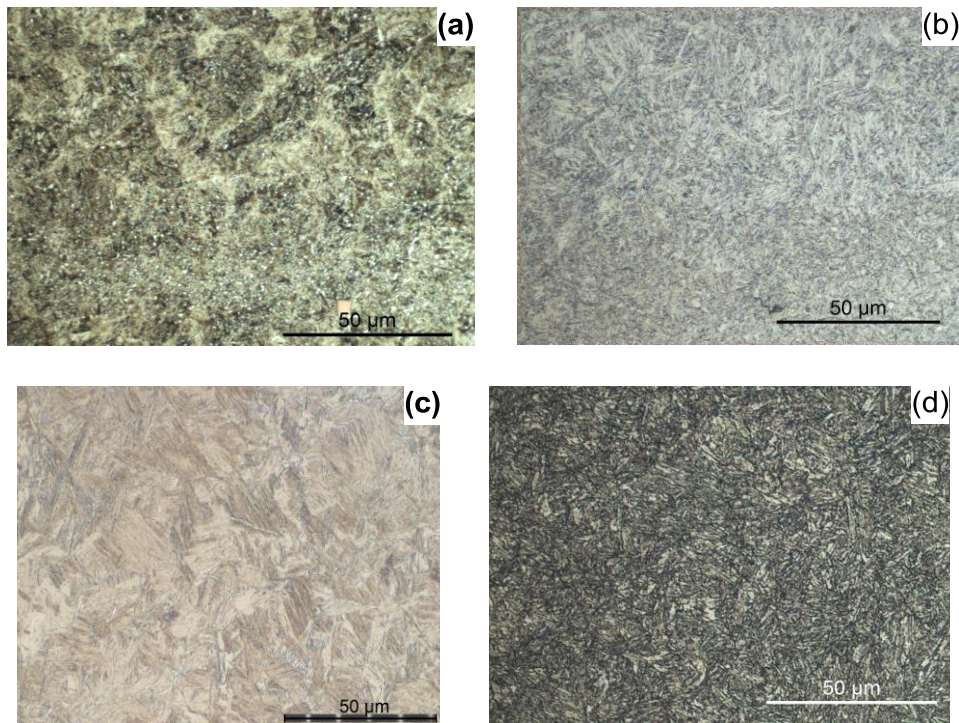
Figure 6. Optical micrographs of the etched material structure; (a) 100Cr6H, (b) Cronidur 30, (c) 20MnCr5 and (d) 36NiCrMoV1-5-7.

Slip-rolling Test Devices

All tribological slip-rolling investigations were carried out on an Amsler-type machine or on an Optimol 2Disk tribometer. Originally developed for simulation of wheel-rail contact processes, twin disk testing machines offer an optimal basis for experiments on highly concentrated contacts in combination with the selected surface roughness to operate in the mixed boundary lubrication regime. Nowadays, new twin disc machines can be used for the characterization of tribological systems under dynamic test conditions in terms of slip ratio. Mimicking the working conditions and contact configuration of gear teeth in contact and ball bearings, these testing machines are widely used.

In the Amsler and 2Disk tribometers, two discs with the same diameter roll against each other on their cylindrical surfaces. Using a single electrical motor and several coupling shafts, which ensure the mixed boundary lubrication regime at the start, the rotation speed is fixed at 390 rpm. To enable a continuous slip of 10%, the second disc, applied as the counterbody, is driven at a speed of 354 rpm. The exact sample configuration in this tribometer is shown in Figure 7.

For the Amsler machine the geometry of the discs, with an outer diameter of 42 mm and a width of 10 mm, generates a contact configuration of the ball-cylinder type. In order to avoid distortion of the test samples due to the heat treatment, pre-forms for the test samples were manufactured from the raw material (steel rod). These pre-forms have a stock allowance of approximately 0.3 mm on the diameter, width and inner hole dimensions. After the heat treatment the samples were processed by grinding and polishing to their final cylindrical and spherical shapes with the desired surface finish. In the present experiments the top, ball-shaped counter discs were mainly uncoated and only pre-polished or ground ($R_a \sim 1.5$ µm). The lower, cylindrical discs were used both in the coated and uncoated states with a highly polished surface ($R_a \sim 0.005$ µm). A normal force was applied by means of a spring, leading to a normal force up to 2,000 N (initial average Hertzian contact pressure $P_{0mean} = 1.94$ GPa) at the contact point (see Table III). The stiffness of the spring (14,650 N/m) and the lever action of the counterbody holder press the discs against each other. By controlling the compression of the spring the normal force can be adjusted in steps of 50 N. For comparison, an average contact pressure of P_{0mean} of 1.25 GPa corresponds to a maximum Hertzian contact pressure of $P_{0max} = 1.875$ GPa, which is equivalent to load stage 12 in the FZG test rig. According to the international standard ISO 14635-1, this load stage is the most demanding test procedure for gears using state-of-the-art gear oils. The hydrocarbon-based lubricant used was a synthetic factory fill-engine oil SAE 0W-30 named VP1 (ACEA A3/B4, long life, $HTHS^{150°C} = 3.0$ mPas) with a content of sulfated ash of 1.20 wt.%. In general, engine oils have much higher additive treatment rates than gear oils, because engine oils require dispersants and detergents beside viscosity index improvers, as well as higher total base numbers (TBN). The kinematic viscosity at 120 °C was $\nu_{120 °C} = 5.33$ mPas and the pressure viscosity coefficient α for 1-1,001 bars at 120 °C was 12.8 GPa^{-1} [13]. The calculated value of minimum oil film thickness h_{min} at T = 120 °C and $F_N = 930$ N (or $P_{0mean} = 1.50$ GPa) is 0.027 µm, for $F_N = 2,000$ N (or $P_{0mean} = 1.94$ GPa) is 0.025 µm or for $F_N = 5,000$ N (or $P_{0mean} = 2.62$ GPa) is ~0.024 µm. The roughness values R_a of the uncoated steels ranged between 0.15-0.35 µm (spherical disk) and ~0.0035 µm (cylindrical disk) in the initial state resulting in a Tallian parameter, λ, between ~0.077 and 0.068, which denotes the regime of boundary friction. At 120 °C, the calculated oil film thicknesses are $\approx 1/10$ of those at RT. The Hertzian contact

stresses are at 120 °C, likely to be transmitted through the micro-asperities and not by hydrostatic pressure generated from a hydrodynamic oil film.
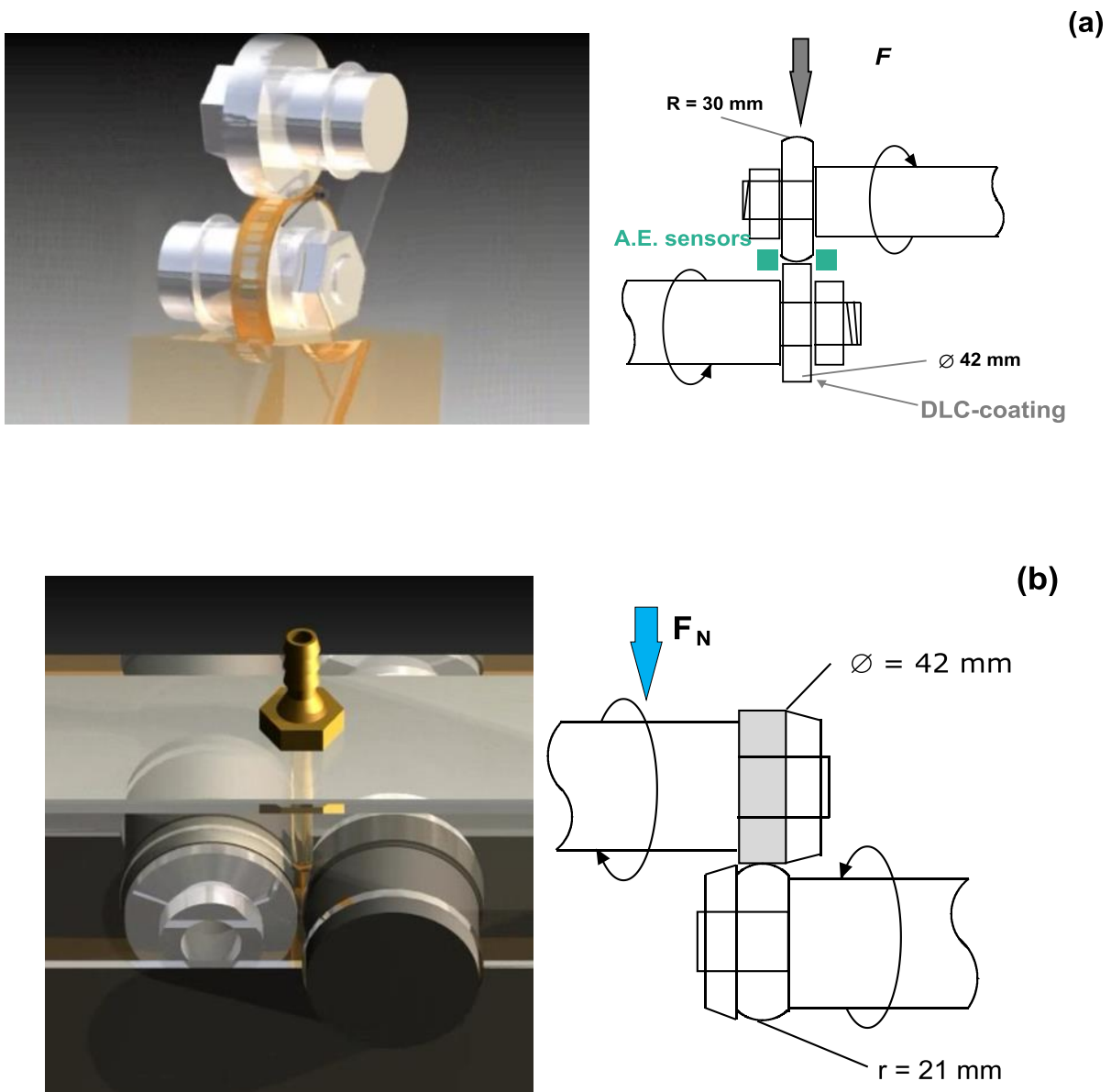

Figure 7. Sample arrangement in the twin disk tribometer; (a) AMSLER tribometer, (b) 2Disk from Optimol Instruments.

Table III. Experimental Conditions

Conditions	Parameter
Dimensions of the discs	Diameter: 42 mm; Width: 10 mm
Contact	Ground/polished curved disc (radius of curvature: 21 mm) against uncoated highly polished cylindrical disc
Substrate	36NiCrMoV1-5-7, 20MnCr5, Cronidur 30, 100Cr6H
Type of motion	Rolling with a fixed slip rate of 10%
Initial average Hertizian contact pressure P_{0mean}	1.5 – 2.62 GPa (F_N = 930 – 5,000 N)
Rotation at speed	390 – 354 rpm
Sliding speed at V_{diff}	0.08 m/s
Load cycles n_{tot}	Up to 10^7 or rupture (damaged surface area of >1 mm^2)
Effective sliding distance	Up to 132 km
Ambient temperature	120 °C oil bath temperature
Lubricant	BMW FF SAE 0W-30 'VP1' ACEA A3/B4 ($v^{120\,°C}$ = 5.33 mPas; $HTHS^{150\,°C}$ = 3.0 mPas)

In order to create experimental conditions as close as possible to real applications, the bath temperature of the oil is set at 120 °C. For safety, the temperature is controlled by a second thermal sensor couple with a programmable relay, reducing the temperature if it exceeds 140 °C. The lower cylindrical disc dips into the heated oil reservoir and drags the lubricant into the contact area due to the rotation. During the tests the friction torque can be measured by the axial torque of the lower shaft rotating at 390 rpm with use of a pendulum as well as a planetary gearing coupled with the mentioned axis. The coefficient of friction (COF) can be evaluated with the following equation:

$$\mu = M/(F_N \cdot r) \tag{1}$$

In this equation, M is the friction torque in Nm, F_N the applied normal force in N and r the radius of the driven sample in m. The deflection of the pendulum is converted into a translation movement for the measurement of the corresponding torque scale. A Linear Variable Differential Transformer (LVDT) permits the transduction of this movement into an electrical signal and records directly the COF [9].

The experimental setup in the newly designed Optimol 2Disk tribometer, similar to the Amsler type tribometer, generates a ball-cylinder contact mechanism using the same test samples. Designed for very high normal forces up to 5,000 N the tribological behavior of thin film coatings and their substrates can be tested under extreme conditions. This tribometer applies average contact pressures up to 2.62 GPa and can realize any slip ratio. Table IV summarizes the normal forces with the corresponding contact pressures (average P_{0mean} and maximum P_{0max}) and total deformation values of both samples according to Hertz' theory [14].

Table IV. Hertzian Contact Pressures for the Sample Geometries Tested

Normal force (N)	930	2,000	4,400	5,000
P_{0mean} (GPa)	1.5	1.94	2.5	2.62
P_{0max} (GPa)	2.25	2.91	3.75	3.92
Total deformation/flattening in the center of contact (µm)	13.4	21.2	37.8	41.2

The 2Disk test rig is powered by two electric motors, which rotate independently of each other. Thus, the slip rate of the two discs, as well as rotation speed, are freely adjustable, driven by an integrated computer control unit. In order to ensure the comparability and consistency of the test results obtained on both test machines, the experimental conditions (rpm, slip rate, lubrication and temperature) are always kept identical, with the exception of the Hertzian contact pressure. As shown in the test arrangement (c.f. Figure 7), the samples are positioned on the same vertical level, whereas the load application is induced by an electrical servomotor. This servomotor compresses a spring fixed between motor and axle of the cylindrical disc. It thereby adjusts the previously set normal force.

The test software is designed to measure the friction force as well as wear rates of both samples and plot it *in situ*. In contrast to the Amsler-type tribometer, the test sample does not dip into the oil reservoir. The oil is fed by a gear-type pump within a circular flow into the contact point of both samples in order to enable high speeds.

The quantification of the volumetric wear rates of the steel samples was taken to be the tribological criterion for the tests. Four profiles on each sample were taken by tactile profilometry perpendicular to the sliding direction, spaced at an angle of 90°. The measured average worn surface $\overline{W_q}$ permits the calculation of the volumetric wear rate, k_V, by the following equation:

$$k_V = \frac{V}{F_N \cdot L} = \frac{\overline{W_q} \cdot 2\ \pi\ r}{F_N \cdot n \cdot 2\ \pi\ r} \tag{2}$$

In this equation, V represents the worn material volume, F_N the applied normal force, r the sample radius, n the number of revolutions and L the distance run under sliding. Due to the low depth of the track, the wear volume V is equal to the planimetric wear surface $\overline{W}_q$ multiplied by the circumference of the sample.

Experimental Results

The slip-rolling tests were carried out by using the aforementioned test devices and conditions at four load stages. At P_{0mean} = 1.5 GPa and 1.94 GPa, the Amsler type tribometers were used. On increasing the applied contact pressure to 2.5 GPa and 2.62 GPa the tests were executed using the high performance Optimol 2Disk tribometer. Following the tests, optical microscopy images were taken of the wear track generated under the applied Hertzian contact pressure. In order to

consider the performance of the different uncoated steels, the evaluated wear rates and coefficients of friction at the beginning and at the end of tests respectively were used for tribological assessment. Figure 8 shows the morphologies of the wear tracks on the cylindrical test sample and on its respective spherical counterbody at the four different load stages. In the case of steels 100Cr6H and 36NiCrMoV1-5-7 the tests at 2.62 GPa contact pressure were not conducted due to failures on the steel surface at a lower load stage.
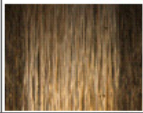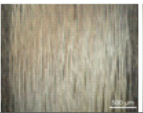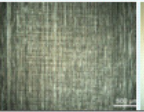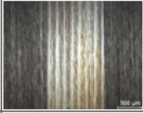
Material	1.5 GPa (930 N)		1.94 GPa (2,000 N)		2.5 GPa (4,400 N)		2.62 GPa (5,000 N)	
	Counterbody	Test Sample	Counterbody	Test Sample	Counterbody	Test Sample	Counterbody	Test Sample
100Cr6H	10^7 cycles		10^7 cycles		6.75 - 10^6 cycles			
Cronidur 30	10^7 cycles		10^7 cycles		10^7 cycles		10^7 cycles	
20MnCr5	10^7 cycles		10^7 cycles					
36NiCrMoV1-5-7	10^7 cycles		10^7 cycles		10^7 cycles			
	1.34 - 10^7 cycles		2.18 - 10^6 cycles		5.14 - 10^6 cycles			
	9.59 - 10^6 cycles		10^7 cycles		10^7 cycles			
	8.88 - 10^6 cycles		10^7 cycles		10^7 cycles			
	9.0 - 10^6 cycles		10^7 cycles					

Figure 8. Optical light microscopy photographs of the typical wear tracks of rolling steel/steel contact displaying their morphology at different load stages, P_{0mean} = 1.5 to 2.62 GPa.

All optical pictures were taken after the upper testing limit of 10 million load cycles or upon the occurrence of the failure criterion (damaged area >1 mm²). In order to make the test results more comparable and reliable the candidate material 36NiCrMoV1-5-7 was tested at 1.5 GPa and 1.94 GPa in each case five times whereas at 2.5 GPa four tribological tests were conducted.

Considering the test results by looking at the light microscopy images taken after testing, it became clearly visible that 36NiCrMoV1-5-7 showed at all load stages a very inhomogeneous material behavior. 36NiCrMoV1-5-7 can be essentially slip-rolling resistant under P_{0mean} of 2.5 GPa, but individual samples failed at each loading level, or level of contact stress, before the end of the test at 420 hours (10 million load cycles) and showed serious damage to the surfaces. This behavior directly raises the question about the reasons as the slip-rolling resistances lie outside of the Lundberg-Palmgren relation.

All test results of 36NiCrMoV1-5-7 are shown in a summary diagram in Figure 9. The logarithmic y-axis indicates the number of cycles reached. In this figure, the load stages are represented by different colors, using at each stage the same lubricant SAE 0W-30 VP1. When the tested steel pairing reached the test end of 10 million slip-rolling cycles, a red dotted line symbolizes the good performance desired, with the indication that the steel could sustain the tribological stresses longer. In the grey boxes, top and bottom, the type of the steel counterbody and test sample are reported. At the base of the bars in the yellow boxes are the wear rates of the spherical and cylindrical samples determined after the tests. (In cases where fatigue failure occurred during the test, no wear rate was calculated.) The small vertical bars represent the coefficients of friction at the beginning (left) and at the end (right) of the tests.
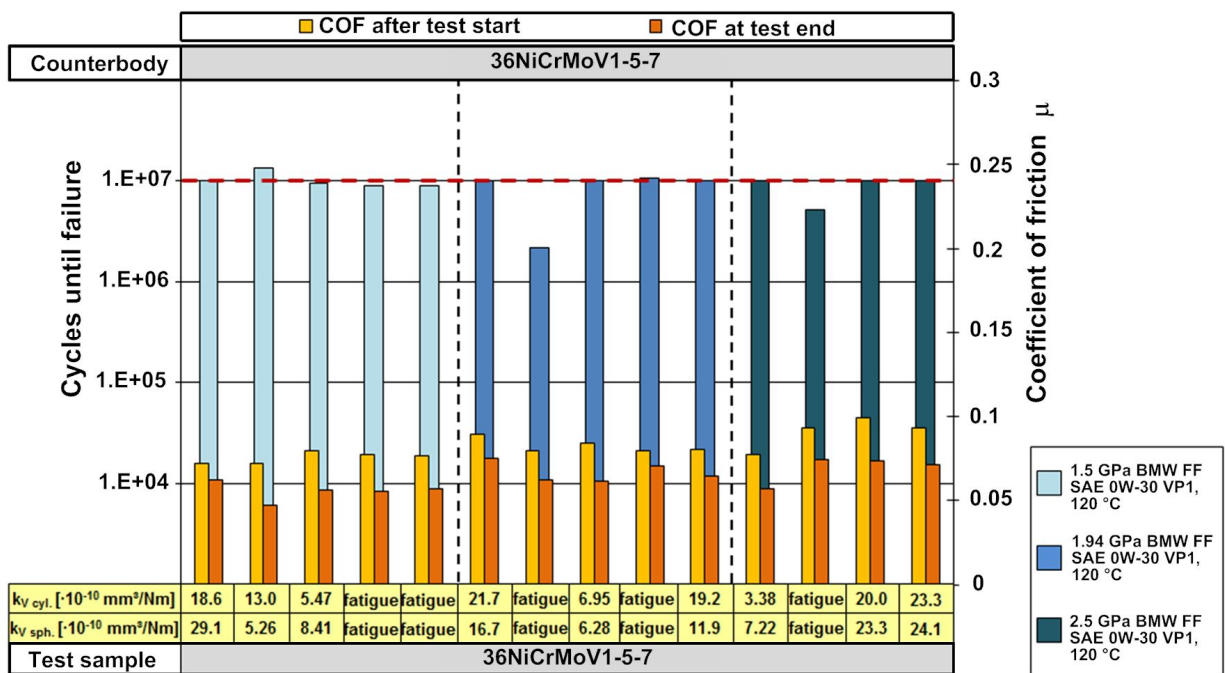

Figure 9. Number of load cycles reached, COF and wear rates of self-mated 36NiCrMoV1-5-7 samples under slip-rolling conditions.

204

Figure 9 illustrates once again the inhomogeneous test results for load cycles obtained as a function of contact pressure. Otherwise, the COF at test beginning and end shows good, reproducible and consistent results. At 1.5 GPa the initial COF ranges from 0.072 to 0.079 and furthermore the COF at test end lies between 0.047 and 0.062. On this occasion, a damaged and roughened surface does not seem to have any influence on the COF. A possible explanation of the inhomogeneous behavior of the 36NiCrMoV-5-7 alloy can be the presence of inclusions throughout the material volume (cf. Figure 10). The analysis revealed calcium sulfide (CaS) as well as aluminum oxide (Al_2O_3) and magnesium oxide (MgO) inclusions, see Figures 10(c) and (d), and alumina-silicates. These result from the calcium-argon treatment (CAB). The significant non-metallic and metallic inclusion populations act as crack initiators, especially when they are locally agglomerated directly beneath the stressed surface. Therefore, inclusions are able to initiate microcracks during the cyclic contact stresses introduced by the rolling load in the shallow layer beneath the raceways. Eventually, the microcracks can break through the raceway surface and spalling may occur, leading to the total failure of the material [15]. Non-metallic inclusions have their origin in melting and casting during the steelmaking process in an air environment. Thus, techniques such as vacuum induction melting (VIM) and vacuum arc remelting (VAR) are necessary to improve the cleanliness and homogeneity of highly stressed steels to avoid rolling contact fatigue.
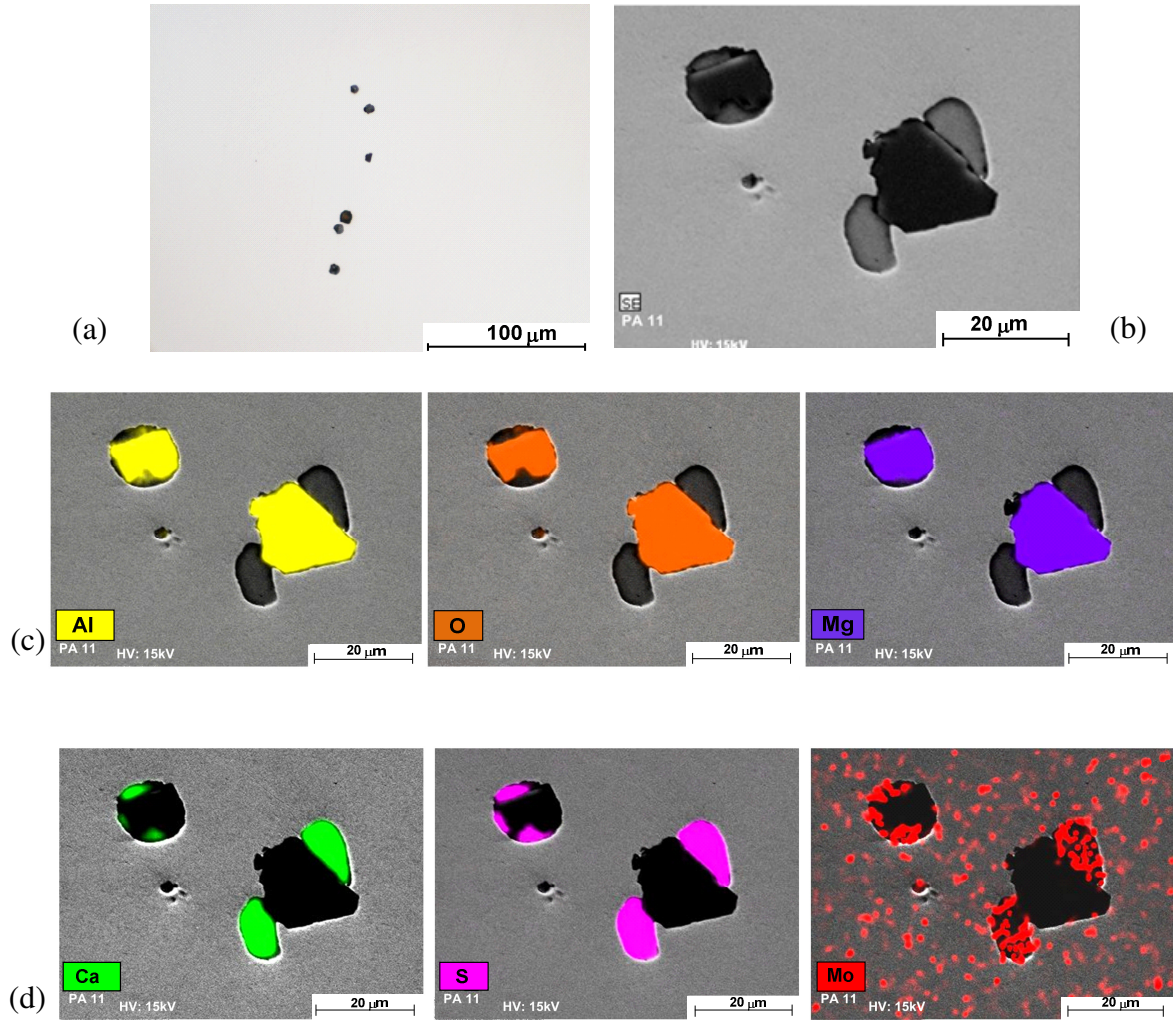
Figure 10. (a) Light microscopic image in cross section of 36NiCrMoV1-5-7 showing the presence of inclusions within the bulk material, (b) SEM image of inclusions in detail, (c) and (d) SEM/EDX element mapping images of inclusions.

Despite the question of "early" failures, the wear data in Figure 9 illustrate that the wear rates of 36NiCrMoV1-5-7 are more or less independent of the contact stress. This means that the load can be increased without compromising the load carrying capacity and wear as well as in terms of adhesive failures (seizures, galling). Furthermore, Figure 9 also reveals that the lower hardness level of ~ 480 HV 0.2 (see Figure 5) does not necessarily increase wear.

Considering the evolution of the coefficient of friction as a function of the test duration (10 million load cycles) in endurance tests conducted in the present work, the tribological benefit of the alternative steel 36NiCrMoV1-5-7 at $P_{0mean} = 1.5$ GPa becomes clearly visible (see Figure 11).

In comparison to conventional bearing steels, such as 100Cr6H and Cronidur 30 tested under identical conditions, 36NiCrMoV1-5-7 could reduce the friction values by approximately 30%.

In order to confirm these results, the test was repeated four to five times, using the same testing machine and conditions. Consequently, the low friction values of around 0.055 and down to 0.050 could be reproduced at $P_{0mean} = 1.5$ GPa. In the light of this comparison, it may be concluded that the reduction of friction by an optimal choice of the interaction between uncoated materials and lubricants could be achieved. Thus it allows the substitution of thin film coatings by an alternative steel, such as 36NiCrMoV1-5-7. However, the inhomogeneous slip-rolling resistance of 36NiCrMoV1-5-7 must be taken into account, which can be improved by different production processes to give a lower inclusion content.
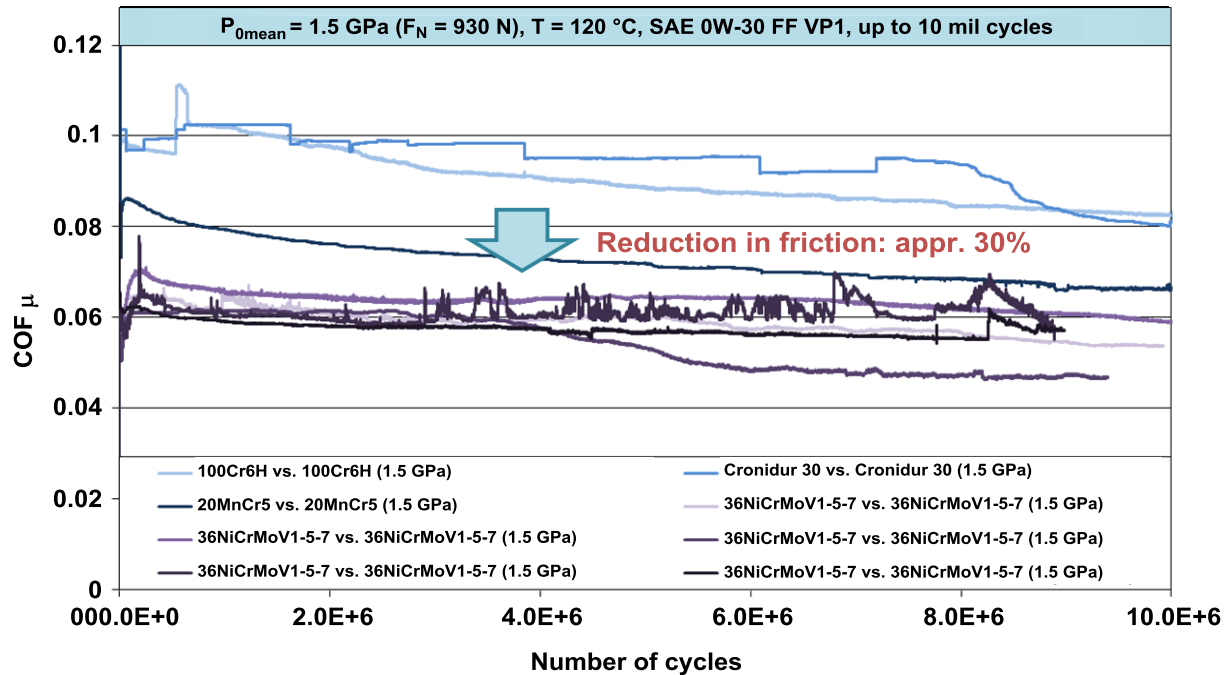

Figure 11. Evolution of the coefficient of friction over the test period of 10 million load cycles at $P_{0mean} = 1.5$ GPa and T = 120 °C in SAE 0W-30 VP1 oil.

Figure 12. Evolution of the coefficient of friction over the test period of 10 million load cycles at P_{0mean} = 1.94 GPa and T = 120 °C in SAE 0W-30 VP1 oil.

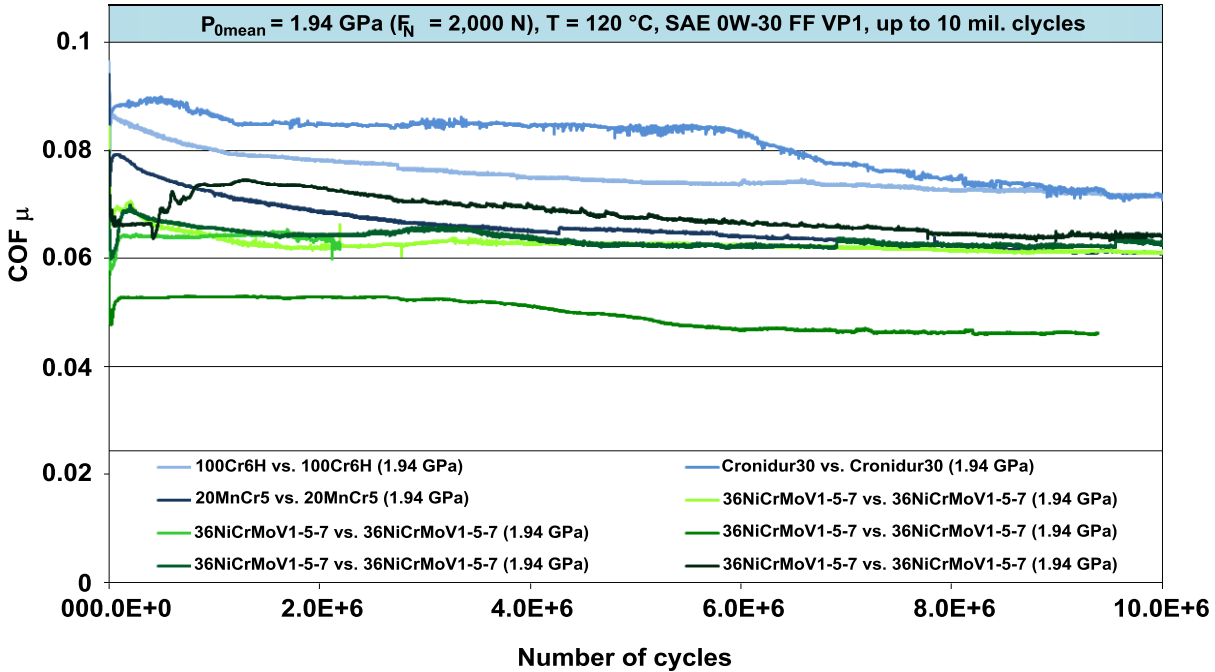Comparing the test results obtained at 1.5 GPa, to those at an average contact pressure of 1.94 GPa, Figure 12, the difference in friction values is less significant than in the case of tests at 1.5 GPa. Here again, 36NiCrMoV1-5-7 offers a friction reduction, in one case down to a value of 0.05. The repeat tests show that the coefficient of friction at test end is situated in most cases around 0.062, slightly higher than that at 1.5 GPa but still clearly lower in comparison to 100Cr6H and Cronidur 30. It was thus possible to show in ten tribological tests and under two contact pressures above FZG 14, using 36NiCrMoV1-5-7 as the test material, that the potential of reducing friction is realized by using the alternative steel without the need for coatings.

Looking at the evolution of the coefficient of friction at P_{0mean} = 2.5 GPa, the frictional advantage of 36NiCrMoV1-5-7 compared with 100Cr6H and Cronidur 30 is still apparent (cf. Figure 13).

As shown above, the frictional profile of highly concentrated contacts or systems can be optimized by a suitable material choice, for example, 36NiCrMoV1-5-7. Similar frictional results can be obtained by applying a highly wear resistant and low friction DLC coating. Therefore, an endurance test series was conducted, with different a-C:H thin film coatings of the BMW Group in order to distinguish the frictional potential of 36NiCrMoV1-5-7. The test series was separated into three parts. First the uncoated steel samples of the materials 100Cr6H, Cronidur 30 and 36NiCrMoV1-5-7 were tested at P_{0mean} = 1.5 GPa. The second part concerned the material pairing of uncoated steel (spherical disk) vs. DLC-coated steel (cylindrical disk). After finishing these tests, the third part followed comprising the DLC-coated steel (spherical disc) vs. DLC-coated steel (cylindrical disk). In order to guarantee the same adhesion properties of the coatings on the steel surface, the ground, spherical bodies were polished in the same manner as the cylindrical disks.
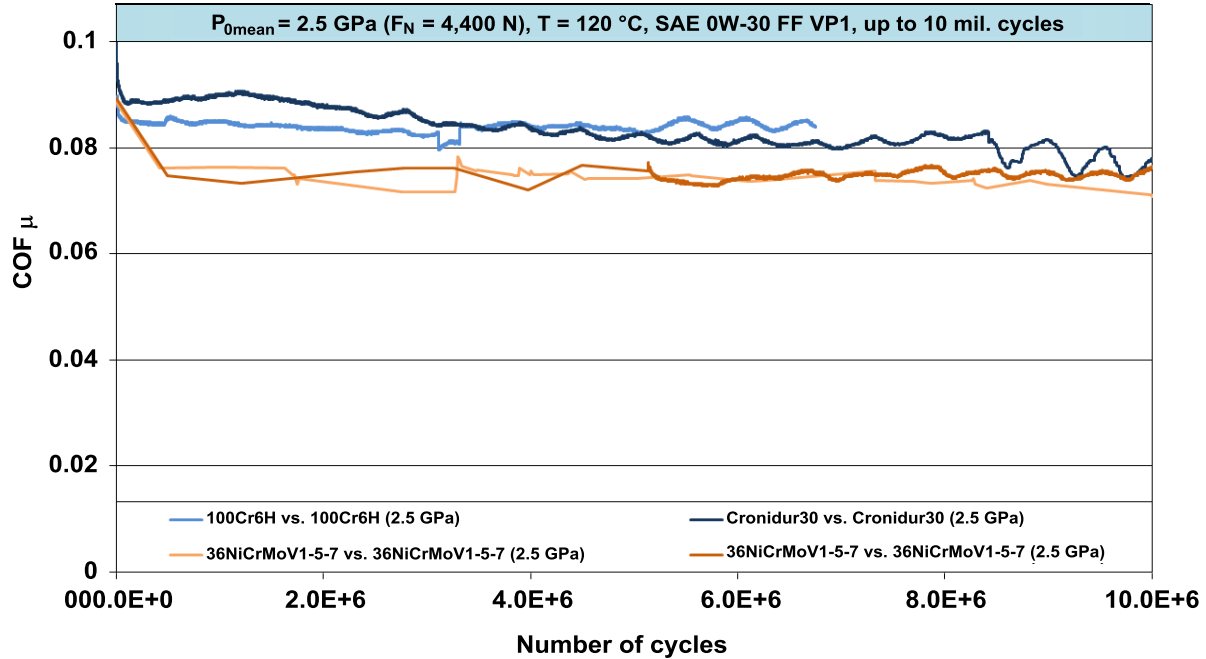
Figure 13. Evolution of the coefficient of friction over the test period of 10 million load cycles at $P_{0mean} = 2.5$ GPa and T = 120 °C in SAE 0W-30 VP1 oil.

The test results are presented in Figure 14, including one endurance test of uncoated Cronidur 30 vs. uncoated 100Cr6H as reference (red curve). Considering the evolution of the coefficient of friction over the test duration (10 million load cycles), this diagram revealed three regions.

The first region represents uncoated steel pairings with average coefficients of friction of 0.075 at test end. The application of a DLC-coating on the cylindrical test sample could reduce the friction values significantly, shown by the second region (green curves) in Figure 14. Considering the course of the pink curve (uncoated 36NiCrMoV1-5-7) it is remarkable that suitable, alternative and uncoated steels could offer the same potential to reduce friction as a DLC coating. When specifically designing the lubricant for such steels, the frictional benefit of uncoated steels could be more pronounced. The blue curves in Figure 14 represent the third region, ie. DLC vs DLC pairings, which showed the most promising results to reduce friction. In comparison to uncoated systems, the combination of DLC coatings in the contact region is, at the moment, the optimum. However, these results were obtained using perfectly finished steel surfaces before the coating process and showed what is potentially possible in future work.
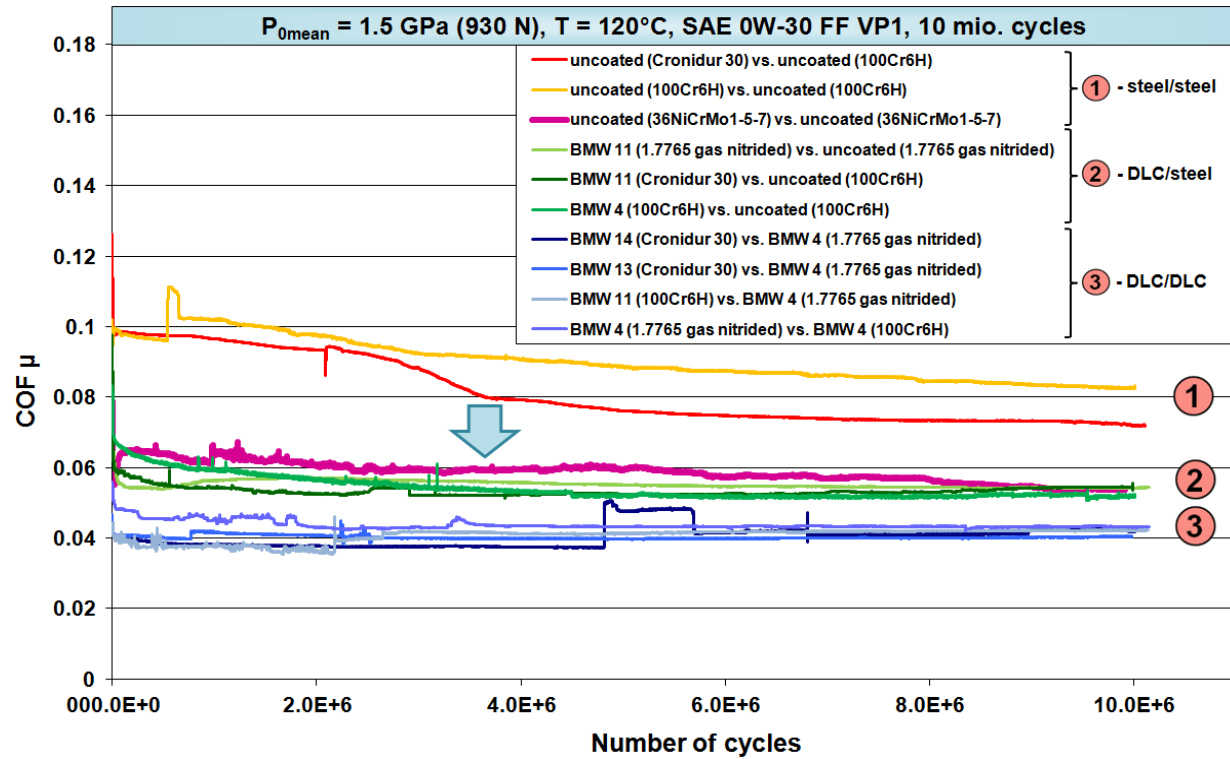
Figure 14. Comparison of friction coefficients of test pairings without any DLC coatings (100Cr6, Cronidur 30, 36NiCrMoV1-5-7), single coated samples and pairings with DLC coatings applied on both samples, tested at P_{0mean} = 1.5 GPa and T = 120 °C in SAE 0W-30 VP1 oil.

Figure 15 benchmarks the global impact of 36NiCrMoV1-5-7 in comparison to thin film coatings and a multitude of uncoated steels [3,4] on friction and wear under mixed/boundary conditions for slip-rolling motion lubricated by SAE 0W-30 FF VP1 oil at 120 °C. The steel 36NiCrMoV1-5-7 investigated in the current paper is compared with the following hardened and tempered steels:

(a) High carbon steels;
  - 100Cr6 (1.3505, VIM-VAR)
  - 102Cr6 (1.2067)

(b) Steels with advanced case hardening;
  - 20MnCr5 (1.7147)
  - CSS-42L (AMS 5932, VIM-VAR)

(c) Nitrogen alloyed steels;
  - Cronidur 30 (1.4108, DESU)

(d) Silicon alloyed steels;
  - NC310YW (40SiNiCrMo1)

Metallurgical details and detailed slip-rolling results are provided in the references [3,4,16]. CSS-42L is a Maraging steel requiring advanced case hardening, which takes some days. Hardening mechanisms based on silicon or nitrogen require both "clean" and "oxygen-free" melting and heat treatment cycles, keeping these alloying elements in solution without forming nitrides or silicides.

(In Figure 15 the horizontal bars represent the spread of results for all the hardened and tempered steels. The individual spreads for 100Cr6H and Cronidur30 in the uncoated condition are indicated by the dark green bars.)
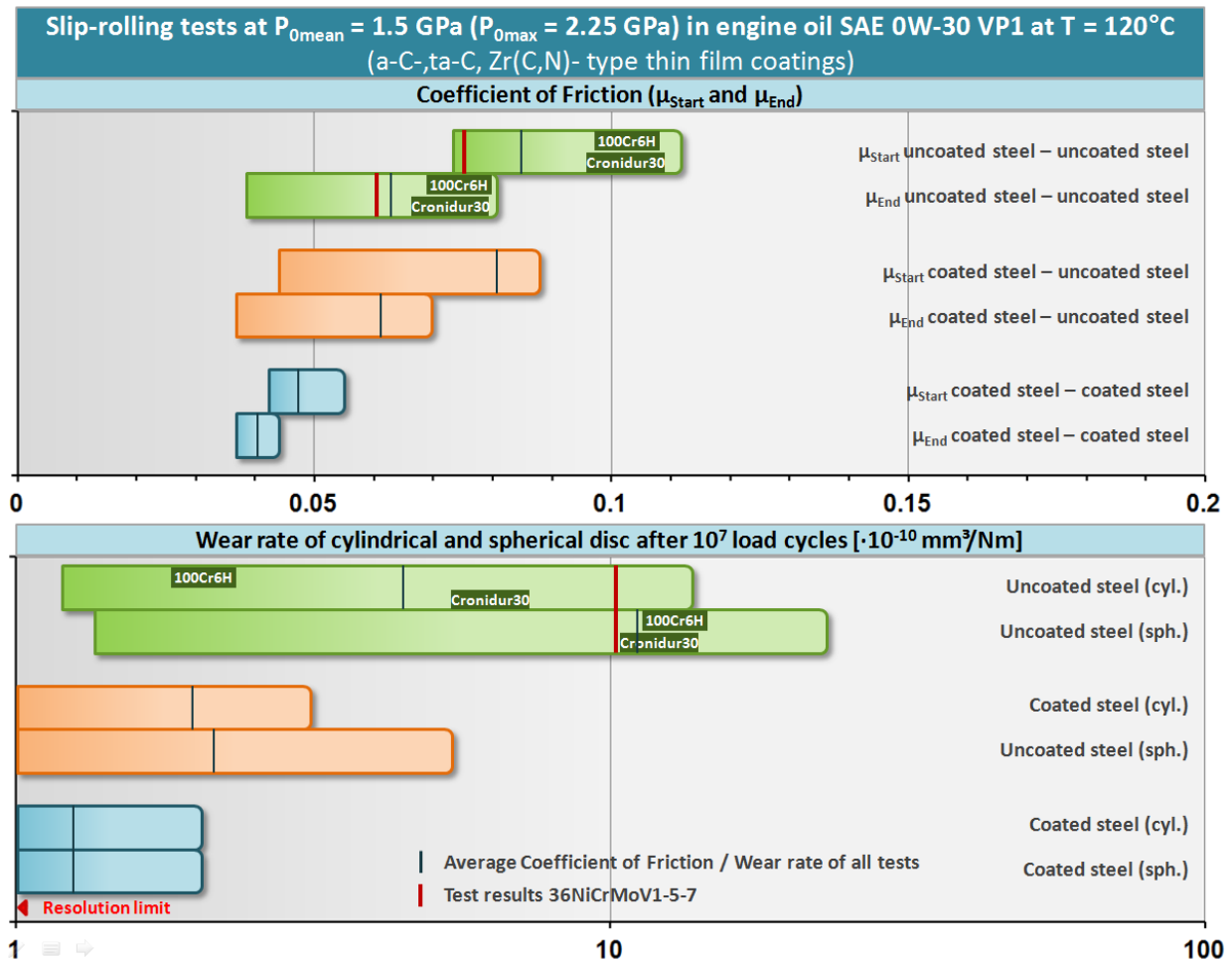

Figure 15. Comparison of friction and wear behavior of uncoated steel pairings, single coated pairings. [4,8,10,11].

It is instantly apparent from Figure 15, that the friction values of completely uncoated systems offered, on average, considerably higher friction coefficients at the beginning of the tests than systems where two DLC coated surfaces [11] are mated.

Conclusions

The majority of uncoated steels presented coefficients of friction between 0.06 – 0.09, but selected iron-based steel metallurgies, such as the high toughness steel 36NiCrMoV1-5-7, can also achieve low values of ~0.06 at test end, in the same range as test pairings rolling DLC against uncoated steel. From this point of view, it can be said that the application of thin film coatings on steel surfaces, with their difficult deposition and quality assurance requirements, can be avoided, if alternative steels are considered at the early design stage and appropriately used.

Basically, for wear resistance it is the same picture as for the frictional behavior. Thin films reduce wear rates by factors of 2–5, rather than by orders of magnitude. However, good slip-rolling resistance of 36NiCrMoV1-5-7 was demonstrated, but its variability needs to be improved by adequate steel production methods.

36NiCrMoV1-5-7 can substitute 100Cr6H and Cronidur 30 and offer similar load carrying capacity and slip-rolling resistance with associated lower friction coefficients.

It has to be noted that the wear resistance of 36NiCrMoV1-5-7 with a "quite low" hardness of 480 HV competes with those of hardened and/or case hardened steels.

References

1. Regulation (EC) No 443/2009 of the European Parliament and the Council, pp. L 140/1 – 140/15, 05.06.2009.

2. D. Spaltmann et al., "Damages of Slip-rolling Tested DLC Coatings on Steel Substrates of Different Hardness, *Materialwissenschaft und Werkstofftechnik*, 36 (2) (2005), 62 – 68.

3. C. Scholz, "Low Friction Slip-rolling Contacts – Influences of Alternative Steels, High Performance Thin Film Coatings and Lubricants," BAM-Ph.D. series, Volume (Band) 96, Berlin, 2013.

4. C. Scholz, D. Spaltmann and M. Woydt, "Slip-rolling Resistance of Thin Films and High Toughness Steel Substrates under High Hertzian Contact Pressures," *Wear*, 270 (7-8) (2011), 506-514.

5. H. Mohrbacher, "Molybdenum in Irons and Steels for Clean and Green Power Generation," IMOA, 2011.

6. F. Hippenstiel, "Tailored Solutions in Microalloyed Engineering Steels for the Power Transmission Industry," *Materials Science Forum,* 539-543 (2007), 4131.

7. H. Mohrbacher, "Synergies of Niobium and Boron Microalloying in Molybdenum Based Bainitic and Martensitic Steels," Fundamentals and Applications of Mo and Nb Alloying in High Performance Steels, TMS (The Minerals, Metals & Materials Society), 2011.

8. M. Woydt et al., "Slip-rolling Resistance of ta-C and a-C Coatings up to 3,000 MPa of Maximum Hertzian Contact Pressure, *Materialwissenschaft und Werkstofftechnik*, 43 (12) (2012), 1019 – 1028.

9. C-A. Manier, "Slip-rolling Resistance of Novel Zr(C,N) Thin Film Coatings under High Hertzian Contact Pressures," BAM-Ph.D. series, Volume (Band) 60, Berlin, 2010.

10. C-A. Manier and H. Ziegele et al., "Zirconium-based Coatings in Highly Stressed Rolling Contacts as Alternative Solution to DLC and ta-C Coatings, *Wear*, 269 (11–12) (2010), 770–781.

11. C-A. Manier et al., "Benchmark of Thin Film Coatings for Lubricated Slip-rolling Contacts," *Wear*, 268 (11–12) (2010), 1442–1454.

12. Energietechnik Essen GmbH: Datenblatt Cronidur30, http://www.energietechnik-essen.de/uk/products/high-nitrogensteels/cronidur-30.html, State 04.01.2012.

13. R. Schmidt, G. Klingenberg and M. Woydt, "Thermophysical and Viscosimetric Properties of Environmentally Acceptable Lubricants," *Industrial Lubrication and Tribology,* 58 (4) (2006), 210-224.

14. H. Hertz, "Ueber die Berührung fester elastischer Körper," *Journal für die reine und angewandte Mathematik*, 92 (1881) 156–171.

15. NSK: Ultra Clean Steel Extends Bearing Life, NSK Motion & Control, http://www.nskamericas.com/cps/rde/xbcr/na_en/10_TechTalk_Ultra_Clean.pdf, 01.06.2012.

16. C. Scholz, D. Spaltmann and M. Woydt, "Höchstbelastbare Wälzkontakte mit geringer Misch/Grenzreibungszahl (Highly Loaded Slip-rolling Contacts under Mixed/Boundary Lubrication), *Tribologie & Schmierungstechnik,* 59. Jg., Vol. 3, (2012), 41 – 47.

TAILORING THE MICROSTRUCTURE FOR MICROALLOYED CARBURIZING STEELS BY AN ICME APPROACH

S. Konovalov and U. Prahl

RWTH Aachen, Intzestraße 1, 52056 Aachen, Germany

Keywords: ICME, Gear Steel Development, Cleanness Improvement, Niobium Microalloying, High Temperature Carburizing, Thermodynamic Calculation

Abstract

Integrative Computational Materials Engineering (ICME) is a new method for efficient development of new materials and new processes by computer-based simulation on different length scales over different process steps. We developed ICME tools and applied them successfully for several new concepts for Nb microalloyed gear steels.

A common ICME platform that combines empirical and rigorous models for casting, rolling, forging, machining, heat treatment and welding has been developed and evaluated for several test cases. The platform requirements and the simulation tools used are described.

Our ICME approach has been successfully demonstrated for the development of new case hardening steels with a reduced Al content to meet the requirements of improved cleanness and lifetime. By microalloying with Nb a stable, fine grain size can be ensured, even for an energy efficient high temperature case hardening heat treatment.

Introduction

An important factor for the optimization of fatigue properties of carburized steels is the oxide steel cleanness [1-3]. Typically, a microalloying concept based on Al is used for deoxidation to reduce the oxygen content in the melt. During this process, hard, round Al-oxides might be formed that eventually limit the life of gear components. Additionally, Al affects the fine-grain stability positively. For the improvement of steel cleanness, various metallurgical methods were successfully implemented in industrial processes [4]. A material-based approach for the improvement of the steel cleanness can be achieved by reducing the Al content. This concept was successfully evaluated for bearing steels [5]. However, such low Al contents cannot ensure fine-grain stability in case hardening steels.

In this work a new alloying concept for steel 25MoCr4, alloyed with Nb and with reduced Al content, is introduced. The aim of the work is to improve the oxide steel cleanness by reducing the Al content, and in parallel increase the fine-grain stability at a high carburizing temperature of about 1050 °C, by substitution of Al by Nb. The development of an Al-free alloying concept is based on thermodynamic calculations. For validation, a laboratory melt has been made and investigated regarding steel cleanness and fine-grain stability at high carburizing temperatures for different process routes.

Procedures

<u>Materials</u>

The reference material is an industrial microalloyed steel, 25MoCr4, with conventional Al, Nb, Ti and N contents, which provides the fine-grain stability during high temperature carburization at 1050 °C for 1 hour 30 minutes [6]. The material was hot rolled to bars of diameter 75 mm and annealed to give a ferrite-pearlite microstructure.

By thermodynamic calculations, target values for the chemical composition were determined for the modified steel, 25MoCr4 with a reduced Al content. The level of S was kept low for an additional improvement of the steel cleanness and the P level was also reduced from 104 to 22 ppm. The new material was melted in a laboratory vacuum furnace with an ingot weight of 80 kg. The casting was made in a square ingot of 140 x 140 mm cross section. The ingot was forged in several passes with repeated intermediate annealing at approx. 1320 °C using the Semi-Product Simulation Center (SPSC) at IEHK. The forged ingot, with a cross-section of 75 x 75 mm, was cooled in air. After cutting of the semi-finished block into two halves, the pieces were forged again to a cross section of 65 x 65 mm from the same homogenization temperature. At the end, the forged material was cooled down to 500 °C in 10 minutes. After the material reached this temperature, the blocks were soaked for 45 minutes in a furnace to attain a bainite structure. The chemical compositions of both investigated materials are shown in Table I.

Table I. Chemical Composition of Investigated Steel Grades 25MoCr4 in wt.%

	C	Si	Mn	P	S	Cr	Mo	Al	N	Nb	Ti	$O_{tot.}$ ppm
Ref	0.24	0.22	0.89	0.0104	0.0172	0.92	0.43	0.0227	0.0161	0.0337	0.0089	17
Al-free	0.23	0.21	0.83	0.0022	0.0016	0.92	0.44	0.0022	0.0137	0.0823	0.0005	17

<u>Determination of the New Material Concept</u>

Thermo-Calc is a commercial software package with integrated CALPHAD-model. Using the thermodynamic database TCFE6, simulation of the amount of precipitation was performed for the microalloyed steel 25MoCr4 and its modified version under equilibrium conditions. The thermodynamic calculation was performed for the given material compositions without consideration of oxide formation. For the determination of microalloying additions, the total volume fractions of Al-nitrides and (Nb,Ti)-carbonitrides were calculated and compared for different conditions. The aim of the calculation was to ensure the same volume fraction of particles in the Al-free case hardening steel as in the classical gear steel, for case hardening temperatures between 950 and 1050 °C.

Experimental Procedure

Three samples were investigated for steel cleanness using DIN EN 50602 in the as-received state for the reference material or in the hot forged state for the Al-free material. After a short austenitization time at 900 °C, followed by quenching in water, the samples were analyzed using the K-value method. An additional comparison of the investigated materials was made for non-metallic inclusions and coarse particles using the SEM (Scanning Electron Microscope). The individual inclusions were analyzed for their chemical composition by EDX (Energy Dispersive X-ray spectroscopy).

For experimental investigations of fine-grain stability, samples were cut from the materials and treated in a conventional furnace under different conditions simulating various industrial process routes with subsequent blank hardening. The dimensions of the treated samples were 25 x 25 x 20 mm. Some of the samples were annealed, to allow dissolution of particles before the heat treatment, at 1300 °C for 30 minutes with the aim to investigate the influence of the solution annealing on the fine-grain stability. The heat treatment of the samples was performed using four different process routes. The first group of samples was annealed to give a ferrite-pearlite structure (FP) using an austenitization treatment at 930 °C for 75 minutes and then holding at 680 °C for 3 hours. A recrystallization annealing (RX) at 700 °C for 3 hours was chosen as the second process route. The samples without the dissolution annealing were additionally tempered at 500 °C for 2 hours or investigated without any heat treatment prior to blank hardening. Figure 1 shows the various process route heat treatments used.
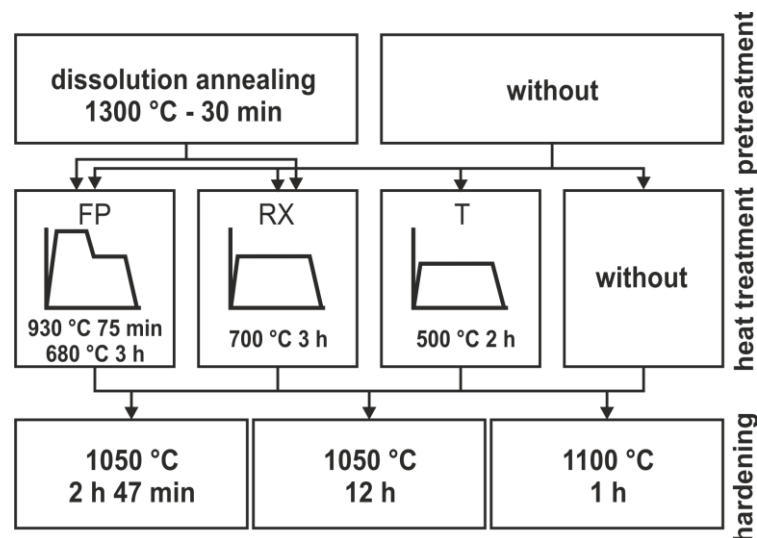

Figure 1. Experimental process routes for investigation of fine-grain stability dependence on heat treatment.

Additional samples were cooled slowly after the hardening step to produce a ferrite-pearlite structure after the heat treatment and investigated with the aim of estimating the thickness of the decarburized layer. This layer was excluded from further investigations. The blank hardening of the samples was carried out at a typical high carburization temperature of 1050 °C for 2 hours 47 minutes or for 12 hours. At an ultra-high carburization temperature of 1100 °C the holding time was only 1 hour.

All investigated samples were sectioned in half in the longitudinal direction before the investigation. The blank hardened samples were etched to reveal prior austenite grains using picric acid. For the elimination of the influence of decarburization, the austenite grain analysis was performed a minimum distance of 3 mm from the edge. The whole sample surface was analyzed for abnormal grain growth. For determination of grain size distribution, several pictures with a total number of over 1000 grains were analyzed. The prior austenite grain size distribution is shown as a cumulative frequency versus the grain size value G according to DIN EN ISO 643. The ideal normal grain size distribution should be a straight line on this scale. Here, a straight line indicates continuous normal grain growth. According to the internal standard of ZF (Zahnradfabrik Friedrichshafen), the material is fine-grain stable if 90% of the investigated area has the grain size G5 or finer and no grain is coarser then G3 [7]. If the cumulative frequency is tending to the region of coarser grains, this is an indication of abnormal or discontinuous grain growth.

For further comparison, a characteristic value G^{90} is introduced. It indicates a maximum grain size for 90% of the investigated area. This means that less than 10% of the investigated microstructure possessed a grain size coarser than G^{90} (Figure 2). For a fine-grain structure without abnormal grain formation, the G^{90} value must be a grain size class G5 or higher and the grain size distribution must be almost a straight line in this type of description.
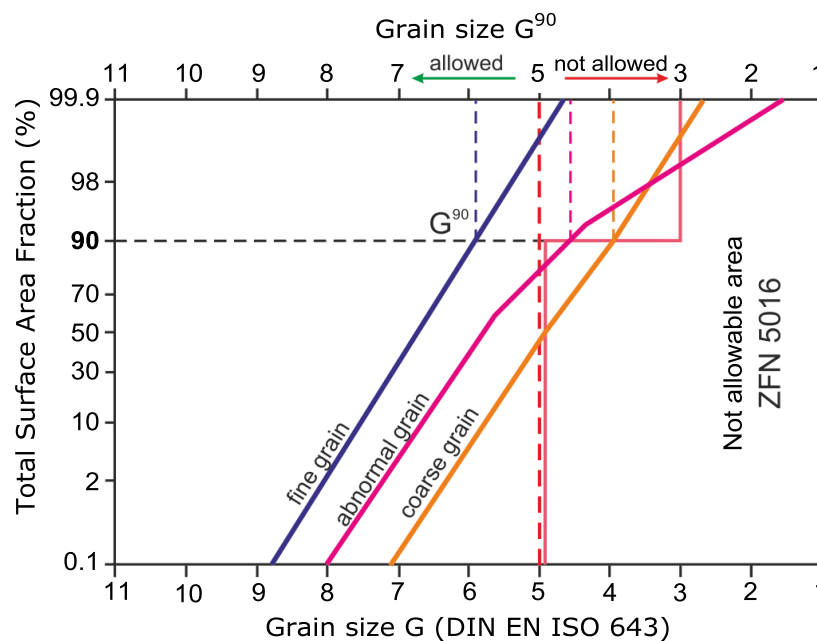

Figure 2. Determination of G^{90} value and presentation of acceptable grain size area.

Thermodynamic and Kinetic Simulations

Determination of the Necessary Nb-addition

An optimal Nb addition was calculated to ensure fine-grain stability during high temperature carburization. Based on the classical description of the Zener-force [8], the grain growth inhibition by a stable microalloying phase depends on the size, the amount and the distribution of the precipitation. The particle size can be changed by heat treatment, but at this stage of material design the particle size is neglected. Here, it is required that the volume fraction of grain growth inhibiting particles at the carburizing temperature of 1050 °C in the Al-free material is equal to the amount in the reference material, under equilibrium conditions. The calculation of the maximum possible precipitation amount and its dependence on temperature was carried out using the thermodynamic software Thermo-Calc.
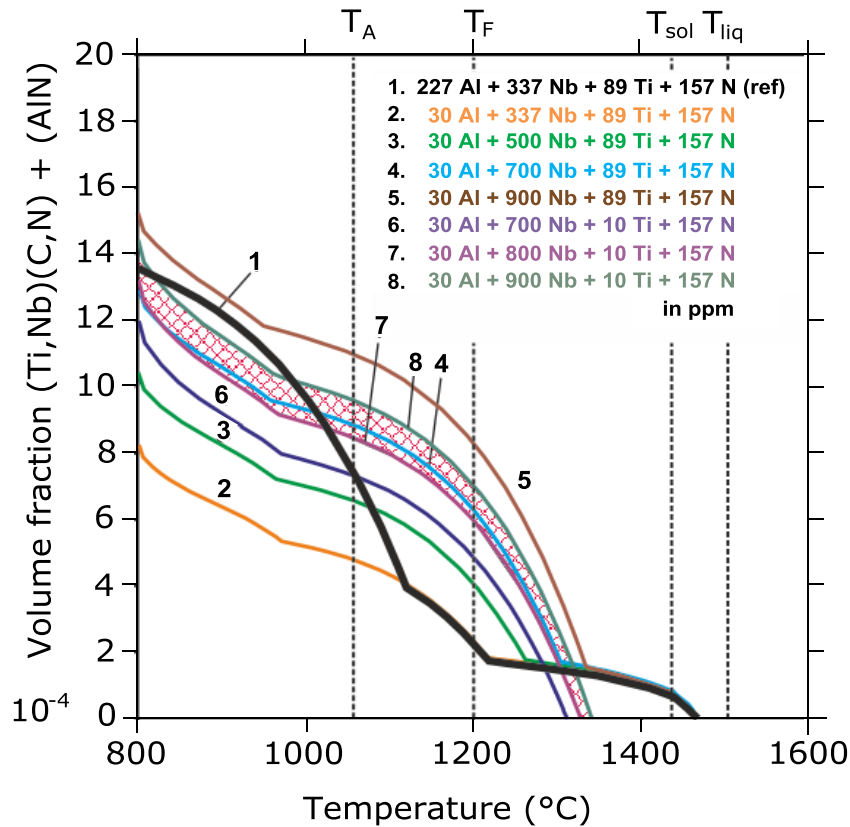

Figure 3. Determination of target alloy system for Al-free carburizing steel
by varying Nb and Ti contents.

For a first approximation, the calculation for the reduced Al content steel was performed at 30 ppm Al and compared with the reference material (Figure 3). The volume fraction of particles at the carburization temperature of 1050 °C (T_A) is noticeably lower in comparison to the reference material. In the following calculations, the Nb-content was increased step by step in order to achieve an equal volume fraction as compared to the reference material.

Additional calculations were performed for a reduced Ti content of around 10 ppm. The analysis of the calculation results shows that at 89 ppm Ti the microalloying phases can be stable in the liquid-solid region and this can lead to the formation of coarse primary particles. Such coarse particles reduce cleanness and are not effective for fine-grain stability. The high formation temperature of particles is caused by the high stability of Ti-nitrides. By reduction of the Ti content, an additional element of material optimization was realized, whereby the formation temperature of particles in the equilibrium state can decrease to approximately 1320 °C. Further reduction of the Ti content has no influence on the formation temperature of particles because of the higher Nb content. The target amounts of 800-900 ppm Nb, <30 ppm Al and approximately 10 ppm Ti have been determined. The target area for the Al-free case hardening steel with the desired fine-grain stability is shown as the hatched area in Figure 3. In line with this calculated microalloying amount, a laboratory melt was produced. The actual alloy contents in the test material are listed in Table I.

A large amount of undissolved precipitates is expected in the Al-free material at typical forming temperatures of around 1200 °C (T_F). This can lead to a decrease in fine-grain stability due to coarsening of the Nb particles. The hot formability as well as recrystallization can be affected by a higher particle volume fraction and precipitation driving force. At temperatures below 1050 °C the particle volume fraction is lower in comparison to the microalloyed reference material, which might cause reduced fine-grain stability at typical carburization temperatures.

Experimental Results

Steel Cleanness

The results of oxide steel cleanness measurements show that the modified Al-free grade has a smaller amount of harmful coarse inclusions. This is associated with improved cleanness, based on K1 and K4 values according to DIN 50602, in comparison to the reference material (Table II). These results are expected because of the reduction of the Al content.

Table II. Oxide Steel Cleanness for Reference and Al-free Material according to DIN 50602

	K1	K4
Ref	3.0	2.1
Al-free	0.5	0.0

The analyses of individual inclusions with SEM show a significantly lower volume fraction of inclusions as well as a smaller size in the modified material (Figure 4). The Mn sulfides are mostly either globular or elongated. The size or the length of the elongated inclusions is smaller than in the reference material. The reason for this is the significantly lower S content in the Al-free material.
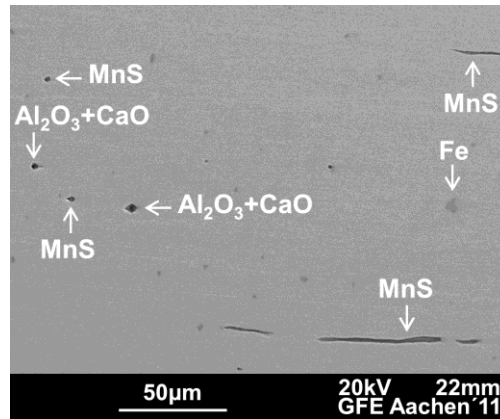
(a) ref
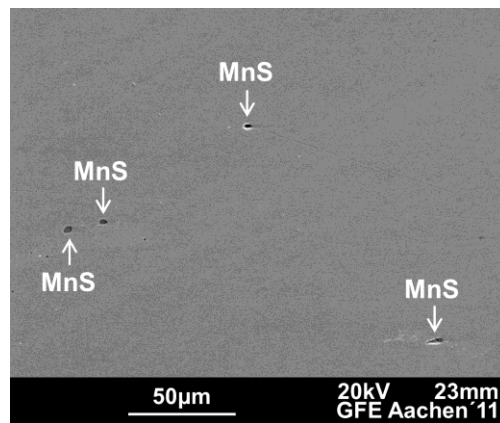
(b) Al-free

Figure 4. SEM analysis of reference (a) and Al-free material (b).

In the reference material, coarse square Ti and Nb particles with sizes larger than 1 µm have been found [9], which were probably formed in the liquid-solid region because of the high stability of Ti-nitrides. These particles are not effective for the suppression of grain boundary movement. The results of the investigation show that the formation of Al-oxides cannot be avoided completely in the low Al steel. However, the probability of formation is much lower in comparison to the reference material.

Results of Fine-grain Stability for Different Process Routes

An overview of the G^{90} results for all of the investigated material conditions and process routes is shown in Table III. The comparison of the investigated materials after blank hardening for 2 hours 47 minutes at 1050 °C demonstrates that fine-grain stability is evident for all the investigated process routes in both materials. The spread of the G^{90} values for the reference material is small. This could be evidence of optimal precipitation conditions in the as-delivered condition. The Al-free material generally has a slightly coarser grain size and a significant dependence of the G^{90} value on the process route could be observed. This means that some potential for optimization exists for the Al-free material regarding the precipitation state. The

process route with the FP-annealing step has the best overall fine-grain stability in the two materials.

The results for other heat treatment processes show the grain size to be coarser than for the 1050 °C for 2.78 hours treatment. However, only the Al-free material can provide sufficient fine-grain stability for holding 12 hours at 1050 °C. The reference material tends to a coarse or abnormal grain growth regime. In the Al-free material only a dissolution heat treatment with RX-annealing can improve the precipitation state to give adequate fine-grain stability. For the Al-free material the temperature for dissolution heat treatment can be insufficient and that can lead to particle coarsening and poor fine-grain stability.

For a hardening temperature at 1100 °C with a holding time of 1 hour, the G^{90}-values for the reference material are lower than the allowed level. In contrast, the Al-free material has still sufficient fine-grain stability for all of the process routes. Furthermore, it should be noted that the process route with an FP annealing step shows significantly finer grains for the Al-free material.

Table III. Grain size of Prior Austenite According to G^{90} Value after Different Process Routes with Blank Hardening at 1050 or 1100 °C (G^{90} <5 – indicates coarse or abnormal grains).

Hardening Treatment	Steel	Dissolution		No Pretreatment			
		FP	RX	FP	RX	T	-
1050 °C	Ref	6.1	6.2	6.9	6.8	6.6	7.1
2.78 hours	Al-free	6.5	5.1	6.2	5.1	5.5	5.7
1050 °C	Ref	**1.4**	5.0	**3.9**	**4.1**	**4.4**	**4.6**
12 hours	Al-free	**2.7**	**3.5**	6.4	5.8	5.0	5.2
1100 °C	Ref	**0.5**	**3.0**	**2.2**	**2.8**	**4.4**	**4.0**
1 hour	Al-free	6.7	5.1	6.5	5.4	5.5	5.5

Discussion

A new microalloying concept for case hardening steel 25MoCr4 has been determined using thermodynamic modeling. The new material has a considerably reduced Al content with a distinctly improved steel cleanness level and can ensure fine-grain stability at high carburizing temperatures up to 1100 °C.

The reduction of the Al content shows a significant positive effect on the oxide steel cleanness as measured by K1 and K4 analysis. Nevertheless, some Al-oxides, Mn-sulfides and coarse (Ti,Nb)-carbonitrides have been detected using SEM with EDX, yet the Al-free material has a significantly smaller amount of Al-oxides and Mn-sulfides as a result of the reduction of the Al and S contents.

The analysis of calculated equilibrium temperatures, using thermodynamic simulation, shows a high stability of Ti-nitrides in the liquid-solid area. This leads to the formation of coarse Ti-particles with a size larger than 1 μm. This can worsen the steel cleanness and reduce the efficiency of Ti-nitrides in preventing grain coarsening. Reduction of the Ti content from 89 to 10 ppm causes the precipitation temperature to be lowered leading to the formation of smaller particles in the solid phase.

The G^{90} value is an extension of an internal ZF standard, ZFN 5016, to quantify the fine-grain stability. The results for the reference material did not show any influence of the process route on the fine-grain stability for a hardening cycle of 2 hours and 47 minutes at 1050 °C. This can be achieved by an optimal particle state before the hardening heat treatment. In contrast, the austenite grain size in the Al-free material can be controlled and influenced by the process route. The FP-annealing produces a fine austenite grain in the Al-free material. The formation kinetics of Nb-carbonitrides are at a maximum at temperatures between 900 – 1000 °C [10-13]. In this temperature range new small particles can be formed sufficiently quickly. Cooling after austenitization above 700 °C decreases Nb diffusion and the particle coarsening effect considerably. This is likely to be the reason for the improved fine-grain stability after the FP-annealing cycle. Al-nitrides can form at temperatures below 700 °C [14,15] and in the case of RX-annealing after a dissolution heat treatment produces a better distribution of small Al-nitrides and consequently sufficient fine-grain stability for long hardening times in the reference material.

The modified Al-free material possessed sufficient fine-grain stability after blank hardening at 1050 °C for 12 hours and in fact fine-grain stability could be achieved for all the process routes which excluded dissolution heat treatment. The Al-free material has G^{90}-values lower than 5 after a solution heat treatment which indicates abnormal grain growth. This can be explained by an incomplete dissolution of precipitates and coarsening of particles. A clearly improved fine-grain stability can be found for the Al-free material after blank hardening at 1100 °C for 1 hour, compared to the reference material, for all process routes.

In the new alloying concept, the Nb content is high enough for Nb carbonitrides to be stable at 1320 °C under equilibrium conditions. Furthermore, the high Nb level can lead to a significant stability increase of Nb carbonitrides in the melt. As a result, Nb particles can be formed with sizes up to 1 μm . These coarse particles can reduce the fine-grain stability of the material. The dissolution of Nb particles and redistribution of Nb requires a further heat treatment of the material. By using kinetic simulations the optimal process parameters for heat treatment and forging will be determined in further work.

Conclusions

In this paper, a new Al-reduced microalloying concept for case hardening steel 25MoCr4 was introduced, which has improved steel cleanness and fine-grain stability at high carburization temperatures.

Al and Ti contents were reduced to avoid the formation of coarse precipitates and oxide inclusions.

The reduction in Al and Ti was compensated by an increase in the Nb level which is beneficial for fine-grain stability.

The required amount of Nb was calculated from thermodynamic simulations. The new material shows a sufficiently high grain coarsening resistance for a range of process routes.

The most stable austenite grain size can be found in the modified Al-free material after blank carburizing and annealing at 1050 °C for 12 hours or by annealing at 1100 °C for one hour after a process chain which includes FP-annealing.

Acknowledgments

References

1. A. Melander et al., "Influence of Inclusion Contents on Fatigue Properties of SAE 52100 Bearing Steels," *Scandinavian Journal of Metallurgy*, 20 (1991), 229–244.

2. Y. Murakami, "Material Defects as the Basis of Fatigue Design," *International Journal of Fatigue*, 40 (2012), 2–10.

3. B. Pyttel et al., "Influence of Defects on Fatigue Strength and Failure Mechanism in the Vhcf-region for Quenched and Tempered Steel and Nodular Cast Iron," *International Journal of Fatigue*, 41 (2012), 107–118.

4. L. Zhang and B.G. Thomas, "State of the Art in Evaluation and Control of Steel Cleanliness," *ISIJ International*, 43 (3) (2003), 271–291.

5. D. Theiry et al., "Aluminiumferier Wälzlagerstahl," *Stahl und Eisen*, 117 (8) (1997), 79–89.

6. S. Konovalov and B. Clausen, "Entwicklung einer Prozesskette zur Herstellung von Schmiedebauteilen für die Hochtemperaturaufkohlung: Abschlussbericht," volume AiF 14841 N I, 2009.

7. S. Hock et al., "Einfluß von Umform- und Wärmebehandlungsfolgen auf Korngröße und Schwingfestigkeit von einsatzgehärteten Bauteilen," *HTM*, 54 (1) (1999), 45–52.

8. T. Gladman, "Grain Size Control," *Old City Publishing*, 2004.

9. S. Konovalov et al., "Entwicklung eines Al-reduzierten Einsatzstahls für die Hochtemperatur-Aufkohlung," *HTM*, 67 (3) (2012), 202–210.

10. H. Watanabe, Y.E. Smith and D. Pehlke, "Precipitation Kinetics of Niobium Carbonitride in Austenite of High-strength Low-alloy Steels," *Conference: The Hot Deformation of Austenite, New York*, 1977.

11. I. Weiss and J.J. Jonas, "Interaction Between Recrystallization and Precipitation During the High Temperature Deformation of HSLA Steels," *Metallurgical Transactions A*, 10 (2) (1979), 831–841.

12. S. Akamatsu et al., "Modelling of NbC Precipitation Kinetics in Hot Deformed Austenite on Nb Bearing Low Carbon Steels," *The Iron and Steel Institute of Japan International*, (1989), 933–940.

13. S.F Medina, "Determination of Precipitation-time-temperature (ptt) Diagrams for Nb, Ti or V Micro-alloyed Steels," *Journal of Materials Science*, 32 (6) (1997), 1487–1492.

14. K. Schwerdtfeger, "Rißanfälligkeit von Stählen beim Stranggießen und Warmumformen," *Stahleisen, Düsseldorf*, 1994.

15. M. Mayrhofer, "Untersuchung zur Auflösungs- und Ausscheidungskinetik von Al-nitrid in Al-beruhigtem Stahl. Monatshefte," *Berg- und Hüttenmännische*, 120 (7) (1975), 312–321.

TECHNOLOGY, PROPERTIES AND APPLICATIONS OF NIOBIUM CARBIDE REINFORCED STEEL AND IRON ALLOYS

H. Mohrbacher[1] and D. Jarreta[2]

[1]NiobelCon bvba, Schilde, Belgium
[2]Metal Prime Technology Pte. Ltd., Singapore

Keywords: Abrasive Wear, Wear Resistant Steels, NbC Particles, White Cast Irons

Abstract

The large cost and considerable downtime caused by replacing worn parts in earth moving and mining equipment, as well as in the materials processing industry, represents a continuous challenge to material development. Components designed for sacrificial wear must in the first place possess adequate abrasion resistance. Frequently, however, they must also have the ability to withstand impact and to resist chemical attack. The requirement of good abrasion resistance in combination with good toughness is generally in contradiction. Typically, hard iron-based materials such as martensite or ledeburite are highly resistant to abrasion, yet very brittle and difficult to machine. An innovative approach is to compose a more ductile iron-based matrix, embedding a much harder wear resistant phase. Amongst those extremely hard phases are carbides of the transition metals titanium, niobium, and tungsten with hardness of over 2000 HV. Particularly, NbC is a very interesting hard phase since its hardness is one of the highest among the transition metals carbides and its density is very similar to that of molten iron, so that gravity segregation effects in the liquid phase are small. Volume fractions up to 35% of NbC can be formed *in-situ* as primary carbide in the liquid phase or added externally using a FeNbC master alloy. The latter approach is particularly applicable when higher amounts of NbC need to be added. Molybdenum additions are important to adjust the properties of the matrix towards high toughness and good ductility. This paper elucidates the strategies and possible technologies of achieving such composite materials and demonstrates several examples of applications along with the achieved sustainability benefits. In particular, fundamental and tribological properties of NbC are presented.

Introduction

The enormous, and at the same time, increasing cost of replacing worn parts in earth moving and mining equipment, as well as in the materials processing industry, represents a continual challenge to material development. Components designed for sacrificial wear must possess, first of all, adequate abrasion resistance. Frequently, however, they must also have the ability to withstand impact and to resist chemical attack. The requirement of good abrasion resistance, in combination with good toughness, is generally rather restrictive. Typically, a material that is highly resistant to abrasion is at the same time hard and brittle.

Wear is defined as the gradual and progressive loss of material due to the relative motion between the active body and a counter-body. Two basic principles can be involved in removing material from the surface: Material can be disintegrated and detached mechanically or by chemical reaction, both actions occurring at the surface. Wear resistance of a material is a system property and not a material property. It is controlled by a multitude of parameters consisting of material and counter-body properties, contact stresses and the environment. Therefore, wear performance can only be evaluated by simulating the real-life situation as closely as possible. Nevertheless, standardized procedures for benchmarking abrasion resistance have been developed, like the rubber wheel test according to ASTM G65.

Abrasion is a form of wear that is mediated by hard particles covering a wide range of sizes. This statement should be qualified to indicate that while the severity of abrasion is expected to increase as the hardness of the particles increases, abrasive wear is not necessarily eliminated if the particles are soft. The particles are almost always mineral substances that are being handled for some engineering or industrial purpose, or that have penetrated into a machine or system as foreign contaminants.

Since solid-liquid mixtures are often handled in the mining industry, the combined effect of abrasion and corrosion must be considered. It is easy to see how abrasive particles can affect corrosion rates by removing protective films and exposing fresh metal to the environment. These films take time to rebuild, and if they are continually destroyed by an abrasion action of slurry, corrosion rates can increase drastically.

Figure 1 compares representative hardness values of mineral species with that of technical alloys. It is evident that many minerals are much harder than standard construction materials, for instance steel or aluminum. Only super hard compounds like carbides of the transition metals represented by groups IVB to VIB in the periodic table of elements, amongst them also molybdenum, can compete with the hardest minerals. Yet these carbides cannot be processed into large-scale components and are also very brittle and expensive. However, they can be dispersed to a certain fraction into a metallic matrix, like a steel or a cast alloy. Another possibility is to clad them on the surface of a metallic substrate by welding or other coating processes. Still, these remain expensive manufacturing processes that also have limitations with regard to component size. For the bulk of applications, abrasive resistant steel is the material of choice. It is available as heavy plate or as hot-rolled strip, allowing the manufacture of large component sizes in an economical way. Typical abrasion resistant steel grades cover a hardness range of 300 to 600 on the Brinell scale. Abrasion resistant steel has a guaranteed high hardness across the entire plate thickness so that its resistance to wear remains adequate, even when material loss has progressed. Thus, it is the material of choice for components exposed to sacrificial wear. Carburizing steel is an alternative material for those applications where wear occurs but dimensional stability of the component should be maintained. The very hard surface layer of carburized steel extends only over a few millimeters at the most. Such material is mainly used for gear and drive systems in equipment exposed to pollution by abrasive particles.
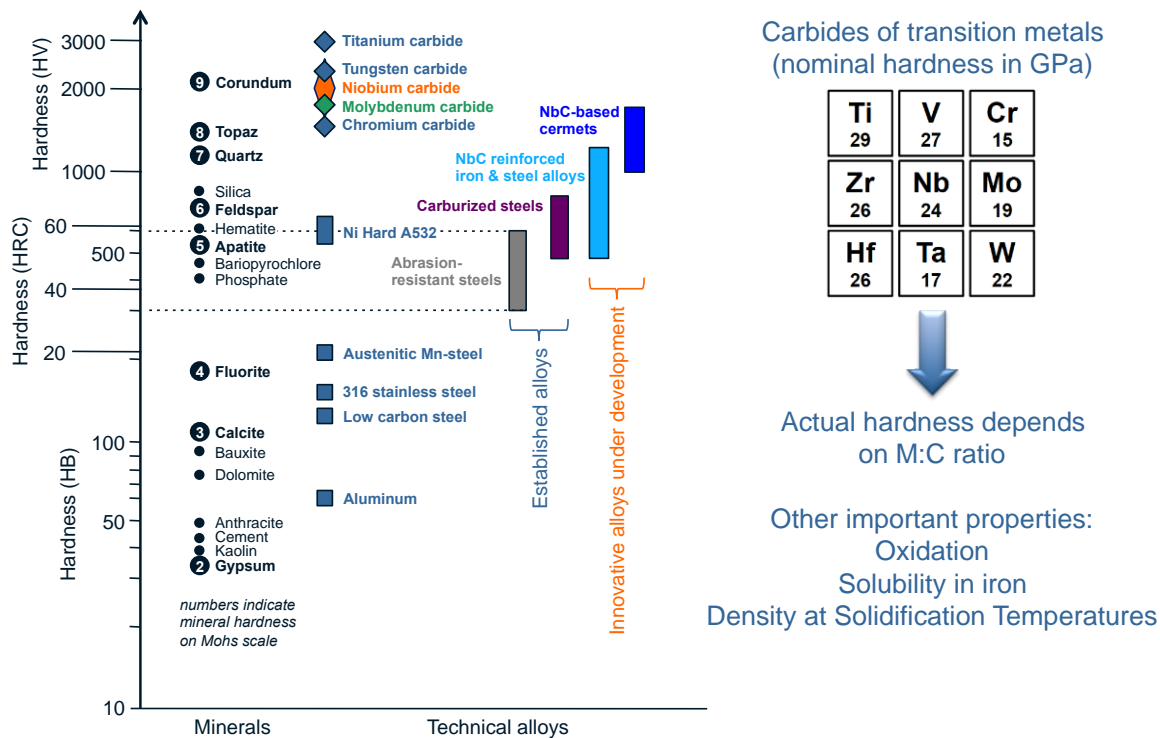
Figure 1. Hardness of mineral species compared to hardness of technical alloys.

Abrasion Resistant Steel

Abrasion-resistant steels are designed to withstand wear that is caused by friction or by the impact of materials, such as minerals, sand or gravel. Abrasion resistance generally increases with hardness of the active body, avoiding scratching and plowing by hard counter-body species. Fatigue strength and toughness are additional properties coming into play, especially when dynamic or impact loads are acting on the active body. Thirdly, some applications may additionally require temperature and oxidation resistance. Accordingly, different abrasion resistant steel classes have been developed. Abrasion resistant steel grades are usually classified based on their hardness levels ranging from 300 up to 600 HB. The standard class focuses primarily on surface hardness and is represented by unalloyed CMn steels. Alloyed steel grades combine hardness with guaranteed toughness and also allow production of heavier gages. Alloyed steel grades with low-carbon equivalent provide increased toughness at lower temperature and simultaneously improved weldability. Super abrasion-resistant grades have a further improved abrasion resistance by incorporating hard second phases in a moderately hard matrix. With the exception of the standard grades, molybdenum is a vital alloying element in achieving the desired property mix.

In addition to the wear-resistant characteristics of steel, such as hardness, work hardening, resistance against crack formation and propagation, the following application oriented criteria need to be considered as well in the selection procedure:

- Toughness;
- Weldability;
- Hot and cold forming capability;
- Machinability;
- Cost-benefit ratio.

Table I. Typical Applications for Abrasion Resistant Steel Grades

Heavy Vehicles and Earth Moving Equipment	• Bulldozer shovels and buckets • Slush plates for bulldozers • Exterior linings of bulldozer buckets • Trailer beds • Vessels for dump and cargo trucks • Dredger buckets
Cement and Mining Industry	• Lining and paddle material for ready-mixed concrete turbine mixer • Conveyor chute for concrete mixing plant • Pug mill for soil cement • Conveyor pipe for solids (pneumatic pipelines for coal mines) • Lining and grates for ball mills • Lifters for Semi-Autogenous Grinding (SAG) mills
Chemical Industry	• Agitators for asphalt plants and finishers • Sand conveyor pipe for sand cracking in naphtha cracking plants • Sulfide mineral bucket elevators
Metallurgical Industry	• Chutes and liners • Ore screens • Lining for rotary mixers and conveyor belts • Raw material and roll feeders
Others	• Earth drills • Shear liners • Tunnel boring machines • Agricultural equipment

Microstructural Influence on Wear Resistance

The microstructure of steel plays a critical role with regard to its wear performance. For the same hardness, austenite is more abrasion resistant than ferrite, pearlite or martensite due to the higher strain hardening capacity and ductility of austenite [1]. In steels with less than l.0% carbon, bainitic microstructures have the highest wear resistance, followed by quenched and tempered microstructures, annealed structures and spheroidized structures, all at the same hardness level [2]. Figure 2 summarizes the effects of steel hardness and microstructures on wear resistance [3]. Figure 3 shows the relationship between hardness and the abrasion resistance ratio [4]. The abrasion resistance was evaluated according to ASTM G65 using silica (SiO_2) as the abrasive. The abrasion resistance was calculated as the ratio of the weight loss of mild steel to the weight loss of abrasion-resistant steel. Analyzing ferritic-pearlitic and martensitic microstructures under the same test conditions reveals a distinctly different impact of the hardness on the wear rate [5]. As shown in Figure 4, hardness increase in a ferritic-pearlitic microstructure results in only a minor improvement of wear resistance. In martensitic steel, on the contrary, increasing the hardness leads to substantial gains in wear resistance. This difference appears to be the consequence of different wear mechanisms acting in both steels. The soft ferrite phase present in ferritic-pearlitic steel is plastically deformed by the indentation of hard particles in the near-surface region leading to work hardening, (Figure 5). Low-cycle fatigue can induce cracking in the work-hardened zone and detach particles. Another mechanism of material removal is caused by adhesion on the abrasive particle.

As-quenched martensitic steel has very high hardness and does not include the presence of a soft, deformable phase. Upon indentation of hard particles into the surface of martensitic steel, micro-cracks can form. When several adjacent micro-cracks link up, a wear particle can be cut lose. Several effects are available to raise the resistance against this crack-based wear mechanism. (1) Increasing the steel hardness raises the elastic limit stress of the material reducing the formation of cracks. (2) Refining the microstructure obstructs the propagation of existing cracks, in particular, increasing the number of large angle grain boundaries. (3) Embedding ultra-hard special carbide phases in the martensitic matrix can carry the highest contact stresses without fracturing. It is important that the size of these carbide phases is big enough compared to the size of the abrasive counter-body to prevent them from being removed by particle plowing. The hard phase can consist of molybdenum or chromium carbides formed during tempering, as well as of primary niobium or titanium carbides that have formed already before rolling. The latter primary carbides are much larger in size than the carbides formed *in situ*. Figure 3 indicates that such a composite material has superior abrasive wear resistance in spite of a relatively moderate hardness of its martensitic matrix.
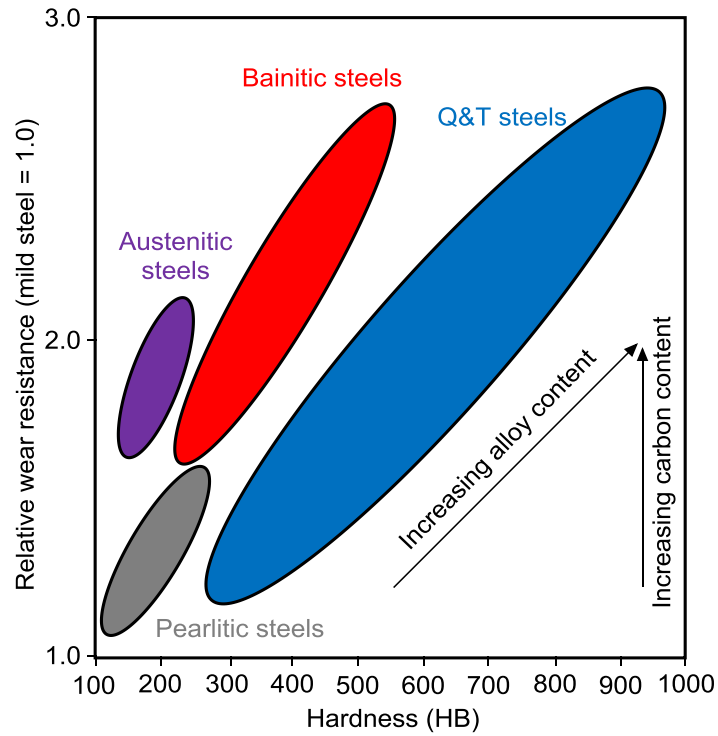
Figure 2. Influence of microstructure and hardness on wear resistance compared to mild steel.
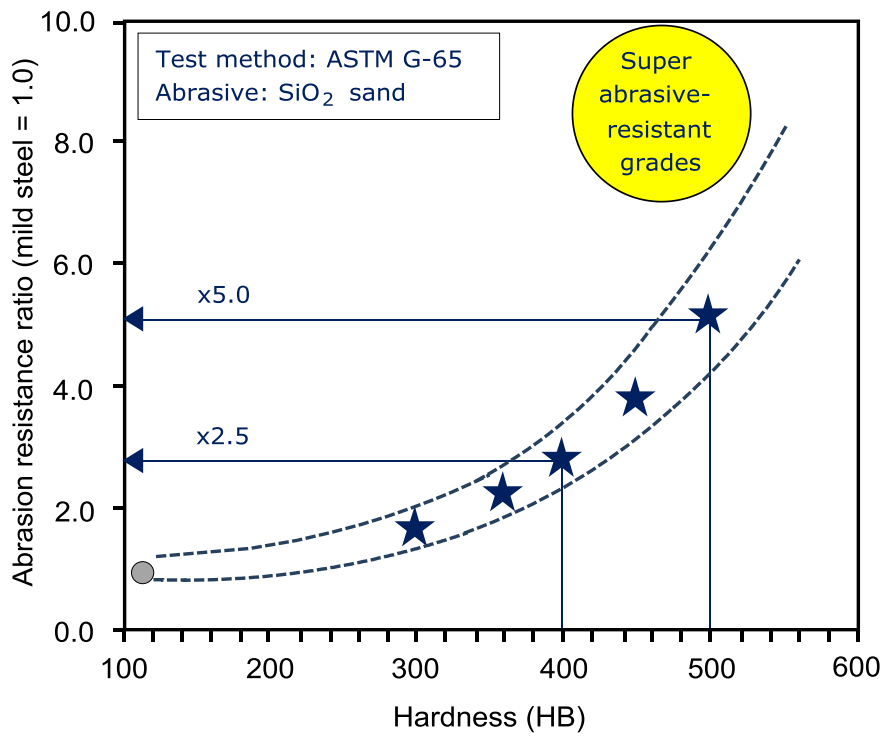

Figure 3. Performance of typical abrasive resistant steel grades and potential of super-abrasive resistant grades.
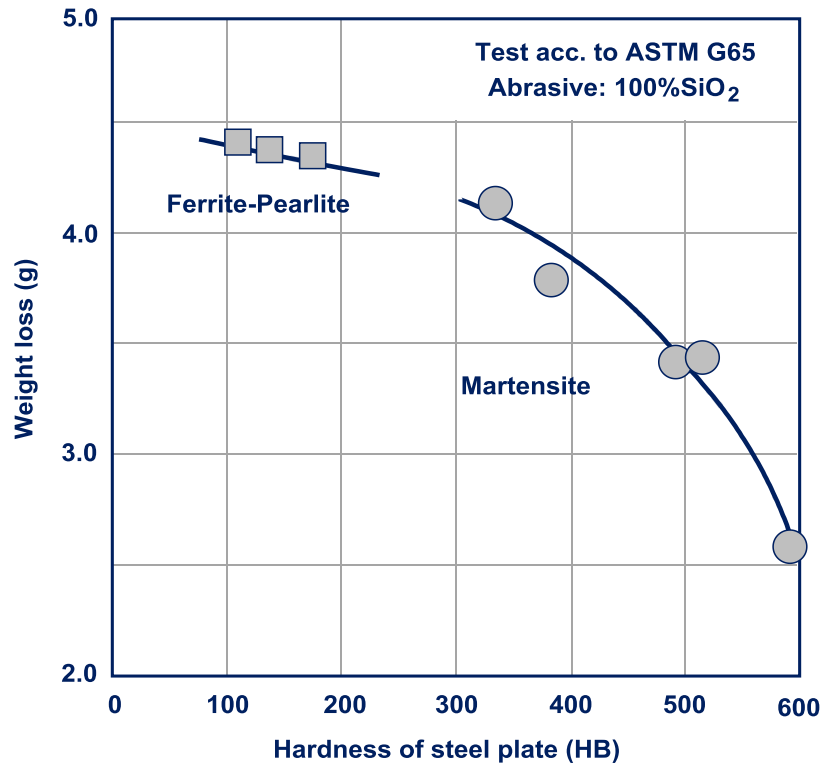
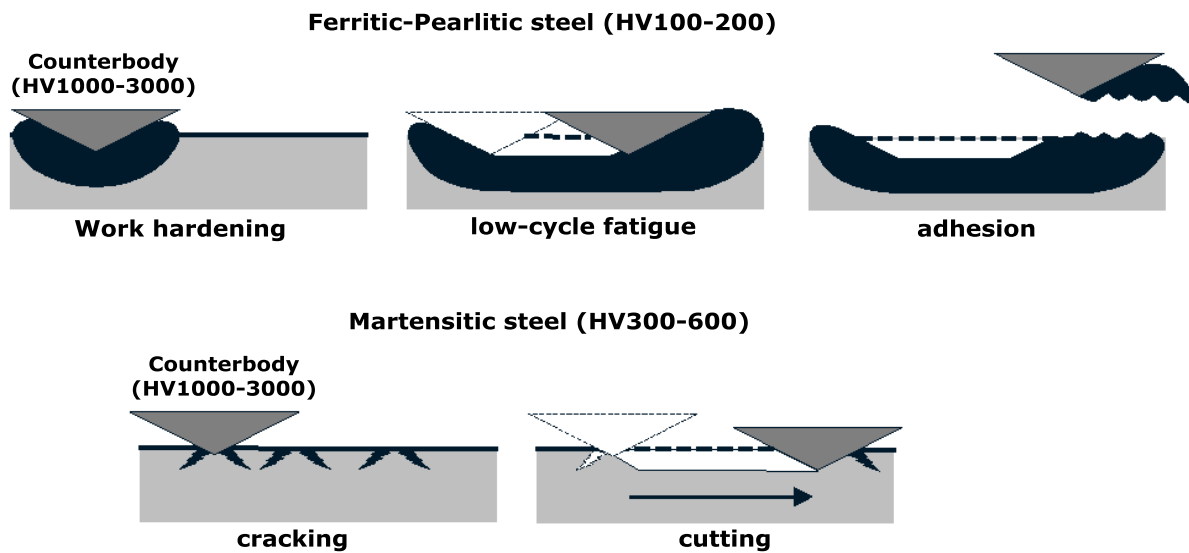Figure 4. Relationship between hardness, microstructure and weight loss in rubber wheel test.

Figure 5. Schematic hard particle wear mechanisms in ferritic-pearlitic and martensitic steels.

Conventional Abrasion Resistant Steels

Conventional abrasion resistant grades are mainly water quenched carbon-manganese steels, often microalloyed with a small amount of boron. In such steel, hardness is determined directly by the carbon content [6]. In the range of up to around 0.40 mass percent carbon, the hardness nearly linearly increases with the carbon content, (Figure 6). However, with increasing hardness the toughness of the quench hardened steel decreases to very low values, (Figure 7). For standard wear resistant grades toughness is not specified and quenched carbon-manganese steel with the required hardness suffices. Nevertheless, toughness in such grades can be improved by several metallurgical measures. Refining the microstructure, ie. particularly the large angle boundary structure, is effective in obstructing crack propagation as will be explained later. Other positive measures are keeping the impurity levels of phosphorous, sulfur and nitrogen low, as indicated in Figure 7. Tempering is another way of increasing toughness, but in such unalloyed grades it simultaneously results in a significant drop of hardness and thus wear resistance.
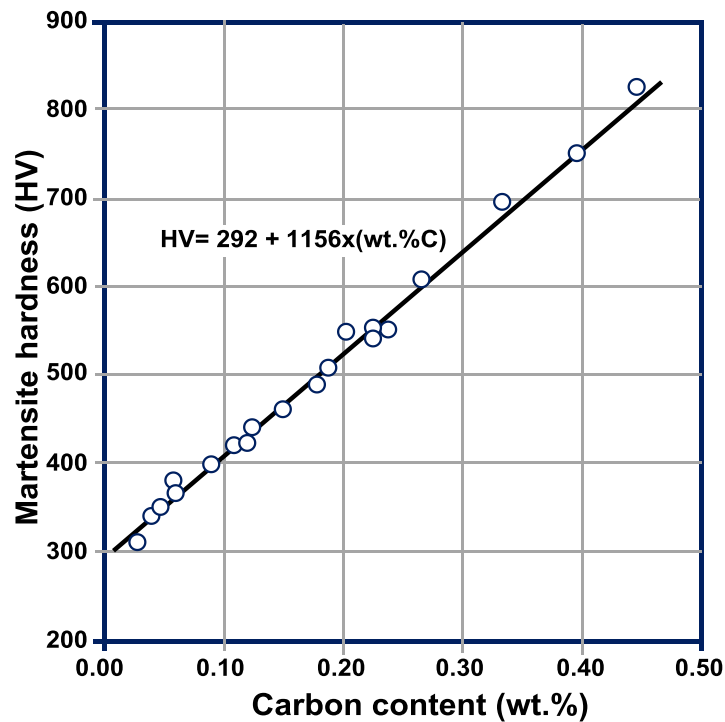

Figure 6. Relationship between carbon content and hardness of fully quenched martensite.
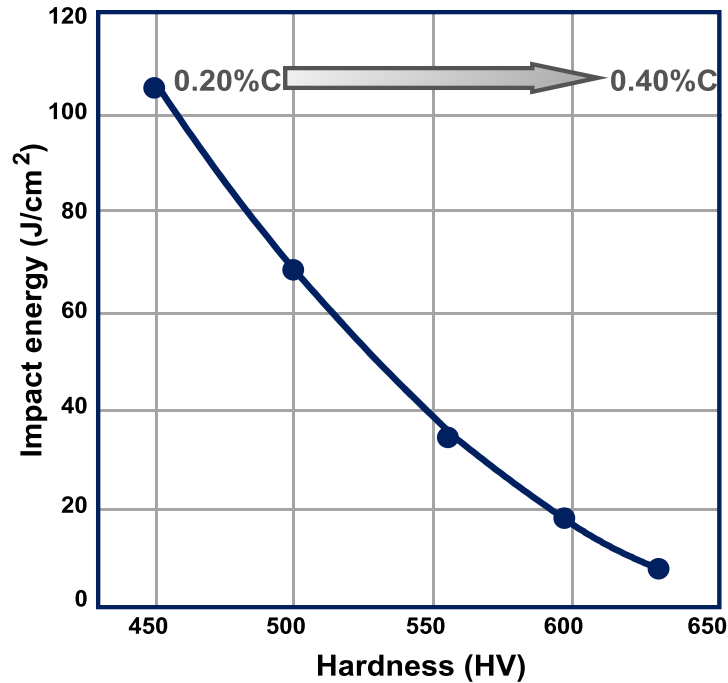
Figure 7. Influence of hardness on impact toughness in fully quenched martensitic steel.

Microstructural Optimization of Martensitic Steel

A key parameter in refining the microstructure of martensitic steel is the prior austenite grain size (PAGS) because the martensitic substructure develops within that perimeter. A prior austenite grain contains a very large number of discrete laths of dislocated martensite. These are organized into packets, in which the laths share the same habit plane. The packets are often subdivided into blocks in which the parallel laths are the same crystallographic variant of the martensitic transformation. Since packet and block boundaries are high angle boundaries, these constituents are considered to be effective grains. In other words, the strength and toughness of lath martensitic steels are strongly related to packet and block sizes. It is known that both the block width and the packet size are proportional to the prior austenite grain size [7,8]. For a very fine prior austenite grain size the packet size approaches that of the prior austenite grain size. The packet size can be considered a good approximation of the effective grain size relevant for toughness and critical fracture stress, (Figure 8).

Several measures can be taken for reducing the PAGS. A relatively low reheating temperature, possibly combined with Ti-microalloying leading to small TiN particles, can limit the austenite growth during long residence time in the furnace. Microalloying by niobium in combination with low finish rolling temperature contributes to refinement of austenite grains through a grain boundary drag effect caused by atoms in solid solution and a pinning effect due to *in-situ* precipitation. That solute drag effect is enhanced by the simultaneous presence of molybdenum. The austenite grain does not recrystallize and is pancaked resulting in a fine-sized ferritic-pearlitic microstructure upon cooling. In the subsequent heat treatment cycle, that refined microstructure is re-austenitized and then quenched into martensite. During the re-austenitizing phase, finely dispersed Nb or NbMo precipitates effectively prevent coarsening of the austenite

grains as demonstrated by Figure 9. This grain size controlling effect is stable over a substantial temperature range and disappears only when temperatures exceed the dissolution temperature of the particles. Over the entire austenitizing temperature range, microalloyed steel provides a smaller PAGS. The difference to conventional steel becomes bigger with increasing austenitizing temperature, (Figure 10). The smaller PAGS with the resulting refined martensitic substructure has evident benefits for the mechanical properties of the steel. Especially the low temperature toughness is substantially improved, as indicated by Figure 11 [9]. A disadvantage of PAGS refinement in unalloyed carbon steels is that hardenability reduced. The grain refined austenite structure renders a higher residual fraction of ferrite upon quenching at the same cooling rate.
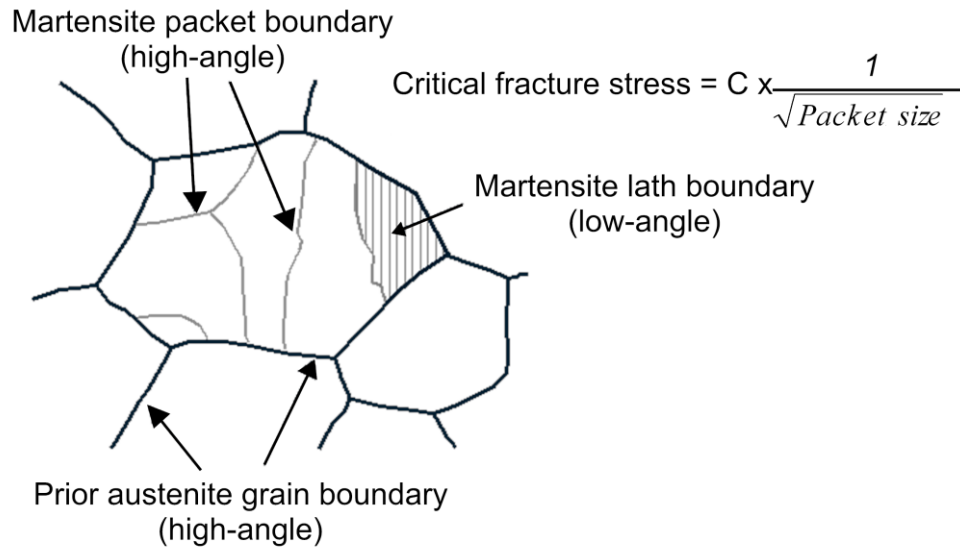
Figure 8. Martensitic substructure developing in the prior austenite grain and relationship of the critical fracture stress to the packet size.
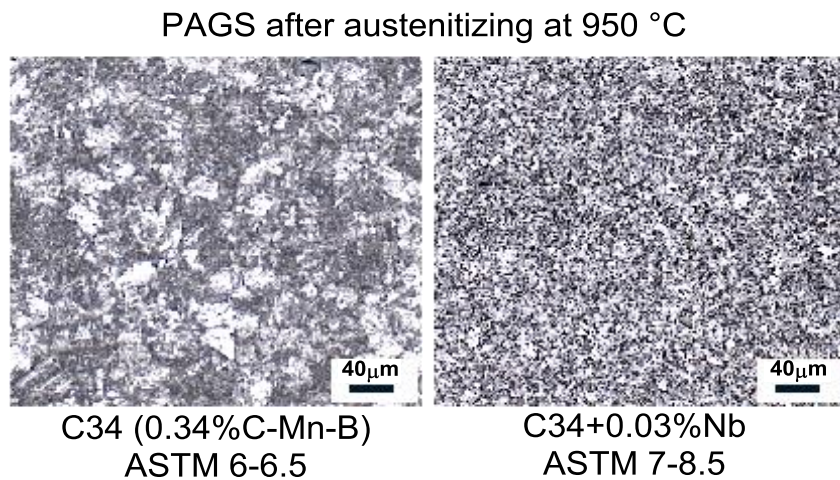

Figure 9. Refinement of prior austenite grain structure in a plain CMn C34 grade (0.34%C) by Nb-microalloying.
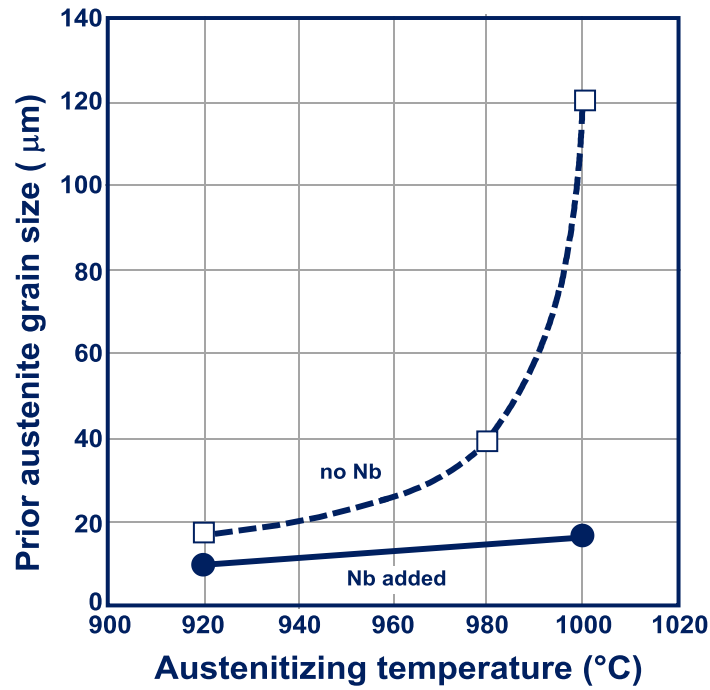
Figure 10. Relationship between prior austenite grain size (PAGS) and reheating temperature before quenching.
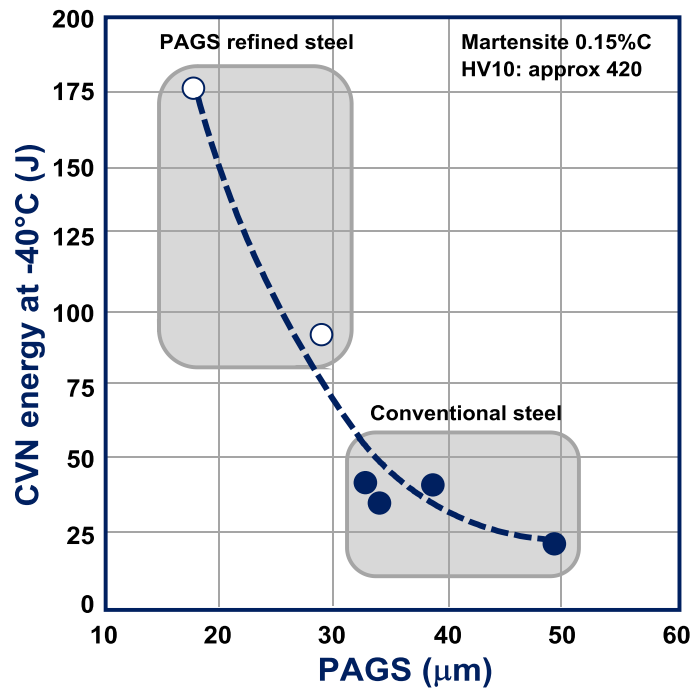

Figure 11. Influence of the prior austenite grain size on the impact toughness (test temperature -40 °C) for fully quenched martensite with 0.15%C.

Alloyed Abrasion Resistant Steels

Alloyed steel types are being applied where toughness matters and where through-hardening at heavier gages is required. Guaranteed minimum toughness (eg. 21 J or 27 J) can be adjusted at low temperature (eg. 0 °C or -40 °C) by controlling the carbon content and the alloying concept in combination with appropriate heat treatment. Such grades comprise an enhanced service lifetime in applications where impact loads are prevailing, especially in cold climates.

In conventional carbon-manganese steel the hardening depth is limited to a few millimeters. However, for specific applications, plate gages of up to 100 mm are required. Thus, a precisely tuned amount of alloying elements in combination with high cooling rates is required to achieve a high hardness value in the core of thicker plate and to obtain a homogeneous microstructure. Even though surface hardness is easily achieved by a quenching treatment, hardness tends to decline towards the core of a heavy gaged steel plate. Therefore, hardenability needs to be enhanced by alloying elements like manganese, molybdenum, chromium, copper and nickel. In estimating hardenability by Grange's technique [10] it is assumed that the hardenable diameter for iron is zero. The influence of single alloying elements on the change of the hardenable diameter can be estimated from Figure 12. Besides carbon, molybdenum has the strongest effect before manganese and chromium. Accordingly, adding 0.25%Mo to the Fe-0.2 %C base alloy would increase the hardenable cylinder diameter with 90% martensite at the center, by approximately 8 mm.

For a first judgment of the achievable hardening depth, the traditional Grossman relationship is often applied [11]. Accordingly, the hardenability of an alloyed steel characterized by the critical diameter D_I can be calculated based on the critical diameter of the iron-carbon base composition (D_{IC}) and multiplying factors (MF) for each alloyed element. As mentioned before, a smaller austenite grain size reduces the base hardenability.

$D_I = D_{IC} \times MF_{Si} \times MF_{Mn} \times MF_{Cr} \times MF_{Mo} \times MF_{Ni} \times MF_V \times MF_{Cu} \times MF_B \times 25.4$ (mm)

$D_{IC} = (C/10)^{1/2} \times (1.70 - 0.09N)$ with C: carbon content and N: austenite ASTM grain size number)

The multiplying factors given by Murota et al. [9] for each alloying element can be used in most cases:

- $MF_{Si} = 0.70Si + 1$
- $MF_{Mn} = 3.33Mn + 1$
- $MF_{Cr} = 2.16Cr + 1$
- $MF_{Mo} = 3.00Mo + 1$
- $MF_{Ni} = 0.36Ni + 1$
- $MF_V = 1.75V + 1$
- $MF_{Cu} = 0.35Cu + 1$
- $MF_B = 1.3$ (B added) or 1.0 (without B addition)

The addition of boron is an efficient method of increasing the hardenability, particularly for lower strength grades, allowing the use of very lean steel compositions. For higher grade abrasion resistant steels more carbon and other alloying elements need to be added for attaining the required mechanical properties. Besides manganese being a standard alloying element, molybdenum is particularly efficient in providing good hardenability. Molybdenum's effect is demonstrated in Figure 13 for steel with a base composition of 0.5%Mn and 0.3%Si at carbon levels of 0.19% and 0.42%, respectively, using the Jominy test.
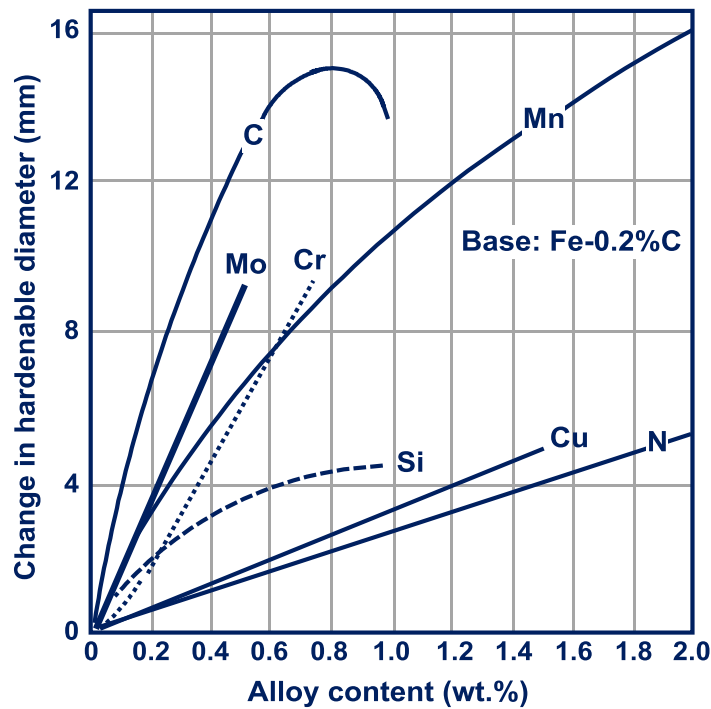

Figure 12. Influence of single alloying elements on the change of the hardenable diameter using Grange's technique [10].
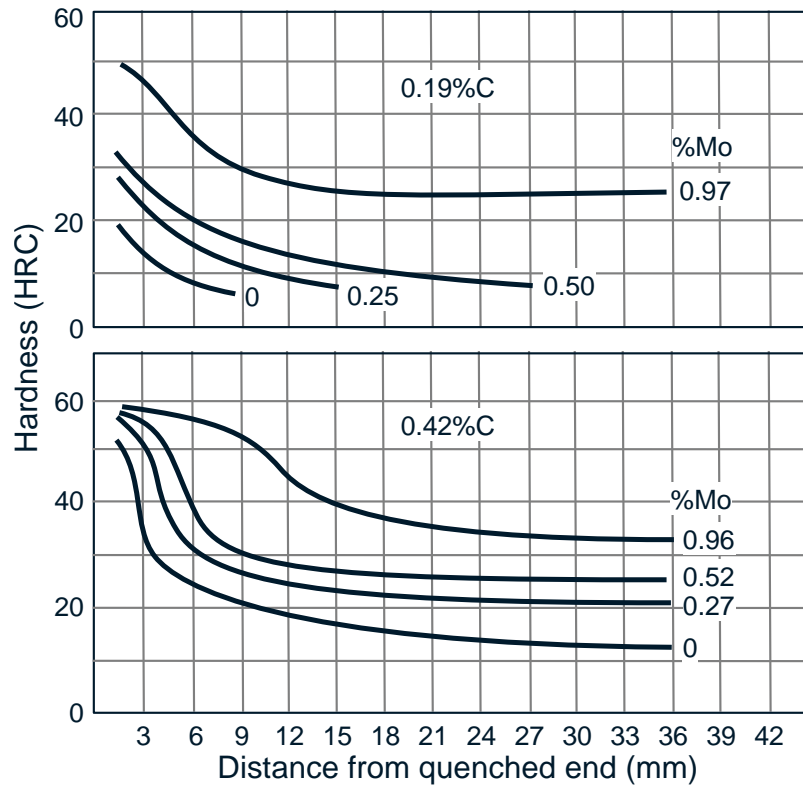
Figure 13. Effect of molybdenum and carbon on the Jominy hardenability curves of steels containing 0.5%Mn and 0.3%Si.

The Grossmann relationship is based on the assumption that there are no interactions between carbon and the alloying elements or between the various alloying elements. However, from Figure 14 it becomes evident that molybdenum's multiplying factor varies with the carbon content [12]. Especially on the low-carbon side, which is most relevant for abrasion resistant steels, the multiplying factor decreases with increasing carbon content, reaching a minimum at around 0.45%C. That means molybdenum is particularly effective in raising the hardenability of abrasion resistant steel with reduced carbon equivalent (CE). Low CE steel is preferred for its superior impact resistance at cold temperatures and its simultaneously improved weldability. The amount of molybdenum needed naturally depends on the plate gage to be produced. Thicker plates require a larger molybdenum addition. Especially at lower carbon levels, the molybdenum multiplying factor also strongly depends on the PAGS [12]. When the grain size decreases, as is the case in the Nb-microalloyed steel concept in combination with controlled rolling, the multiplying factor increases progressively, (Figure 15). Thus molybdenum alloying can effectively counteract the loss of hardenability caused by grain refinement.

With regard to further increasing hardenability, the combination of molybdenum with chromium appears to have a strong synergy. The combined effect of these two elements is much stronger than that of manganese and chromium, (Figure 16). Accordingly, the production of heavy gaged abrasive steel typically relies on combined alloying of molybdenum and chromium. The further addition of nickel and boron may become necessary to ensure a uniform property profile in the through thickness direction for grades in the high hardness range (500-600 HBW). Table II indicates representative ranges of alloying elements for abrasion resistant grades of different hardness levels, and their Cold Cracking Susceptibility Parameters, CET, at two gages. The actual alloying concept largely depends on the possibilities and preferences of the particular steel mill. In general, it is aimed to keep the carbon content as low as possible at a given target hardness and gage to optimize toughness and weldability. Thus, carbon ranges from 0.15% to nearly 0.5% over the product spectrum. Chromium addition of up to 1.5% has proven to be very effective against wear in weakly acid media enhancing the wear life by more than 35% [13]. Toughness and cold-forming behavior as well as resistance to impact wear are increased by grain refinement due to Nb-microalloying, (Figure 11). Comparing a standard 450 HBW grade with a Nb-microalloyed variant under abrasive wear by hard minerals revealed that the service life can be increased by around 20% [14].
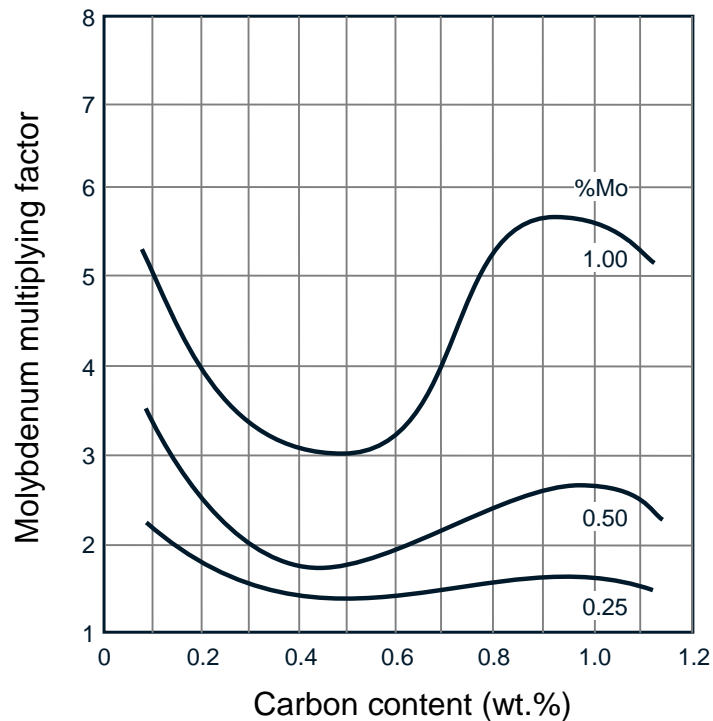

Figure 14. Effect of molybdenum and carbon on the molybdenum multiplying factor of steels containing 0.5%Mn and 0.3%Si.
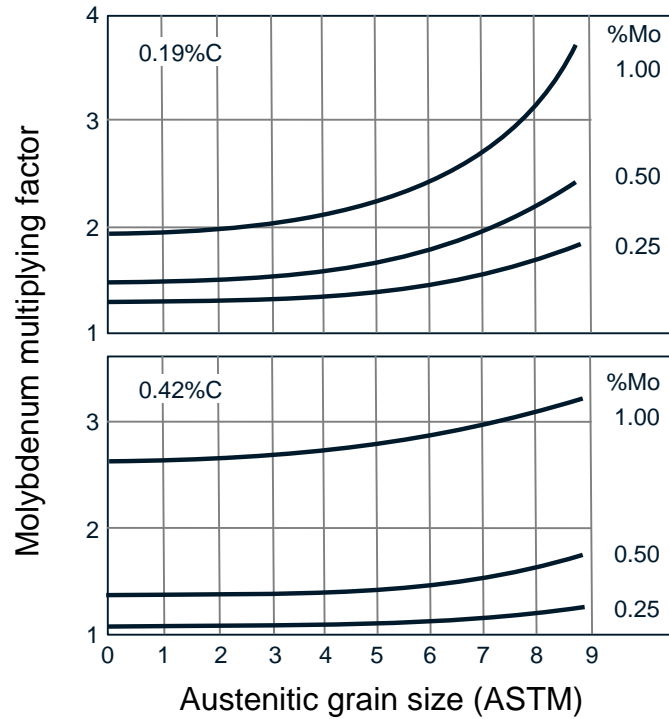
Figure 15. Effect of austenite grain size on the molybdenum multiplying factor of steels containing 0.5%Mn and 0.3%Si.
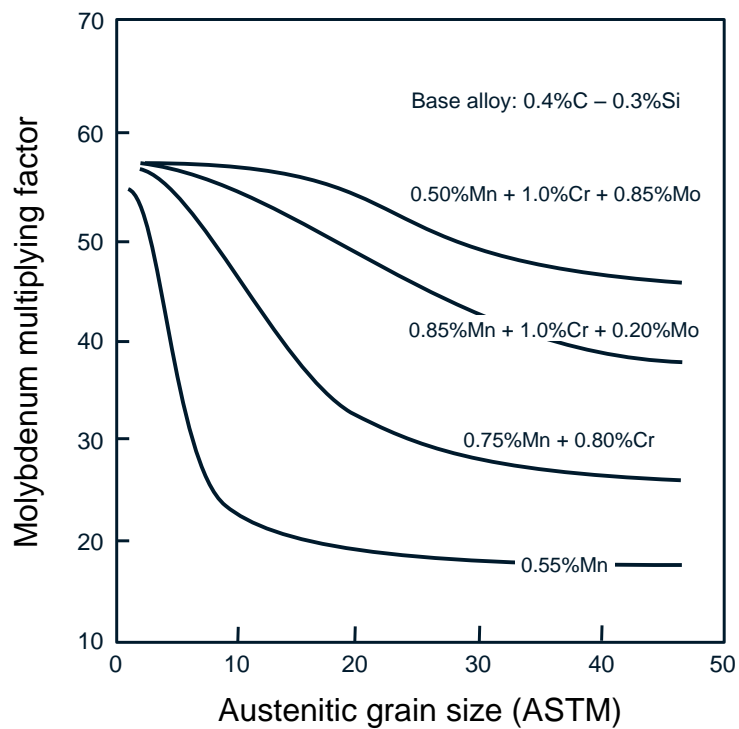

Figure 16. Effect of alloying elements on the Jominy hardenability curves of steel containing 0.4%C and 0.3%Si.

Table II. Typical Chemical Composition of Abrasion Resistant Steel Grades
in the Range of 400-600 HB

Target hardness (HB)	Max. plate gage (mm)	Chemical composition (max. %)						Typ. CET (%) at gage	
		C	Si	Mn	Cr	Ni	Mo	8 mm	40 mm
400	100	0.20	0.80	1.50	1.00		0.50	0.26	0.37
450	100	0.22	0.80	1.50	1.30		0.50	0.38	0.38
500	100	0.28	0.80	1.50	1.00	1.50	0.50	0.41	0.41
600	40	0.40	0.80	1.50	1.50	1.50	0.50	0.55	0.55

Abrasion Resistant Steels Containing Hard Phases

Embedding ultra-hard particles in a relatively softer steel matrix can further increase the abrasion resistance, (Figure 17). Such embedded hard particles consist typically of transition metal carbides, such as those of titanium, niobium, vanadium, tungsten, molybdenum or chromium, of which the hardness is indicated in Figure 1. Titanium and niobium have a very low solubility product and hence tend to form carbides already in the liquid phase or during solidification. *In-situ* formed primary carbides can achieve a relatively large size of tens of micrometers. All carbide-forming elements can also precipitate as secondary carbides in the steel matrix under suitable tempering conditions. These secondary carbides are typically less than 100 nm in size. Secondary carbides have the potential to raise the strength and hardness of the steel matrix, especially when their size is smaller than 10 nm. Molybdenum has a relatively good solubility in steel. Nevertheless, it can participate to some extent in primary titanium or niobium carbides [15,16]. Typically, molybdenum appears as secondary precipitates after a tempering treatment, contributing to strength and hardness increase of the steel matrix. The larger-sized primary carbides act as hard barriers in the surface and are load bearing to abrasive particles. As such they can interrupt particle plowing or even break an abrasive particle, as indicated by Figure 18, resulting in reduced chipping and material loss.
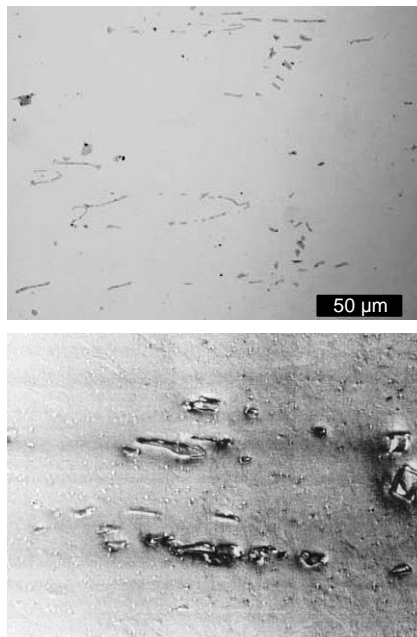

Figure 17. Micrographs of *in-situ* precipitated primary TiC particles in martensitic steel matrix.
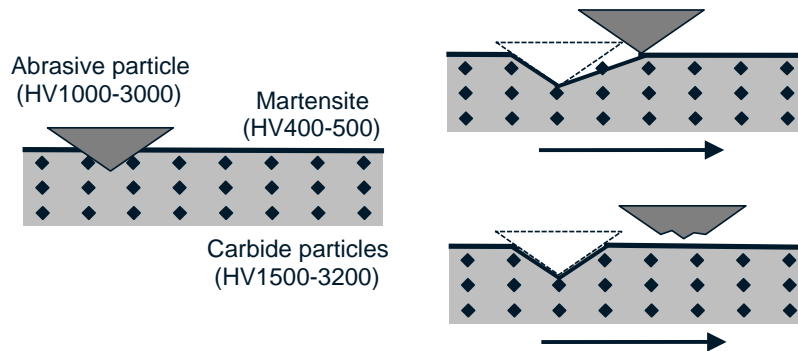
Steel matrix containing carbide particles

Figure 18. Schematic effect of superhard particles embedded in a martensitic steel matrix on abrasive wear resistance.

One alloying strategy is primary precipitation of transition metal carbides from the melt using appropriate element concentrations. Thereby the addition of carbide former and carbon has to correspond to the stoichiometric ratio. For instance 0.15 weight percent of carbon is needed to fix 0.6 weight percent of titanium forming TiC, since the stoichiometric ratio (by atomic weight) is around 1:4. That means the initial carbon content in the steel melt must be enhanced to around 0.4% when the target carbon content of the final steel matrix is intended to be 0.25 percent. Because titanium causes technical casting problems owing to its high affinity for oxygen, and vanadium has a relatively high solubility in the steel matrix, niobium appears to be a particularly interesting carbide forming element in alloy design. Another important aspect with regard to the final material properties is the carbide morphology. Compact shaped carbide particles that are not too large in size and that are homogeneously distributed are preferable. Large carbides with a dendritic three-dimensional morphology are disadvantageous with regard to fracture mechanics and toughness. Favorable carbide morphology can be achieved by optimizing carbide nucleation conditions and dwell time in the ladle [17]. However, when adding higher amounts of carbide former to liquid iron it becomes generally difficult to control shape and size of the *in-situ* forming carbide. Hence the addition of niobium in such alloys has typically been restricted to a few weight percent thus far.

Addition of NbC Particles as Hard Phase in Iron-based Alloys

A possible solution for introducing higher amounts of hard carbide phase into iron-based alloys is to add already formed carbides with defined size and shape to the liquid phase. This requires that firstly the carbide does not melt and secondly does not dissolve in the liquid iron bath. NbC fulfills both requirements. Its melting point is 3522 °C and its solubility is exceptionally low. Another very beneficial property is the density of NbC, around 7.7 g/cm^3, being very similar to that of liquid iron. Consequently gravity segregation of solid NbC added to liquid iron is quite limited contrary to other hard carbides like TiC, VC (lighter) or WC (heavier). Furthermore, VC and WC also have an appreciable solubility in iron. To avoid segregation and solubility issues, sintering routes have been developed to produce iron-based alloys with high contents of hard phases. An example is ferro-titanite where powders of FeTi mixed with a matrix alloy and graphite is forming *in-situ* a TiC rim structure having a core of martensitic steel, (Figure 19).

Apart from being a rather expensive production route, sintering routes have limitations in size and geometry of parts as compared to castings.

A recently developed innovative ferroalloy type developed by CBMM comprises an iron matrix with embedded NbC particles, (Figure 20). This ferroalloy can be directly produced during alumino-thermic reduction of Nb-oxide in the presence of iron and carbon. The primary NbC particles formed in this process have a compact blocky shape and are typically in the size range of 5 to 20 µm. The volume fraction of particles in the ferroalloy is around 50%. This ferroalloy as such can be considered as a metal-matrix composite (MMC) and has an extremely high wear resistance. When adding it to the ladle the iron matrix will melt and release solid NbC particles into the metal bath. The volume fraction of NbC can thus be diluted to any level below 50%. The shape and size of the carbide will only marginally change if at all due to the low solubility of NbC. In this way, larger amounts of carbide having a compact morphology can be introduced to a cast alloy.
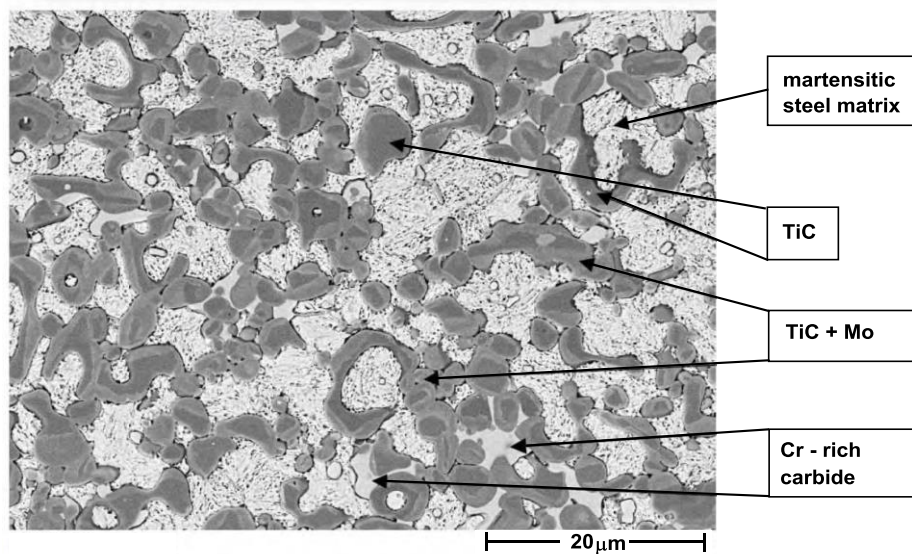

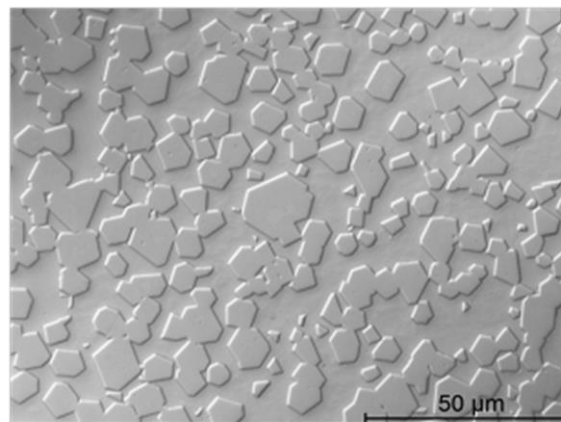Figure 19. Microstructure of ferro-titanite WFN grade [18].

Figure 20. Microstructure of a ferroalloy with iron matrix containing primary NbC.

245

Metallurgical Functionality of Niobium and Molybdenum Alloying in White Cast Iron

White cast iron (WCI) is a well-established material for many applications requiring high hardness and wear resistance. Over the years different grades of WCI have been developed, ranging from conventional white cast iron to Ni-hard, Ni-resist and high chromium white cast iron. High Cr WCI offers the best balance of hardness and toughness of all these due to an optimized balance of carbide type and morphology. Nickel-chromium white irons develop carbide types like Fe_3C or $(Fe,Cr)_3C$. The hardness of these carbides is comparable to that of quartz. In chrome-molybdenum white irons a primary $(Cr,Fe)_7C_3$ carbide is being developed with a hardness of nearly twice that of quartz. The $(Cr,Fe)_7C_3$ carbides in chrome-molybdenum white irons are embedded in an austenite/martensite matrix providing the higher toughness.

A typical representative of chrome-molybdenum white irons is Climax 15-3 or variations thereof. The hardness of the primary carbide in the high-alloy white irons is about twice that of silica, most often the primary gang material in the ore that is being processed, resulting in superior abrasion resistance. Figure 21 shows a comparison of the linear abrasion rate of various cast irons after testing in a silica-based slurry [19]. The superior performance of the chrome-molybdenum white iron is reflected in the lowest abrasion rate.
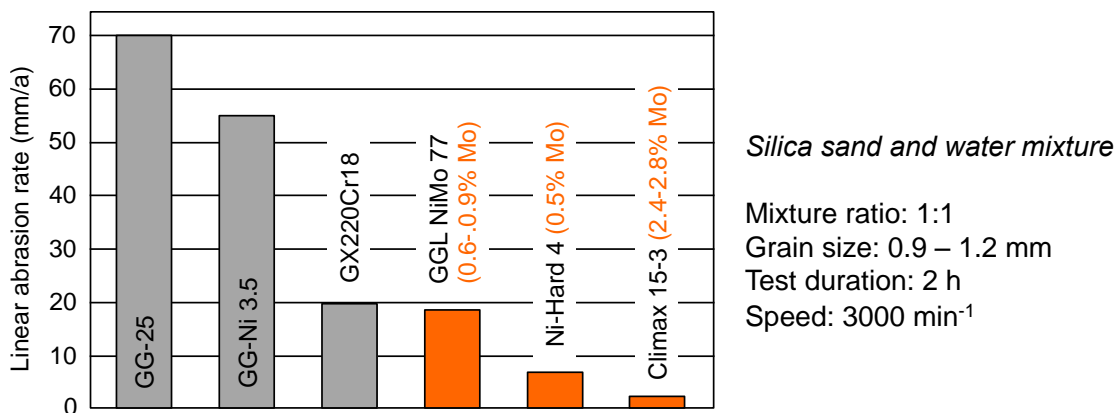

Figure 21. Abrasion rates of various cast materials exposed to hydro-abrasive wear in a silica-based slurry [19].

Molybdenum is primarily used to stabilize the austenite phase during cooling after solidification, as well as to prevent the formation of pearlite. One of the major advantages of molybdenum is that it has little effect on the Ms temperature, compared with other elements that tend to decrease the Ms temperature and over-stabilize the austenite. Molybdenum contents of less than about 1.0% are insufficient to suppress pearlite formation in heavy section castings, while amounts greater than 3.0% have no additional benefit in suppressing pearlite formation. Molybdenum partitions partly into austenite and partly into M_7C as well as MC carbides [20]. With molybdenum alloy additions below 1%, that proportion partitioned into austenite becomes too low to effectively suppress pearlite formation. Niobium was found to enhance the pearlite retarding effect of molybdenum when alloyed in combination in high chromium iron. This synergistic effect saturates above niobium additions of 1%, (Figure 22) [21].
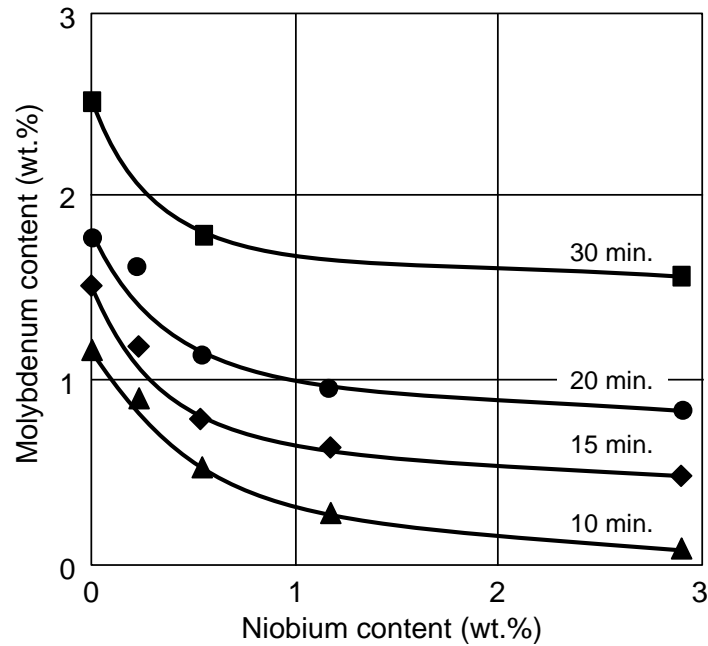
Figure 22. Combined effect of niobium and molybdenum alloying on the time required for 5% pearlite formation at a temperature of 700 °C in a 18%Cr – 3%C white cast iron (after W.L. Guesser [21]).

Adding niobium to a white cast iron alloy has several metallurgical effects and consequences. Since niobium is a very strong carbide former, the amount of M_7C_3 species is being reduced with increasing niobium addition to the alloy, (Figure 23) [22]. The replacement of M_7C_3 by the harder NbC is noticed in an increased macro hardness of alloys with niobium addition. Furthermore, the formation of NbC also has an influence on the matrix metallurgy. NbC binds more carbon than M_7C_3, hence the matrix is more carbon depleted. The consequence is a lower amount of retained austenite after heat treatment. This, together with the higher effectiveness of molybdenum in the presence of niobium, results in an increased matrix hardness. The macro hardness reflects a combination of the harder matrix, as well as the harder NbC fraction. On the other hand, the reduced volume fraction of M_7C_3 leaves a higher content of free chromium in the matrix, being beneficial for hardenability and corrosion resistance.
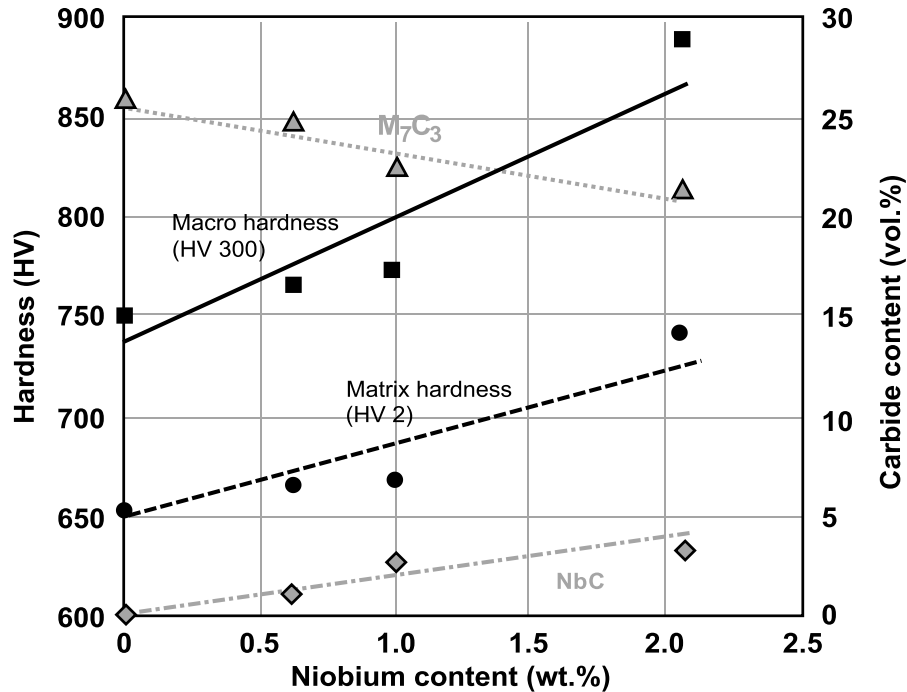
Figure 23. Macro (HV 300) and matrix micro-hardness (HV 2), and carbide content, versus niobium addition for a 2.94%C, 16.7%Cr, 0.83%Mo and 0.72%Cu iron (heat treated) [22].

The high chromium (11-30%) and carbon (1.8-3.6%) contents in high-Cr white cast iron generate an as-cast microstructure of hard eutectic M_7C_3 type carbides in an austenitic matrix [23]. Hypereutectic high chromium cast irons are often the preferred alloys for hard facing and ultra-high wear applications. Their excellent abrasion resistance is based on the high volume fraction of hard (1300-1800 HV) Cr_7C_3 carbides in the microstructure. The as-cast austenitic matrix is often destabilized by heat treatment to form a mixture of martensite/austenite with small precipitated secondary carbides within the prior austenite dendrites providing maximum hardness in the system [24]. During solidification, Cr_7C_3 carbides grow as rods and blades with their long axes parallel to the heat flow direction in the mold. The carbides can reach a size in the order of 0.5 mm [25] and are interconnected throughout the microstructure, providing an easy and low energy path for crack propagation [26]. Accordingly, such microstructures tend to have low fracture toughness.

Consequently, the research trend in high wear resistant cast irons has been to control the shape, size, interconnection, volume fraction and distribution of hard particles by modifying the alloy design or changing the processing metallurgy.

Previous work was performed in order to control the structure of alloy white cast irons [24,25,27-35]. Increasing the cooling rate during conventional casting can reduce the carbide size, but this process modification is limited by the section thickness, being effective only for sections thinner than 50 mm. Therefore, it is not applicable for manufacturing larger components. Hanlon et al. [25] characterized the spray forming process of alloy WCI, achieving one order of magnitude reduction in carbide size. This technique considerably improves the wear resistance. However, the spray forming process substantially increases the production cost.

248

Various attempts of alloy chemistry modification have been done as well. Boron was added to a 13%Cr iron [27] and to a 28%Cr iron [28] generating changes in the carbide morphology from interconnected, coarse and clustered rods to a parallel distribution of isolated and fine rods. Rare earth elements have been successfully used to modify the carbide structure of low chromium white irons [29-32]. However, the rare earth elements showed no apparent effect on the morphology of the M_7C_3 type carbides of high-Cr WCI [31]. Powell and Randle [33] observed a reduction in the carbide interconnectivity with the addition of 1.3% silicon to 18%Cr iron. Laird and Powell [24] affirmed that silicon inhibits the nucleation of the M_7C_3 carbides in 18%Cr iron, while on the other hand, Shen and Zhou [34] reported an increase in carbide phase nucleation due to similar silicon additions.

Carbide forming elements, such as niobium, titanium, vanadium, tungsten, hafnium, tantalum and zirconium were also added (from 0.10 up to 7.0 wt.%) to WCI castings, WCI-based hard-facing overlay and also high speed steels. All sources and authors converge to the same conclusion, considering that the presence of such elements significantly affects the mechanical properties by influencing the structure of the hard phases (hard particles) and also enhancing the strength of the matrix. The changes in the hard phases generate an improvement of the tribological properties by changing the chemical composition and dispersion of these particles throughout the microstructure [37-40].

Hence, it is clear that the control of the hard particles goes beyond just basic carbide morphology by altering the growth mechanism; it can be done by enhancing the nucleation rate via innovative alloying techniques that promotes the formation of primary carbides that would not only hinder the growth of Cr_7C_3 and boost the toughness, but also act as harder particles to improve even further the wear resistance.

Experience with NbC Reinforced White Cast Iron

Hard facing overlay is an application that is currently already using niobium additions to enhance the wear resistance. Commercial grades of WCI based hard facing overlay consumables include CORODUR 60TM, AI 1543TM and HARDFACE CN-O/S/GTM. These consumables have a basic chemistry of 5.5%C, 22%Cr, 1%Si and 7%Nb by adding a mechanical mixture of ferroalloys (FeNb, HCFeCr and FeSi ground together) directly in the cored-wire, so the carbides are formed *in-situ* during the arcing time of the hard facing process. The result is an increased wear resistance due to the presence of NbC and the refining effect of the primary NbC. This technique is limited to 8.0 wt.% of niobium addition, because the arcing time is too short (5 to 10 seconds) leaving insufficient time for NbC to form and disperse homogeneously in the weld deposit. Figure 24 compares the effect of niobium addition on the microstructure and carbide morphology in a WCI hard facing layer.
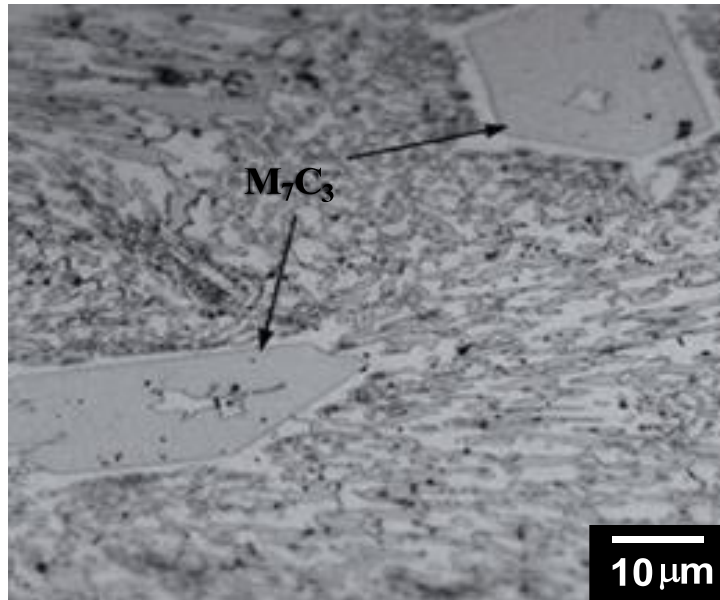
27%Cr; 4.2%C; 0.5%Mn; 0.5%Si
(30 vol.% hard particles)
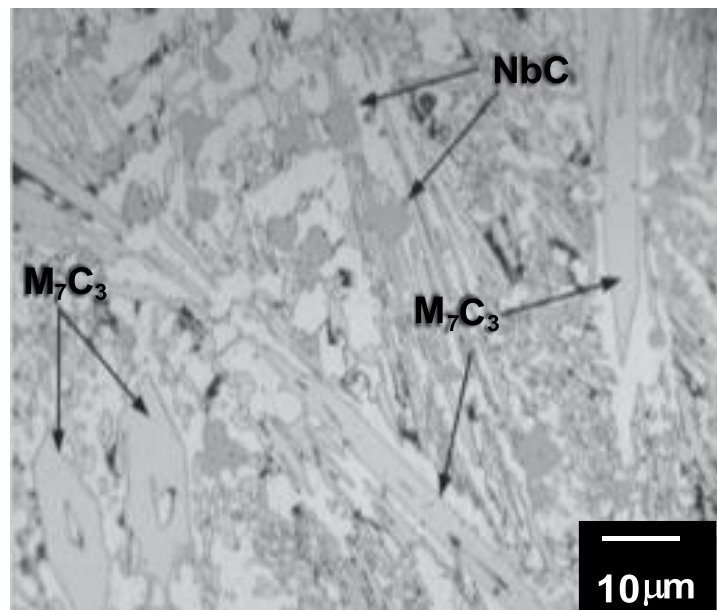
22%Cr; 4.5%C; 0.5%Mn; 0.5%Si; 6.5%Nb
(55 vol.% hard particles)

Figure 24. Size and morphology of carbides in high-Cr WCI without and with Nb addition [41].

An improved hard-facing consumable production method allows the addition of higher amounts of carbide forming elements [36] including niobium, resulting in the formation of a very homogeneous dispersion of hard particles in the as-cast microstructure. The idea is to produce a homogeneous melt with the required concentration of the key elements, being: Fe, C, Cr, and Nb. This homogeneous melt is being produced from solid raw materials (ie. steel scrap and/or WCI scrap, HCFeCr, FeNb, as well as a source of free carbon such as graphite). It must be held liquid sufficiently long to dissolve the carbon and homogenize the composition of the melt so as to produce the desired level of combined-carbon (carbides). After casting the heat in small ingots, a powder is produced from it by crushing and milling operations to fill the cored-wires for the defined hard-facing procedure. Additions up to 35 wt.%Nb were tested on laboratory and industrial scale with positive results. The wear resistance was significantly improved providing up to a 4-fold increase of service life in specific applications by adding 20 wt.%Nb. Figure 25 demonstrates a quite homogeneous distribution of compact NbC particles at a level of 15 vol.% in high-Cr white cast iron [41].
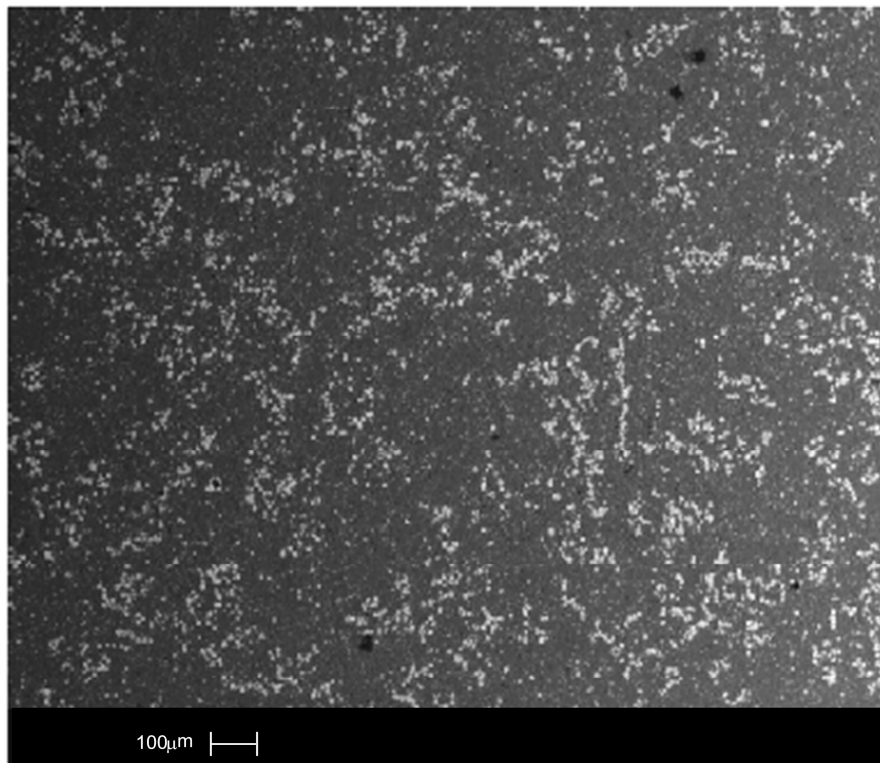

Figure 25. NbC particle distribution (bright contrast) in the microstructure of high-Cr WCI added with 15 wt.%NbC [41].

The same approach can be used for casting components. The wear resistance of high-Cr WCI castings can be greatly enhanced by macro-additions of niobium. An example of such a concept is the production of slurry pump impellers for the mining industry. A new alloy concept comprises WCI with up to 25 wt.%NbC, and the results show substantial improvement of the casting part service life [42]. A field trial with a slurry pump impeller made from white cast iron containing 15 wt.%NbC particles at CBMM's mining site in Araxá, Brazil revealed a 300% increase in the service life as compared to the NbC-free standard alloy, (Figure 26).
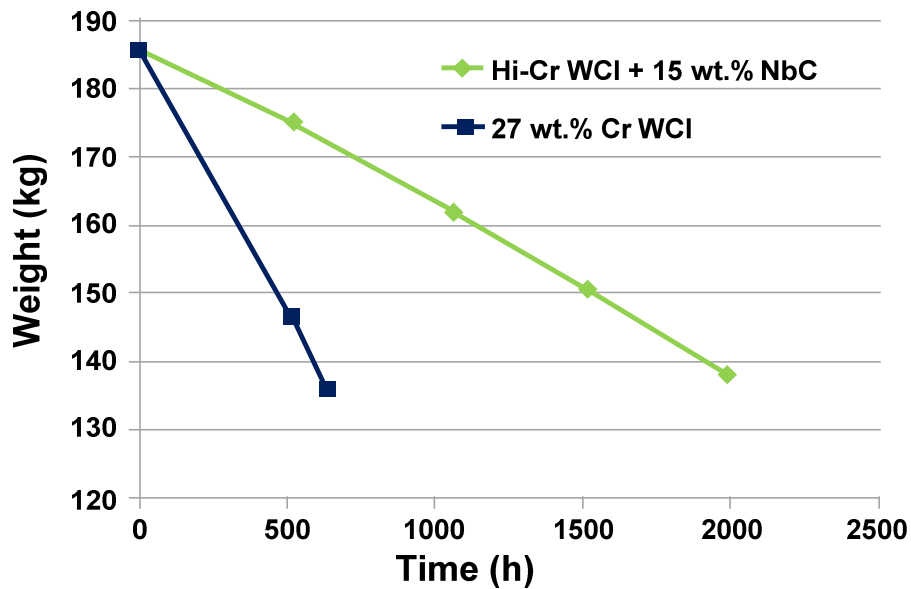

Figure 26. Field trial results demonstrating the service life increase of a slurry pump impeller at CBMM mine (Araxá, Brazil) due to the addition of 15 wt.%NbC to white cast iron (WCI).

Conclusions

Molybdenum is an established and essential alloying element in many abrasion resistant iron and steel alloys. It increases hardenability most efficiently. This is particularly important when producing plate or cast components with large dimensions. Under particular processing conditions molybdenum also enables a TRIP effect by preserving retained austenite providing high work hardening during service. Molybdenum either by itself or in combination with other alloying elements forms hard carbide particles that are dispersed in the steel matrix. Such hard carbide precipitates further contribute to wear resistance. Combined alloying of molybdenum and niobium enables synergies such as a more efficient prior austenite grain size control and increased tempering resistance.

Niobium has been introduced more recently as an alloying element in abrasion resistant alloys. Micro additions of niobium to abrasion resistant steel refine the microstructure and mainly increase toughness. Larger additions of niobium can produce either primary or eutectic carbide particles. NbC particles are extremely hard and significantly enhance wear resistance. The formation of macroscopic NbC particles also reduces the amount of other transition metal carbides. Accordingly, a larger proportion of molybdenum and chromium stay in solution, contributing to increased hardenability and corrosion resistance.

Friction and wear properties of pure NbC have been recently investigated in detail for the first time. The results indicate a very high tribological performance of NbC in contact against metallic and ceramic materials [43].

References

1. J.H. Tylczak, "Effect of Material Properties on Abrasive Wear" ASM Handbooks Online, volume 18, Friction, Lubrication and Wear Technology, (Materials Park, OH: ASM International, 2002).

2. L. Xu and N.F. Kennon, "A Study of the Abrasive Wear of Carbon Steels," *Wear,* 148 (August 1991), 101-112.

3. K-H. Zum Gahr, *Microstructure and Wear of Materials,* (Amsterdam, Netherlands: Elsevier Science Publishers, 1987), 132-292.

4. Anon. "Abrasion-resistant Steels Plates of JFE Steel" (JFE Technical Report No. 11, June 2008), 26-28.

5. N. Ishikawa et al., "High-performance Abrasion-resistant Steel Plates with Excellent Low-temperature Toughness," *Proceedings of the 2011 International Symposium on the Recent Developments in Plate Steels,* AIST Winter Park (2011), 81-91.

6. R.A. Grange, C.R. Hibral and L.F. Porter, "Hardness of Tempered Martensite in Carbon and Low-alloy Steels," *Metallurgical Transactions A*, 8A (1977), 1775.

7. T. Maki and I. Tamura, "Morphology and Sub-structure of Lath Martensite in Steels," *Tetsu-to-Hagané*, 67 (1981), 852-866.

8. S. Morito et al., "Effect of Austenite Grain Size on the Morphology and Crystallography of Lath Martensite in Low Carbon Steels," *The Iron and Steel Institute of Japan International*, 45 (1) (2005), 91-94.

9. Y. Murota et al., "High Performance Steel Plates for Construction and Industrial Machinery Use —New Steel Plates for Construction and Industrial Machinery Use with High Strength and Superior Toughness Combined with Good Weldability and Formability" (JFE Technical Report No. 5, 2005), 60-65.

10. R.A. Grange, "Estimating the Hardenability of Carbon Steels," *Metallurgical Transactions*, 4 (1973), 2231.

11. M.A. Grossman, "Hardenability Calculated From Chemical Composition," *Transactions of the American Institute of Mining, Metallurgical, and Petroleum Engineers,* 150 (1942), 227 - 259.

12. R.V. Fostini and F.J. Schoen, "Effects of Carbon and Austenitic Grain Size on the Hardenability of Molybdenum Steels" (Paper presented at the Symposium on Transformation and Hardenability in Steels, Climax Molybdenum Company, 1967), 195-209.

13. ThyssenKrupp Steel Europe, XAR-Steels for Reliable Use and Long Service Life in Crushing and Screening Plants, Market Focus Crushers, (2005), Company Brochure.

14. A. Kern and U. Schriever, "Niobium in Quenched and Tempered HSLA-Steels," *in: Recent Advances of Niobium Containing Materials in Europe* (Verlag Stahleisen, 2005), 107-120.

15. F. Bouchaud et al., "New Wear Resistant Steel, 'Cruesabro Dual'," *Proceedings of the 2011 International Symposium on the Recent Developments in Plate Steels,* AIST Winter Park (2011), 93-101.

16. JFE Steel Company Brochure, JFE EVERHARD EH-SP.

17. W. Theisen, S. Siebert and S. Huth, "Wear Resistant Steels and Casting Alloys containing Niobium Carbide," *Steel Research International,* 78 (12) (2007), 921-928.

18. P. Schütte, "Aufbau einer Kurzzeitsinteranlage zur Herstellung Verschleißbeständiger Verbund Werkstoffe" (Ph.D. thesis, Ruhr-University Bochum, 2012).

19. KSB AG Company Brochure: Cast Materials from KSB, Pegnitz (Germany), www.ksb.com.

20. C.R. Loper and H.K. Baik, "Influence of Molybdenum and Titanium on the Microstructures of Fe–C–Cr–Nb White Cast Irons," *Transactions of the AFS,* 97 (1989), 1001-1008.

21. W.L. Guesser, "Niobium in High-chromium Irons," *Foundry Management and Technology* (September 1985), 50-52.

22. M. Fiset, K. Peev and M. Radulovic, "The Influence of Niobium on Fracture Toughness and Abrasion Resistance in High-chromium White Cast Irons," *Journal of Material Science Letters,* 12 (1993), 615-617.

23. C.P. Tabrett, I.R. Sare and M.R. Gomashchi, "Microstructure-property Relationships in High Chromium White Iron Alloys," *International Materials Reviews*, 41 (1996) 59.

24. G. Laird and G. Powell, "Solidification and Solid-state Transformation Mechanisms in Si Alloyed High-chromium White Cast Irons," *Metallurgical and Materials Transactions A*, 22 (1993), 981.

25. D. Hanlon, W.M. Rainforth and C.M. Sellars, "The Rolling/Sliding Wear Response of Conventionally Processed and Spray Formed High Chromium Content Cast Iron at Ambient and Elevated Temperature," *Wear,* 225–229 (1999), 587.

26. P.A. Morton, R.B. Gundlach and J. Dodd, "Factors Affecting Austenite Measurements in High Chromium White Cast Irons," *Transactions of the AFS,* 93 (1985), 879.

27. H. Fusheng and W. Chaochang, "Modifying High Cr–Mn Cast Iron with Boron and Rare Earth-Si Alloy," *Materials Science and Technology,* 5 (1989), 918.

28. N. Ma, Q. Rao and Q. Zhou, "Effect of Boron on the Structures and Properties of 28%Cr White Cast Iron," *Transactions of the AFS*, 98 (1990), 775.

29. M.A. Qian, W. Chaochang and S. J. Harada, "Modification of Hypoeutectic Low Alloy White Cast Irons," *Materials Science,* 31 (1996), 1865.

30. J. Li and R.W. Smith, "Growth Modification of Austenite-(Fe,Cr)3C Pseudo-binary Eutectic," *Proceedings of the IVth Decennial International Conference on Solidification Processing,* (1997), 481.

31. G.Y. Liang and J.Y. Su, "The Effect of Rare Earth Elements on the Growth of Eutectic Carbides in White Cast Irons Containing Chromium," *International Journal of Cast Metals Research*, 4 (1992), 83.

32. Y. Qingxiang et al., "Effect of Rare Earth Elements on Carbide Morphology and Phase Transformation Dynamics of High Ni–Cr Alloy Cast Iron," *Journal of Rare Earths,* 16 (1998), 36.

33. G. Powell and V. Randle, "The Effect of Si on the Relationship Between Orientation and Carbide Morphology in High Chromium White Irons," *Journal of Materials Science,* 32 (1997), 561.

34. J. Shen and Q.D. Zhou, "Solidification Behaviour of Boron-bearing High-chromium Cast Iron and the Modification Mechanism of Silicon," *International Journal of Cast Metals Research,* (1988), 79.

35. F. Han and C. Wang, "Modifying High Cr–Mn Cast Iron with Boron and Rare Earth–Si Alloy," *Materials Science and Technology,* 5 (1989), 918.

36. K.F. Dolman, Patent: Hardfacing Ferroalloys Materials. US 2008/0251507 A1, 2008.

37. H.Q. Wu et al., "Solidification of Multialloyed White Cast Iron: Type and Morphology of Carbides," *Transactions of the AFS,* 104 (1996), 103.

38. H.K. Baik and C.R. Loper Jr., "The Influence of Niobium on the Solidification Structure of Fe-C-Cr Alloys," *Transactions of the AFS,* 96 (1988), 405.

39. P. Dupin and J.M. Schissler, "Influence of Additions of Silicon, Molybdenum, Vanadium and Tungsten upon the Structural Evolution of the As-cast State of a High-chromium Cast Iron (20%Cr, 2.6%C)," *Transactions of the AFS,* 92 (1984), 355.

40. R. Kesri and M. Durand-Charre Jr., "Phase Equilibria, Solidification and Solid State Transformations of White Cast Irons Containing Niobium," *Journal of the Materials Society*, 22 (1987), 2959.

41. A.C. Lima and V.A. Ferraresi, "Analysis of Microstructure and Wear Strength of Hardfacing used by the Sugar and Alcohol Industry," *Soldagem e Inspeção São Paulo*, 14 (2) (Apr/Jun 2009), 140-150.

42. WEIR MINERALS LTD Patent: Hard Metal Materials WO 2011/094800 A1, 2011.

43. M. Woydt and H. Mohrbacher, "Friction and Wear of Binder-less Niobium Carbide," *Wear,* 306 (2013), 126-130.

DISSOLUTION OF FeNb IN LIQUID STEEL

E.B. Cruz[1], D.P. Fridman[1], M.C. Carboni[2], R.C. Guimarães[1] and M.A. Stuart Nogueira[2]

[1]CBMM, Araxá, MG, Brazil
[2]CBMM, São Paulo, SP, Brazil

Abstract

Niobium is a well-established microalloying element for the production of High-Strength Low-Alloy (HSLA) steels and it is usually added in amounts smaller than 0.10% in the form of standard ferroniobium (FeNb) [1]. The operational practice at the melt shop, as well as controlled dissolution trials in the laboratory and on an industrial scale, have shown that standard FeNb dissolves very rapidly and with high recovery yields. It was verified that the addition of FeNb requires good control of some parameters, such as deoxidation temperature, stirring time and particle size. For each application, CBMM produces lumpy material in a wide range of size distributions. Taking advantage of using very fine particles, recently CBMM has developed a new briquetting process in order to agglomerate FeNb fines smaller than 2 mm to make them robust enough for easy handling during their addition to the molten steel. This paper aims at presenting a review of the FeNb characterization, the dissolution rate of lumpy and briquetted fines, as well as showing the mechanism of dissolution at the FeNb/steel interface. In the laboratory trials it was observed that briquetted FeNb fines dissolve faster than the lumpy material at temperatures of 1560 °C, 1600 °C and 1640 °C. It was verified that the difference between the dissolution rate of FeNb briquettes and lumpy material is less significant for higher temperatures (1640 °C). The industrial trials showed that the complete dissolution of briquettes and lumpy material occurred in less than 10 minutes at 1570 °C and that the yield of the niobium addition was higher than 98% for both materials.

Introduction

Niobium is a well-established microalloying element for the production of HSLA steels and it is usually added in amounts smaller than 0.10% in the form of standard FeNb [1]. The operational practice at the melt shop, as well as controlled dissolution trials in the laboratory and on an industrial scale have shown that standard FeNb dissolves very rapidly and with high recovery yields. It was verified that the addition of FeNb requires a good control of some parameters, such as deoxidation temperature, stirring time and particle size, as is the case for all alloy additions in general. For each application, CBMM produces lumpy material in a wide range of size distributions. Taking advantage of using very fine particles, recently CBMM has developed a new briquetting process in order to agglomerate FeNb fines, smaller than 2 mm, to make them robust enough for easy handling during their addition to the molten steel.

This paper presents a review of the FeNb characterization, the dissolution rate of lumpy and briquetted fines, as well as showing the mechanism of dissolution at the FeNb/steel interface.

Characterization of Standard FeNb

As can be seen in Figure 1(a), standard FeNb is a high-niobium alloy containing approximately 65 wt.% niobium [2]. Its microstructure consists of two predominant zones: (a) primary laths of the intermetallic $Fe_{21}Nb_{19}$ (μ) and (b) eutectic zones (e). The eutectic zones are in turn formed by the following stable phases: (e_1) $Fe_{21}Nb_{19}$ and (e_2), terminal globules of high content, as well as a third metastable phase Fe_2Nb_3 (e_3), Figure 1(b) [3,4].
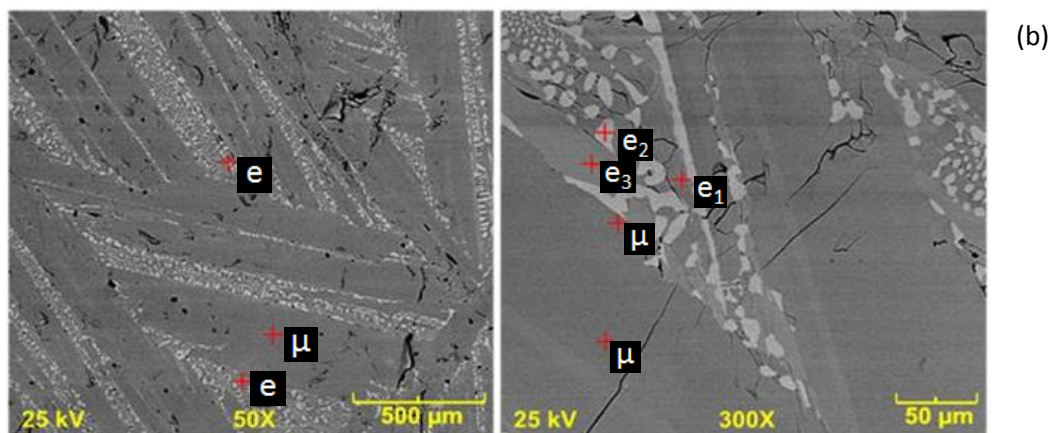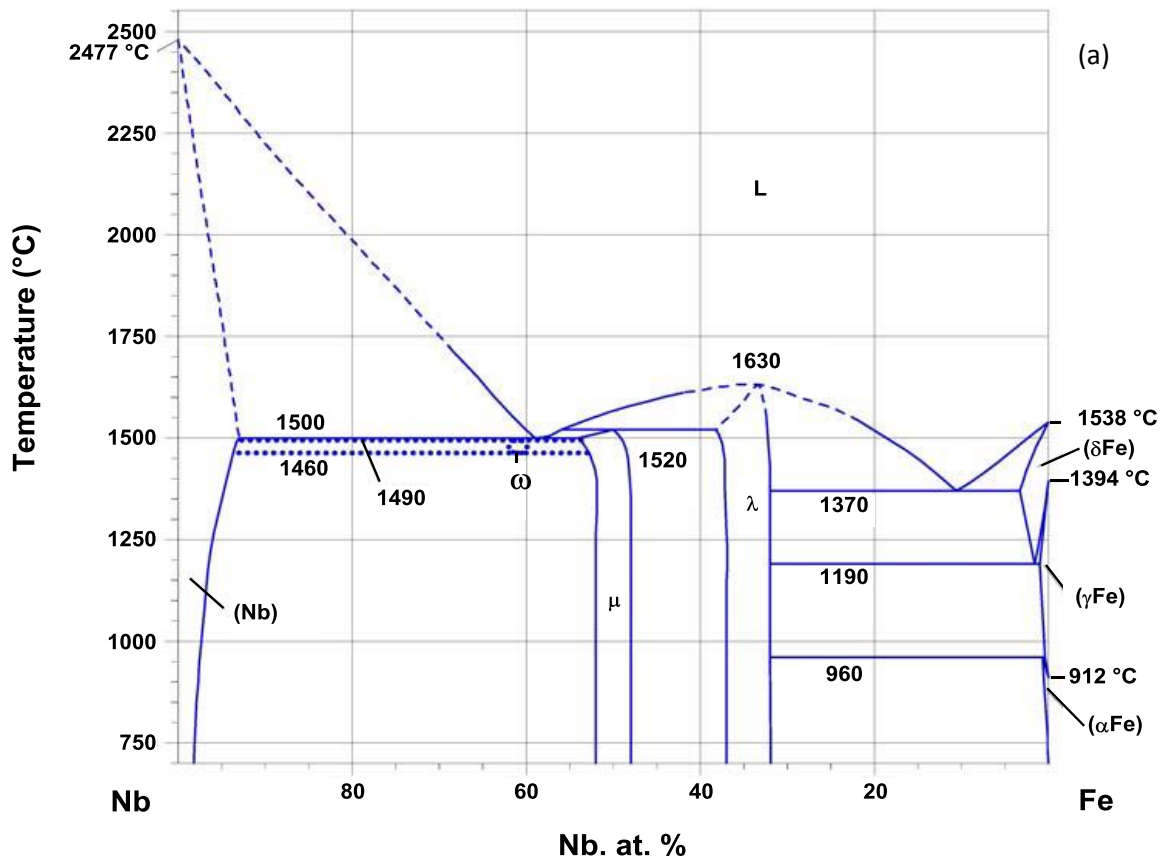
Figure 1. FeNb phase diagram according to Zelaya-Bejarano [2] (a) and typical microstructure of standard FeNb (b) [3,4].

Dissolution of Standard FeNb

In order to study the dissolution rate of briquetted FeNb fines (<2 mm) and lumpy material (20, 30 and 40 mm in equivalent diameter), laboratory and industrial comparative dissolution trials were carried out by addition of these particles to steel baths at temperatures between 1560 and 1640 °C. The appearance of the briquettes and lumps is shown in Figure 2. The binder used for briquetting was an inorganic silicate based material.

The laboratory trials were carried out in an induction furnace by dropping the briquettes or lumps on the surface of deoxidized low carbon steel baths (35 kg) heated up to 1560, 1600 and 1640 °C. Samples of liquid metal were taken by suction into quartz tubes in order to follow the niobium increase in the steel bath during the dissolution process.

The industrial trials were carried out by simple dropping of FeNb briquettes or lumps on steel baths at 1570 °C contained in a 70 ton ladle. The lumpy material comprised particles with size distributions from 5 to 15 mm and from 15 to 30 mm. The briquettes were 40 mm in equivalent diameter. The metallic charge was melted down in an electric arc furnace and then poured into the ladle for manganese, silicon and aluminum deoxidation to achieve an active oxygen content below 20 ppm. Samples were taken during the heats and the temperature was adjusted in accordance with standard procedures for steel casting.


Figure 2. FeNb lump (top) and briquette (bottom).

With the aim of describing the dissolution mechanism at the interface between the briquettes or lumps and the steel bath, six interrupted dissolution trials were also carried out in a laboratory scale induction furnace. For this purpose, the particles were partially immersed in the steel baths at 1550 °C, 1600 °C and 1650 °C, held in for 10 seconds and then water quenched for metallographic analysis.

Results

The results of the laboratory scale and industrial dissolution trials are shown in Figures 3 and 4 respectively in terms of the increase of niobium content in the steel bath during the heats.

In Figure 3 it is possible to observe that the dissolution of FeNb briquettes was faster than the dissolution of lumpy material for all the temperatures established for the trials. However, the difference between the dissolution rate of FeNb briquettes and lumpy material was less significant for higher temperatures. For both, the dissolution rate increased by increasing the bath temperature from 1560 °C up to 1640 °C. It was noticed that briquettes and lumps dissolved in less than 1 minute at the highest temperature (1640 °C). As in previous work [3,4], it was verified that the dissolution rate of lumpy material increases by decreasing the particle size.
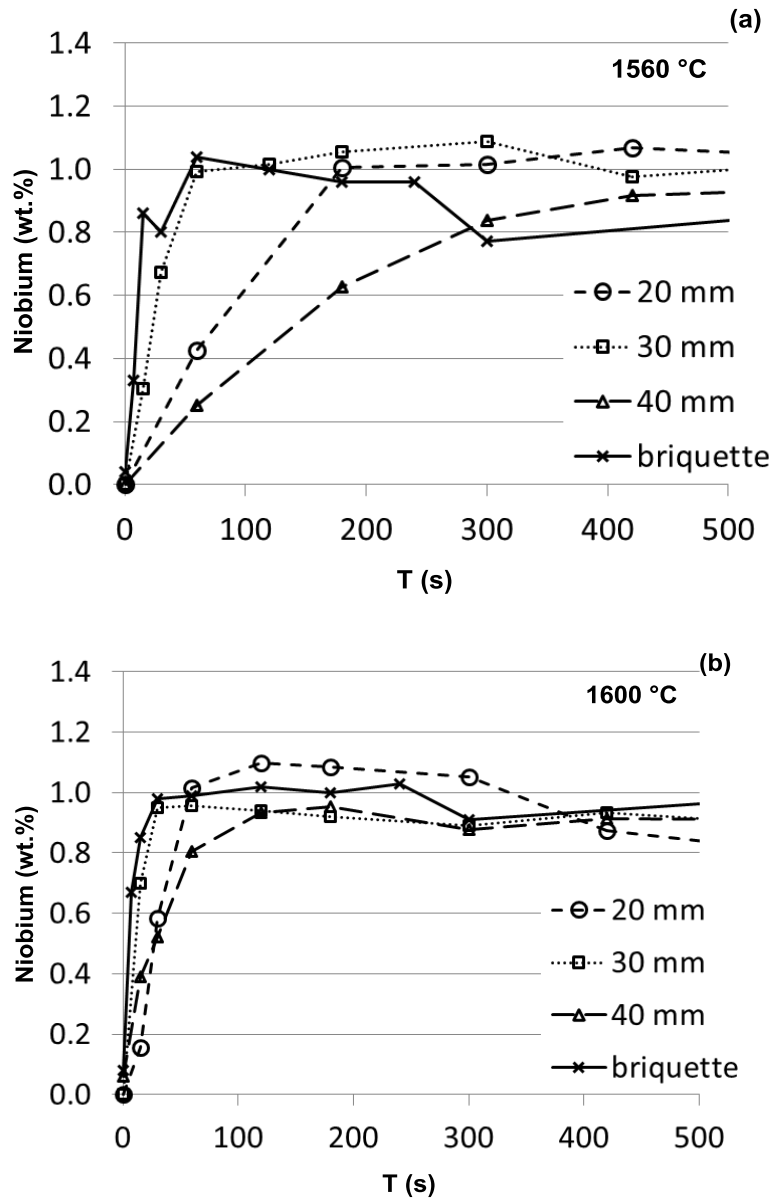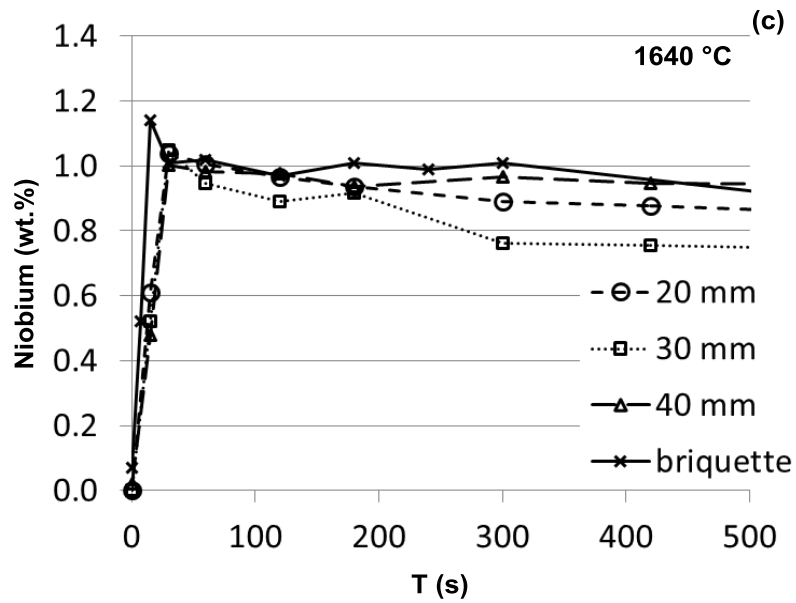
Figure 3. Niobium content as a function of time during the dissolution of FeNb briquettes and lumps at; (a) 1560 °C, (b) 1600 °C and (c) 1640 °C (laboratory scale trials).
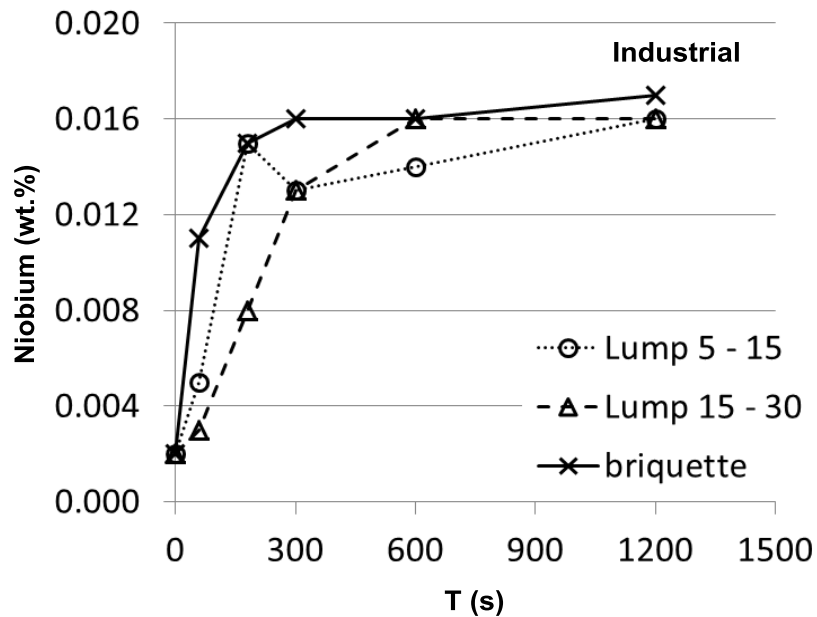

Figure 4. Niobium content as a function of time during the dissolution of FeNb briquettes and lumps at 1570 °C (industrial scale trials).

In Figure 4 it can be seen that in the industrial trials the dissolution rate of briquettes was higher than for lumpy material in the same way as was observed in the laboratory trials. The FeNb briquettes dissolved in less than 5 minutes at the temperature of 1570 °C. As was observed in the laboratory scale trials, the dissolution rate of the lumpy material increased by decreasing the particle size. The yield of the niobium addition at the steel shop was higher than 98% for briquettes and lumpy material.

In the interrupted dissolution trials, conducted at different temperatures, both briquettes and lumps formed a frozen steel shell around them, Figure 5. The thickness of the steel shell decreased as the bath temperature increased, Figures 5(b) and (c). At the interface, the briquettes presented a large number of small (bonded and loose) particles while the lumps consisted of bigger pieces, some of them with cracks filled by thin iron-rich threads.
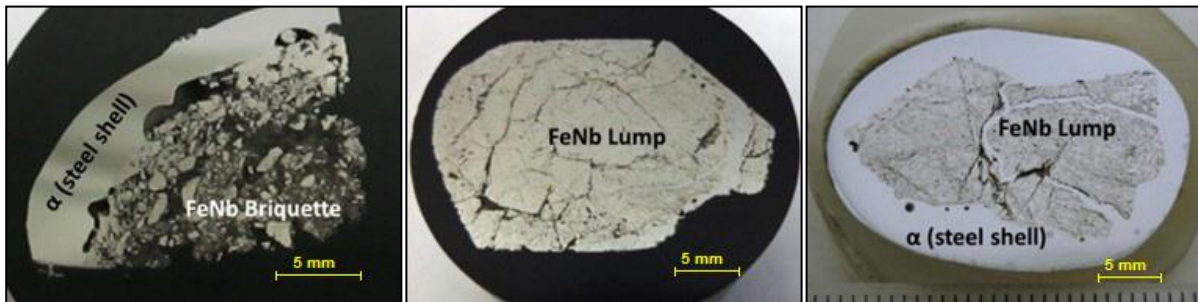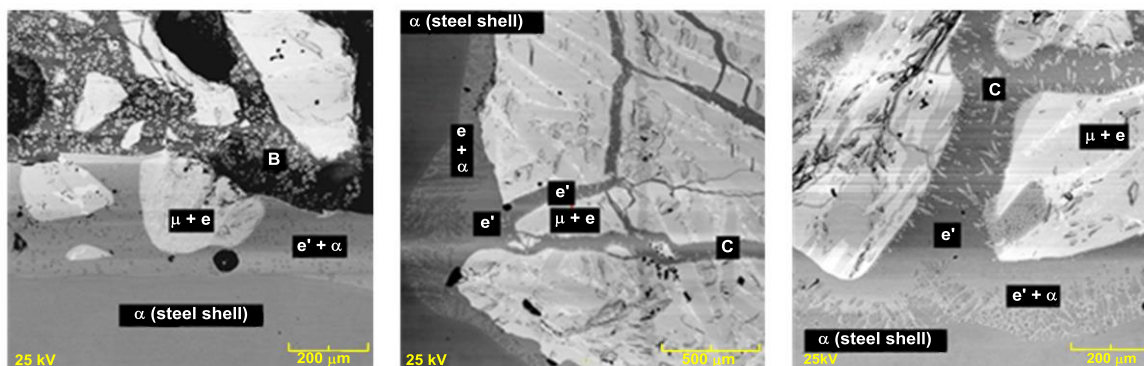

FeNb Briquette – 1550 °C (a)   FeNb Lump – 1550 °C (b)   FeNb Lump – 1600 °C (c)

Figure 5. Steel frozen shells around the FeNb briquette and lump.

Figure 6 shows a microstructural view of the interface between the FeNb briquettes and lump and the steel bath at 1550 °C. The following regions can be recognized:

- The steel shell itself (α) was constituted by an iron-rich layer solidified around the briquettes or lumps during their immersion in the metal bath. The steel shell has the same composition as the steel bath;
- The reaction layer that propagates inwards into the briquette through the binder (b) or into the lump through pre-existing cracks (c). This reaction layer (e'+ α) is composed of an iron rich terminal phase (α) and a low niobium content eutectic zone (e');
- The core of the briquette or lump has the same chemical composition and micro-constituents as the original lumps or briquettes - primary laths of µ and the eutectic zones (e).

Briquette – 1550 °C (a)   Lump – 1550 °C (b)   Lump – 1550 °C (c)

Figure 6. Microstructure of FeNb briquettes and lump at the interface with the steel bath.

The aspect of the interface at 1600 °C and 1650 °C for both lump and briquette was similar, but the steel shell (α) was thinner than for 1550 °C. It was observed that for all the temperatures adopted for the tests, the briquetted FeNb fines, as well as the lumpy material, began to melt down within the eutectic zones.

Discussion

The faster dissolution of the briquettes in relation to the lumpy material, as shown in Figure 3, can be explained by the higher reaction surface area of FeNb fines that are readily released from the binder and immediately brought into contact with the liquid steel. In fact, in Figure 6 it is possible to observe that a large number of small loose FeNb particles are completely exposed in the reaction layer that was formed between the briquette and the steel bath. As soon as the inorganic binder melted down, the FeNb particles were released to the liquid steel and the silicate inclusions floated to the slag.

In Figure 6 it can also be observed that the briquetted FeNb fines, as well as the lumpy material, began to melt down within their eutectic zones. As is shown in the phase diagram in Figure 1, the eutectic zones begin to melt down at approximately 1500 °C, well below the typical steelmaking temperatures of about 1600 °C. The remaining primary laths of $Fe_{21}Nb_{19}$ (μ) melt down also below the typical steelmaking temperatures, when reaching the liquidus temperatures, between 1530 °C and 1570 °C. This behavior explains why both briquettes and lumps dissolve very quickly when added to the liquid steel bath at the melt shop.

As had been verified for lump FeNb [3,4], in the present work, it was possible to verify that the dissolution of briquetted fines occurs through the same mechanism, Figure 7:
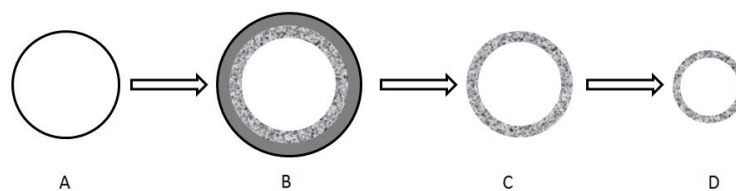

Figure 7. Mechanism of dissolution of FeNb particles in liquid steel.

1st stage (A→B): As soon as the particles at room temperature are added to the steel bath at steelmaking temperatures of around 1600 °C, they begin to heat up and locally freeze the liquid steel, forming a solidified steel shell around them;

2nd stage (B→C): The steel shell achieves its maximum thickness when the temperature equals the steel liquidus temperature and then it begins to remelt. Even before the remelting of the shell begins, the FeNb particles achieve temperatures higher than 1500 °C, whereupon the eutectic regions melt down and begin to react forming the reaction layer below the frozen steel shell, as shown in Figure 6. After the complete remelting of the steel shell, the partially melted FeNb particle comes into direct contact with the liquid steel leading to its rapid dissolution in the liquid. The rapid dissolution of the FeNb particles for all the temperatures adopted indicates that the remelting of the steel shell formed around the particle is not the controlling stage for the mechanism of dissolution;

3rd stage (C→D): In this stage, the dissolution occurs through a combined mechanism of melting and liquid/solid diffusion of the FeNb particles, both controlled by heat transfer.

The small difference between the dissolution rate of FeNb briquettes and lumpy material at higher temperatures (1600 $^{\circ}$C and 1640 $^{\circ}$C) can be explained by the fact that the effect of particle size is minimized when a higher superheat is applied to the steel bath as was shown by Webber [5]. At the higher temperatures the eutectic zones are quickly melted down at exposing the remaining primary laths of $Fe_{21}Nb_{19}$ (μ) phase to the melt.

The high and similar addition yields for both briquettes and lumpy material indicates that the differences in the dissolution rate are strictly related to kinetics once the FeNb particles have the same physicochemical properties.

Conclusions

1.   In the laboratory trials it was observed that briquetted FeNb fines dissolve faster than the lumpy material at temperatures of 1560 °C, 1600 °C and 1640 °C. It was verified that the difference between the dissolution rate of FeNb briquettes and lumpy material is less significant at higher temperatures (1640 °C).

2.   The industrial trials showed that the complete dissolution of briquettes and lumpy material occurred in less than 10 minutes at 1570 °C and that the yield of the niobium addition was higher than 98% for both materials.

3.   The dissolution rate of FeNb briquettes and lumpy material increased by increasing the bath temperature.

4.   Both briquettes and lumps initially formed a frozen steel shell around them. However, while lumpy material exhibited bigger pieces, the briquettes exhibited a large number of small loose FeNb particles at the interface, which may explain their higher dissolution rates.

5. The dissolution of FeNb briquettes and lumps occurs readily through a combined mechanism of melting and liquid/solid diffusion, both controlled by heat transfer.

References

1. M.C. Carboni et al., "Industrial Results for Ferroniobium Dissolution in Liquid Steel" (Paper presented at the 43rd Steelmaking Seminar – International, eds. Belo Horizonte: ABM, 2012), 430 – 438.

2. J.M. Zelaya-Bejarano et al., "The Iron – Niobium Phase Diagram," *Z. Metallkunde,* 84 (1993), 160-164.

3. E.B. Cruz et al., "Dissolution of Ferroniobium in Liquid Steel and Best Addition Practices" (Paper presented at the 41st Steelmaking Seminar – International, eds. Resende: ABM, 2010), 188 – 200.

4. E.B. Cruz et al., "Dissolution of FeNb in Liquid Steel and Best Practices to Increase Niobium Recovery during Ladle Refining" (Paper presented at the 4th Baosteel Biennal Academic Conference, eds. Shanghai: Baosteel, 2010), B34 – B39.

5. D.S. Webber, "Alloy Dissolution in Argon Stirred Steel" (Ph.D. thesis, Missouri University of Science and Technology, 2011), 1-179.

Common Acronyms and Abbreviations

α	Ferrite
α	Pressure Viscosity Coefficient
γ	Austenite
δ	Delta Ferrite
λ	Tallian's Parameter
ν_{120}	Kinematic Viscosity at 120 °C
ρ	Density
σy	Yield Strength
A	Impact Energy
A_{50mm}	Elongation over 50 mm Gauge Length
A_{80mm}	Elongation over 80 mm Gauge Length
AC	Accelerated Cooling
AE	Acoustic Emission
AHSS	Advanced High Strength Steels
AISI	American Iron and Steel Institute
AMS	Aerospace Materials Standard
API	American Petroleum Industry
APT	Atom Probe Tomography
ASTM	American Society for Testing and Materials
Av	Impact Energy
B	Bainite
BCC	Body Centered Cubic
BF	Bainitic Ferrite
BH_2	Bake Hardening Index

BM	Base Metal
B-N	Baker-Nutting
CAB	Calcium Argon Blowing Treatment
CCT	Continuous Cooling Transformation
CEIIW, CE	Carbon Equivalent
CET	Cold Cracking Susceptibility Parameter
CGHAZ	Coarse Grained Heat Affected Zone
COF	Coefficient of Friction
CR	Cooling Rate
CT	Coiling Temperature
CVN	Charpy V-Notch
$D_{C\ 20\%}$	Cut off Grain Size at 80% Accumulated Area Fraction
Delta T_{8-5}	Cooling Time between 800 and 500 °C
DIN	Deutsches Institut fur Normung (Standard)
DLC	Diamond-like Carbon Coating
DLP/NNBB	Discrete Lattice Plane/Nearest Neighbor Broken Bond
D_{mean}	Mean Grain Size
DNV	Det Norske Veritas
DP	Degenerate Pearlite
DP	Dual Phase
DSAW	Double Submerged Arc Welding
DWT	Drop Weight Test
DWTT	Drop Weight Tear Test
E	Young's Modulus
EBSD	Electron Back Scattered Diffraction
EDS, EDX	Energy Dispersive Spectroscopy/Energy Dispersive X-ray Spectroscopy

EHT	Case Hardening Depth to Specified Hardness (HV)
F	Ferrite, Allotromorphic Ferrite
FCC	Face Centered Cubic
FE	Finite Element
FEGSEM	Field Emission Gun Scanning Electron Microscope
FFT	Fast Fourier Transform
FL	Fusion Line
F_N	Applied Normal Force
FP	Ferrite/Pearlite
F_{Pin}	Retarding Force due to Pinning of Dislocations by Precipitate Particles
F_R	Driving Force for Recrystallization Front Migration
FRT	Finish Rolling Temperature
FZG	Type of Gear Wear Test
G	Grain Size according to DIN EN ISO 643
GB	Granular Bainite
GF	Granular Ferrite
GMA	Gas Metal Arc
GRHAZ	Grain Refined Heat Affected Zone
HAADF	High Angle Annular Dark Field
HAZ	Heat Affected Zone
HB or HBW	Brinell Hardness
HDG	Hot Dip Galvanized
h_{min}	Minimum Oil Film Thickness
HRC	Rockwell C Hardness
HRTEM	High Resolution Transmission Electron Microscopy
HSC	High Speed Cutting
HSLA	High Strength Low Alloy

HTHS	High Temperature/High Shear
HTP	High Temperature Processing
HV	Vickers Hardness
ICA	Intercritical Anneal
ICCG	Intercritically Reheated Coarse Grained
ICHAZ	Intercritically Reheated HAZ
ICME	Integrative Computational Materials Engineering
IFFT	Inverse Fast Fourier Transform
IIW	International Institute of Welding
ISIJ	Iron and Steel Institute of Japan
ISO	International Organization for Standardization
JCF	Jet Cooling Zone
K_{1C}	Fracture Toughness Parameter
KAM	Kernel Average Misorientation
K-S	Kurdjumov-Sachs
KV	Charpy Toughness
L	Liquid (steel)
LSW	Lifshitz-Slyozov–Wagner (Particle Coarsening Relationship)
LVDT	Linear Variable Differential Transformer
M	Martensite
M(γ)	Martensite (Austenite at the temperature of note)
MA, M-A, M/A	Martensite/Austenite Phase
MF	Massive Ferrite
MFS	Mean Flow Stress
MMC	Metal Matrix Composite
Ms	Martensite Start Temperature
n total	Load Cycles

n value	Work Hardening Exponent
NOF	Non-Oxidizing Furnace
OEM(s)	Original Equipment Manufacturer(s)
OM	Optical Metallography
P	Lamellar Pearlite
P_{0max}	Contact Stress
PAGS	Prior Austenite Grain Size
PBQ	Premium Bearing Quality
Pcm	Composition Parameter - alternative to Carbon Equivalent
PESR	Pressure Electroslag Remelting
P_f	Time at which Precipitation Hardening reaches a maximum
PF	Polygonal Ferrite
PN	Pressed Notch
PP	Pressed Part
ppm	Parts Per Million
P_S	Start Time of Precipitation
PTT	Precipitation-Time-Temperature
Q&T	Quenched and Tempered
QF	Quasipolygonal Ferrite
Ra	Surface Roughness Value
RCS	Rapid Cooling Section or Round-corner Square
Rm	Tensile Strength
$R_{P0.2}$	0.2% Proof Strength
RT	Room Temperature
RTF	Radiant Tube Furnace
RX	Recrystallization Annealing
SAD	Selected Area (Electron) Diffraction

SAE	Society of Automotive Engineers
SAG	Semi-autogenous Grinding
SAW, SA	Submerged Arc Welding
SCHAZ	Subcritically Reheated Heat Affected Zone
SCS	Slow Cooling Section
SDAS	Secondary Dendrite Arm Spacing
SEM	Scanning Electron Microscope
SEM-EDX	Scanning Electron Microscope - Energy Dispersive X-ray
SMTS	Specified Minimum Tensile Strength
SMYS	Specified Minimum Yield Strength
S-N	Stress v Life (Fatigue Curve)
SRP	Solute Retardation Parameter
SRX	Static Recrystallization
STEM	Scanning Transmission Electron Microscope
T	Temperature
T_A	Carburization Temperature
TBN	Total Base Number
TEM	Transmission Electron Microscope
T_F	Forming Temperature
t_{ip}	Interpass Time
TMCP	Thermomechanical Controlled Processing
Tnr	Temperature for No Recrystallization
Tp	Peak Temperature
TRIP	Transformation Induced Plasticity
TS	Tensile Strength
UOE	Pipe Forming Process
VAR	Vacuum Arc Remelting

Vdiff	Sliding Speed
VIM	Vacuum Induction Melting
WCI	White Cast Iron
XRD	X-ray Diffraction
YS	Yield Strength
Z	Maximum Pinning Force

AUTHOR INDEX
Fundamentals and Applications of Mo and Nb Alloying in High Performance Steels: Volume 2

SUBJECT INDEX
Fundamentals and Applications of Mo and Nb Alloying in High Performance Steels: Volume 2